AEDC-TR-85-26

Flow Field Mapping of Carbon Dioxide Nozzle Expansion into Vacuum

A. B. Bailey and L. L. Price
Calspan Corporation

July 1985

Final Report for Period October 1, 1983 – September 30, 1984

APPROVED FOR PUBLIC RELEASE, DISTRIBUTION
IS UNLIMITED - 4 JAN 1999 - AEDC/PA 99-004
APPLIES. OPR: AEDC/DOS

ARNOLD ENGINEERING DEVELOPMENT CENTER
ARNOLD AIR FORCE STATION, TENNESSEE
AIR FORCE SYSTEMS COMMAND
UNITED STATES AIR FORCE

UNCLASSIFIED
SECURITY CLASSIFICATION OF THIS PAGE

REPORT DOCUMENTATION PAGE

1a REPORT SECURITY CLASSIFICATION
UNCLASSIFIED

1b RESTRICTIVE MARKINGS

2a SECURITY CLASSIFICATION AUTHORITY

2b DECLASSIFICATION/DOWNGRADING SCHEDULE

3 DISTRIBUTION/AVAILABILITY OF REPORT
See Reverse of This Page.

4 PERFORMING ORGANIZATION REPORT NUMBER(S)
AEDC-TR-85-26

5 MONITORING ORGANIZATION REPORT NUMBER(S)

6a NAME OF PERFORMING ORGANIZATION
Arnold Engineering
Development Center

6b. OFFICE SYMBOL (If applicable)
DOT

7a NAME OF MONITORING ORGANIZATION

6c. ADDRESS (City, State and ZIP Code)
Air Force Systems Command
Arnold Air Force Station, TN 37389-5000

7b ADDRESS (City, State and ZIP Code)

8a. NAME OF FUNDING/SPONSORING ORGANIZATION Arnold
Engineering Development Center

8b OFFICE SYMBOL (If applicable)
DOS

9 PROCUREMENT INSTRUMENT IDENTIFICATION NUMBER

8c ADDRESS (City, State and ZIP Code)
Air Force Systems Command
Arnold Air Force Station, TN 37389-5000

10 SOURCE OF FUNDING NOS

PROGRAM ELEMENT NO	PROJECT NO	TASK NO	WORK UNIT NO.
65807F			

11 TITLE (Include Security Classification)
See Reverse of This Page.

12. PERSONAL AUTHOR(S)
Bailey, A. B. and Price, L. L., Calspan Corporation, AEDC Division

13a. TYPE OF REPORT
Final Report

13b TIME COVERED
FROM 10/1/83 TO 9/30/84

14 DATE OF REPORT (Yr., Mo., Day)
July 1985

15 PAGE COUNT
144

16 SUPPLEMENTARY NOTATION
Available in Defense Technical Information Center (DTIC).

17 COSATI CODES

FIELD	GROUP	SUB GR
20	04	
09	02	

18 SUBJECT TERMS (Continue on reverse if necessary and identify by block number)
flow field mapping
nozzle flow
carbon dioxide expansion
backflow region
plume properties
(Cont)

19 ABSTRACT (Continue on reverse if necessary and identify by block number)

A series of tests has been completed at the Arnold Engineering Development Center (AEDC) to define the flow field of a nozzle plume in a hard vacuum. The purpose of these tests was to provide an experimental data base which could be used to verify currently available computer codes that are used to predict plume properties in the nozzle backflow region. Interest in such measurements derives from the fact that the currently available codes cannot accurately define nozzle flow in the backflow region of the nozzle where sensitive spacecraft surfaces and sensors can be positioned. In the present investigation, plume characteristics of carbon dioxide expansions from three 15-deg half-angle conical nozzles with a common exit diameter of 4 in. (10 cm) and area ratios of 16, 44.4, and 400 have been evaluated. A range of flow diagnostics including electron beam fluorescence, rotary liquid-nitrogen-cooled quartz crystal microbalance, free-molecule heat-transfer probe, free-molecule pressure probe, and a rotary pitot probe were used in this evaluation.
(Cont)

20 DISTRIBUTION/AVAILABILITY OF ABSTRACT
UNCLASSIFIED/UNLIMITED ☐ SAME AS RPT ☒ DTIC USERS ☐

21 ABSTRACT SECURITY CLASSIFICATION
UNCLASSIFIED

22a. NAME OF RESPONSIBLE INDIVIDUAL
W. O. Cole

22b TELEPHONE NUMBER (Include Area Code)
(615)454-7813

22c OFFICE SYMBOL
DOS

DD FORM 1473, 83 APR

EDITION OF 1 JAN 73 IS OBSOLETE

UNCLASSIFIED
SECURITY CLASSIFICATION OF THIS PAGE

3. DISTRIBUTION/AVAILABILITY OF REPORT

~~Distribution limited to U.S. Government agencies and their contractors; critical technology; July 1985. Other requests for this document shall be referred to Arnold Engineering Development Center/DOS, Arnold Air Force Station, TN 37389-5000.~~

Public Domain
AEDC/PA 99-004 applies
4 Jan 1999

11. TITLE

Flow Field Mapping of Carbon Dioxide Nozzle Expansion Into Vacuum

18. SUBJECT TERMS (Concluded)

computer codes
flow diagnostic techniques

19. ABSTRACT (Concluded)

Measurements of number density, rotational temperature, heat transfer, mass flux, flow angle, and pitot pressure are presented with a delineation of the effect that changes in lip geometry, chamber background pressure, and backflow cryopumping have upon nozzle plume properties.

PREFACE

The work reported herein was conducted at the Arnold Engineering Develoment Center (AEDC), Air Force Systems Command (AFSC). The results were obtained by Calspan Corporation, AEDC Division, operating contractor for the aerospace flight dynamics test facilities at the AEDC, AFSC, Arnold Air Force Station, Tennessee, under AEDC Project Number D26VW (V32M-CU). The Air Force Project Managers were Capt. Kenneth Leners and Mr. D. A. Duesterhaus. Data analysis was completed on September 30, 1984, and the manuscript was submitted for publication on March 11, 1985.

The following have been contributors to this project: J. H. Jones—interfacing of chamber control systems with the computer; B. Seiber, R. Reeves, and B. J. McClure—installation and operation of instrumentation systems; C. Kidd and W. Scott—fabrication and calibration of the hot-wire probes; T. Isbell—fabrication of nozzle and probe support hardware; B. E. Wood—advice on the operation and interpretation of the quartz crystal microbalance; and Dr. F. Collins (University of Tennessee Space Institute)—design of hot-wire control system and analysis of hot-wire measurements.

CONTENTS

Page

1.0 INTRODUCTION 7
2.0 DESCRIPTION OF EXPERIMENTAL FACILITY AND APPARATUS 9
  2.1 Experimental Test Facility 9
  2.2 Nozzles and Gas Supply 10
3.0 PURE-GAS FLOW DIAGNOSTICS 17
  3.1 Pitot Pressure Measurements 17
  3.2 Free-Molecule Pressure Probe 21
  3.3 Quartz Crystal Microbalance 23
  3.4 Free-Molecule Heat-Transfer Probe 25
  3.5 Electron Beam Fluorescence Technique 28
4.0 TEST DESCRIPTION 29
  4.1 Test Unit and Nozzle Operating Conditions 29
  4.2 Diagnostic Measurements 34
5.0 DISCUSSION OF RESULTS 36
  5.1 Pitot Pressure Measurements 36
  5.2 Quartz Crystal Microbalance 58
  5.3 Effect of Nozzle Lip Geometry on Plume Characteristics 75
  5.4 Free-Molecule Pressure Probe 80
  5.5 Effect of Chamber Background Pressure on Nozzle Flow 96
  5.6 Free-Molecule Heat-Transfer Probe Measurements 113
  5.7 Electron Beam Fluorescence Measurements 119
6.0 CONCLUSIONS AND RECOMMENDATIONS 126
REFERENCES 129

ILLUSTRATIONS

Figure

1. Schematic of the 4-by 10-ft Research Vacuum Chamber 9
2. Exit-Plane Mach Number for Nozzle Expansions into a Vacuum 12
3. Sketch of Conical Nozzles 13
4. Stainless Steel Sonic Orifice 14
5. Gas Inbleed to Nozzle Stilling Chamber 15
6. Schematic of the Nozzle, Stilling Chamber, and Traverse Assembly 15
7. Gas Addition System 16

Figure Page

8. Relationship Between Pitot and Dynamic Pressure 18
9. Pitot Tube Data—Supersonic Nozzles, September 1967 (N_2) (Fig. A-1 from Ref. 24) 20
10. The Berkeley Controls MK9 Contamination Sensor 24
11. Sketch of Rotatable Quartz Crystal Microbalance 26
12. Sketch of Free-Molecule Heat-Transfer Probe 27
13. Prototype of Free-Molecule Heat-Transfer Probe 27
14. Chamber and Nozzle Operating Characteristics 32
15. Typical Computer Printout, Run 230 33
16. Typical Data Plots, Run 230 34
17. Centerline Pitot Pressure Measurements—Basic Repeatability of Test Conditions 36
18. Centerline Flow Field Properties as a Function of Axial Distance 38
19. Radial Pitot Pressure Profiles at Several Axial Positions Downstream of Exit Plane—Raw Data 42
20. Nondimensionalized Radial Pitot Pressure Profile 43
21. Variation of Pitot Pressure with Angle of Probe to Flow 44
22. Effect of Probe Misalignment to Flow Velocity Vector on Radial Pitot Pressure Measurements 46
23. Effect of Probe Reynolds Number on the Variation of Pitot Pressure with Probe Angle to the Flow 47
24. Pitot Pressure Measured with Probe Aligned with Velocity Vector—Raw Data 48
25. Effect of Pitot Probe Size on Flow-Angle Measurements 49
26. Effect of Pitot Probe Size on Radial Pitot Profiles Close to the Nozzle Exit 51
27. Experimental Measurements of Flow Angle 53
28. Flow Angle as a Function of Axial and Radial Location 54
29. Spatial Map of Constant CO_2 Flow-Angle Values 55
30. Nonradial Nature of Expanding Flow 57
31. Spatial Map of Constant CO_2 Pitot Pressure Values, Uncorrected for Viscous Effects 58
32. Strip Chart Record of QCM Output 60
33. QCM Strip Chart Record with Varying Probe Angle 61
34. Mass Flux as a Function of Probe Angle 62
35. Spatial Map of Constant CO_2 Mass Flux Values 64
36. Mass Flux in Nozzle Background 66
37. Mass Flux Measurements as a Function of Radial and Angular Position 68
38. Angular Variation of Number Density, Mass Flux, and Dynamic Pressure at a Fixed Radius from the Center of the Nozzle Exit Plane 69

Figure | Page

39. Comparison of Mass Flux Measurements 71
40. Angular Variation of Number Density at a Fixed Radius from the Center of the Nozzle Exit Plane 73
41. Effect of Lip Geometry and State-of-the-Gas on the Angular Distribution of Number Density 74
42. Effect of Molecular Weight of Gas on Mass Flow into the Backflow Region 75
43. Effect of Lip Geometry on Radial Profiles of Pitot Pressure and Flow Angle 76
44. Effect of Lip Geometry on Centerline Mach Number as a Function of Axial Distance 80
45. Free-Molecule Pressure Probe—Basic Flow-Angle Measurements 82
46. Flow-Angle Measurements Obtained with a Cylindrical Free-Molecule Pressure Probe 83
47. Free-Molecule Pressure Probe Measurements in the Nozzle Plume 84
48. Pressure Variation with Angle of Orifice to Flow 85
49. Free-Molecule Pressure Probe Calibration 87
50. Effect of Cryopumping in Backflow Region on Exit-Plane Pitot Profiles 89
51. Pressure Variation with Angle of Orifice to Flow—No Background Cryopumping 90
52. Flow Characteristics with No Backflow Cryopumping 94
53. Effect of Cryopumping in Backflow Region on Flow Angle 95
54. Effect of Partial Cryopumping in Backflow Region on Flow Angle 96
55. Flow Profiles at Elevated Chamber Pressure—Raw Data 97
56. Flow Profiles with Varying Chamber Pressure 99
57. Radial Pitot Profiles for $A/A^* = 400$ Nozzle 104
58. Effect of Ambient Pressure on Exit-Plane Pitot Pressure Profiles 107
59. Effect of Varying Background Pressure on Wall Static and Centerline Pitot Pressure 110
60. Wire Resistance as a Function of Applied Power 114
61. Free-Molecule Heat-Transfer Probe Measurements 115
62. Heat-Transfer and Pitot Pressure Profiles 117
63. Number Density on Axial Centerline 120
64. Number Density Radial Profiles 121
65. Spatial Map of Constant CO_2 Number Density Values 122
66. Continuous Wavelength CO_2^+ Scan Near Exit Plane Centerline 123
67. Comparison of 108 K Experimental Scan with 100 K Synthetic Spectra 123
68. Band Intensity Ratio Versus CO_2 Rotational Temperature 124
69. Radial Profiles of CO_2 Rotational Temperature 125
70. Spatial Map of Constant CO_2 Rotational Temperature Values 126

Page

TABLES

1. Estimate of Nozzle Exit-Plane Characteristics 13
2. Free-Molecule Pressure Probe Characteristics 23
3. Quartz Crystal Microbalance Characteristics 24
4. Basic Test Variables 31
5. Mass Flux Calibration 66

APPENDIX

A. Estimate of Uncertainties 135

NOMENCLATURE 139

1.0 INTRODUCTION

The contamination of spacecraft surfaces and components by exhaust products from spacecraft thrusters, whether solid-, liquid-, or electric-propellant, is of considerable concern to the spacecraft design community. This concern is attributable to the development of more sophisticated spacecraft systems designed to perform multiple, noninterfering missions for long periods of time in space. Contamination and subsequent degradation of sensitive spacecraft surfaces and components such as thermal control coatings, solar cells, antennas, optical devices, and cooled infrared sensors can compromise mission objectives and lead to a reduction in spacecraft lifetime. For example, contamination of surfaces which normally have low absorptivity-to-emissivity properties (required for passive control of spacecraft temperatures) can result in a heat imbalance with a subsequent change in spacecraft temperature, thus affecting the spacecraft mission and/or lifetime.

It is apparent from a consideration of the operational characteristics of presently available space simulation chambers that experimental studies directed toward the simulation of rocket plumes in space is limited to small, low-thrust motors. Accordingly, computational codes are in the process of development (e.g., Ref. 1) to predict the characteristics of the plumes generated by large rocket motors at high altitudes. A number of experimental investigations of the plume characteristics of small liquid-propellant rocket motors exhausting into a hard vacuum have been carried out in ground-based space simulation chambers (Refs. 2, 3, and 4.) It was intended to use the results of these experimental studies (i.e. Refs. 2, 3, and 4) to validate computer codes of the type described in Ref. 1. However, the difficulties associated with the correct modeling of the chemical and fluid dynamic processes that occur when these small liquid-propellant motors exhaust into a hard vacuum were such that it has not been possible to this time to accomplish the validation of the computer code in a completely satisfactory manner.

In an effort to reduce both computational and experimental complexity, the Air Force Rocket Propulsion Laboratory (AFRPL) recently instituted an experimental test program at the Arnold Engineering Development Center (AEDC) to define the flow characteristics of pure-gas expansions into a hard vacuum. The results of a study (Refs. 5 and 6) of nitrogen and carbon dioxide expansions from a small-scale high area ratio nozzle into a hard vacuum show that the nozzle boundary layer is affected by nozzle wall temperature, nozzle lip geometry, condensation in the expanding core flow, and chamber background pressure. Furthermore, electron beam fluorescence measurements of rotational temperature in the expansion of the nozzle boundary layer into a vacuum have shown significant regions of rotational nonequilibrium. It was also found that computations of the nozzle boundary-layer characteristics in the nozzle exit plane using a code developed by Whitfield (Ref. 7) were not in agreement with the experimental data. This was an unexpected result, since a review of nozzle boundary-layer codes by Edwards (Refs. 8), indicated that Whitfield's technique was an acceptable, appropriate approach. This inability to predict accurately the boundary-layer characteristics of an ideal gas nozzle expansion (nitrogen with no condensation) into a hard vacuum suggests that the currently available techniques used to predict the flow characteristics of more complex nozzle expansions, e.g., monopropellant, bipropellant, and solid-propellant rocket motor, may be of questionable validity. As a result of these and other experimental studies (Refs. 3 and 6) it has been concluded that additional basic studies of the properties of nozzle expansions into a vacuum are required in order to provide a more complete and accurate experimental data base which can be used for computational code validation. The basic objective of the present experimental test program was to obtain a comprehensive data base which could be used to validate computational codes that are under development at AFRPL. To accomplish this objective, a basic measurements program was designed to characterize the flow field of the plume that results from the expansion of carbon dioxide from a conical nozzle into a vacuum. The experimental program was formulated to be conducted in the 4- by 10-ft Research Vacuum Chamber (RVC) at the AEDC. A number of basic investigations of various low-density flow phenomena have been carried out in this test facility (e.g., Refs. 3, 5, 6, and 9 through 14). Although this test chamber does have a 20 K gaseous helium cryopumping capability, for the present application the chamber has been modified to utilize 77 K liquid nitrogen (LN_2) cryopumping only. A wide range of flow diagnostic techniques has been used to determine the characteristics of these plumes,

- Pitot pressure probes—flow angle, dynamic pressure
- Free-molecule pressure probe—flow angle, speed ratio
- Free-molecule heat-transfer probe—heat transfer, adiabatic wall temperature
- Quartz crystal microbalance (QCM)—flow angle, mass flux
- Electron beam fluorescence (EBF)—number density, rotational temperature

The effects of nozzle area ratio, lip geometry, chamber pressure, condensation, and cryopumping in the nozzle backflow region on the characteristics of the plume have been evaluated using these diagnostic techniques.

2.0 DESCRIPTION OF EXPERIMENTAL FACILITY AND APPARATUS

2.1 EXPERIMENTAL TEST FACILITY

The 4- by 10-ft Research Vacuum (RVC), Fig. 1, is a stainless steel cylindrical vacuum chamber with an internal diameter of approximately 3.5 ft (1.07 m) and an overall length of approximately 14 ft (4.27 m). The RVC is comprised of three sections, movable, stationary, and an instrumentation spool piece which are 4, 8.5, and 1.5 ft (1.2, 2.6, and 0.46 m) in length, respectively. Vacuum conditions within the RVC are achieved through the use of mechanical pumps, diffusion pumps, and LN_2 cryopumps (77 K). In the present application the 77 K, LN_2 cryoliners are used to pump the carbon dioxide test gas, whereas the mechanical and oil diffusion pumping systems remove the small quantities of N_2, O_2 and other noncondensible contaminants contained in the commercially available gas. It should be noted that the LN_2 cryoliners in the movable and stationary sections can be operated independently of each other. Thus, the cryoliner in the movable section, which pumps the plume gases in the backflow region, can be operated independently of the cryoliners in the stationary section which pumps the gases in the forward-flow region of the nozzle. This operational characteristic permits studies of the effect of plume gas scattering from the warm chamber wall on the flow of plume gases into the backflow region by simply not cooling this section of the RVC.

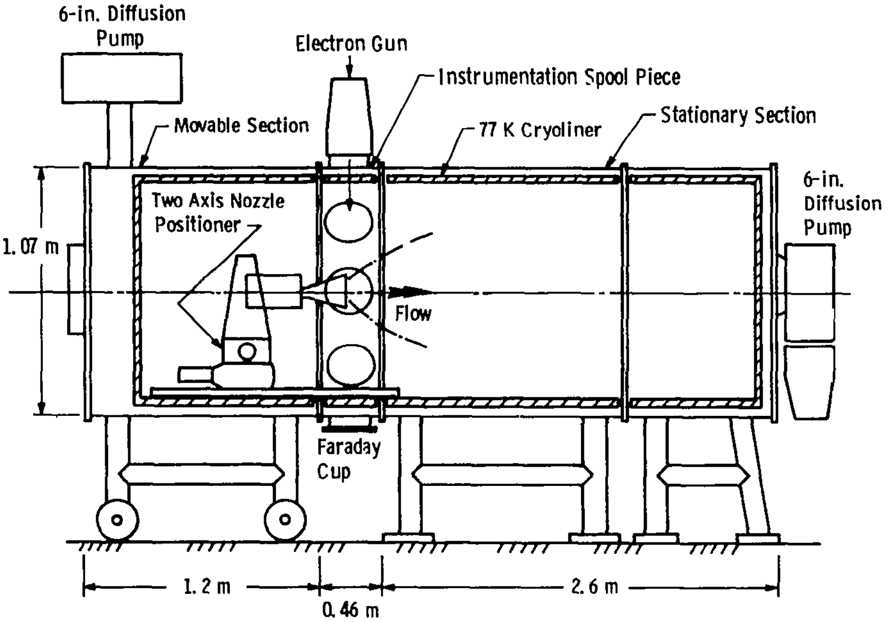
6-in. Diffusion Pump
Electron Gun
Instrumentation Spool Piece
Movable Section
77 K Cryoliner
Stationary Section
6-in. Diffusion Pump
Two Axis Nozzle Positioner
1.07 m
Flow
Faraday Cup
1.2 m
0.46 m
2.6 m

Figure 1. Schematic of the 4- 10-ft Research Vacuum Chamber.

2.2 NOZZLES AND GAS SUPPLY

The requirements of the test program, the operational characteristics of the 4- by 10-ft RVC, and the results of an earlier AFRPL-sponsored study in the RVC were taken into consideration in the design of the test nozzles and the choice of the test gas.

The evaluation of the mechanism affecting the flow of gas into the nozzle backflow region was an area of prime interest in the present study. It is generally accepted that this gas flow derives from the expansion of the nozzle boundary layer. Therefore, one of the requirements for the present study was that the nozzle boundary layer in the nozzle exit plane should be of a sufficient thickness to permit resolved flow field measurements, i.e. on the order of 1 in. (2.54 cm). The number density on the exit-plane centerline should be on the order of $10^{15}/\text{cm}^3$ in order to minimize the magnitude of the quenching corrections required for electron beam fluorescence measurements. The stagnation temperature of the gas should be controlled such that condensation in the expanding flow will occur downstream of the nozzle exit plane. To simplify nozzle design and fabrication, it was decided to limit the present study to 15-deg half-angle conical configurations with a fixed exit diameter, 4 in. (10.2 cm), and various throat diameters.

An evaluation of the experimental data presented in Refs. 5 and 6 indicated that flow field measurements in carbon dioxide expansions were as valid as those made in nitrogen. At this stage in the development of computational codes, the additional complexity introduced by the use of CO_2 rather than N_2 is inconsequential since the currently available codes cannot provide accurate predictions for ideal N_2 expansions. From an operational point of view, the use of CO_2 is desirable in that it requires LN_2 cryopumping rather than the significantly more expensive GHe cryopumping that would be required with the use of N_2.

Earlier studies in the 4- by 10-ft RVC with CO_2 as the test gas (Refs. 5 and 6) have shown that acceptable background pressures (10^{-5} torr) can be achieved with nozzle flow rates on the order of 2 gm/sec. Therefore, in the present study, it was decided to design the nozzles for a flow rate of approximately this magnitude.

Given the choice of exit diameter of 4 in. (10.2 cm), test gas of CO_2, nozzle half-angle of 15 deg, and a mass flow of approximately 2 gm/sec, there remained to be defined the nozzle stagnation conditions and throat diameter that would produce an acceptable flow in the nozzle exit plane. An engineering approach was taken to this problem. There is a significant body of experimental data which defines the exit-plane flow characteristics of conical and contoured nozzle expansions into a vacuum (Refs. 5, 6, 7, 9 and 15 through 22). An analysis of these measurements suggests that for engineering purposes the exit-plane Mach number, M, can be related to the (1) limiting Mach number M_L defined by the nozzle geometric area ratio, (2) throat Reynolds number, Re_0r^* (Ref. 7), (3) nozzle wall temperature, (4) stagnation temperature, and (5) the mean geometric half-angle of the nozzle. The results of this analysis are summarized in Fig. 2.

The operating conditions for the nozzles that were selected for use in the present investigation are given in Table 1. Conditions 1 and 2 (Table 1) were selected to ensure that condensation could not occur in the nozzle exit plane, i.e. no flow supercooling. Condition 3, on the other hand, does permit the possibility of condensation in the exit plane as the flow is supercooled. (It should be noted that the presence of supercooling in the flow does not necessarily result in condensation, cf. Ref. 12).

Sketches of the conical nozzles and the sonic orifice are presented in Figs. 3 and 4. With the exception of the 0.2-in-diam (0.51-cm) throat configuration (Fig. 3c), the nozzle lip was honed to a knife edge having a thickness on the order of 1×10^{-3} in. (2.5×10^{-3} cm). In subsequent discussions of nozzle configurations in this report, this will be referred to as the "thin-lip" configuration. This is to distinguish it from the "thick-lip" configuration which was obtained by slipping a cylindrical ring having a thickness of 0.25 in. (0.63 cm) over the end of the thin-lip configuration. The 0.2-in.-diam. (0.51-cm) throat nozzle existed in the thick-lip version only (Fig. 3c).

Each of the nozzles and the sonic orifice were welded directly to a stilling chamber which consisted of an 8.5-in.-long (21.6-cm), 4.0-in.-diam (10.2-cm) schedule 40 pipe. In an attempt to ensure a uniform distribution of the inlet gas throughout the stilling chamber, the gas inlet tube within the stilling chamber was modified as shown in Fig. 5. Provision was made to measure the total temperature of the gas within the stilling chamber with a shielded Chromel®-Alumel® thermocouple. The temperature distribution along the nozzle and stilling chamber wall was monitored with Chromel-Alumel themocouples attached to the outer wall. Stilling chamber pressure was measured with an absolute 5-psia Taber® pressure transducer.

An 800-w in-line serpentine heater positioned immediately upstream of the stilling chamber, Fig. 6, can heat the test gas to temperatures approaching 1,000 K. Four 750-w band heaters strapped to the stilling chamber are capable of raising the stilling chamber wall to a temperature on the order of 1,000 K. Thus, it is possible to operate with the stilling chamber and inlet gas at approximately the same temperature.

The nozzle and stilling chamber assembly was mounted on a traversing table located in the movable section of the RVC (Fig. 6). This table provides 6 in. (15.2 cm) of motion in

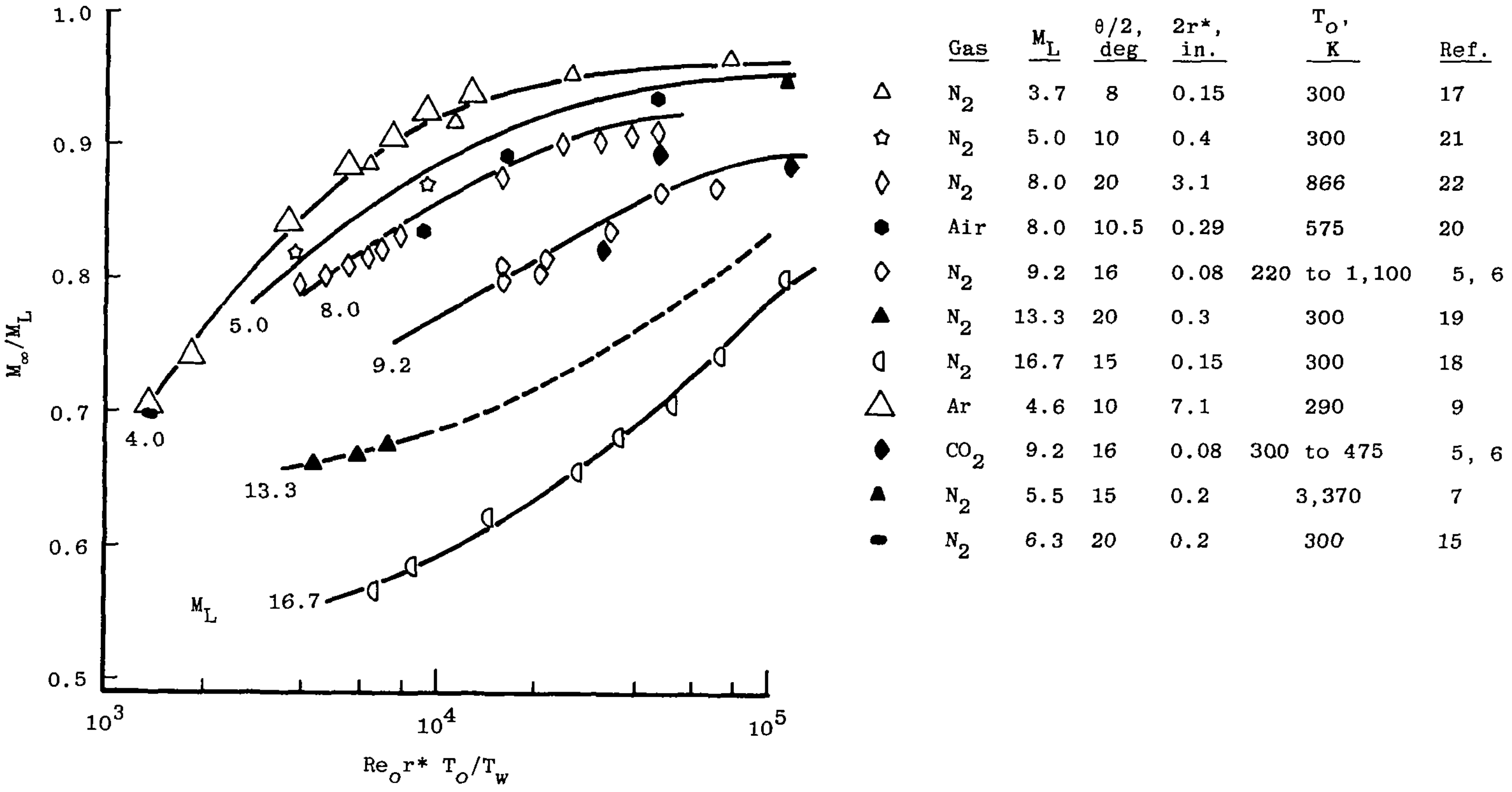

	Gas	M_L	θ/2, deg	2r*, in.	T_o, K	Ref.
△	N_2	3.7	8	0.15	300	17
✩	N_2	5.0	10	0.4	300	21
◊	N_2	8.0	20	3.1	866	22
⬢	Air	8.0	10.5	0.29	575	20
◇	N_2	9.2	16	0.08	220 to 1,100	5, 6
▲	N_2	13.3	20	0.3	300	19
◖	N_2	16.7	15	0.15	300	18
△	Ar	4.6	10	7.1	290	9
◆	CO_2	9.2	16	0.08	300 to 475	5, 6
▲	N_2	5.5	15	0.2	3,370	7
⬬	N_2	6.3	20	0.2	300	15

Figure 2. Exit-plane Mach number for nozzle expansions into a vacuum.

Table 1. Estimates of Nozzle Exit-Plane Characteristics

Flow Conditions	$2r^*$, in.	$(M_\infty)_{cl}$	p_o, torr	T_o, K	p_∞, torr	T_∞, K	n_∞, cm^{-3}	Core Diam, in.
1	1.0	4.0	10	500	0.063	119	5×10^{15}	3.0
2	0.6	5.1	33	700	0.056	113	4.7×10^{15}	3.0
3	0.2	8.0	257	700	0.031	51	5.8×10^{15}	2.70

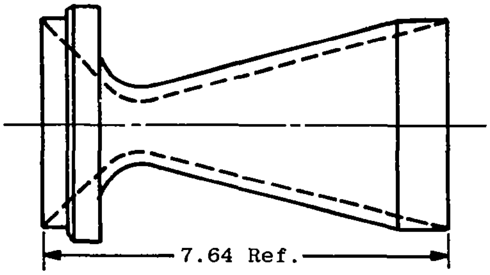

a. Throat diameter, 1.0 in.; area ratio, 16; lip thickness ≈ 0.001 in.

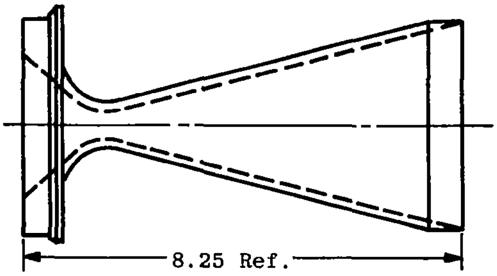

b. Throat diameter, 0.6 in.; area ratio, 44.4; lip thickness ≈ 0.001 in.

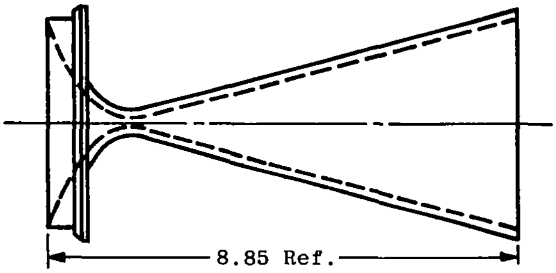

All Dimensions, in.

Nozzle Half-Angle, 15 deg

c. Throat diameter, 0.2 in.; area ratio, 400; lip thickness ≈ 0.125 in.

Figure 3. Sketch of conical nozzles.

both the lateral and axial directions to an accuracy of ± 5×10^{-4} in. (1.3×10^{-3} cm). This degree of motion and positioning accuracy has been accomplished through the use of two commercially available Aerotech® stepping-motor-driven positioning tables. It should be noted (cf. Fig. 6) that the nozzle positioning tables and the various flow diagnostic probes are mounted to a common support structure. This arrangement allows for the accurate positioning of a particular probe configuration with respect to the nozzle prior to the evacuation of the chamber. No relative motion of these components would be expected to occur subsequent to chamber evacuation.

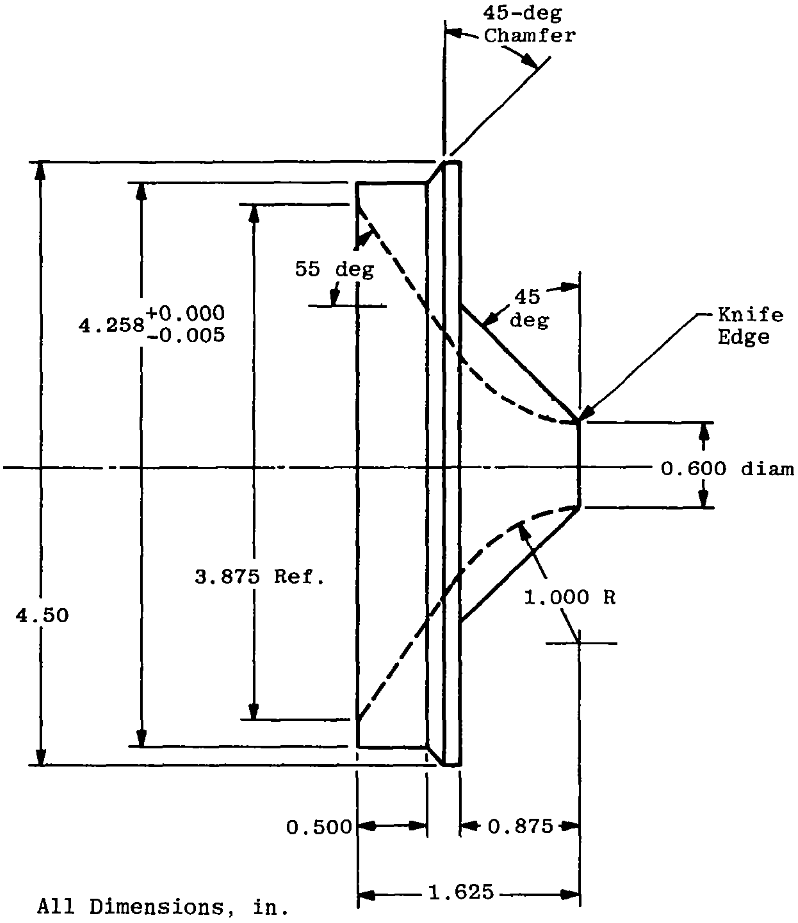

Figure 4. Stainless steel sonic orifice.

One of the objectives of the present program was to investigate the flow of gas into the nozzle backflow region. To minimize the effect that the nozzle, stilling chamber, and the support structure have upon the flow of this region, a liquid-nitrogen-cooled plate, having internal and external diameters of 4.5 and 9.5 in. (11.4 and 24.2 cm), respectively, was positioned in the region of the nozzle throat (Fig. 6).

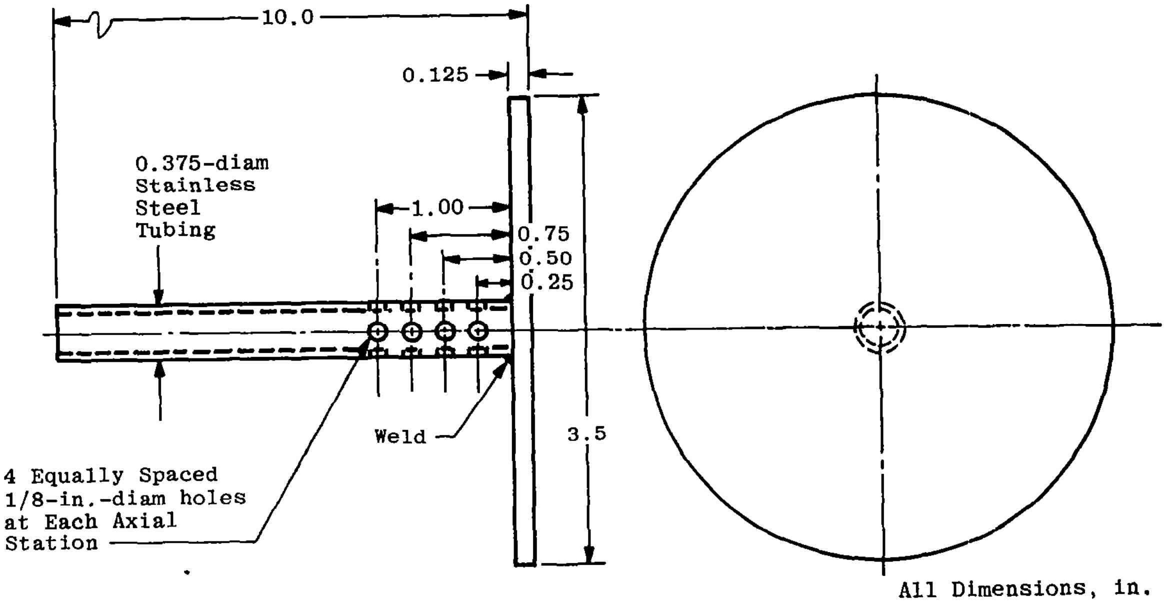
10.0
0.125
0.375-diam Stainless Steel Tubing
1.00
0.75
0.50
0.25
Weld
3.5
4 Equally Spaced 1/8-in.-diam holes at Each Axial Station
All Dimensions, in.

Figure 5. Gas inbleed to nozzle stilling chamber.

Thin, circular orifices operating at supercritical pressure ratios provide a simple, inexpensive, and accurate means for the measurement of the mass flow rate of a gas. Provided supercritical flow can be maintained, it can be shown that the mass flow through

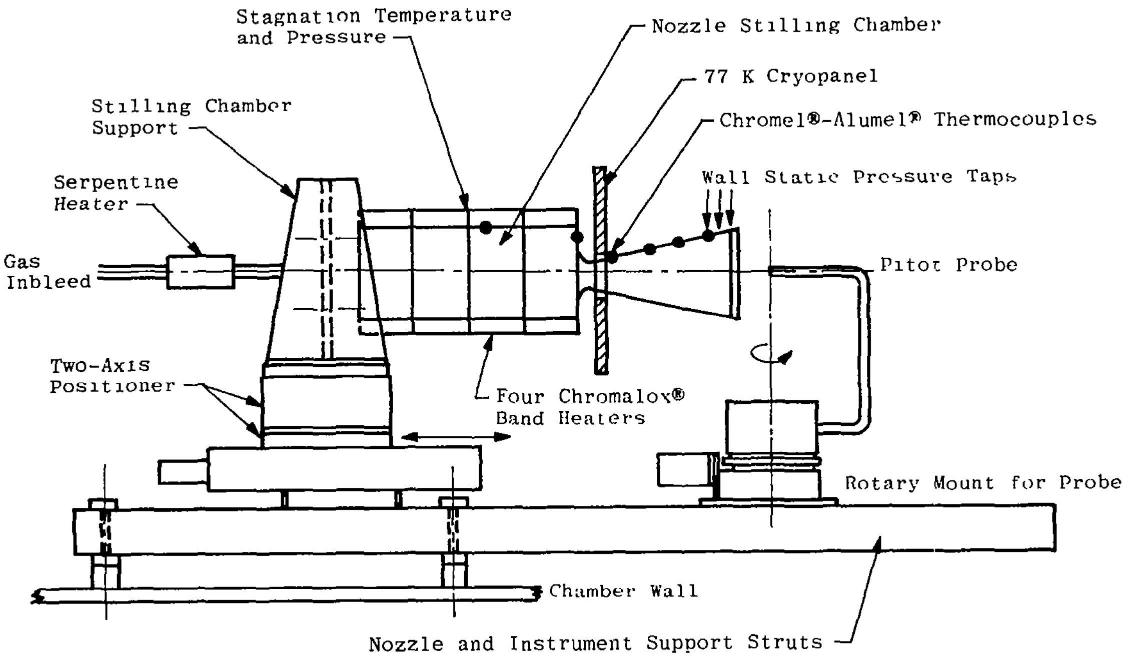
Stagnation Temperature and Pressure
Nozzle Stilling Chamber
77 K Cryopanel
Chromel®-Alumel® Thermocouples
Stilling Chamber Support
Serpentine Heater
Wall Static Pressure Taps
Gas Inbleed
Pitot Probe
Two-Axis Positioner
Four Chromalox® Band Heaters
Rotary Mount for Probe
Chamber Wall
Nozzle and Instrument Support Struts

Figure 6. Schematic of the nozzle, stilling chamber, and traverse assembly.

the orifice is directly proportional to $p/(T)^{1/2}$, where p and T are the pressure and temperature of the gas upstream of the orifice. Normally, flow meters of this type are individually calibrated by flowing a known mass of gas through the orifice and monitoring the pressure, temperature, and elapsed time. The flow meter used in the present study consisted of a 0.072-in.-diam (0.18-cm) hole in a 1-in.-diam (2.54-cm) thin stainless steel disc. This plate was positioned in the center of a 24-in.-long (60.8-cm), 1-in.-diam (2.54-cm) length of stainless steel tubing. After preliminary evaluations of the test nozzle, the desired nozzle operating conditions were established, and the corresponding flow meter pressure and temperature were noted. The gas flow to the nozzle was determined by metering a measured mass of gas through the orifice over a measured time period at these flow meter conditions. The results of this calibration indicated that the gas flow to the nozzle was 1.77 ± 0.06 gm/sec. The mass flow to the three nozzle configurations was maintained at this value throughout the entire test program. A schematic of the gas addition system showing the location of the orifice flow meter is given in Fig. 7.

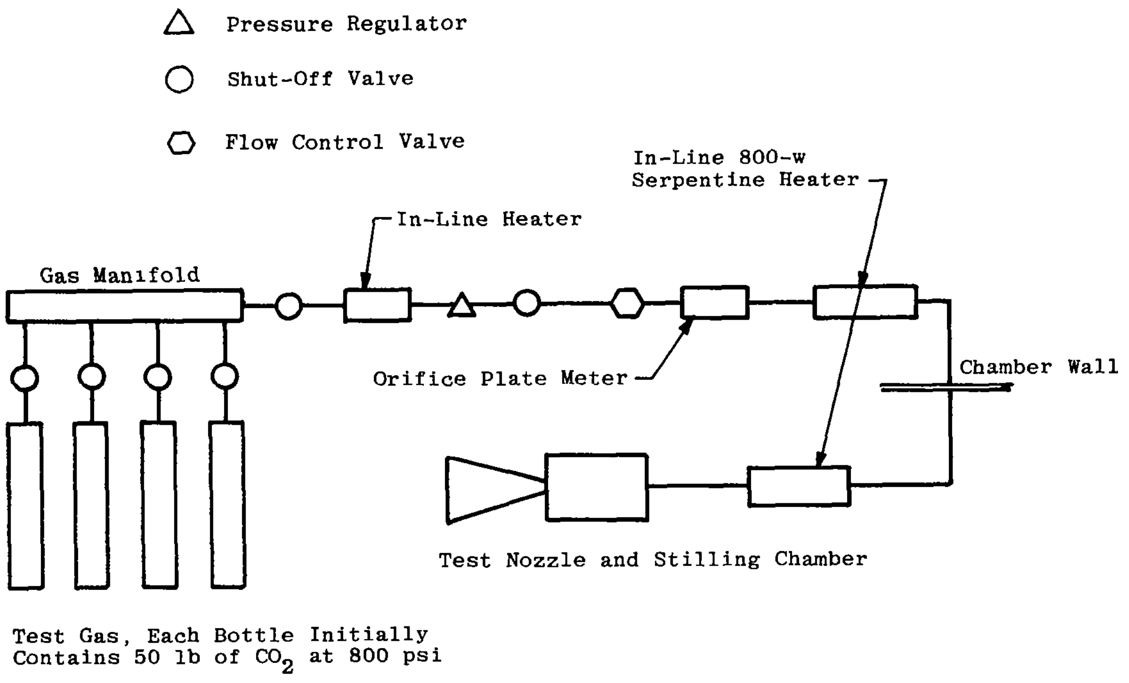
Pressure Regulator
Shut-Off Valve
Flow Control Valve
In-Line 800-w Serpentine Heater
In-Line Heater
Gas Manifold
Orifice Plate Meter
Chamber Wall
Test Nozzle and Stilling Chamber
Test Gas, Each Bottle Initially Contains 50 lb of CO2 at 800 psi

Figure 7. Gas addition system.

The specification for the carbon dioxide used in the present experimental program was quoted as CO_2 min 99.5 percent, N_2 max 0.342 percent, O_2 max 0.086 percent, and H_2O max 0.072 percent. All of the gas used in this program was analyzed prior to use and was found to meet the above specification.

3.0 PURE-GAS FLOW DIAGNOSTICS

3.1 PITOT PRESSURE MEASUREMENTS

For high Reynolds number flows, i.e. $Re_2d > 300$, a knowledge of the pitot pressure together with either the static or reservoir pressure is sufficient to determine the flow Mach number, provided the gas can be treated as a perfect gas, and the change in flow properties across the probe bow shock are adequately defined by the Rankine-Hugoniot relations. For flows that meet these requirements, the pitot probe is a simple and effective diagnostic technique. In its simplest form, the pitot probe consists of nothing more than a flat-faced, open-ended tube aligned parallel to the flow, with the open end facing the oncoming gas flow and the other end connected to a pressure transducer. The probe can be sized according to (1) the requirements of the flow field under investigation and (2) the required response time for the measurement which is in turn dependent upon the physical characteristics of the probe and the pressure transducer. With the advent of small absolute pressure transducers (e.g., the 170 series Baratron Pressure Measurement System from MKS® Instruments, Inc.), accurate absolute measurements of pitot pressure can be made over a wide range of pressures, e.g., 1×10^{-5} to 1,000 torr. For tests of the type discussed herein, this has meant that a compact, fast-response probe/transducer combination can be mounted on a traversing mechanism within the test chamber.

As noted earlier, Mach number can be defined if the free-stream static and pitot pressures are known. In tests of the present type, the difficulties associated with the accurate measurement of free-stream static pressure in a freely expanding plume are such that no consideration has been given to such measurements. Within a diverging nozzle, it has been assumed (e.g., Ref. 23) that, at a particular axial station in the nozzle flow, the measured wall static pressure is equal to the free-stream static pressure on the nozzle centerline. The rationale for this is the assumption that the static pressure at a nozzle axial station is constant throughout the isentropic core flow and the nozzle boundary layer. Rothe (Ref. 15) has shown that this is not an appropriate assumption when the nozzle boundary layer is thick. For the nozzle conditions of the present investigation, there will be a thick viscous layer so that although wall static pressure measurements will be made, it is anticipated that it may not be possible to derive meaningful values of Mach number from measurements of wall static pressure when used in conjunction with pitot or stagnation pressure. The significant differences in Mach number that can result from the use of wall static pressure measurements in conjunction with either pitot or stagnation pressure measurements are shown in the experimental data presented in Fig. 4 of Ref. 23. Therefore, in the present study attention has been confined to the following relationship to define Mach number:

$$p_o/p_o' = [(2\gamma M_\infty^2 - \gamma + 1)/(\gamma + 1)]^{\frac{1}{\gamma-1}} \{[2 + (\gamma - 1) M_\infty^2]/[(\gamma + 1) M_\infty^2]\}^{\frac{\gamma}{\gamma-1}} \quad (1)$$

which is limited to isentropic flow conditions. Pitot pressure can be related to dynamic pressure through the following relationship:

$$p_o' = K\varrho_\infty U_\infty^2/2 \quad (2)$$

where K is a function of Mach number and the specific heat ratio of the gas (Fig. 8). For $\gamma = 1.4$ (which is considered to be appropriate for the test conditions of this study), it can be seen that for $5 \leq M \leq 10$ that $\varrho_\infty U_\infty^2 \approx 1.08\ p_o'$. It is of interest to note that K is relatively insensitive the exact value of the specific heat ratio, since for $1.2 \leq \gamma \leq 1.67$ and $M > 5.0$ the value of K varies by less than 10 percent (Fig. 8).

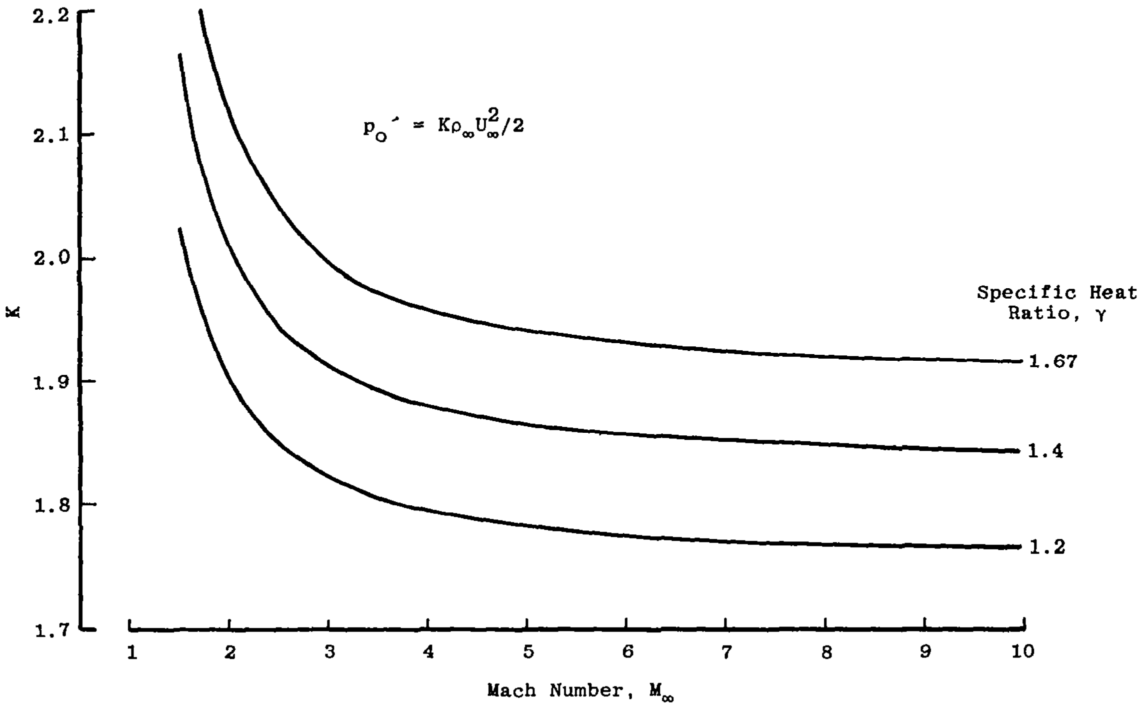

Figure 8. Relationship between pitot and dynamic pressure.

When pitot pressure is associated with an independent measurement of density (e.g., electron beam fluorescence technique, Refs. 5 and 6), an estimate of flow velocity can be obtained from

$$U_\infty = (2p_o'/K\varrho_\infty)^{1/2} \quad (3)$$

This relationship is of value in flow regions outside of the central isentropic core, where the relationship given by Eq. (1) is no longer directly appropriate because p_0 is unknown. In these regions of the flow field where $Re_2d \leq 10$, the measured pitot pressure can be significantly greater than the true value. This increase in measured pressure is a manifestation of the viscous rarefaction effects experienced by the probe. Thus, before pitot pressure measurements can be used to define velocity [cf. Eq. (3)], an appropriate correction for these viscous rarefaction effects has to be made. Normally, the deviation of the measured from ideal pressure is expressed as the ratio (p_0') measured/(p_0') ideal. The determination of the magnitude of this parameter as a function of probe shape, Reynolds number, Mach number, and total temperature has been the subject of numerous experimental studies in low-density flow facilities. Two of the more recent comprehensive evaluations of this ratio are those attributable to Stephenson (Ref. 24) and Graybeal (Ref. 25). As a result of an evaluation of pitot probe measurements made in a wide variety of low-density flow facilities for both monatomic and diatomic gases, Stephenson (Ref. 24), has shown that (p_0') measured/(p_0') ideal correlates well with Re_2d for fixed values of stagnation temperature. Some of these results are summarized in Fig. A-1 of Ref. 24 which is presented herein as Fig. 9. The results of Graybeal's (Ref. 25) studies of viscous and rarefaction effects for low-density carbon dioxide flows were found to be in good agreement with Stephenson's (Ref. 24) measurements. This is not a surprising result since Graybeal (Ref. 25) indicates for the conditions of his experiments, CO_2 behaves as a gas which has a specific heat ratio of 1.4. On the basis of this agreement, it has been concluded that the high-temperature data (i.e. $T_0 > 300$ K) obtained by Stephenson (Ref. 24) is applicable to the $430 \leq T_0 \leq 700$ K experiments reported herein.

An open-ended, flat-faced, thin-wall tube configuration was selected for use in the present investigation because (1) it has a simple reproducible form; (2) it is comparatively insensitive to small changes in angle of attack; and (3) the large pressure sensing orifice minimizes the magnitude of the thermal transpiration effect present at low absolute pressure (Ref. 26).

At the beginning of this investigation, it was anticipated that pitot pressure measurements would be made in the (1) central isentropic core flow, (2) the nozzle boundary layer, (3) forward-flow area, (4) regions of steep density and flow angle gradients, e.g., the lip region of the nozzle and (5) nozzle backflow region. To make measurements in these widely different flow fields, four basic probes were constructed having diameters of 0.03, 0.05, 0.125, and 0.25 in. (0.076, 0.129, 0.318, and 0.635 cm). Each of these probes was approximately 20 diam in length with a sensing orifice not less than 80 percent of the probe diameter.

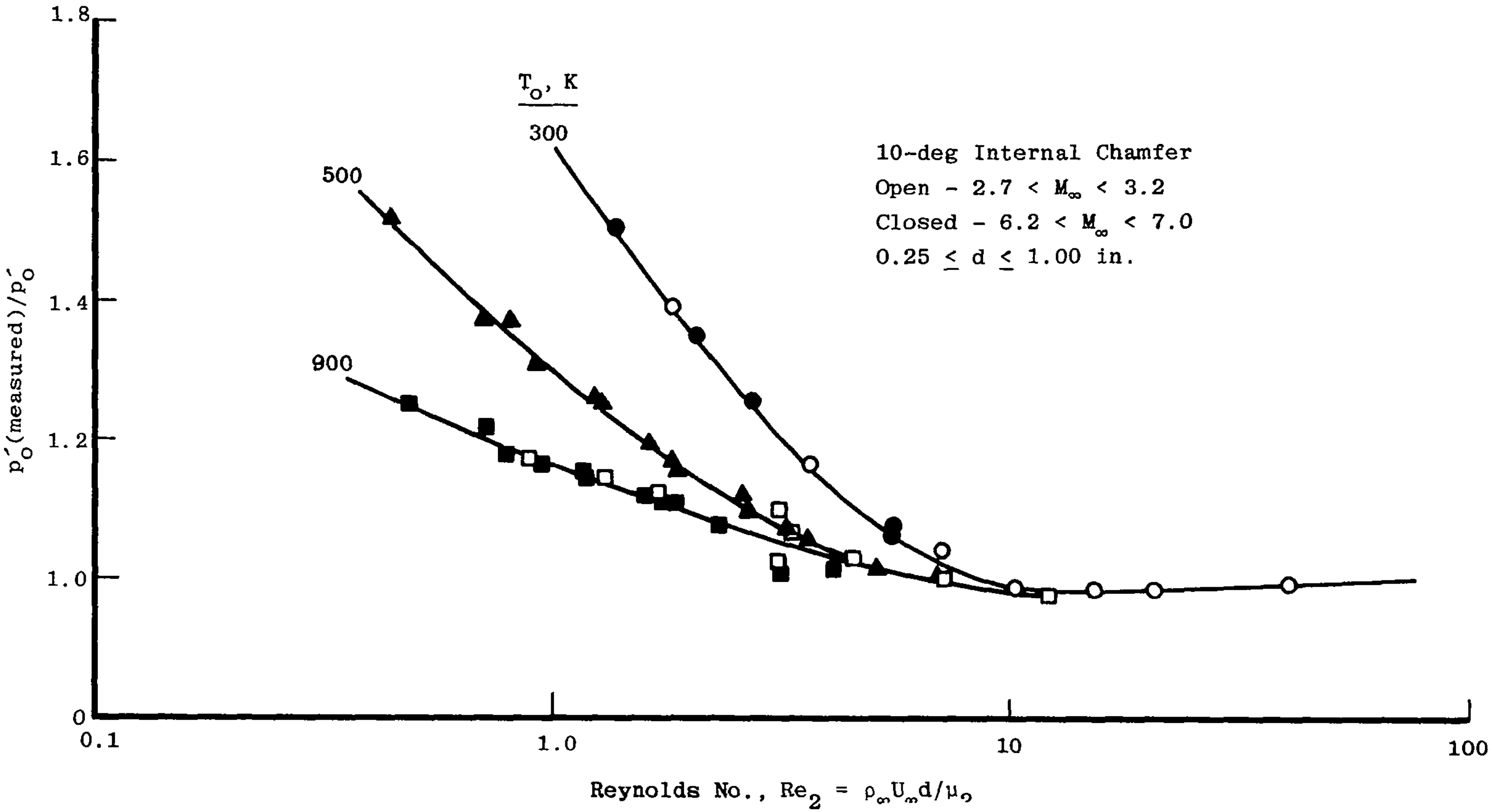

Figure 9. Pitot tube data—supersonic nozzles, September 1967 (N_2) (Fig. A-1 from Ref. 24).

While a pitot probe of this type is comparatively insensitive to small changes in angle to the incident flow, Pollard (Ref. 27) has shown that when this angle exceeds 20 deg, the effect of probe misalignment to the flow results in a measured pressure which is less than the true pressure. Since in the present application it was intended to make pitot pressure measurements in flow field regions where the angle of the velocity vector to the nozzle axis could exceed 90 deg, a method for aligning the probe to the local velocity vector was essential if meaningful pitot pressure measurements were to be made. To achieve this capability, it is necessary to be able to rotate the probe about the vertical axis through the front face of the probe with the probe face remaining at a fixed position in the nozzle flow field. In the present study, this was accomplished by mounting the pitot probe directly to the pressure transducer which was mounted directly to a motor-driven rotary table (Accudex® ARS 304) in such a manner that the vertical axis through the front face of the probe was positioned over the center of rotation of the table. This complete mechanism was mounted on the nozzle support struts within the 4- by 10-ft RVC (Fig. 6). The major portion of the pitot pressure measurements discussed herein was obtained with this configuration which was built around an MKS® Type 370, 0- to 10-torr absolute pressure transducer. For the tests involving the effect of chamber pressure on the performance of the nozzles, a nonrotary, 01.25-in.-diam (0.318-cm) pitot probe was used in conjunction with a Datametrics Barocel®, 0- to 1-torr absolute pressure tranducer, also mounted within the RVC.

3.2 FREE-MOLECULE PRESSURE PROBE

Patterson (Ref. 28) has presented, "the theory of a pressure probe in the form of an orifice in the side of a tube which may be orientated [sic], in any direction relative to that of the mass motion and which is so small compared with the local mean free path, that free-molecule flow occurs. The theory shows that such a tube will measure the local speed ratio in isentropic and nonisentropic flows." Patterson's analysis for isentropic flows, boundary layers, and shock waves of moderate strength indicated that if the temperature inside the probe adjacent to the orifice is not affected by the orientation of the orifice with respect to the flow velocity vector, then the local speed ratio of the flow is given by

$$S = (p_0 - p_{180})/2\pi^{1/2}p_{90} \qquad (4)$$

where p_0, p_{90} and p_{180} are the pressures measured at 0, 90, 180 deg with respect to the flow velocity vector. This expression can be simplified for those flow conditions where $S \gtrsim 3$ to

$$S = p_0/p_{90}\pi^{1/2} \qquad (5)$$

Perhaps the main limitation to the implementation of this flow diagnostic in this form is that the above theory is only applicable to an infinitely thin orifice. In a further development of the application of orifice type probes to the measurement of flow properties in free-molecule flow, Hughes (Ref. 29) has developed a theory to account for the finite thickness of the orifice. The results of this analysis (Ref. 29) will be used to interpret the experimental data obtained in the present investigation. As a part of the present investigation, a free-molecule probe configuration was tested in the flow field generated by the expansion of gas from a circular orifice into a vacuum. The flow field properties generated by such an expansion have been extensively studied (Ref. 30), and it is generally accepted that the detailed flow field properties can be calculated accurately.

Although it cannot be stated with certainty that accurate measurements of speed ratio can be made in these nozzle plumes, it has been shown that accurate measurements of the angle of the flow velocity vector can be made (Refs. 5 and 6) with such a probe in the plume generated by the expansion of a gas from a high area ratio nozzle into a vacuum. The primary application for the free-molecule pressure probe in the present study is to define speed ratio and local flow angle in those regions of the plume where the mean free path is large. Earlier studies in nozzle plumes (Refs. 5 and 6) have shown that the reliable operation of such a probe requires (1) an accurate means for pressure measurement for pressures less than 10^{-3} torr, and (2) an accurate repeatable method for rotating the cylindrical probe about its longitudinal axis.

Two pressure measurement systems have been selected for use with the free-molecule pressure probe (1) Schultz-Phelps ion gage tube which operates in the pressure range from 5×10^{-6} to 5×10^{-1} torr and (2) MKS Type 370 absolute pressure transducer with ranges 0 to 1 and 0 to 10 torr which are capable of accurate absolute pressure measurements to as low as 10^{-5} torr. The probe system using the Schultz-Phelps ion gage is more compact and for this reason is better suited to measurements in the nozzle backflow region. However, it suffers from the fact that, being an ion gage, it is sensitive to the type of gas under test and cannot make absolute pressure measurements, unless it has been calibrated for the test gas. In contrast, the MKS system measures absolute pressures directly, and its accuracy is independent of gas composition. However, it is significantly larger, a factor which does impose some limitations on its use in the nozzle backflow region. Both types of probe/pressure sensors can be mounted directly to the Accudex rotary positioning table in such a manner that the longitudinal axis of the cylindrical probe is aligned with the center of rotation of the table. In this way, accurate measurements of pressure as a function of probe angle can be obtained at a fixed point in the flow field. If it is assumed that Hughes' (Ref. 25) analysis is correct, then it is theoretically possible to determine the local values of speed ratio and flow angle from the measured variations of pressure with the angle of the orifice to the flow. The physical characteristics of the free-molecule pressure probes constructed for this study are listed in Table 2.

Table 2. Free-Molecule Pressure Probe Characteristics

Probe Diameter, in. cm	0.50 1.27	0.250 0.635	0.125 0.318	0.205 0.511	0.50 1.27
Orifice Diameter, in. cm	0.039 0.10	0.062 0.157	0.031 0.079	0.031 0.079	0.061 0.156
Orifice Length, in. cm	0.0015 0.004	0.002 0.005	0.012 0.030	0.011 0.029	0.015 0.038
Diameter/Length	25	30	2.6	2.7	4.1
Probe Number	1	2	3	4	5

3.3 QUARTZ CRYSTAL MICROBALANCE

When a piezoelectric crystal, vibrating at its resonant frequency, experiences a deposition of mass on its exposed surface, there is a readily observable change in crystal frequency. Theoretical and experimental evaluations of the quartz crystal microbalance (QCM) have shown that for a particular QCM configuration there is a well-defined relationship between the mass deposited and frequency change. The QCM's ability to measure accurately low levels of mass flux led to its use for such measurements in the far field of nozzle plumes in a hard vacuum at Jet Propulsion Laboratory (JPL), Pasadena, California (Ref. 31). Similar studies have been made at the AEDC (Refs. 3 and 4) using QCM's based on the JPL design. Mass flux measurements in these tests (Refs. 3, 4, and 31) were obtained using a number of QCM's located at fixed angles and radial positions with respect to the nozzle exit. This arrangement of QCM's limited the amount of mass flux information that could be obtained for a particular nozzle test condition. It also required that each QCM be accurately calibrated such that any small differences between the performance characteristics of the individual QCM's were properly accounted for. Ideally, to make mass flux measurements in the plume of a nozzle expansion, a single cryogenically cooled QCM is required whose angular orientation and position with respect to the nozzle exit plane can be controlled. Changes in the position of the QCM with respect to the nozzle exit plane can be accomplished by positioning the QCM at a fixed location in the RVC and moving the nozzle with the axial and lateral traversing tables described earlier. The angular orientation of the QCM sensor surface with respect to the nozzle exit plane can also be controlled by mounting the sensor on the Accudex ARS 304 motor-driven rotary positioning table that has been used with the pitot and free-molecule pressure probes described earlier.

An MK9 quartz crystal microbalance manufactured by Berkeley Controls, Inc., was chosen for this application. The characteristics of this unit are given in Table 3 and show

Table 3. Quartz Crystal Microbalance Characteristics

Berkeley Controls, Inc. Mark 9 Contamination Sensor, MK9-3-1-S-SS-S-P	
Crystal Frequency	10 MHz
Mass Sensitivity	4.43×10^{-9} gm/cm^2-Hz
Cryogenic Temperature Range	77 to 123 K
Supply Voltage	10 vdc
Sensor Output	Beat Frequency 1 to 100 kHz
Internal Oscillator/Hybrid Chip	~140 mw at 10 vdc
Dimensions	3.18-cm diam, 3.18-cm long
Crystal Area Exposed to Mass Flux	0.316 cm^2

that the crystal cut best suited for operation at liquid-nitrogen temperatures was chosen for the present application. An exploded view of the sensor and a layout of the sensor components are given in Fig. 10. It will be noted in Fig. 10b that there is a unit identified as the plug-in crystal/heater assembly. The crystals used in this sensor are 10 MHz, AT-cut crystals (cut at a 35-deg angle to the Z axis of the mother crystal; temperature variations have little effect on its natural vibration frequency) which are powered by the electronic oscillator mixer module. A platinum resistance element is positioned between the sensing and reference crystals. This element can be used either to measure crystal temperature or as a heater to control the crystal temperature (When it is operating as a heater, it does not measure temperature). In the present application, the heater mode of operation was used to

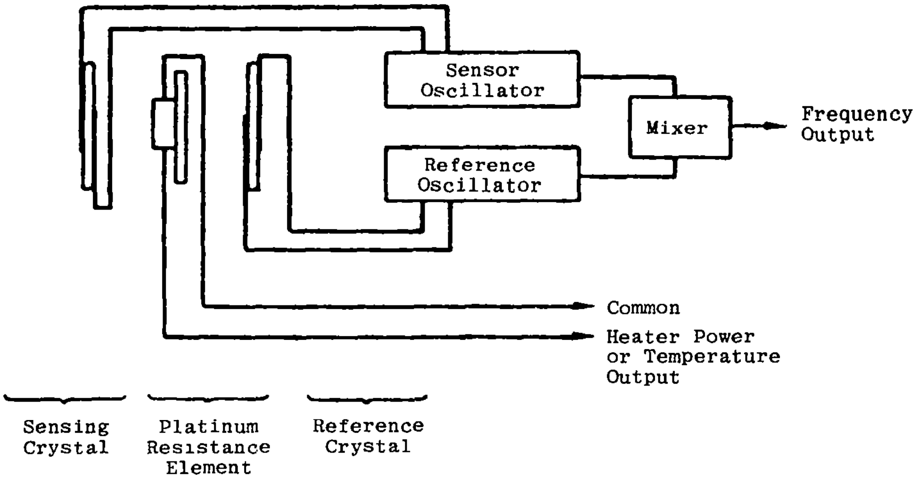
Sensor Oscillator
Reference Oscillator
Mixer
Frequency Output
Common
Heater Power or Temperature Output
Sensing Crystal
Platinum Resistance Element
Reference Crystal

a. Sensor components
Figure 10. Berkeley Controls MK 9 contamination sensor.

remove gases condensed on the crystal when the mass deposited had resulted in the saturation of the crystal.

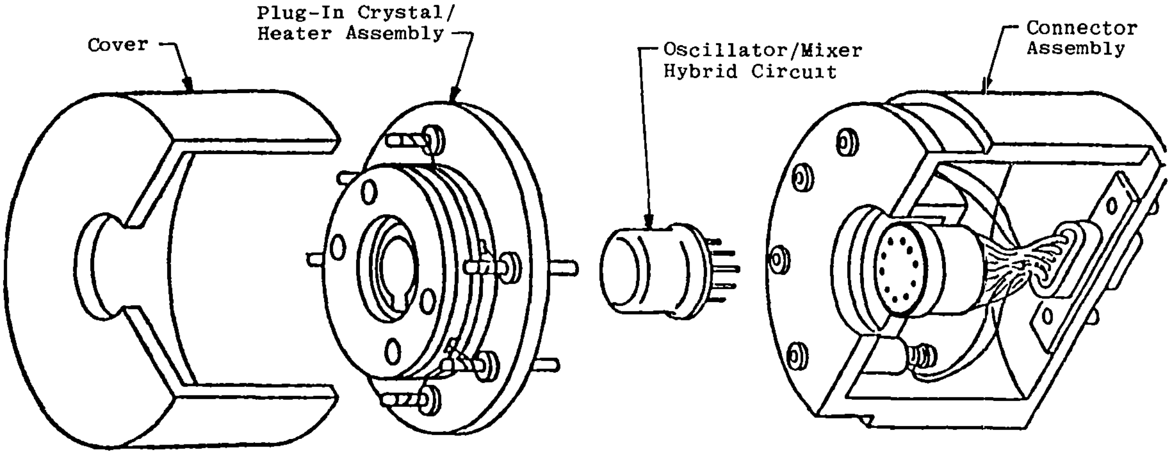

b. Exploded view of sensor
Figure 10. Concluded.

A sketch of the rotatable QCM is shown in Fig. 11. In the final assembly of this probe, particular attention was directed towards ensuring that the vertical axis of the sensing crystal was coincident with the center of rotation of the rotary table. This ensured that when the probe was rotated, the center of the QCM sensing crystal remained at the same location in the plume.

3.4 FREE-MOLECULE HEAT-TRANSFER PROBE

A number of attempts have been made in the past to use the free-molecule heat-transfer probe to define the flow characteristics of rarefied flows (Refs. 32 through 40). While useful information has been obtained with probes of this type at these flow conditions, their full potential has not yet been achieved because of the difficulties associated with the correct accounting for probe radiation and wire support conduction losses. An attempt to use this technique in the present investigation has been prompted by (1) the necessity for making flow field measurements in the nozzle boundary layer upstream of the nozzle lip (Ideally, when the measurements obtained with this probe are combined with pitot pressure measurements, local values of speed ratio, pressure, temperature, density, velocity, and enthalpy can be derived, cf. Ref. 38) and (2) the development by Gottesdiener (Ref. 39) of an apparently successful method for accounting for the wire support conduction losses. This was accomplished by positioning small-bead thermistors at each end of the heated wire and using them as nonlinear heat sources in a temperature control system that keeps the wire at a constant uniform temperature. In this manner, it was possible to eliminate conduction losses. Radiation losses were accounted for by operating the probe in a vacuum.

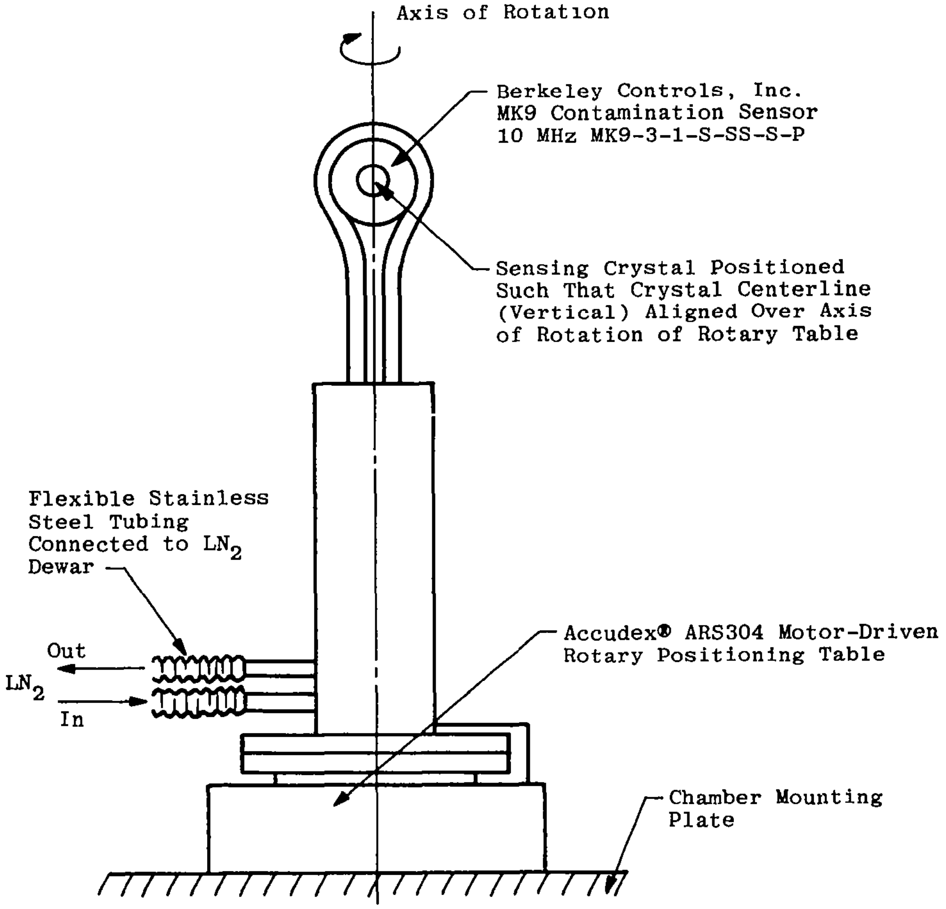
Axis of Rotation
Berkeley Controls, Inc.
MK9 Contamination Sensor
10 MHz MK9-3-1-S-SS-S-P
Sensing Crystal Positioned Such That Crystal Centerline (Vertical) Aligned Over Axis of Rotation of Rotary Table
Flexible Stainless Steel Tubing Connected to LN2 Dewar
Out
LN2
In
Accudex® ARS304 Motor-Driven Rotary Positioning Table
Chamber Mounting Plate

Figure 11. Sketch of rotatable quartz crystal microbalance.

In the present investigation, a number of probes have been designed and constructed based on Gottesdiener's (Ref. 39) design. A detailed description of the underlying theory of the probe, probe construction, electronic control circuitry, and operation are beyond the scope of the present paper (private communication, F. G. Collins, University of Tennessee Space Institute, September 1983). Sketches of the probe and a photograph of one of the prototypes (not used for flow field measurements) are given in Figs. 12 and 13.

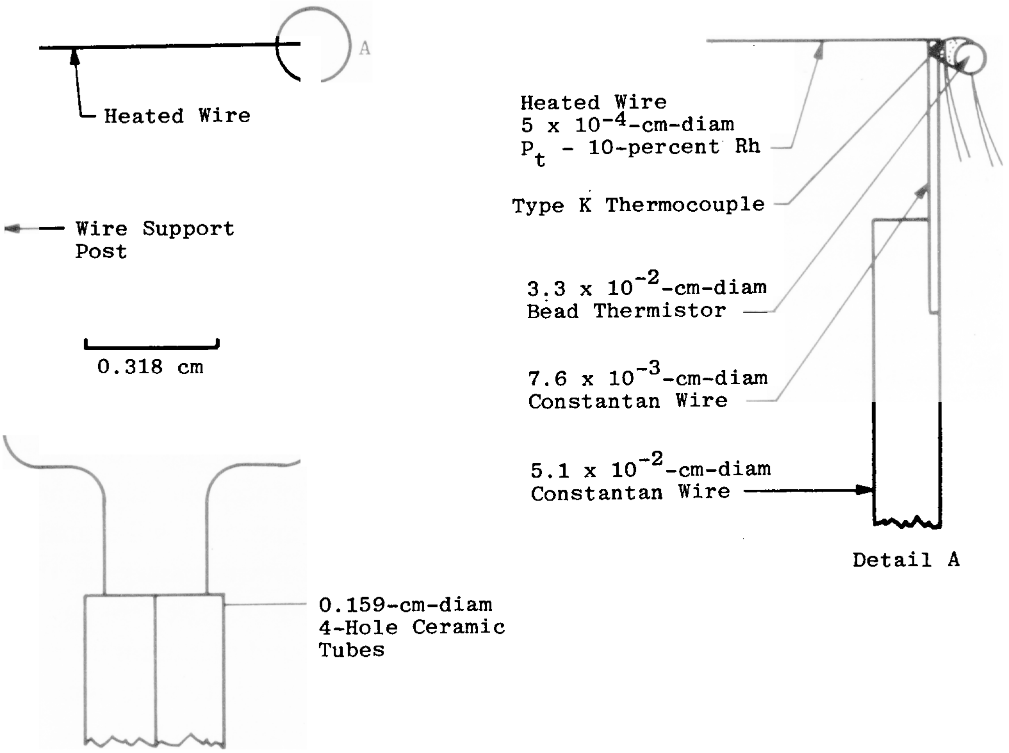
A
Heated Wire
Wire Support Post
0.318 cm
0.159-cm-diam 4-Hole Ceramic Tubes
Heated Wire 5 x 10^{-4}-cm-diam P_t - 10-percent Rh
Type K Thermocouple
3.3 x 10^{-2}-cm-diam Bead Thermistor
7.6 x 10^{-3}-cm-diam Constantan Wire
5.1 x 10^{-2}-cm-diam Constantan Wire
Detail A

Figure 12. Sketch of free-molecule heat-transfer probe.

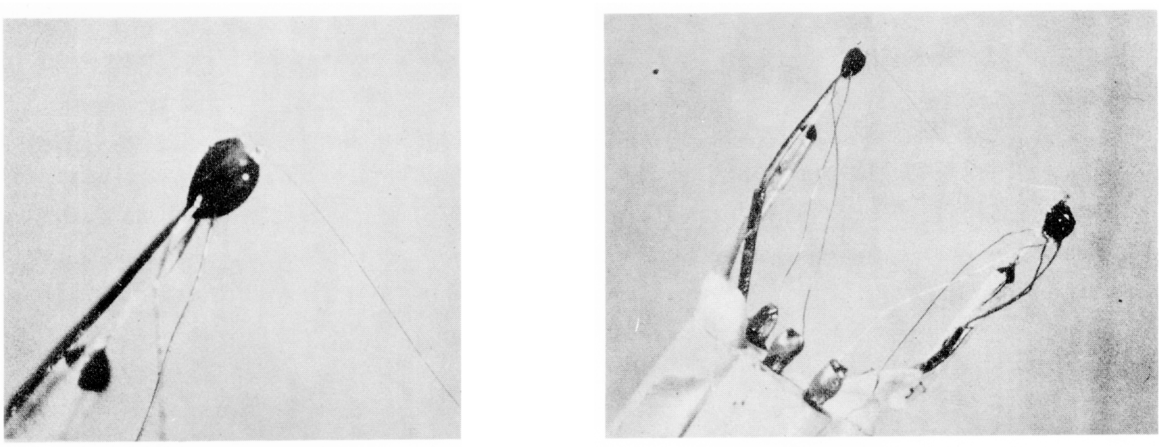

Figure 13. Prototype of free-molecule heat-transfer probe.

3.5 ELECTRON BEAM FLUORESCENCE TECHNIQUE

The electron beam fluorescence technique (Ref. 41) has been used extensively over the past 20 years to provide spatially resolved measurements of absolute number density and rotational temperature in a variety of nozzle flows, e.g., Refs. 3, 5, 6 and 15. In order to obtain accurate measurements of absolute number density using this technique, it is necessary to calibrate the system in a gas of known number density. A technique that has been used in the past, e.g., Ref. 3, has been to utilize the flow field that results when the gas under investigation is expanded through a thin, circular orifice into a hard vacuum. Extensive studies by a variety of independent investigators have shown that the detailed properties of such flows are accurately defined by the work of Ashkenas and Sherman (Ref. 30). For a number of experimental investigations, such as the short-duration liquid-propellant rocket motor tests described in Ref. 3, this is an accurate and comparatively simple means for number density calibration. While such an approach will probably always be necessary for tests of the type described in Ref. 3, it is not necessary for the present investigation. In a recent experimental program at the AEDC (Ref. 6) involving the expansion of CO_2 through a nozzle into a vacuum, it was found that accurate estimates of the number density on the nozzle centerline could be determined from the measured pitot pressure, stagnation pressure, and the assumption of isentropic flow. These calculated values were used for calibration of number density. The validity of this approach was confirmed by comparing these derived values of number density with some independent absolute measurements obtained by Williams (Ref. 42) at the same nozzle flow condition using a laser UV Raman scattering technique. In the present investigation, the number density on the nozzle centerline (derived in the above manner) was used for calibration.

Values of number density using the electron beam fluorescence technique are derived from measurements of the light intensity within a given spectral interval of a vibrational-rotational band of a molecular species generated as a result of the interaction of a narrow collimated beam of electrons with the gas species. The corresponding rotational temperature is determined by the measurement of the spectral line intensity distribution within the band. As a result of the electron/molecule interaction, the molecules are excited to elevated electronic states. Fluorescence characteristic of the initial state-of-the-gas occurs upon transition from these elevated states to a lower state.

While measurements of CO_2 number density have been made in the past at the AEDC and are currently being documented in a technical report, the limitations of the available instrumentation were such that rotational temperature measurements were not possible. The difficulty in making such measurements derived from the fact that for CO_2, the band rotational lines are so closely spaced that with the available spectrometer gratings, the band spectra could not be adequately resolved without losing the required sensitivity. Beylich (Ref. 43) has shown that with appropriate instrumentation, rotational temperature measurements are possible in CO_2 plumes. Higher resolution gratings were obtained that satisfied the resolution and sensitivity requirements for rotational temperature measurements. Synthetic spectral band shapes for a number of rotational temperatures were developed in an independent study (Ref. 44). Rotational temperature in the flow is determined from a comparison of the synthetic and experimental spectra. Implicit in the determination of rotational temperature in this manner is the requirement that the flow be in equilibrium.

In the present investigation, an RCA Model VC2126 V4 electron gun was used to produce a 30-kev, 1-ma electron beam having a diameter on the order of 1 mm. The pressure within the electron gun was maintained at a level less than 1×10^{-5} torr when the gun was exposed to the RVC environment through a 1.3-mm-diam orifice. After passage through the flow field of interest, the electron beam was collected by a water-cooled Faraday cup positioned at the bottom of the RVC (Fig. 1). Two brass screens were positioned at the cup entrance with the inner one charged to a negative potential of 45 v to repel and entrap the secondary electrons created as a result of the electron beam impacting the bottom of the cup.

Electron beam fluorescence was dispersed and detected by a Spex Industries 0.85-m double spectrometer, whose 2,400 grove/mm gratings produced a reciprocal linear dispersion of 2.3 Å/mm, and a thermoelectrically cooled RCA C31034A photomultiplier tube. Light emitted within the observation volume was collimated by a 50-cm focal length fused silica lens and focused onto the spectrometer slit by an identical lens. Both lenses were apertured to match the f-number of the spectrometer. A mirror configuration was used to rotate the vertical image through 90 deg onto the spectrometer slit. This rotation ensured the complete collection of the beam image diameter and, thus, independence of number density measurements on beam spreading effects. In their final form, number density values are corrected for beam current variations, system dead time, background signal, and quenching effects. A detailed description of these correction factors is contained in a technical report currently being prepared at the AEDC.

4.0 TEST DESCRIPTION

4.1 TEST UNIT AND NOZZLE OPERATING CONDITIONS

The 4- by 10-ft RVC background pressure was monitored during all nozzle operations with (1) a nude Bayard-Alpert ionization gage positioned behind and above the nozzle throat, (2) a Schultz-Phelps ionization gage positioned behind and to the side of the nozzle mount and traversing mechanism within the LN_2-cooled cryoliner with the sensing element facing in the direction of the flow on the nozzle centerline, and (3) a Bayard-Alpert ionization gage which measured the pressure in a 6-in.-diam (15.2-cm), 12-in.-long (30.4-cm) cylinder attached to the wall of the RVC close to the nozzle exit plane. For those test conditions which required the deliberate elevation of chamber background pressure, additional pressure gages were used to monitor this pressure, i.e. MKS and Barocel absolute pressure transducers and a Granville-Phillips Convectron Series 275 gage.

The base pressure achieved in the 4- by 10-ft RVC prior to the initiation of nozzle flow was less than 1×10^{-6} torr. This base pressure was achieved with LN_2 cryopumps and oil diffusion pumps. When nozzle flow was initiated, the two ionization gages within the test chamber registered pressures on the order of 2×10^{-5} torr, whereas the remaining ionization gage registered 2×10^{-4} torr. In subsequent discussions of chamber pressure, it can be assumed that (unless stated otherwise) it will have been measured with the internal gages. From mass spectrometric analyses of the gas composition within the cryopumped and noncryopumped sections of the RVC, it was found that the water peak was significantly higher in the noncryopumped section. On the basis of these measurements, it has been assumed that the external ionization gage was affected by the presence of water vapor and was, therefore, not truly representative of the pressure within the cryopumped chamber.

It was noted in Section 2.1 that one of the purposes for the two 6-in. oil diffusion pumps was to scavenge the N_2, O_2, and any other noncondensible gases that were known to be in the test gas. Subsequent experience with the RVC pumping system has shown that, provided these contaminants do not exceed the levels described in Section 2.2, the background pressure indicated above, i.e. 2×10^{-5} torr, could be maintained with the flowing gas with both diffusion pumps isolated from the chamber. (A possible explanation for this is that the noncondensible constituents are sorption pumped by the CO_2 frost on the LN_2 cryoliners.) Therefore, in those tests that require a deliberate elevation of the background pressure, it was found that this could be achieved in a controllable manner by valving out the diffusion pumps and metering a small quantity of argon into the chamber through a micrometer needle valve. In this manner, it was possible to set the background chamber pressure at any desired level between 2×10^{-5} and 5×10^{-1} torr. Recovery from the elevated background pressure to the normal background pressure was accomplished through the successive use of the main chamber roughing pump and the diffusion pumps.

Depending upon the requirements of the test, it was found that on the order of 2 to 3 hr was required to bring the chamber and nozzle to the desired operating conditions, i.e. nozzle wall temperature, gas temperature, and cryoliner temperature. Sufficient temperature and pressure instrumentation was available to monitor the performance of the complete chamber/test article configuration. This information was continuously presented on a video screen and a printout was obtainable at any of a wide variety of selected frequencies (determined primarily by the requirements of the test). An example of the nozzle and chamber operational characteristics is given in Fig. 14 for a test to determine the effect of cryopumping in the nozzle backflow on nozzle flow characteristics where (1) channels 109 to 114 monitor the nozzle stilling chamber and band heater temperatures, (2) channels 115 and 705 monitor the temperature and pressure of the orifice plate meter, (3) channel 210 records the temperature of the LN_2-cooled disk behind the nozzle, and (4) channel 401 records the output of the nude ion gage. As would be expected, the nozzle and flow meter characteristics are virtually unchanged over this 5-hr test period, whereas the deliberate changes in LN_2 use are reflected in the temperature changes recorded by channel 210, and the resultant small change in background chamber pressure is recorded by channel 401. The printout and data plot for a typical data run are presented in Figs. 15 and 16. Flow-angle variation with radial position at a fixed axial station for the free-molecule pressure probe was being determined at this time. It is of interest to note that the pumping efficiency of the LN_2 cryopumps underwent no observable degradation in performance even though as much as 98 lb (44.5 kg) of CO_2 were flowed into the chamber.

Table 4 summarizes the nozzle/chamber conditions covered in the test progarm.

Table 4. Basic Test Variables

Throat Diam, in. cm	1.0 2.54	0.6 1.52	0.2 0.51	0.6 1.52	0.2 0.51
Stagnation Pressure, torr	10.8	36.5	283	24	188
Stagnation Temperature, K	487	710	710	288	300
Thin Lip	X	X		X	X
Thick Lip	X		X		
Varying Background Pressure	X	X	X	X	X
Varying Background Cryopumping	X	X			
Pitot Probe	X	X	X	X	X
Free-Molecule Pressure	X	X			
Free-Molecule Heat Transfer		X			
Electron Beam	X	X			
QCM	X	X			

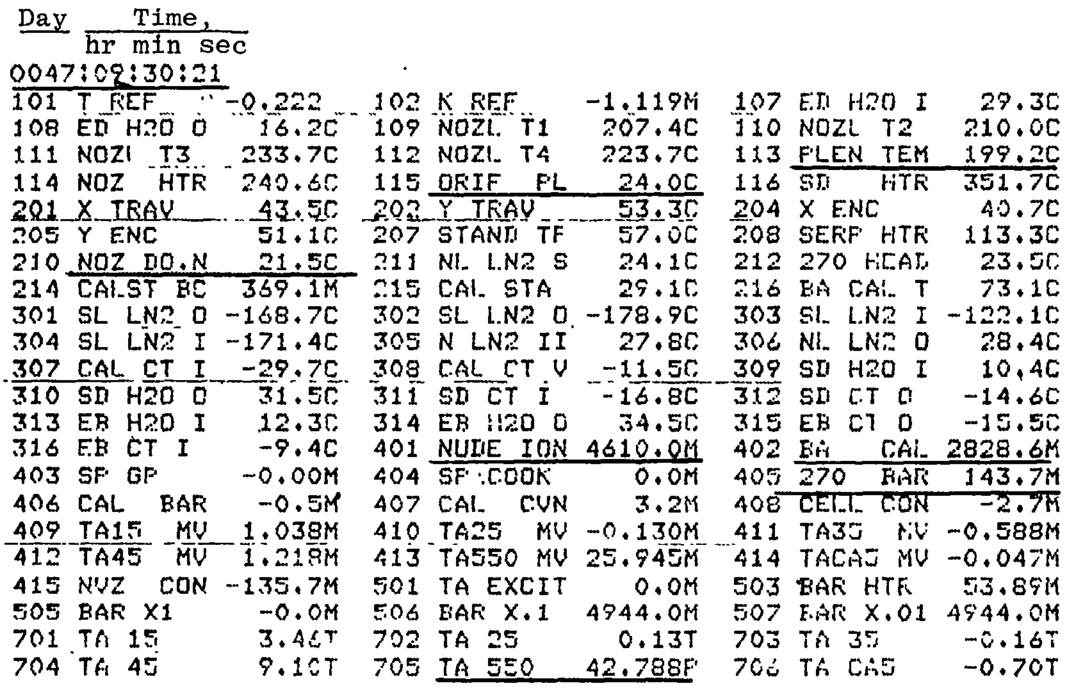

```
Day    Time,
       hr min sec
0047:09:30:21
101 T REF     -0.222   102 K REF    -1.119M   107 ED H2O I    29.3C
108 ED H2O O   16.2C   109 NOZL T1   207.4C   110 NOZL T2    210.0C
111 NOZL T3   233.7C   112 NOZL T4   223.7C   113 PLEN TEM   199.2C
114 NOZ  HTR  240.6C   115 ORIF PL    24.0C   116 SD  HTR    351.7C
201 X TRAV     43.5C   202 Y TRAV     53.3C   204 X ENC       40.7C
205 Y ENC      51.1C   207 STAND TF   57.0C   208 SERP HTR   113.3C
210 NOZ DO.N   21.5C   211 NL LN2 S   24.1C   212 270 HEAD    23.5C
214 CALST BC  369.1M   215 CAL STA    29.1C   216 BA CAL T    73.1C
301 SL LN2 O -168.7C   302 SL LN2 O -178.9C   303 SL LN2 I  -122.1C
304 SL LN2 I -171.4C   305 N LN2 II   27.8C   306 NL LN2 O    28.4C
307 CAL CT I  -29.7C   308 CAL CT V  -11.5C   309 SD H2O I    10.4C
310 SD H2O O   31.5C   311 SD CT I   -16.8C   312 SD CT O    -14.6C
313 EB H2O I   12.3C   314 EB H2O O   34.5C   315 EB CT O    -15.5C
316 EB CT I    -9.4C   401 NUDE ION 4610.0M   402 BA   CAL 2828.6M
403 SP GP     -0.00M   404 SP COOK     0.0M   405 270  BAR  143.7M
406 CAL  BAR   -0.5M   407 CAL  CVN    3.2M   408 CELL CON    -2.7M
409 TA15  MV  1.038M   410 TA25  MV -0.130M   411 TA35  MV -0.588M
412 TA45  MV  1.218M   413 TA550 MV 25.945M   414 TACAS MV -0.047M
415 NVZ  CON -135.7M   501 TA EXCIT    0.0M   503 BAR HTR    53.89M
505 BAR X1     -0.0M   506 BAR X.1  4944.0M   507 BAR X.01 4944.0M
701 TA 15      3.46T   702 TA 25       0.13T   703 TA 35      -0.16T
704 TA 45      9.10T   705 TA 550    42.788P   706 TA CAS     -0.70T
```

a. No backflow cryopumping

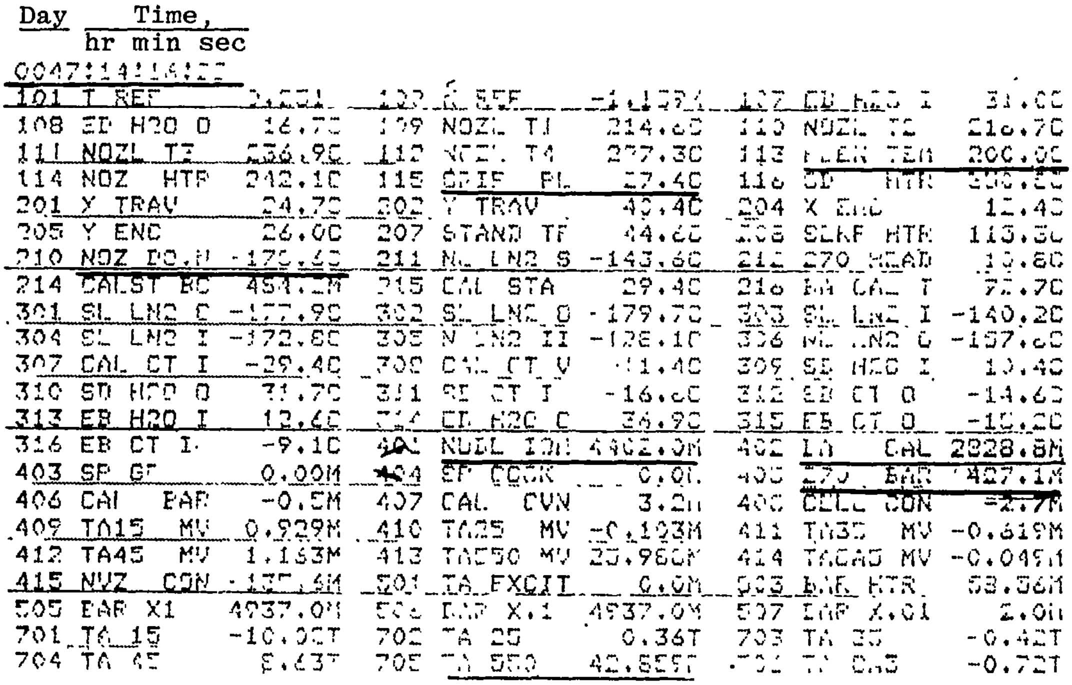

```
Day    Time,
       hr min sec
0047:14:1[illegible]
101 T REF   [illegible]    102 K REF    -1.1[illegible]   107 ED H2O I    31.0C
108 ED H2O O   16.7C   109 NOZL T1   214.6C   110 NOZL T2    216.7C
111 NOZL T3   236.9C   112 NOZL T4   277.3C   113 PLEN TEM   200.0C
114 NOZ  HTR  242.1C   115 ORIF PL    27.4C   116 SD  HTR  [illegible]
201 X TRAV     24.7C   202 Y TRAV     40.4C   204 X ENC       12.4C
205 Y ENC      26.0C   207 STAND TF   44.6C   208 SERP HTR   113.5C
210 NOZ DO.N -175.6C   211 NL LN2 S -143.6C   212 270 HEAD    10.8C
214 CALST BC  45[illegible]M   215 CAL STA    29.4C   216 BA CAL T    72.7C
301 SL LN2 O -177.9C   302 SL LN2 O -179.7C   303 SL LN2 I  -140.2C
304 SL LN2 I -172.8C   305 N LN2 II -128.1C   306 NL LN2 O  -157.6C
307 CAL CT I  -29.4C   308 CAL CT V  -11.4C   309 SD H2O I    10.4C
310 SD H2O O   31.7C   311 SD CT I   -16.6C   312 SD CT O    -14.6C
313 EB H2O I   12.6C   314 EB H2O O   36.9C   315 EB CT O    -15.2C
316 EB CT I    -9.1C   401 NUDE ION 4402.0M   402 BA   CAL 2828.8M
403 SP GP      0.00M   404 SP COOK     0.0M   405 270  BAR  427.1M
406 CAL  BAR   -0.5M   407 CAL  CVN    3.2M   408 CELL CON    -2.7M
409 TA15  MV  0.929M   410 TA25  MV -0.123M   411 TA35  MV -0.619M
412 TA45  MV  1.163M   413 TA550 MV 25.960M   414 TACAS MV -0.049M
415 NVZ  CON -13[illegible].4M   501 TA EXCIT    0.0M   503 BAR HTR    53.36M
505 BAR X1   4937.0M   506 BAR X.1  4937.0M   507 BAR X.01    2.0M
701 TA 15   -10.0[illegible]T   702 TA 25       0.36T   703 TA 35      -0.42T
704 TA 45      9.63T   705 TA 550    42.85[illegible]   706 TA CAS     -0.72T
```

b. Backflow cryopumping

Figure 14. Chamber and nozzle operating characteristics.

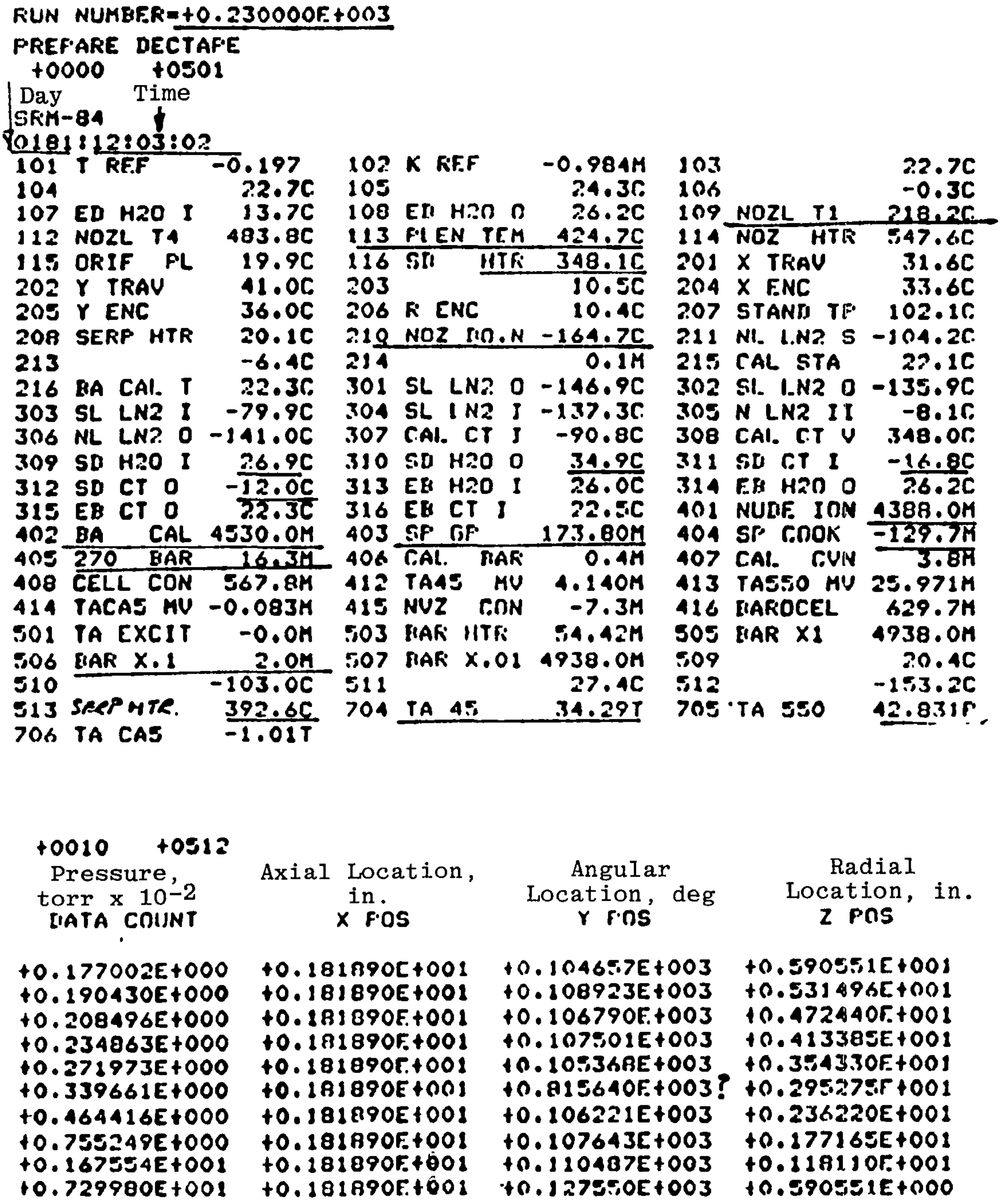

```
RUN NUMBER=+0.230000E+003
PREPARE DECTAPE
 +0000   +0501
 Day      Time
SRM-84
0181!12!03!02
101 T REF      -0.197    102 K REF      -0.984M   103               22.7C
104             22.7C    105             24.3C    106               -0.3C
107 ED H2O I    13.7C    108 ED H2O O    26.2C    109 NOZL T1      218.2C
112 NOZL T4    483.8C    113 PLEN TEM   424.7C    114 NOZ  HTR     547.6C
115 ORIF  PL    19.9C    116 SD   HTR   348.1C    201 X TRAV        31.6C
202 Y TRAV      41.0C    203             10.5C    204 X ENC         33.6C
205 Y ENC       36.0C    206 R ENC       10.4C    207 STAND TP     102.1C
208 SERP HTR    20.1C    210 NOZ DO.N  -164.7C    211 NL LN2 S    -104.2C
213             -6.4C    214              0.1M    215 CAL STA       22.1C
216 BA CAL T    22.3C    301 SL LN2 O  -146.9C    302 SL LN2 O    -135.9C
303 SL LN2 I   -79.9C    304 SL LN2 I  -137.3C    305 N LN2 II      -8.1C
306 NL LN2 O  -141.0C    307 CAL CT I   -90.8C    308 CAL CT V     348.0C
309 SD H2O I    26.9C    310 SD H2O O    34.9C    311 SD CT I      -16.8C
312 SD CT O    -12.0C    313 EB H2O I    26.0C    314 EB H2O O      26.2C
315 EB CT O     22.3C    316 EB CT I     22.5C    401 NUDE ION   4388.0M
402 BA   CAL  4530.0M    403 SP GP     173.80M    404 SP COOK    -129.7M
405 270  BAR    16.3M    406 CAL  BAR     0.4M    407 CAL  OVN      3.8M
408 CELL CON   567.8M    412 TA45  MV   4.140M    413 TA550 MV   25.971M
414 TACA5 MV  -0.083M    415 NVZ  CON    -7.3M    416 BAROCEL     629.7M
501 TA EXCIT   -0.0M     503 BAR HTR    54.42M    505 BAR X1     4938.0M
506 BAR X.1      2.0M    507 BAR X.01  4938.0M    509               20.4C
510           -103.0C    511             27.4C    512             -153.2C
513 SERP HTR.  392.6C    704 TA 45      34.29T    705 TA 550      42.831P
706 TA CA5     -1.01T


 +0010     +0512
 Pressure,          Axial Location,        Angular               Radial
torr x 10^-2              in.          Location, deg       Location, in.
 DATA COUNT              X POS              Y POS               Z POS

+0.177002E+000     +0.181890E+001     +0.104657E+003     +0.590551E+001
+0.190430E+000     +0.181890E+001     +0.108923E+003     +0.531496E+001
+0.208496E+000     +0.181890E+001     +0.106790E+003     +0.472440E+001
+0.234863E+000     +0.181890E+001     +0.107501E+003     +0.413385E+001
+0.271973E+000     +0.181890E+001     +0.105368E+003     +0.354330E+001
+0.339661E+000     +0.181890E+001     +0.815640E+003?    +0.295275E+001
+0.464416E+000     +0.181890E+001     +0.106221E+003     +0.236220E+001
+0.755249E+000     +0.181890E+001     +0.107643E+003     +0.177165E+001
+0.167554E+001     +0.181890E+001     +0.110487E+003     +0.118110E+001
+0.729980E+001     +0.181890E+001     +0.127550E+003     +0.590551E+000
```

Figure 15. Typical computer printout, Run 230.

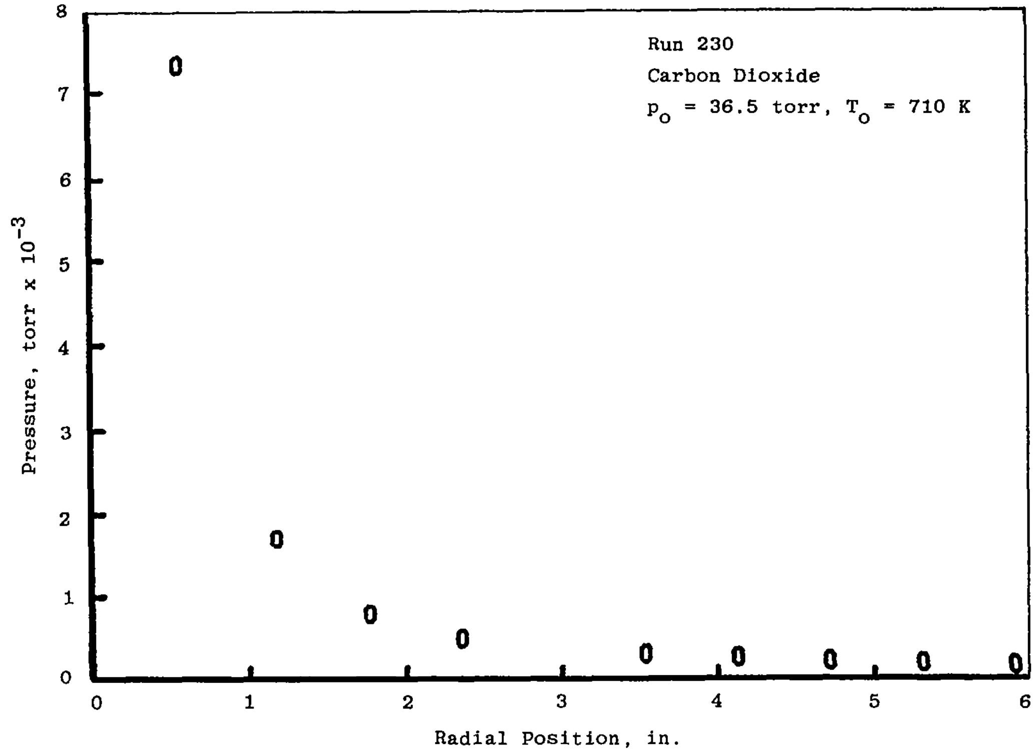

a. Pressure variation with radial position
Figure 16. Typical data plots, Run 230.

4.2 DIAGNOSTIC MEASUREMENTS

For the probe diagnostics, i.e. free-molecule pressure probe, QCM, free-molecule heat-transfer probe, and the pitot probe, the probes were accurately positioned both axially and radially with respect to the nozzle exit plane prior to the chamber pump down. It was not possible to detect any movement of the probe or nozzle as a result of chamber evacuation. However, as the chamber was cooled and the nozzle heated, axial movement in the lip of the nozzle was detected with a scope that had been aligned with the nozzle lip when the chamber/nozzle configuration was at room temperature. An accurate measure of this growth was determined by tracking the nozzle axially until the lip was once again aligned with the scope. This correction was made for all nozzle configurations. Although it was not possible to measure the radial growth of the nozzle, it was determined from complete radial surveys in the exit plane that the nozzle axis did not move radially with nozzle heating. Therefore, each of the above probes was normally referenced to the unheated centerline which was established prior to chamber pump down.

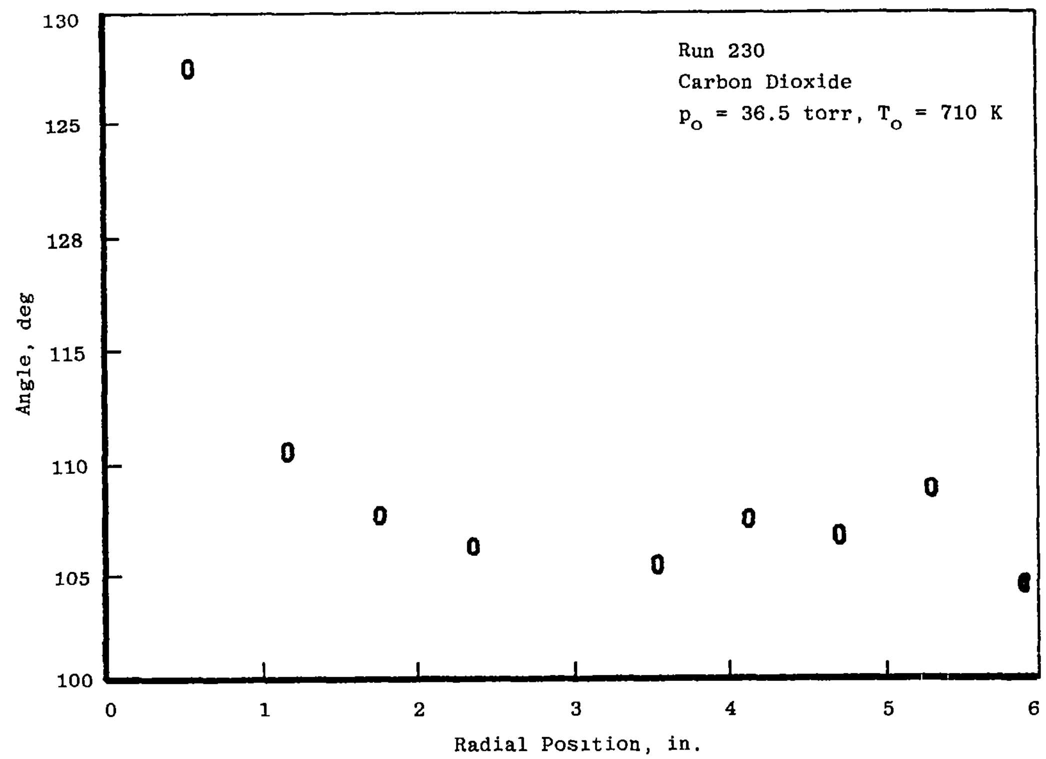

b. Angle variation with radial position
Figure 16. Concluded.

The movement of the nozzle and probe motion tables could be controlled either wholly with the computer, wholly manually, or with a combination of both. For example, the free-molecule probe data illustrated in Figs. 15 and 16 were obtained by the test monitor rotating the probe until the pressure signal peaked, at which time the computer recorded the pressure and angle and moved the nozzle to the next predetermined radial position.

A detailed alignment of all electron beam components was performed prior to chamber pump down. Refinements to the alignment were made after the chamber was at test conditions by adjustments to the external lens assemblies. Prepumpdown adjustments included alignment of the electron beam axis along the vertical centerline of the nozzle. This alignment failed to hold after pump down, and the determination of the position of the electron beam with respect to the nozzle centerline and exit plane was made from visual observations of the interaction of the beam with the nozzle lip.

5.0 DISCUSSION OF RESULTS

5.1 PITOT PRESSURE MEASUREMENTS

5.1.1 Nozzle Test Conditions

Measurements of centerline pitot pressure as a function of axial distance were made for each of the nozzles to establish the basic characteristics of these nozzles. In the course of this test program, these measurements were made with probes having diameters of 0.05, 0.125, and 0.25 in. (0.127, 0.318, and 0.635 cm). Absolute pitot pressure measurements obtained for the A/A* = 16 and 44.4 nozzles are presented in Fig. 17. These measurements illustrate

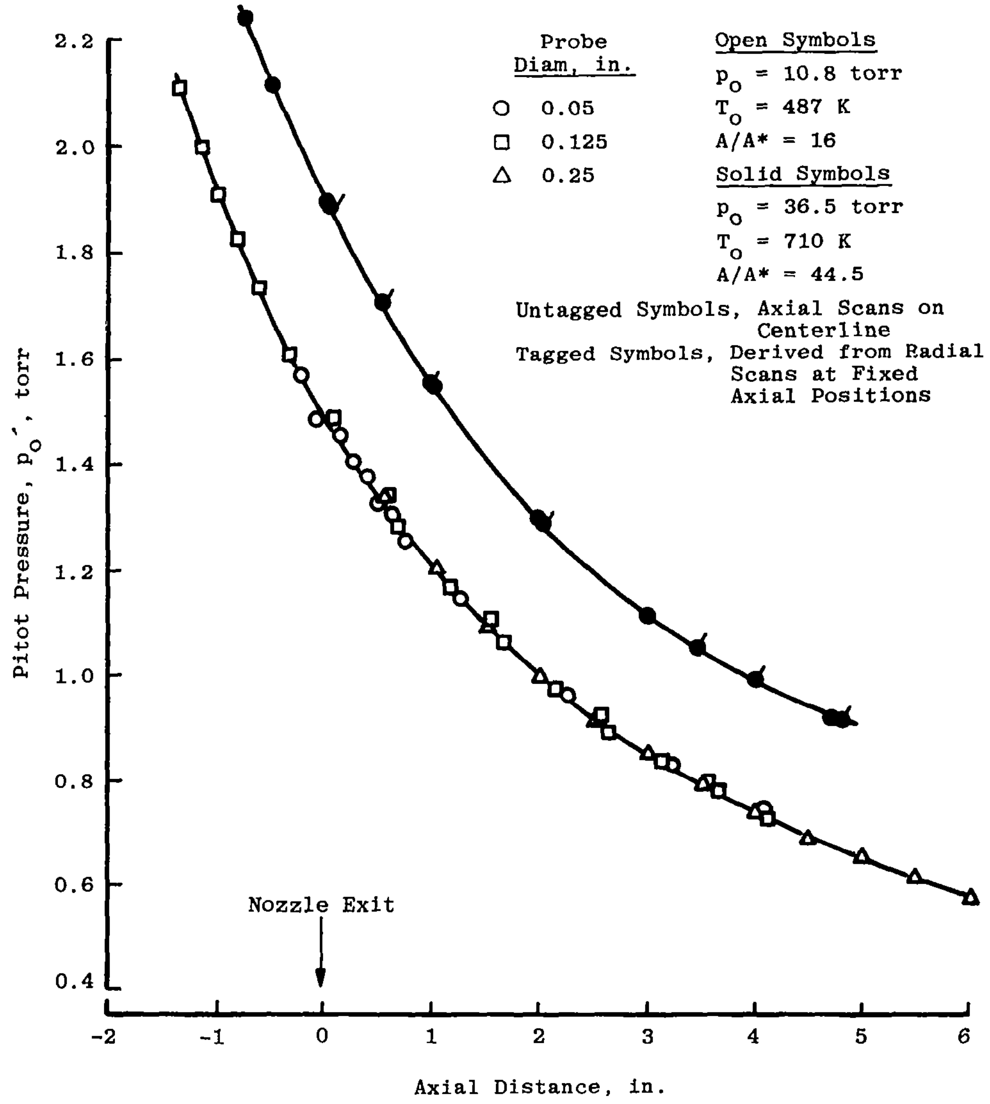

Figure 17. Centerline pitot pressure measurements—basic repeatability of test conditions.

the basic repeatability (± 1 percent) and reproducibility of the test conditions. They also illustrate that for the flow conditions on the nozzle centerline, the pitot pressure is essentially independent of probe size.

The values of the flow field properties on the nozzle centerline, e.g., M_∞, p_∞. T_∞, etc., derived from the measured values of pitot pressure, stagnation pressure, and stagnation temperature using the isentropic relationship given in Eq. (1) with the assumption that $\gamma = 1.4$, are presented in Fig. 18. These calibrations show that the exit-plane Mach number ranges from approximately 4 to 8. It is apparent from the data presented in Figs. 18a and b that there is a small degree of supercooling in the exit-plane flow (on the order of 15 K). Lewis and Williams (Ref. 45), in studies of condensation in the expansion of nitrogen from conical nozzles, have shown that supercooling of 40 K can exist without any detectable condensation in the flow. Therefore, it has been assumed in the present study that for this degree of supercooling (i.e. 15 K), condensation in the exit plane is unlikely. For the expansions presented in Figs. 18c and d, there is a probability of the occurrence of condensation in the exit plane because of the significant degree of supercooling (greater than 70 K). However, it should also be noted that Williams and Lewis (Ref. 46) have shown that CO_2 expansions from sonic orifices can be supercooled up to 100 K before condensation occurs.

The expansion of gas from a axisymmetric nozzle into a hard vacuum should result in the symmetrical distribution of flow field properties about the centerline of the nozzle. For a variety of reasons, possibly associated with probe/plume/chamber pumping interactions (Ref. 23) radial profiles of flow properties downstream of the exit have been found to be asymmetrical. An earlier study by Bailey et al. (a technical report is currently in preparation), has shown that symmetrical radial profiles of pitot pressure can be obtained in the 4- by 10-ft RVC. The difference between the present investigation and the earlier project was that in the present study, the probe and the probe support structure presented a considerably larger nonpumping area to the incident flow and, thus, increased the potential for interactions with the plume. Therefore, to determine whether the presence of the probe mechanism within the chamber resulted in a distortion of the nozzle expansion, complete radial profiles were obtained at a number of axial stations at and downstream of the nozzle exit plane. Examples of some of these profiles are presented for five axial stations in Fig. 19. To illustrate the symmetry of these radial profiles the exit-plane data have been replotted about the nozzle centerline in Fig. 20. Having established the basic symmetry of the flow, subsequent radial measurements were made from the nozzle centerline rather than both sides of the centerline.

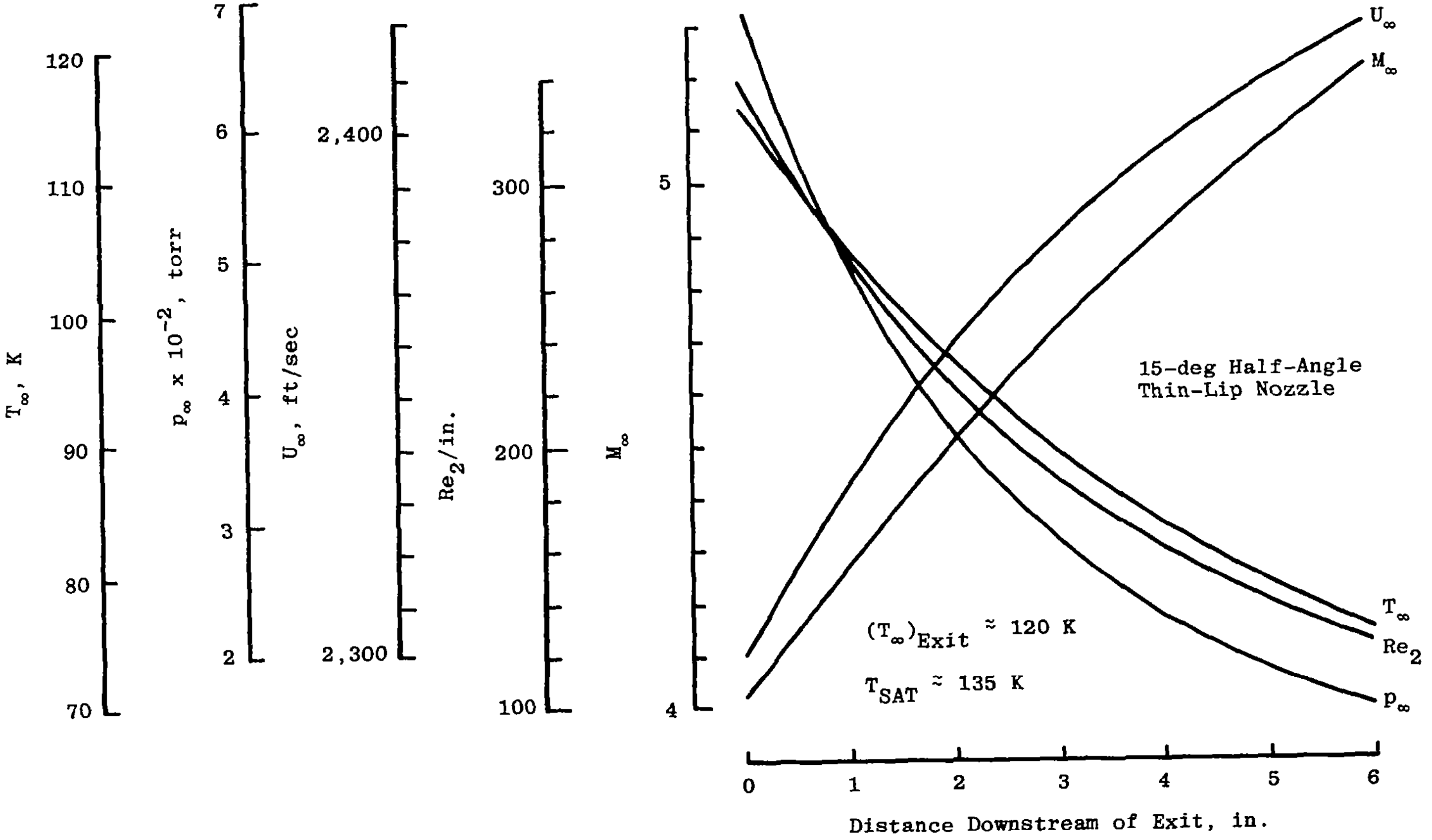

a. $A/A^* = 16$, $p_0 = 10.8$ torr, $T_0 = 487$ K

Figure 18. Centerline flow field properties as a function of axial distance.

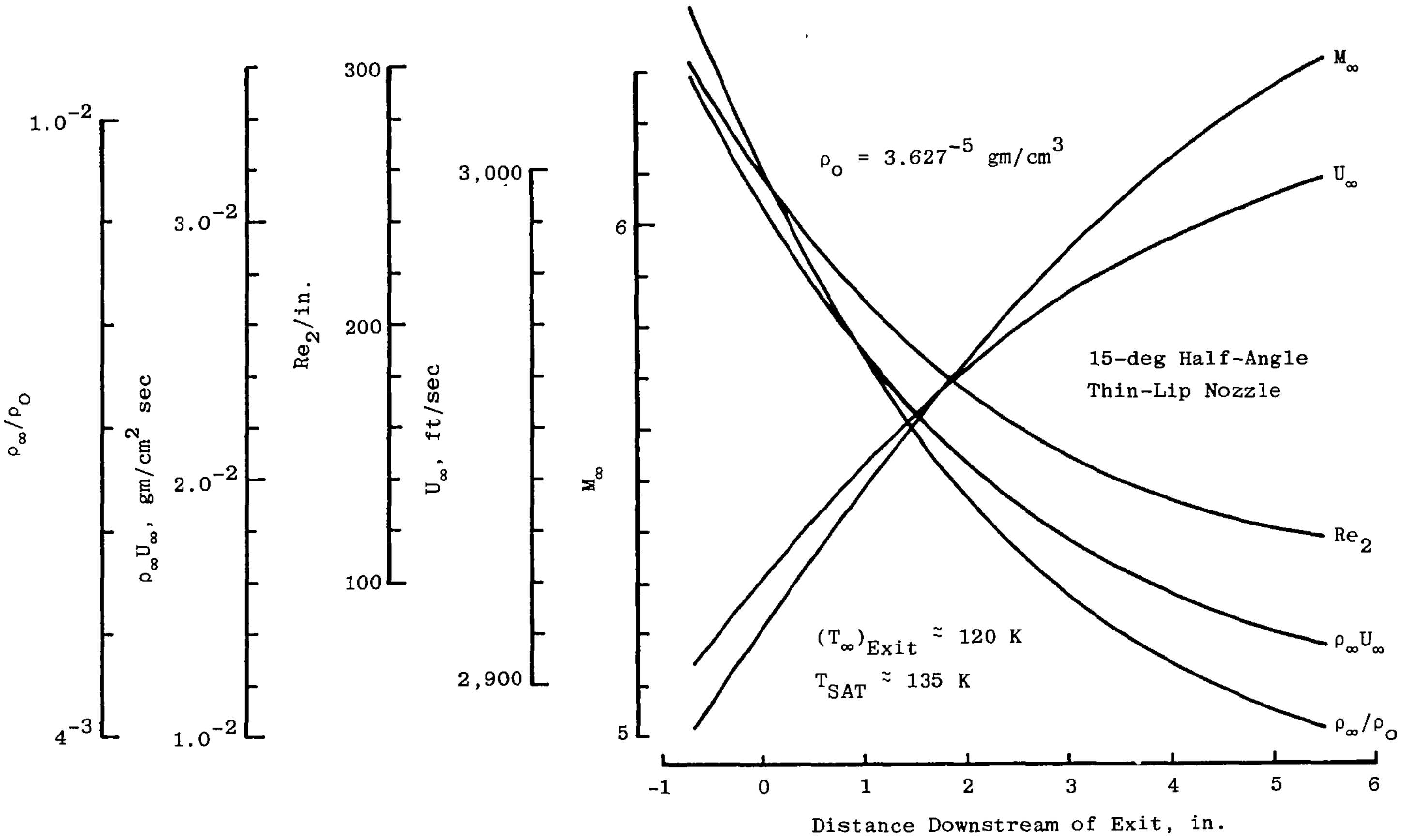

b. A/A* = 44.4, p_0 = 36.5 torr, T_0 = 710 K
Figure 18. Continued.

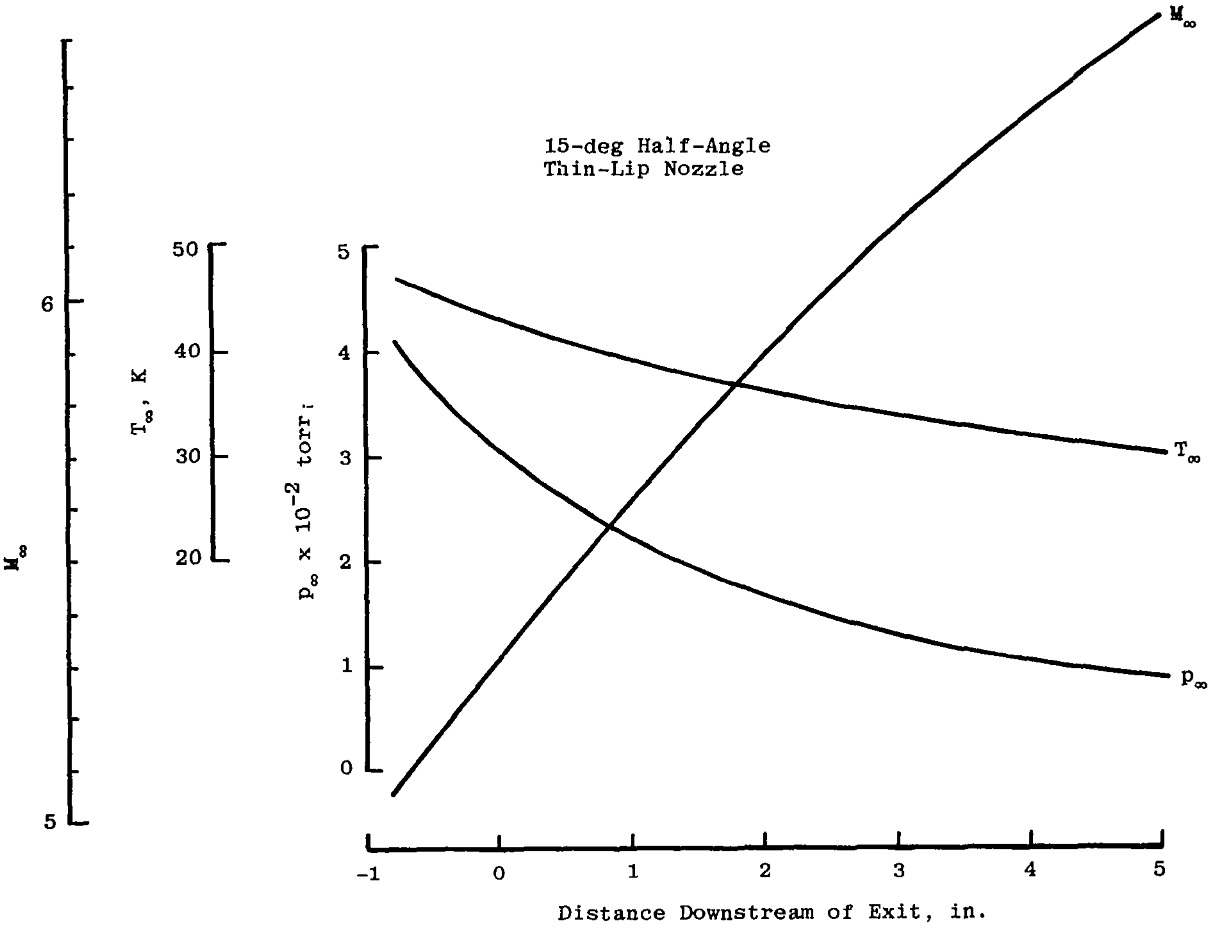

c. $A/A^* = 44.4$, $p_0 = 23.6$ torr, $T_0 = 288$ K
Figure 18. Continued.

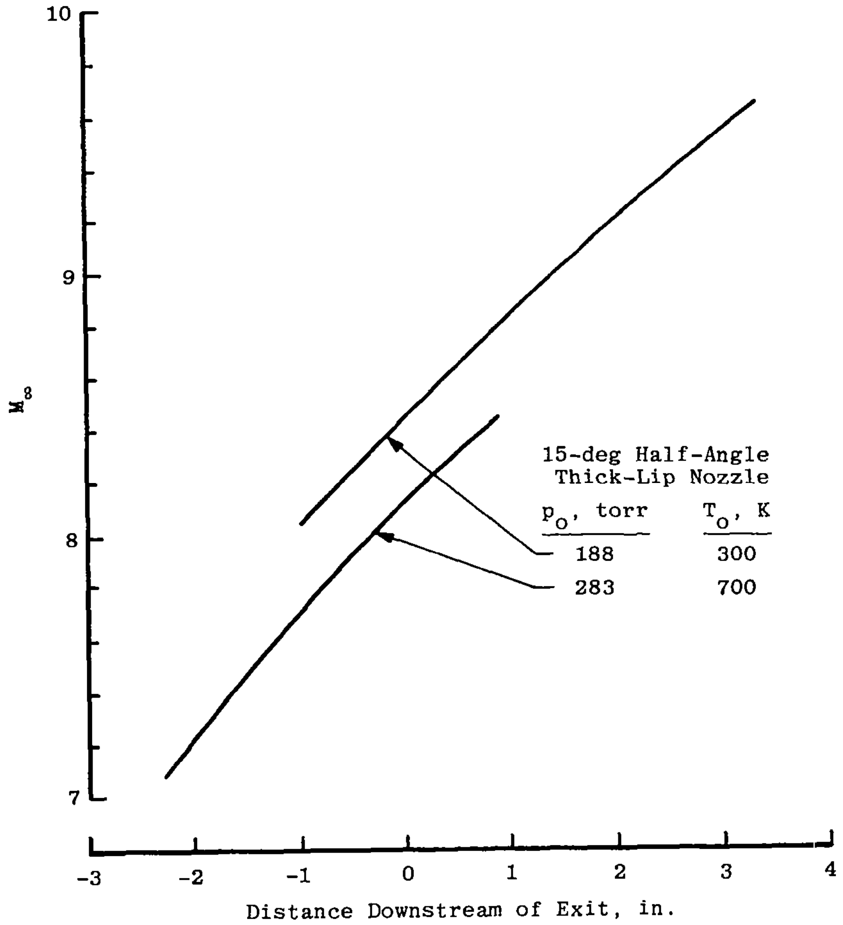

d. A/A* = 400

Figure 18. Concluded.

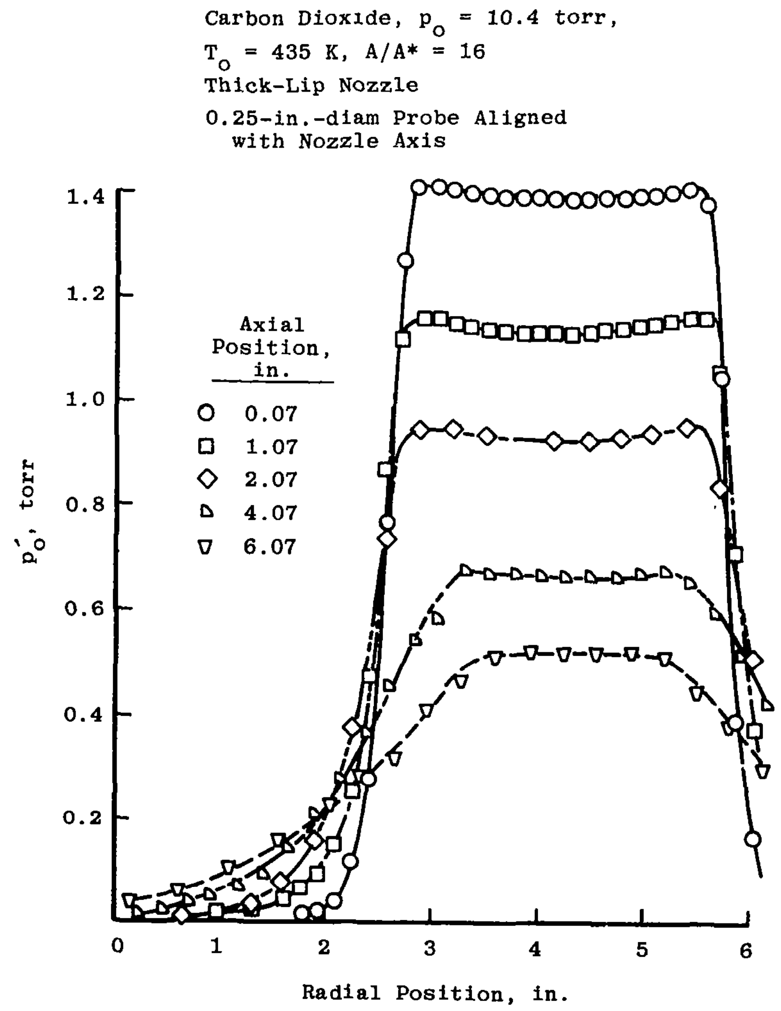

Figure 19. Radial pitot pressure profiles at several axial positions downstream of exit plane—raw data.

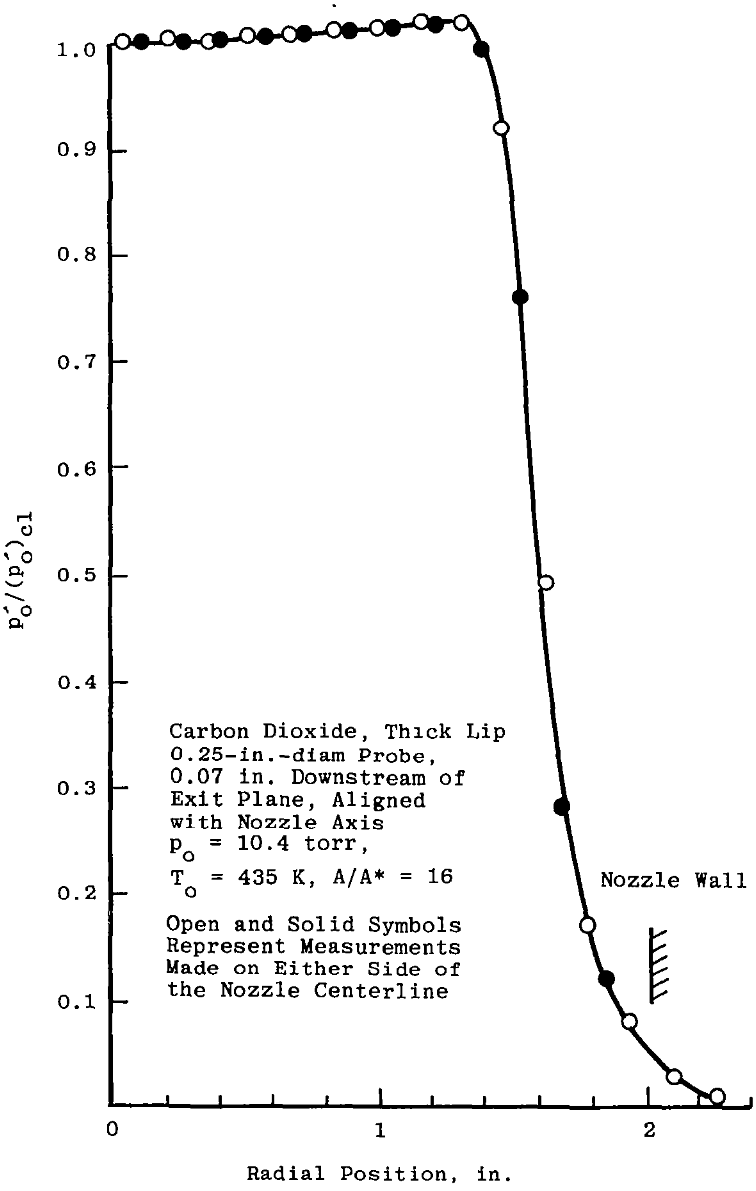

Figure 20. Nondimensionalized radial pitot pressure profile.

5.1.2 Flow Angle and Dynamic Pressure Measurements

The variation of pitot pressure with probe angle to the incident flow for two probe sizes (Fig. 21) illustrates that well-resolved measurements can be made to pressures as low as 1 × 10^{-3} torr. The degree of symmetry of these measurements (cf. Fig. 21a) is good, and the angle at which p_0'(max) occurs is well defined. It has been assumed, therefore, that the angle at which the maximum occurs in the measured value of p_0' is the angle of the flow velocity vector at that position in the nozzle plume.

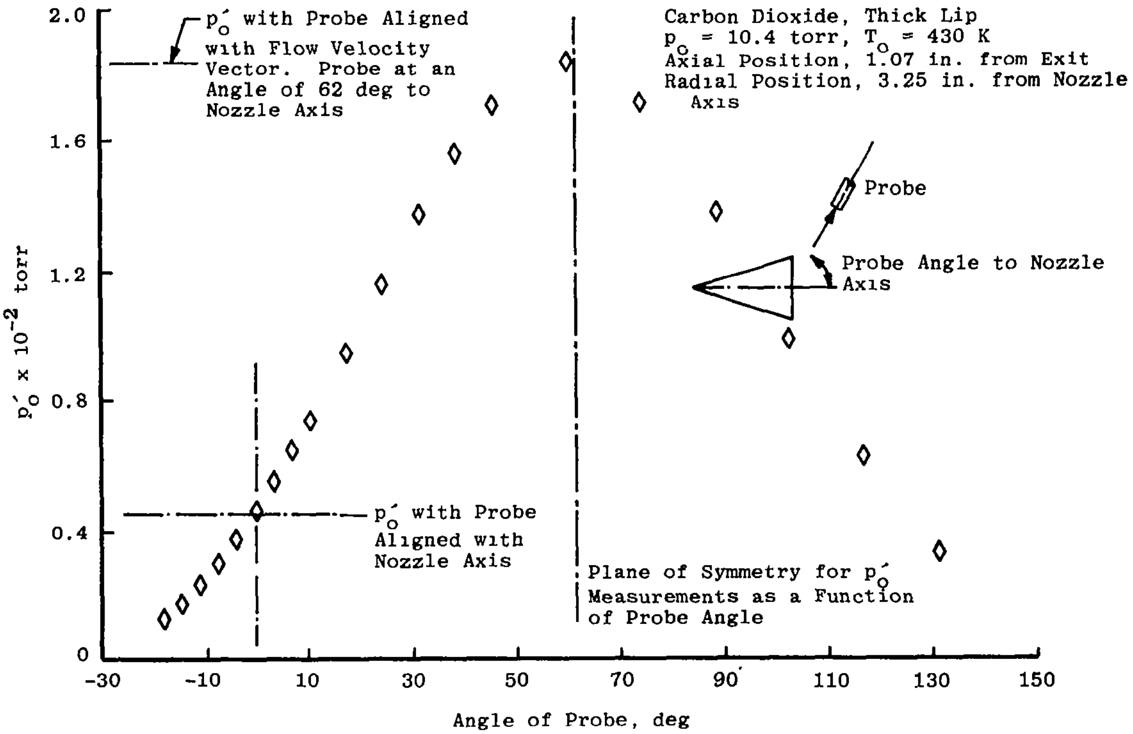

a. Probe diam, 0.25 in.

Figure 21. Variation of pitot pressure with angle of probe to flow.

The data presented in Fig. 21a illustrates clearly that there is a significant difference between the measured values of p_0' when the probe is aligned with the velocity vector or with the nozzle axis (i.e. a factor of approximately 4) when such measurements are made far from the nozzle centerline. The variation of the nondimensionalized pitot pressure with radial distance (Fig. 22) with the probe aligned (1) with the nozzle axis and (2) with the velocity vector indicates that for the radial extent of these measurements, there can be pressure differences on the order of a factor of 10 depending upon the probe alignment. The magnitude of the effect of misalignments of the probe with the velocity vector are further illustrated when the data presented in Fig. 21a are replotted as a function of angle to the flow velocity vector (Fig. 23). For angles greater than 75 deg, the measured value is less than 0.1 of the true value. Thus, any attempt to measure pitot pressure external to the nozzle in the region of the lip would result in dynamic pressures that are significantly in error if the probe used to make such measurements is aligned with the nozzle axis.

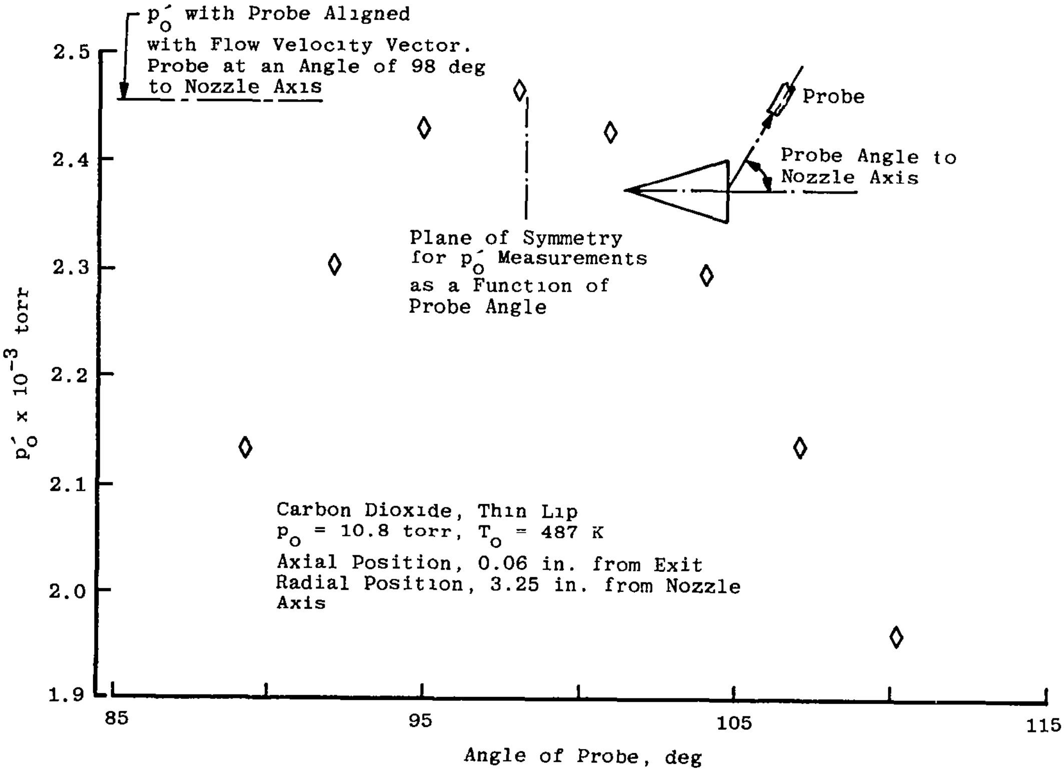

b. Probe diameter, 0.125 in.
Figure 21. Concluded.

At the outset of this program, it was intended to develop a relationship between $(p_o')_\theta/(p_o')_{\theta=0}$ and angle to the flow, e.g., Fig. 23, such that probe measurements made with the probe aligned with the nozzle axis could be corrected for probe misalignments to the flow. The data presented in Fig. 23 indicate that the form of this variation is a strong function of probe Reynolds number, a factor which complicates the above approach to such a degree as to make it infeasible. (It is of interest to note that the $Re_2d \approx 100$ data of the present study is in reasonable agreement with similar data obtained by Pollard, Ref. 27, in a low-density wind tunnel.) Within the constraints of the present program, it was not considered to be feasible to determine local flow angles from pitot pressure measurements of the type shown in Fig. 21a for every point of interest in the nozzle plume. The technique that was used, evolved from the observation that for pressures as low as 1×10^{-3} torr (cf. Fig. 21), the probe/transducer response to changes in angle was rapid enough that p_0'(max) could be determined by monitoring the gage output as the probe angle was varied. The validity of this approach was determined by comparing flow angle and p_0' values obtained in this manner with those obtained by the method exemplified by the data in Fig. 21 (cf. Fig. 25). Examples of p_0' and flow angle measurements as a function of radial position using this technique are presented in Fig. 24 for the 0.050-in.-diam (0.127-cm) probe. These measurements indicate that rapid changes in flow angle occur at the edge of the inviscid core in the free shear layer and that the flow angle to the nozzle axis is on the order of 80 deg at a radial position of approximately 5-in. (12.5-cm) off centerline.

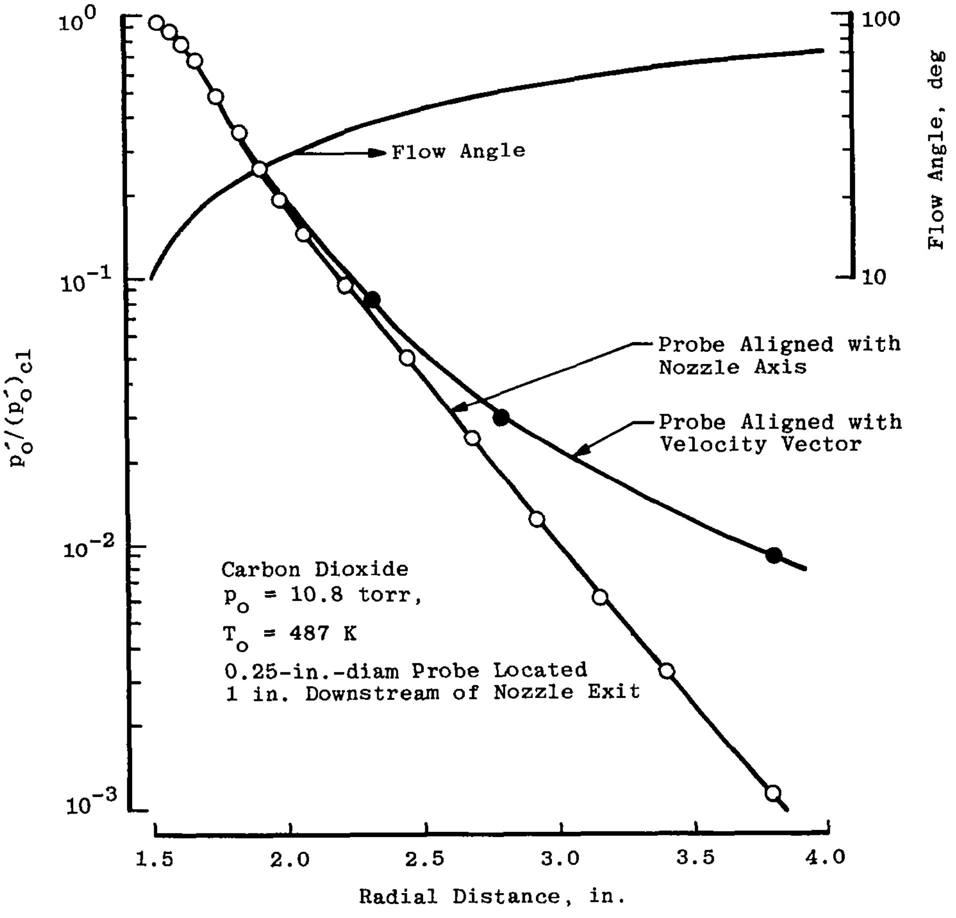

Figure 22. Effect of probe misalignment to flow velocity vector on radial pitot pressure measurements.

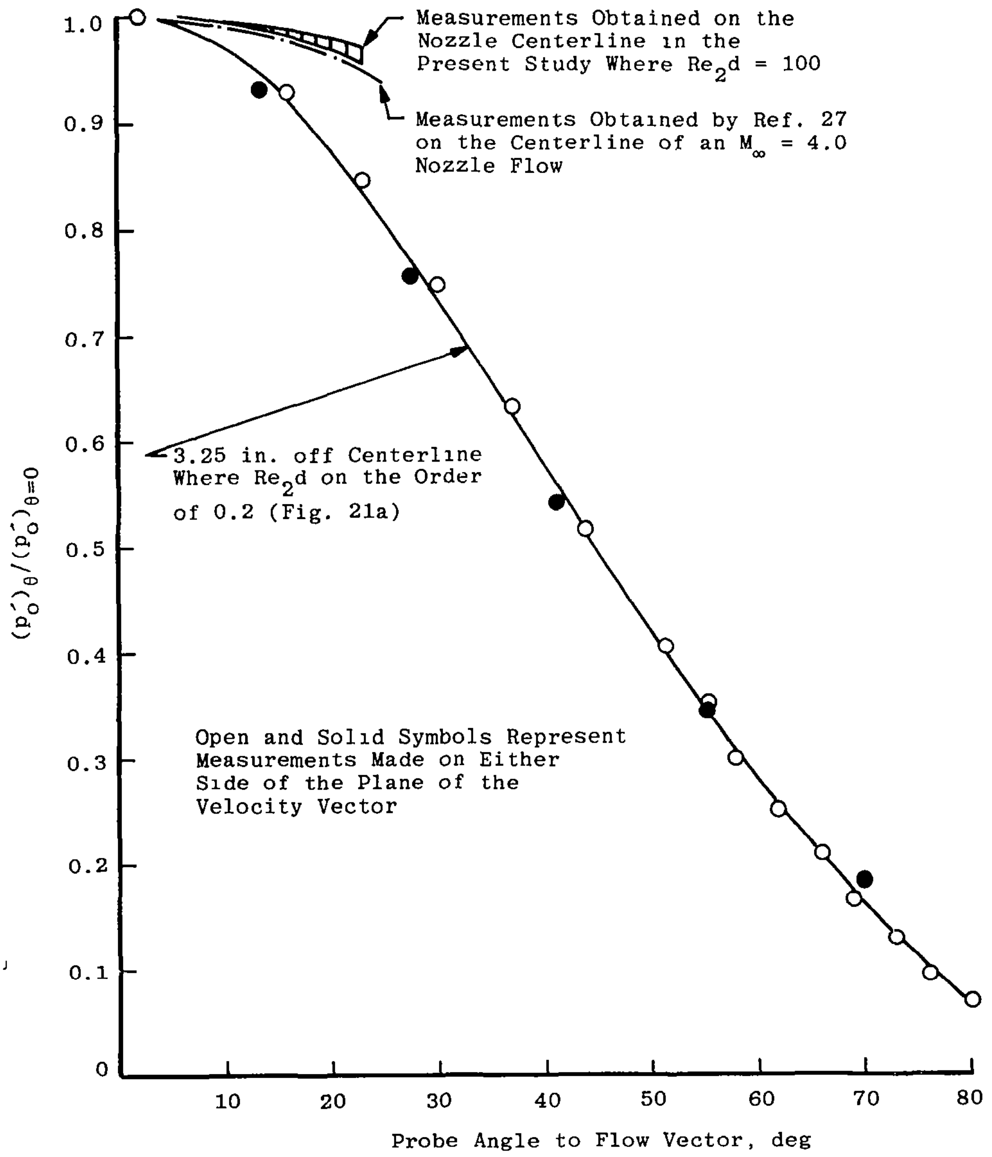

Figure 23. Effect of probe Reynolds number on the variation of pitot pressure with probe angle to the flow.

In the initial stages of this investigation, it became apparent that flow-angle measurements at the edge of the inviscid core in the region of rapidly decreasing pitot pressure were questionable in that in this flow regime the apparent flow direction was toward the nozzle axis rather than away from it. The form of this variation is illustated in

Fig. 25 where, in the region of the outer edge of the inviscid core, there is a rapid decrease in flow angle with both the 0.25- and 0.125-in.-diam (0.635 and 0.318-cm) probes indicating negative flow angles (i.e. flow towards the nozzle axis) of 20 deg. As can be seen from the data in Fig. 25a, these negative angles were observed when complete rotary scans were made to identify the flow angle and $p_0'(\max)$ and when $p_0'(\max)$ and flow angle were determined by peaking the p_0' signal. Similar experiments by Pollard (Ref. 27) in the free shear layer also demonstrate effects of this type. In the present study, the effects of this probe/shear layer interaction have been minimized through the use of the 0.050-in.-diam (0.127-cm) probe (Fig. 25). As the pressure gradient in the shear layer decreases with increased distance downstream of the nozzle exit plane, e.g., Fig. 25b, the magnitude of the probe-size effect decreases until at 6 in. (15 cm) downstream of the exit, flow-angle measurements are essentially independent of probe size. A possible explanation for the form of the flow-angle variation in the immediate region of the nozzle lip [i.e. radial location 2.0 in. (5 cm)] could be attributable to the interaction of the probe bow shock with the nozzle lip. The similarity in the form of the flow-angle variation in this region for the two larger probes appears to support this suggestion.

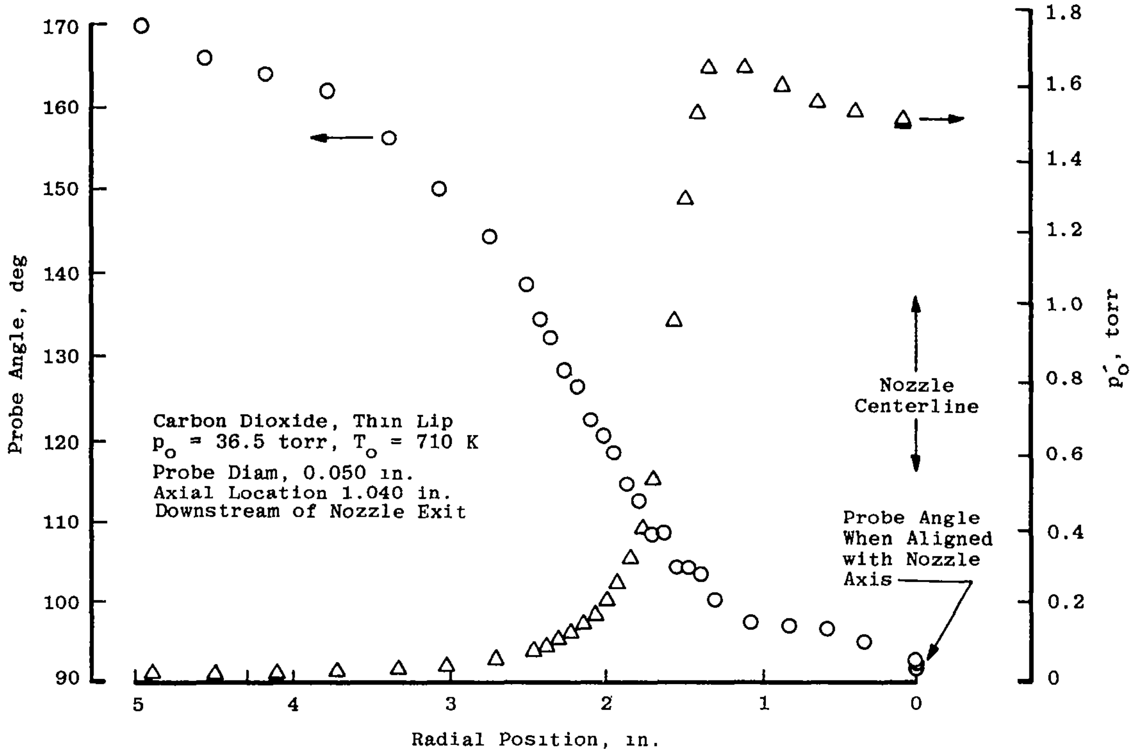

Figure 24. Pitot pressure measured with probe aligned with velocity vector—raw data.

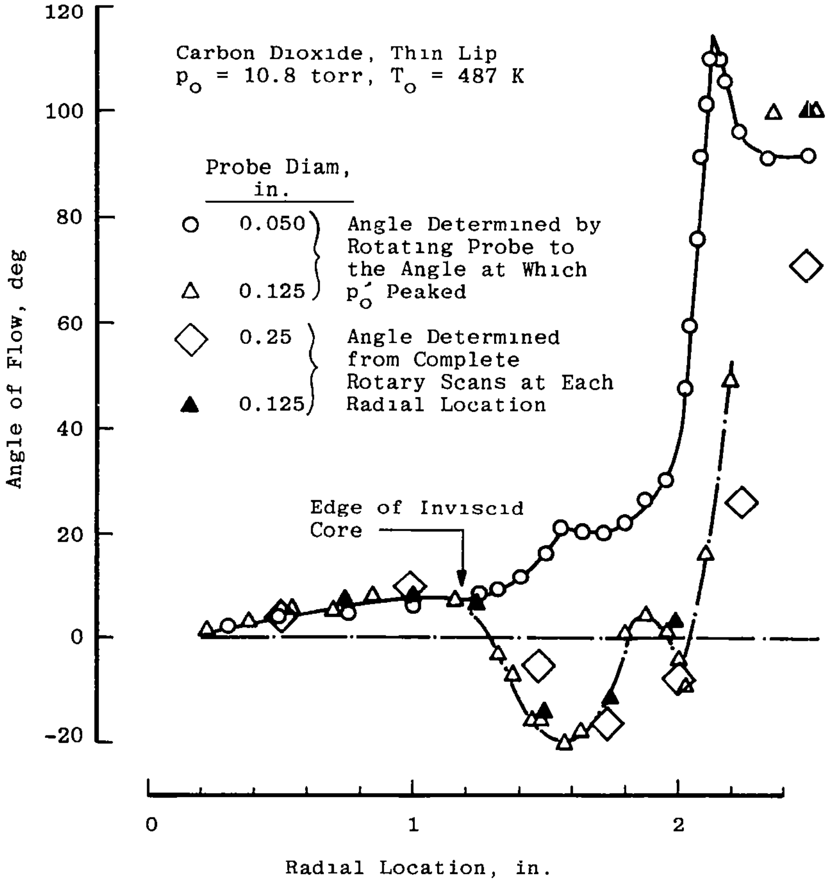

a. 0.05 in. downstream of exit plane
Figure 25. Effect of pitot probe size on flow-angle measurements.

Despite the significant differences in the measured flow angle in the immediate region of the inviscid core edge, there are no detectable effects upon the measured pitot pressure in this area (Fig. 26a). However, there are readily identifiable effects in the outer regions of the shear layer in the region of the nozzle lip (Fig. 26b).

Detailed measurements of flow field angle, both in the forward and backflow regions of the nozzle expansion, have been made for the heated flow conditions for the two smaller area ratio nozzles, i.e., $A/A^* = 16$ and 44.4. A complete summary of these experimental measurements for the $A/A^* = 44.4$ nozzle using the 0.050-in.-diam (0.127-cm) pitot probe is presented in Fig. 27. It is readily apparent from a consideration of these measurements, that flow angles in excess of 140 deg were measured. It should not be assumed that the measurements represent the maximum angle through which the flow turns. Rather, it is

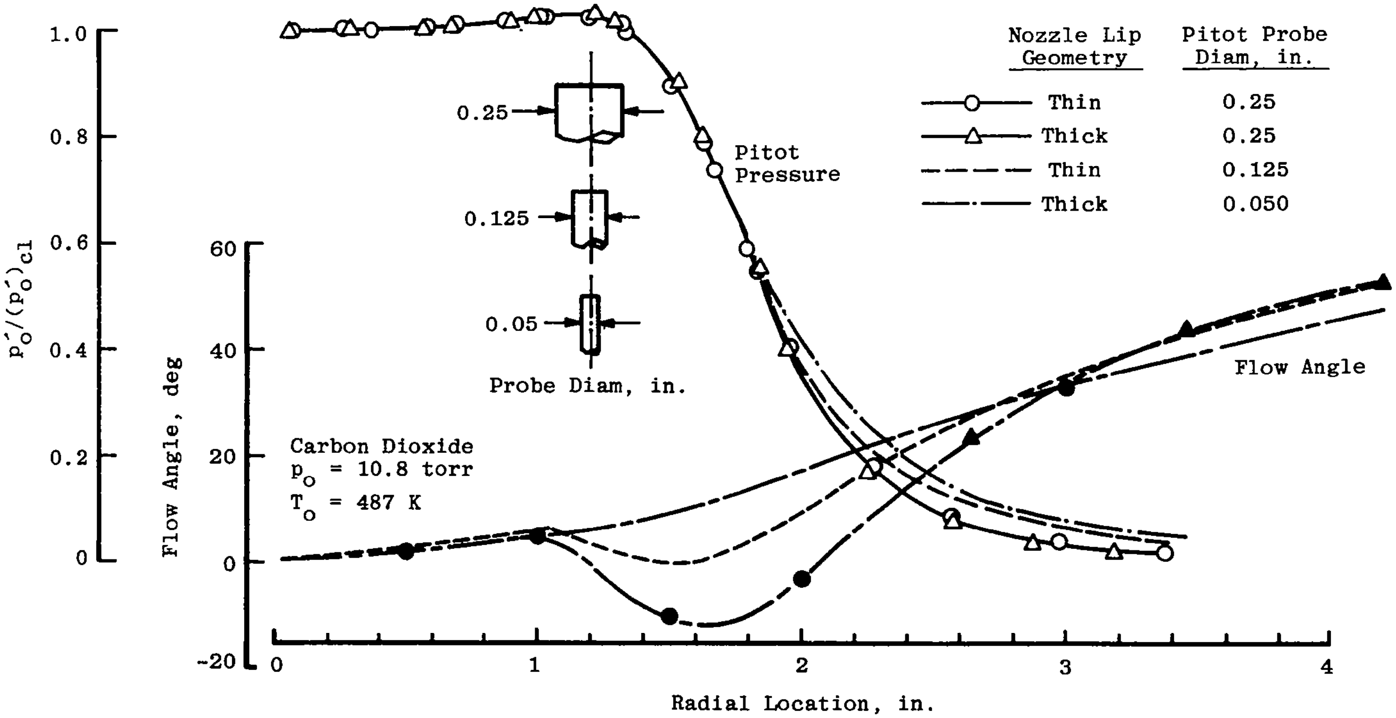

b. 2.1 in. downstream of exit plane
Figure 25. Concluded.

representative of a physical limitation of the probe/rotary mechanism configuration. The physical size of the probe/transducer/rotary mechanism was such that it was not possible to make measurements at greater angles in the backflow region of the nozzle. There was qualitative evidence to suggest that for both of these nozzle configurations, the flow angle in the backflow region may have been as great as 180 deg. This conclusion is based on the fact that after several hours of continuous nozzle operation (greater than 4 hr), a thin layer of CO_2 frost could be seen on the LN_2-cooled plate positioned slightly upstream of the nozzle throat section. As noted earlier, the inner and outer diameters of this plate are 4.5 and 9.5 in. (11.4 and 21.4 cm), respectively. Since the exit diameter of the nozzle is 4 in. (10 cm), an inference that may be drawn from this experimental observation is that the flow around the lip turns through approximately 180 deg. While it is possible that nozzle gas could have been deposited on this plate as a result of a recirculatory flow developing upstream of the lip, experimental measurements obtained with the QCM and the free-molecule pressure probe (to be discussed later) do not indicate the presence of circulatory flow when this plate is cold enough to pump CO_2.

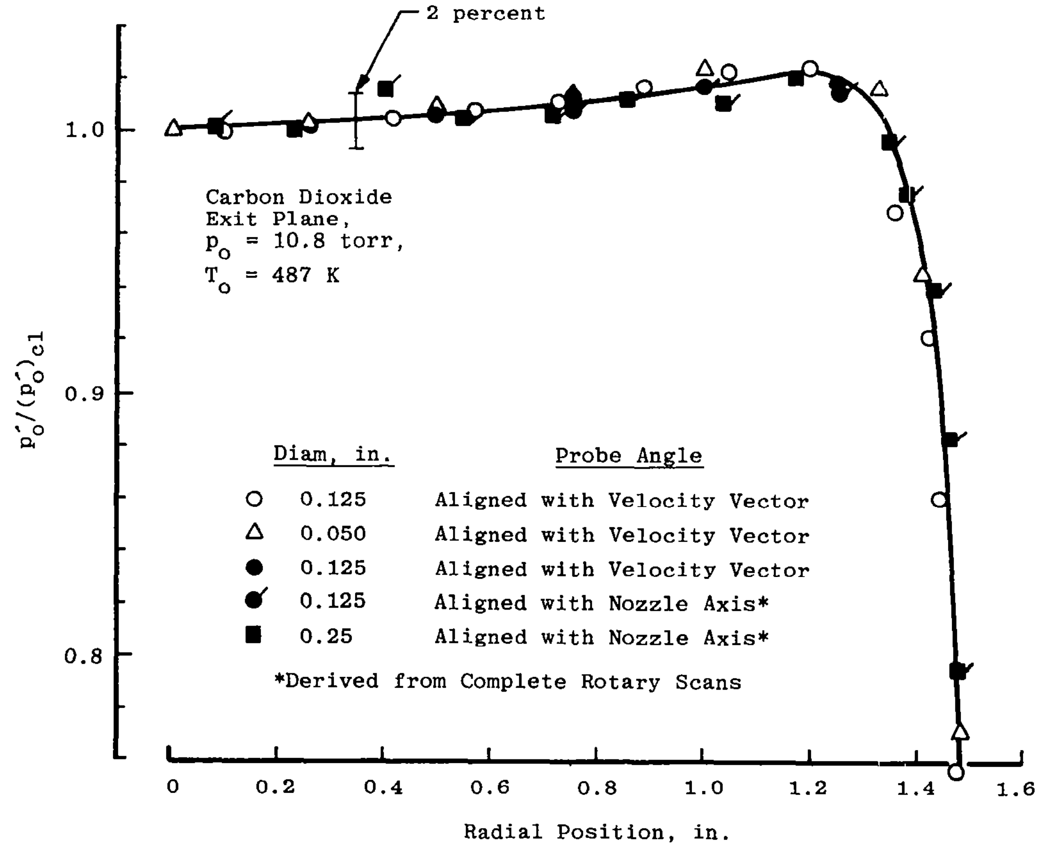

a. Inviscid core

Figure 26. Effect of pitot probe size on radial pitot profiles close to the nozzle exit.

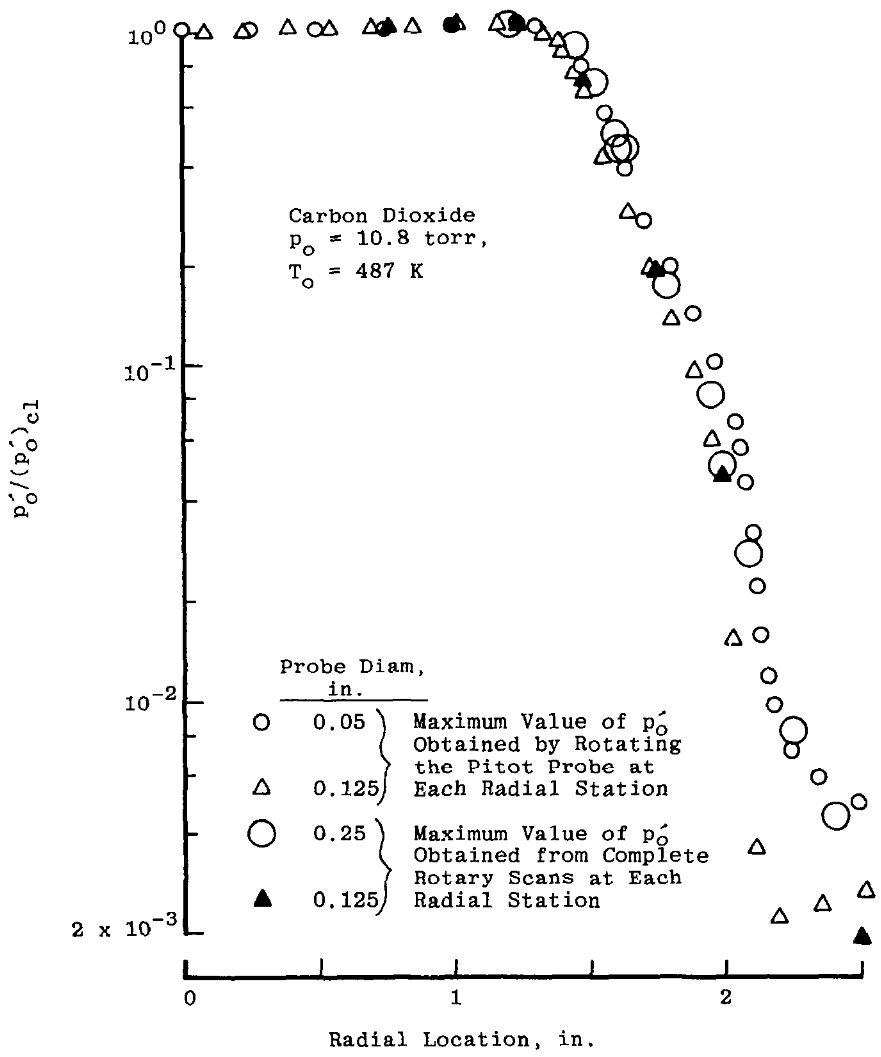

b. Shear layer
Figure 26. Concluded.

In the present study, it has been chosen to present the flow-angle data as contours of constant flow angle. To accomplish this, best fit lines (by eye) were drawn through the experimental data (cf. Fig. 27), and the flow-angle data were replotted as shown in Fig. 28. From a consideration of these two presentations of the experimental data, the constant flow-angle contours were developed and are presented in Fig. 29. As is noted in Fig. 29, in some areas of the plume, these flow-angle measurements have been supplemented with similar measurements obtained with the free-molecule pressure probe and the QCM.

Based on these flow-angle measurements, a number of observations may be made which support observations that have been arrived at from a wholly theoretical viewpoint. Based on studies involving the Monte Carlo technique, Bird (Ref. 47) has shown that in the boundary-layer flow upstream of the nozzle lip, the local flow angle is greater than the local angle of the nozzle wall, i.e., the local flow is directed towards the nozzle wall rather than being parallel to it. The present experiment (Figs. 25a and 29) indicates that flow angles of up to 30 deg are possible in the exit plane, indicating local flow angles with respect to the wall of 15 deg, which is of the magnitude observed in Bird's theoretical studies (Ref. 47).

From a consideration of the measured flow angles in the region of the lip, it may be inferred that the gas entering the backflow region must originate in the very thin layer of gas close to the nozzle wall in the region of the nozzle lip. From theoretical considerations, Bird

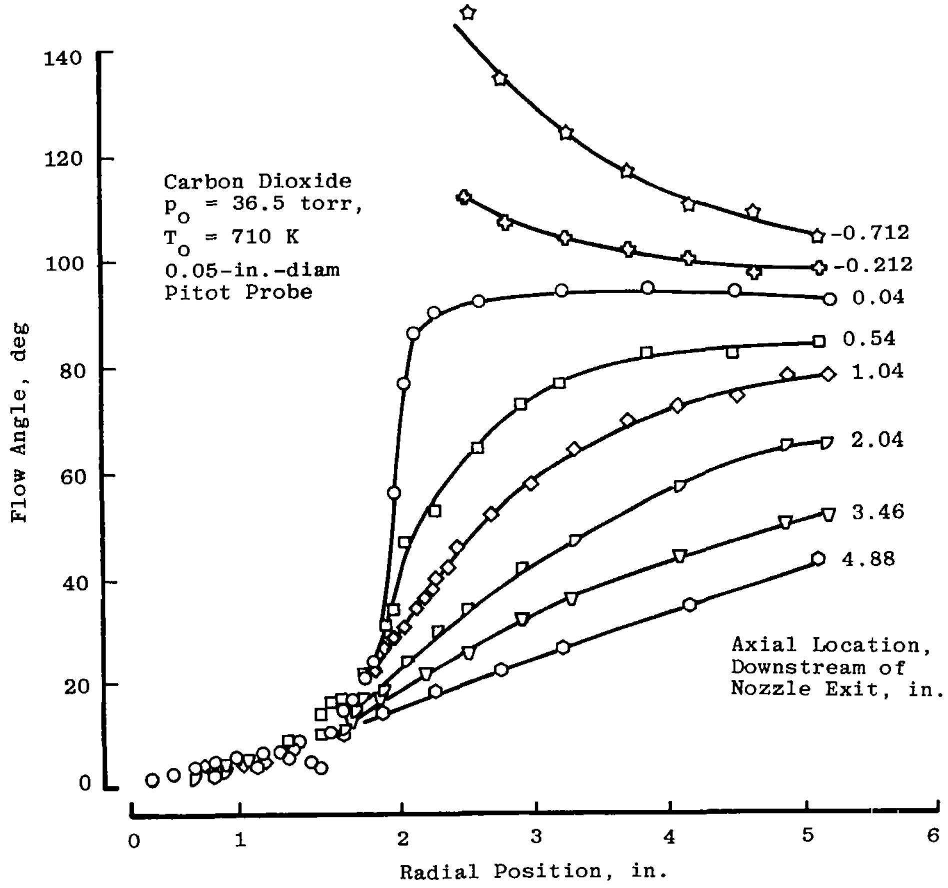

Figure 27. Experimental measurements of flow angle.

(Ref. 47) has concluded that the flow in this region of the nozzle boundary layer is the primary source for the plume backflow gases. An assumption that has been made with regard to nozzle expansions into a vacuum is that the resulting plume becomes source-like in form close to the nozzle (e.g., Refs. 4 and 31). An analysis of the present flow-angle measurements close to the nozzle exit plane (Fig. 30) revealed nonradial flow close to the nozzle. The deviations from radial flow are greater in the backflow region than in the forward-flow region. The larger deviation in the backflow region may be a reflection of the fact that in this region of the expansion, the flow of gas is determined by the detailed shape of the lip. Bird (Ref. 47) has emphasized the importance of the flow geometry in this region of the expansion in the determination of how much gas enters the backflow region.

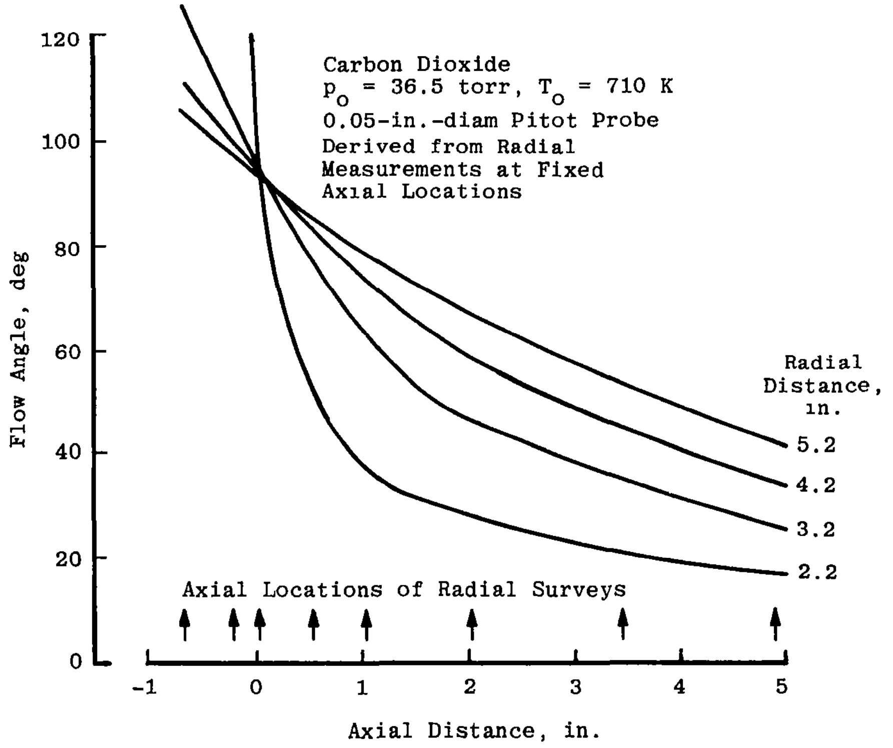

Figure 28. Flow angle as a function of axial and radial location.

Radial pitot pressure profiles (e.g., Figs. 19 and 20) were obtained at a number of axial stations both upstream and downstream of the nozzle exit plane. These measurements were summarized and are presented as contours of constant pitot pressure as a function of axial and radial position in the nozzle plume, Fig. 31. It will be noted that these measurements are presented in their uncorrected form. The magnitude of the viscous corrections can be determined from the viscous correction information presented in Fig. 9. Graybeal (Ref. 25) indicated that when the pitot probe Reynolds number is on the order of 0.01, it can reasonably be assumed that the probe is in the free-molecule flow regime. Based on the QCM measurements (to be discussed later), which measure $\varrho_\infty U_\infty$ and a viscosity based on conditions downstream of the normal shock (i.e. T_2) for the centerline conditions, a value of Re_2d has been calculated. The boundary marking the occurrence of the onset of free-molecule flow, using Graybeal's criterion, is given in Fig. 31.

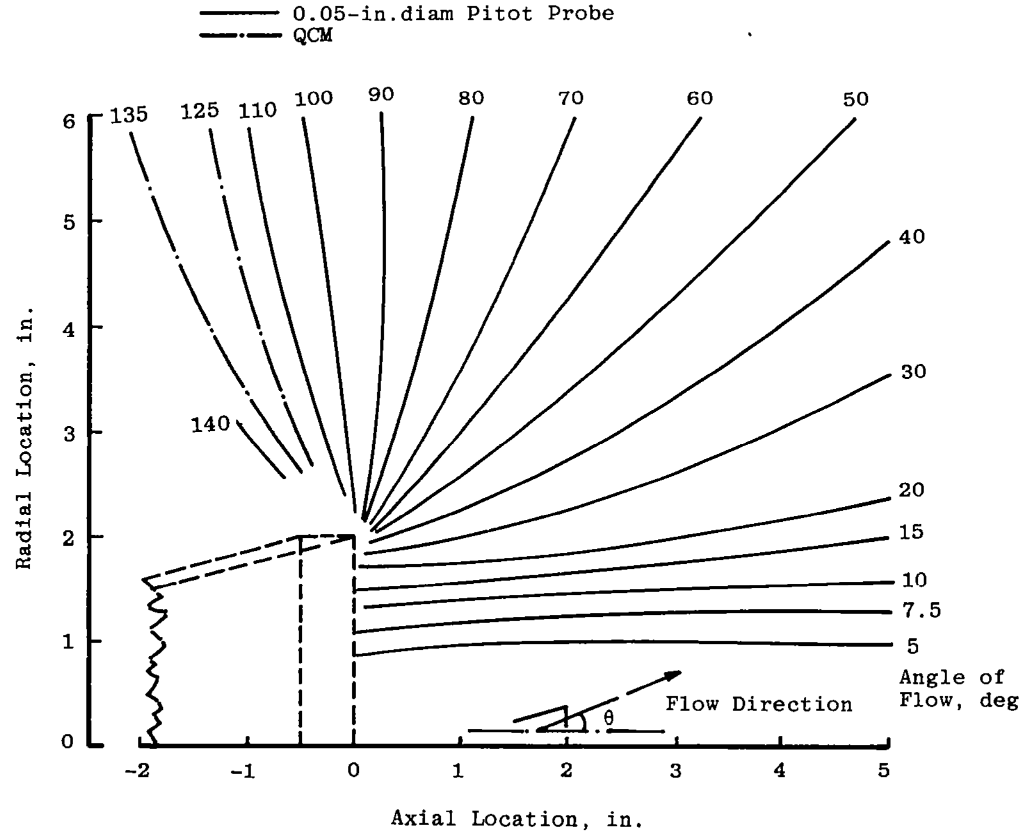

a. Carbon dioxide, p_0 = 36.5 torr, T_0 = 710 K
Figure 29. Spatial map of constant CO_2 flow-angle values.

It is tempting to attribute the off-axis peaks in the radial pitot pressure profiles (Fig. 31) to a probe/flow interaction phenomenon. As will be seen in a later section, nonintrusive number density profiles obtained with the electron beam fluorescence technique, show similar off-axis peaks in the radial profiles. It should be noted that pitot pressure and

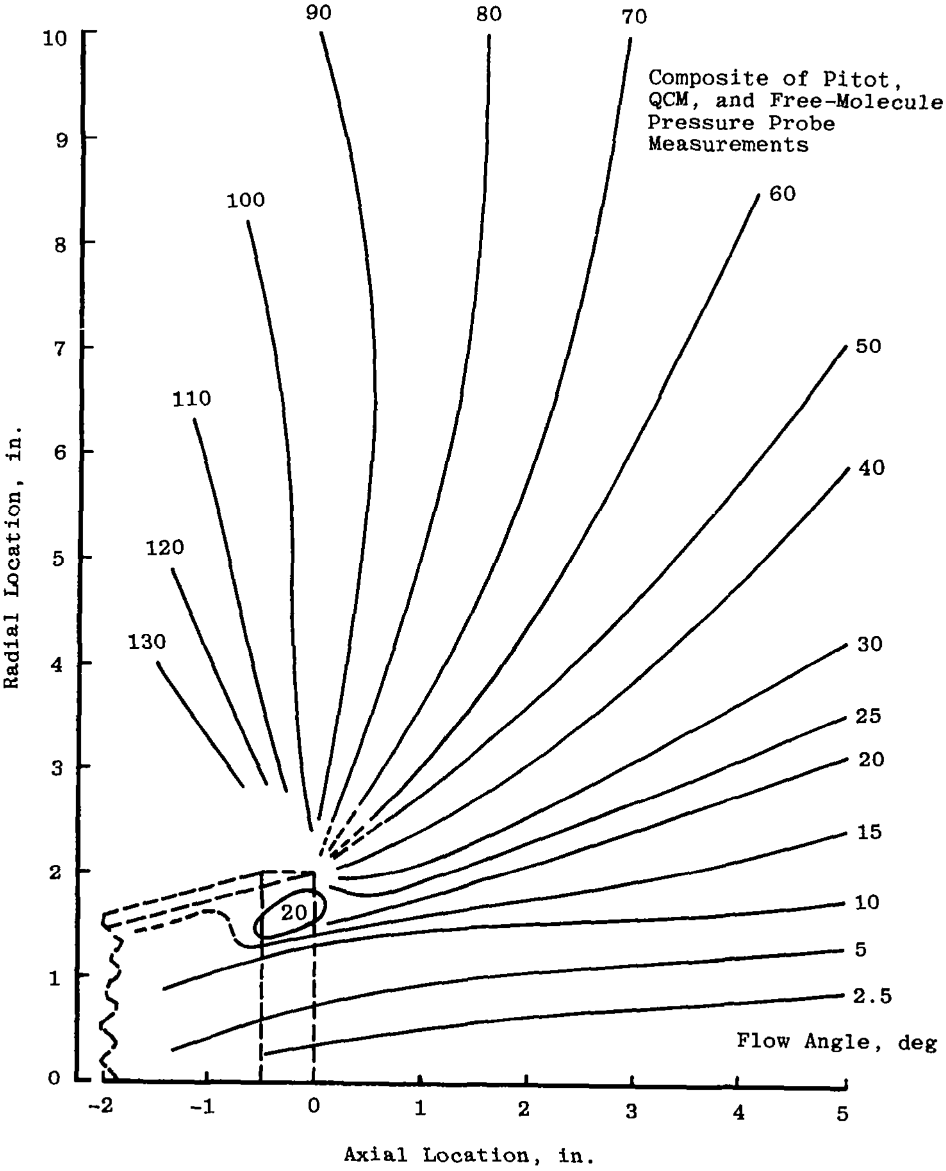

b. Carbon dioxide, p_0 = 10.8 torr, T_0 = 487 K
Figure 29. Concluded.

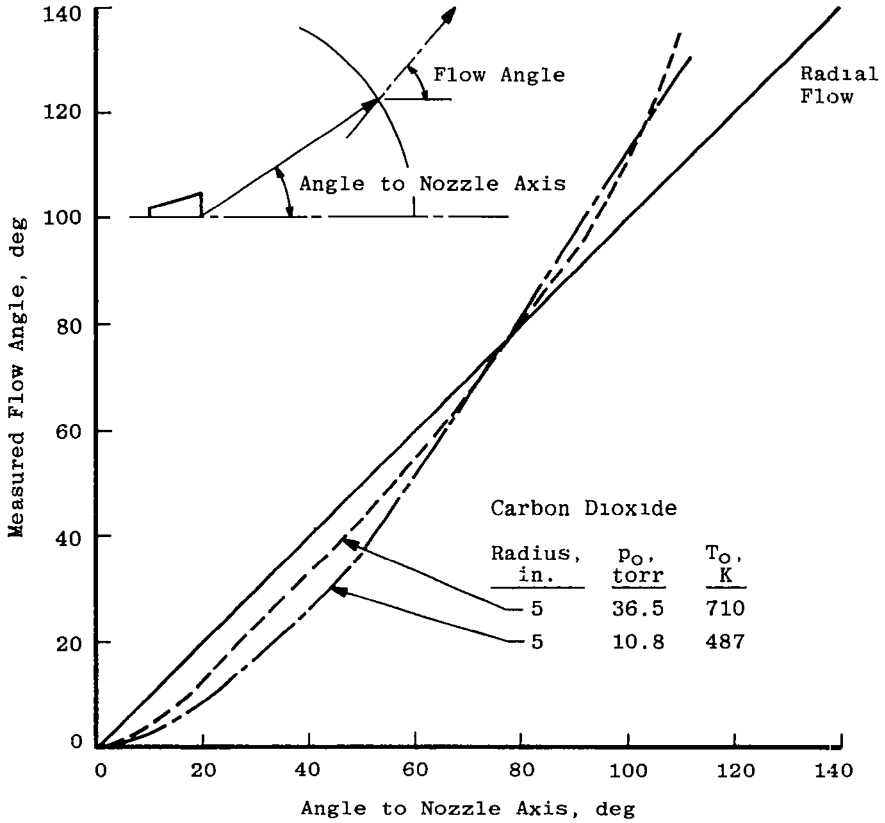

Figure 30. Nonradial nature of expanding flow.

electron beam measurements made in an earlier test program by Bailey et al. show similar profiles as does an electron beam study by Wada (Ref. 20). Thus, these off-axis peaks are a flow phenomenon related to the expanding nozzle flow rather than to the method for making the measurement. This is not to say that probe/flow interaction cannot affect such measurements (e.g., Ref. 23) but that for the present test, they are not a significant effect.

As a result of this phase of the test program, it has been shown that appropriately designed pitot pressure probes can make (1) accurate pressure measurements over a 4-decade range of pressure and (2) measurements well into the backflow region of an expanding nozzle plume. Drzwiecki et al. (Ref. 48) have demonstrated that an array of pitot probes positioned in the forward-flow region of a small pulsed motor can provide accurate pitot pressure measurements at pressures as low as 2×10^{-2} torr. The present study suggests that this type of approach to the definition of the flow properties of a pulsed motor in a ground-based vacuum chamber can be extended to measurements in the backflow region. This approach to the definition of nozzle plume properties has the advantage of simplicity and low cost.

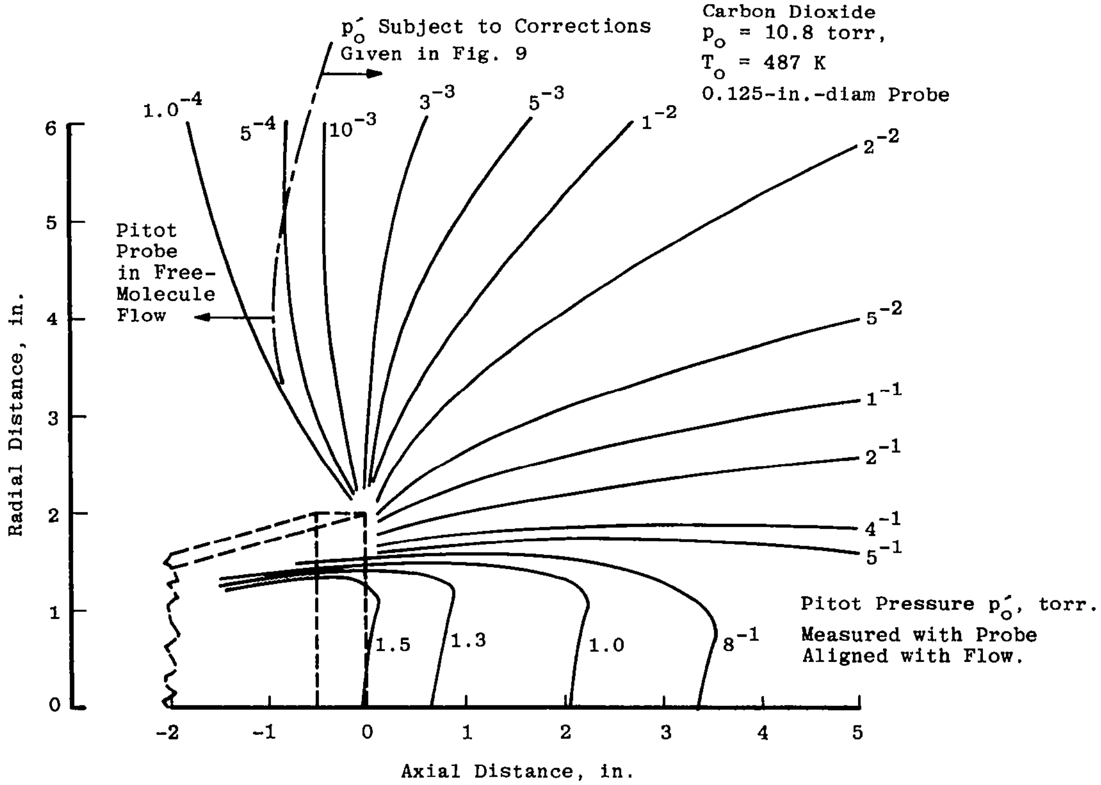

a. $A/A^* = 16$

Figure 31. Spatial map of constant CO_2 pitot pressure values, uncorrected for viscous effects.

5.2 QUARTZ CRYSTAL MICROBALANCE

5.2.1 Mass Flux Measurements

The rotary QCM (Fig. 11) was positioned such that mass flux measurements could be made in both the forward and backflow regions of the nozzle plume generated by the two smaller area ratio nozzles under heated flow conditions. The Berkeley Controls, Inc., QCM Model MK9 was used in conjunction with a Model 1700 QCM signal processor to measure the mass deposited on the crystal and the crystal temperature. These outputs were displayed on a strip chart record.

As noted earlier, the QCM responds to mass condensed on the sensing crystal. In the present instance LN_2 cooling of the crystal should result in the capture of all CO_2 incident upon it. In the pumpdown and cool down of the chamber, the cool down of the QCM crystal was delayed in order that any chamber-related water vapor would be condensed on the chamber

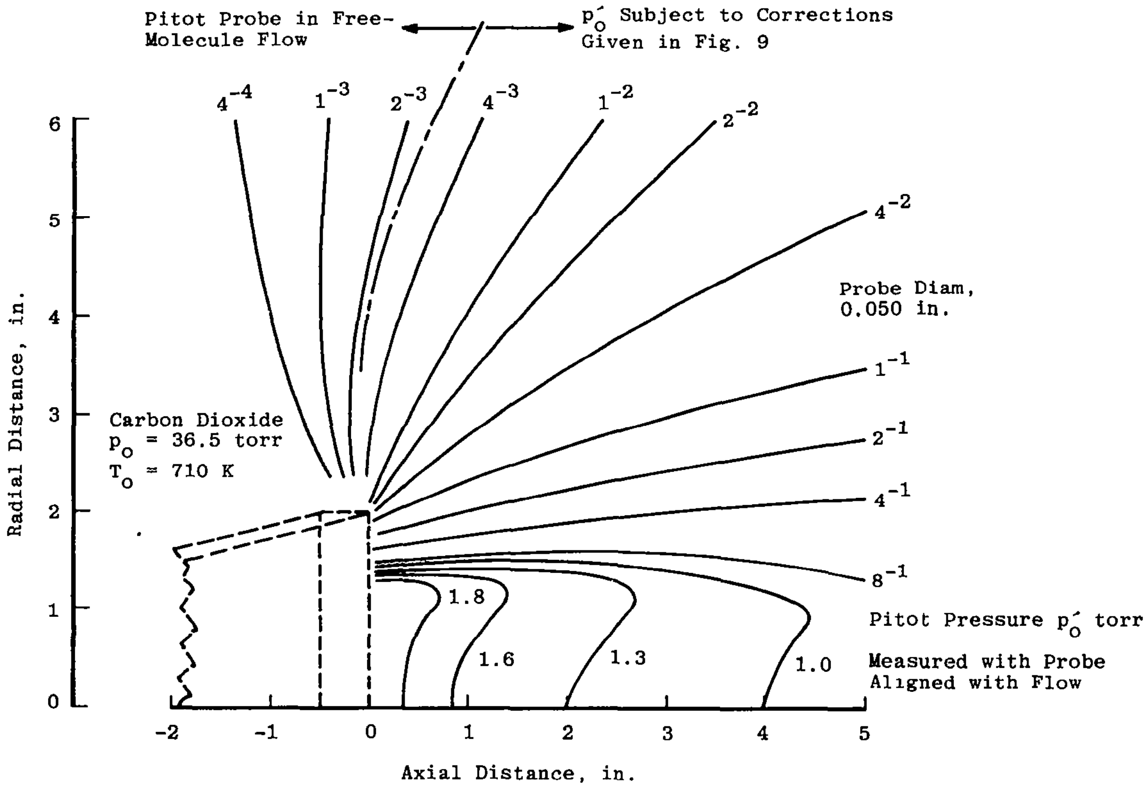

b. A/A* = 44.4
Figure 31. Concluded.

cryopanels rather than on the QCM crystal. This is one of the primary reasons that the QCM used in this investigation was cooled by LN_2 supplied from a Dewar that was independent of the main cryopumping systems used in the 4- by 10-ft RVC. When the chamber and nozzle flow were well established and stable, cool down of the sensor was started. In this cool-down phase, care was taken to orient the QCM so that it was not looking at the nozzle flow in order to avoid premature mass deposition before the crystal was completely cold. It was found that satisfactory performance of the QCM could be realized when the crystal was cooled to at least 83 K. For crystal temperatures above this value, erratic performance of the QCM was observed. When the crystal was saturated, the gas load was vaporized by operating the crystal heaters. After the initial cool down of the crystal, it required about 15 min to warm up a saturated crystal and return it to a clean condition.

Prior to the present test entry, other than a brief evaluation of the QCM in a static environment, no operational experience with this QCM was available for the types of flow situations encountered in this investigation. It was intended to position the QCM at a particular position in the plume and orient the QCM to the local flow angle that had been obtained with pitot/free-molecule probes (cf. Fig. 29). An example of the type of record that results with this approach is presented in Fig. 32. It will be noted that there is a linear variation of mass deposited as a function of time. It was readily apparent from a consideration of this record that accurate determinations of mass flux could be made without saturating the crystal at each probe location. The experimental data presented in Fig. 33 show that a number of probe angle settings are possible before the crystal becomes saturated. In this particular instance, the probe angle has been varied at a particular location in the plume. An appreciation for the degree of repeatability of the measurements can be gained from a comparison of the measurements obtained at an angle of 165 deg. A number of rotary scans were obtained at several fixed positions with respect to the nozzle (Fig. 34). As would be expected, these scans indicate that mass variation with probe angle to the flow was well represented by a cosine variation. This relationship has been invoked to make flow field measurements in the high mass flow regions in the forward flow. With the assumption that the flow field angle was well defined by the independent pitot and free-molecule probe measurements, the QCM was set at a large angle to the flow (> 60 deg), and the measured mass flux was adjusted for this angle difference using the cosine relationship. Summaries of the experimental measurements are presented as constant mass flux contours in Fig. 35.

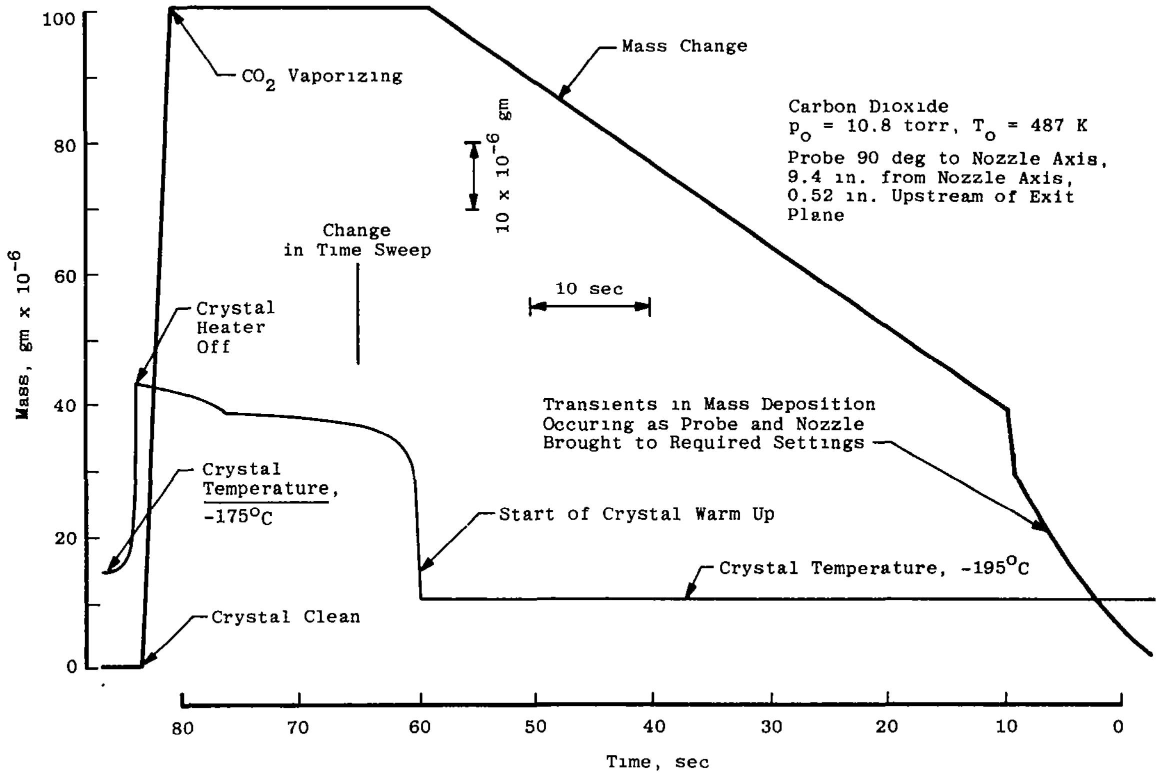

Figure 32. Strip chart record of QCM output.

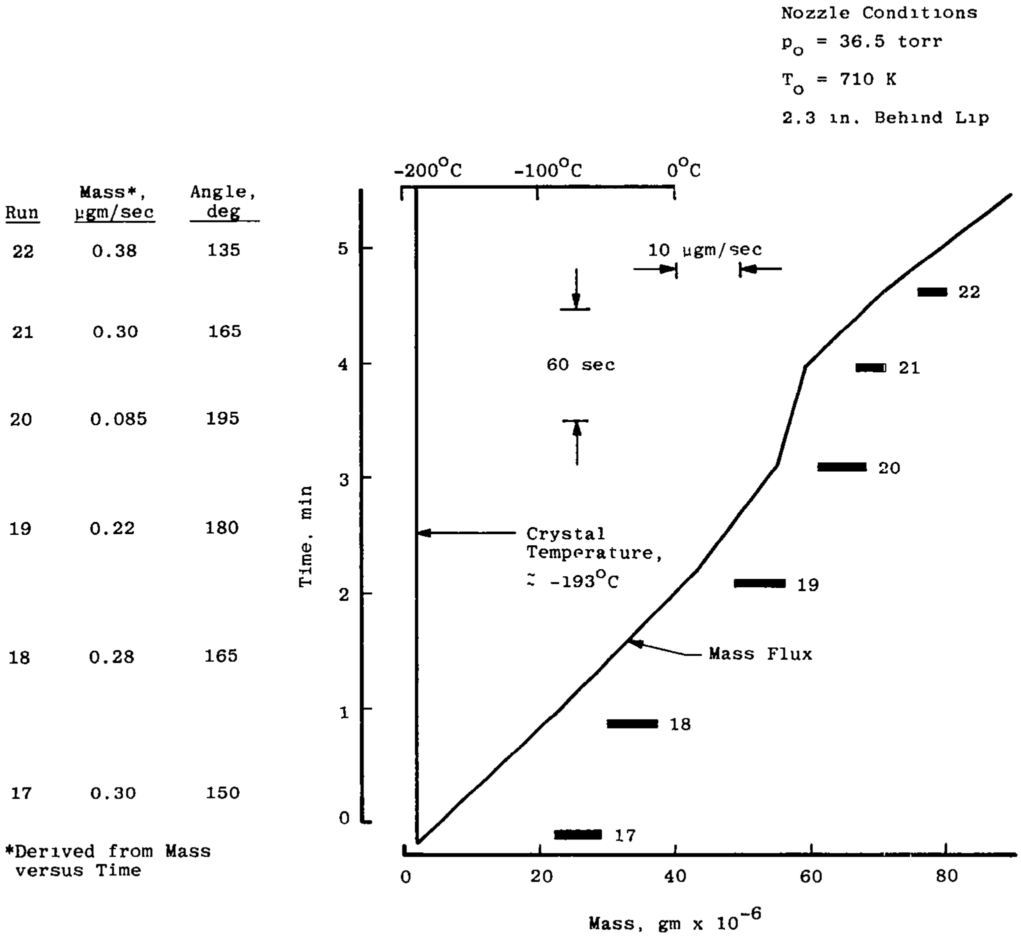

Run	Mass*, μgm/sec	Angle, deg
22	0.38	135
21	0.30	165
20	0.085	195
19	0.22	180
18	0.28	165
17	0.30	150

*Derived from Mass versus Time

Figure 33. QCM strip chart record with varying probe angle.

Also shown in Fig. 35, are profiles of a Reynolds number, Re_2d. The Reynolds number, Re_2d, is defined as $\varrho_\infty U_\infty d/\mu_2$ where the viscosity μ_2 is determined from a knowledge of the temperature T_2 and $\varrho_\infty U_\infty$ can be determined directly from the QCM measurements. For the purposes of the present analysis of the data, it has been assumed that the nozzle centerline values of T_2 (determined from normal shock values) obtain throughout the flow field. This is a realistic approximation in the forward-flow region but may overestimate T_2 (and hence underestimate Re_2d) in the backflow region. A knowledge of the magnitude of Re_2d is required if more detailed analyses of the pitot pressure measurements (Fig. 31) are to be made.

A calibration of the QCM was made by positioning the QCM in the flow field generated by the 0.6-in.-diam (1.52-cm) sonic orifice described earlier (cf. Fig. 4). The QCM was positioned at a distance of 17.5 in. (44.45 cm) from the exit plane of this nozzle, and the mass

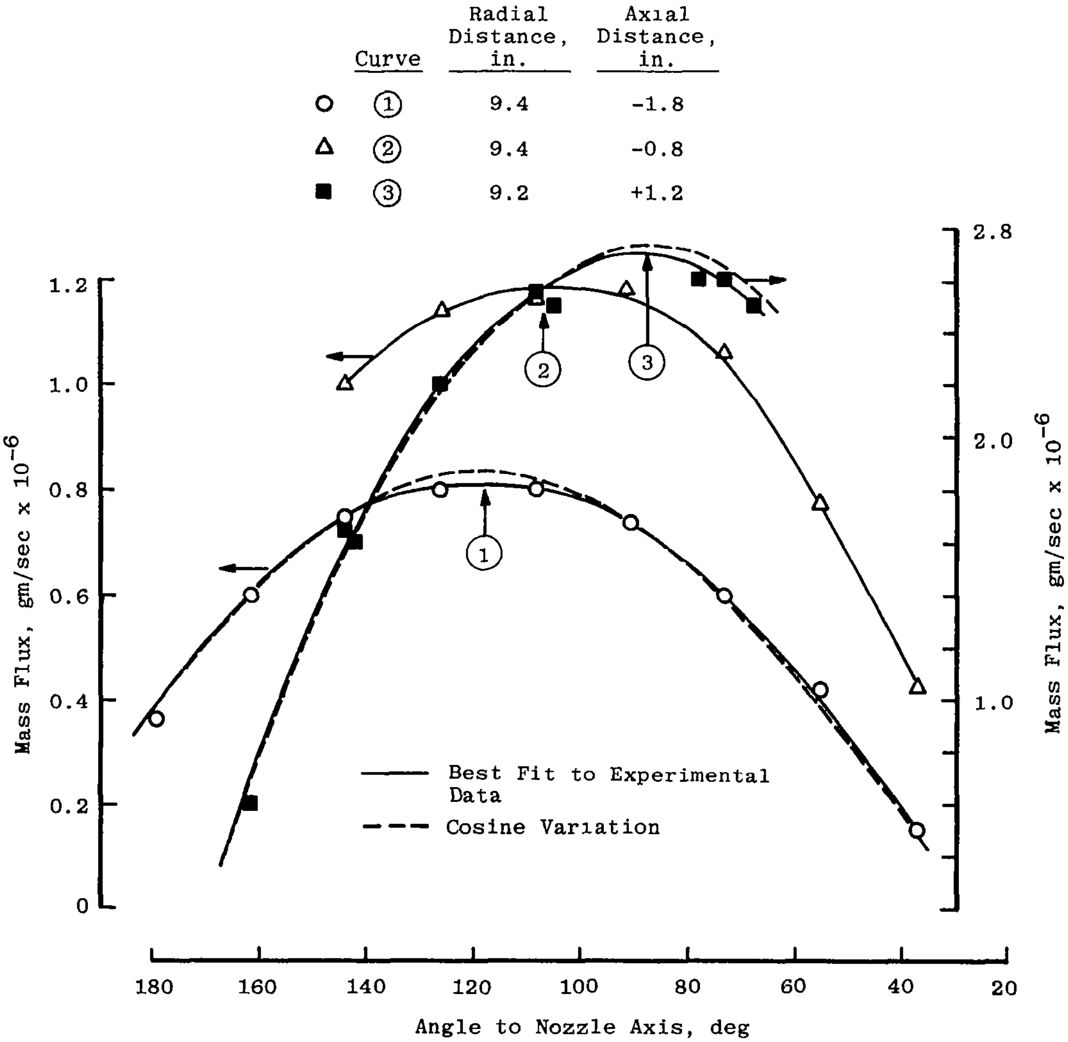

	Curve	Radial Distance, in.	Axial Distance, in.
○	①	9.4	-1.8
△	②	9.4	-0.8
■	③	9.2	+1.2

a. p_0 = 10.8 torr, T_0 = 487 K

Figure 34. Mass flux as a function of probe angle.

flux was measured for a number of orifice conditions. The results of this calibration are presented in Table 5, where the experimental results are the average of as many as four separate runs. Also presented in this table are values of estimated mass flux that have been derived from the relationships developed by Ashkenas and Sherman (Ref. 30) for sonic orifice flow. As yet, no attempt has been made to determine whether viscous effects change these estimated values. It can be seen from the data presented in Table 5 that there is good agreement beween the estimated and measured values of mass flux, i.e. differences of about 10 percent. It should be noted that the differences between the calculated and measured values are least for the highest value of orifice Reynolds number. This suggests that when an appropriate accounting is made for viscous effects, the estimated and measured values will be in closer agreement.

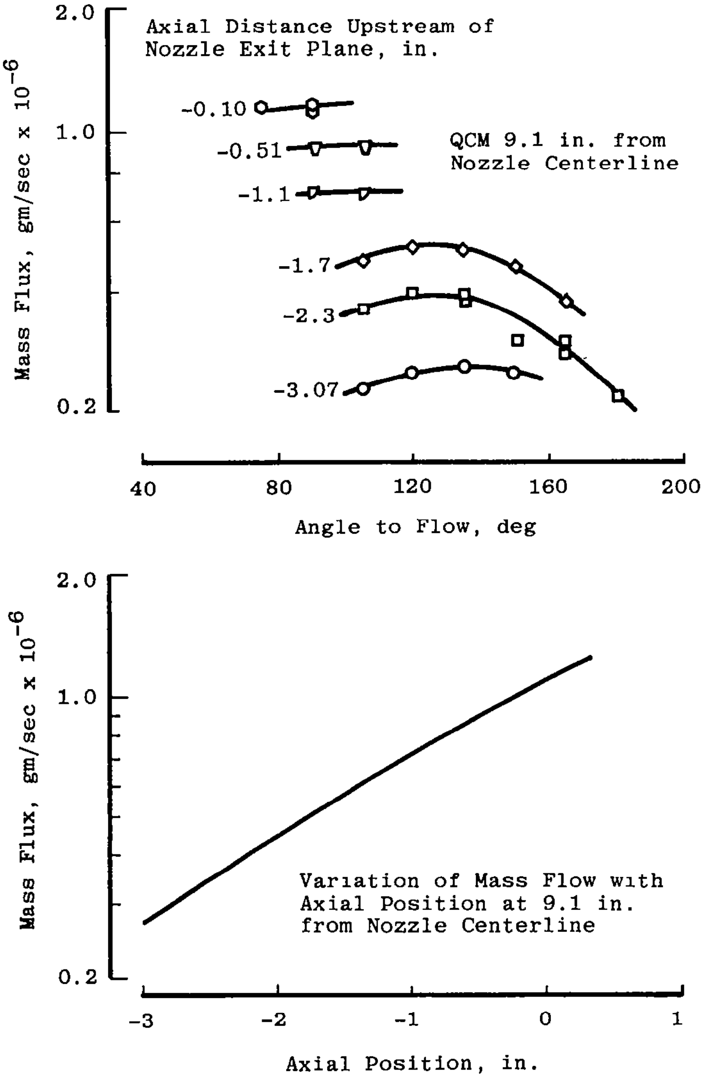

b. p_0 = 36.5 torr, T_0 = 710 K
Figure 34. Concluded.

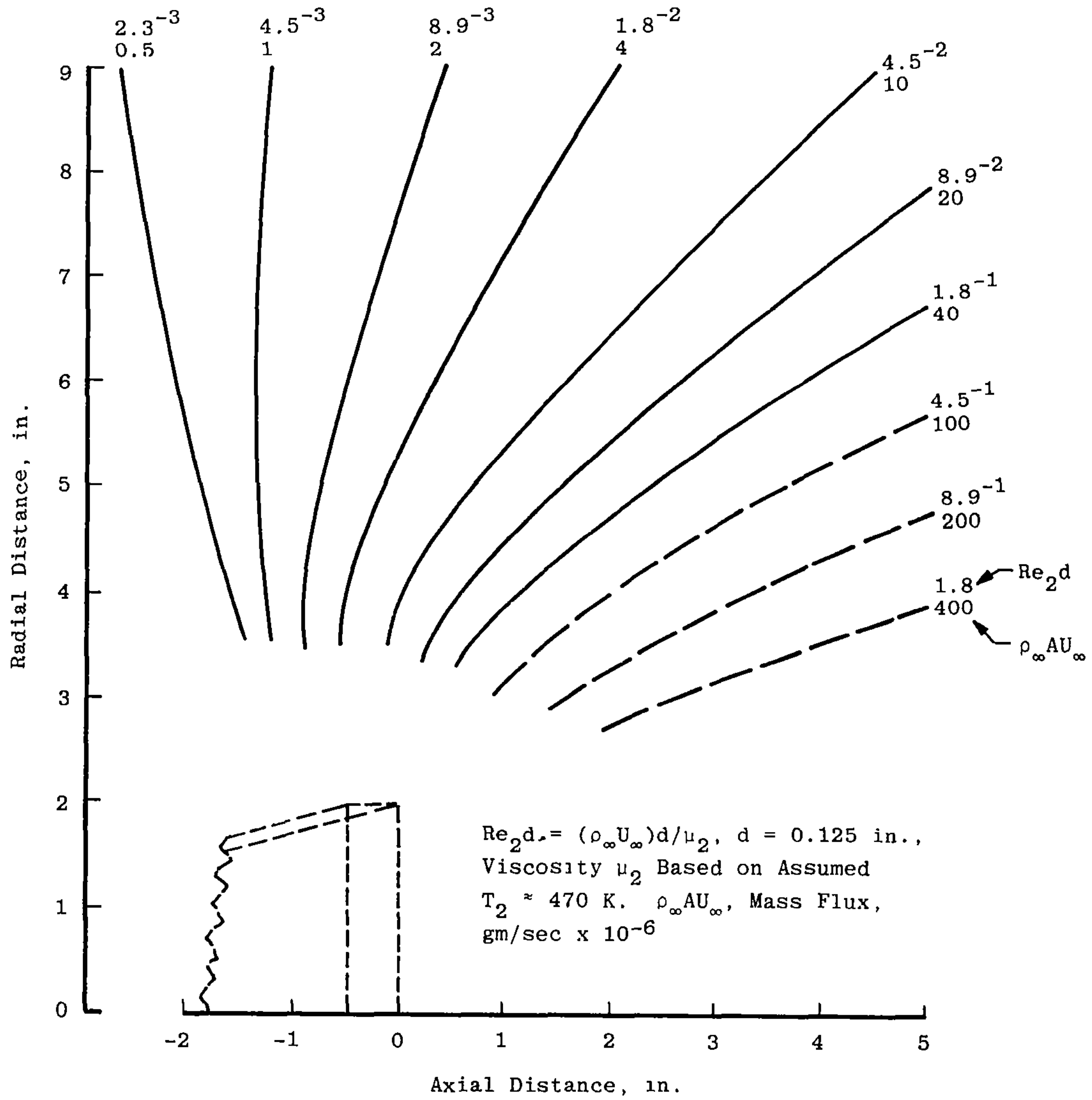

a. p_0 = 10.8 torr, T_0 = 487 K

Figure 35. Spatial map of constant CO_2 mass flux values.

A concern with QCM measurements in the backflow region is the possibility that they are affected by backscattering of the plume gases from the cryopanels. Alt (Ref. 4) established the magnitude of these effects by positioning a number of QCM's within the test chamber such that they did not have a geometrical view of the test nozzle. In the present study, similar efforts were made to determine the magnitude of the backscattered flux (Fig. 36). The QCM was rotated such that the crystal was normal to the axis of the nozzle, and the QCM was then positioned 3 in. (7.5 cm) behind the exit plane and successively at 3 and 8 in. (7.5 and 20.0

cm) from the nozzle axis. The effect of this was that the QCM looked directly at the (1) LN_2-cooled plate positioned in the region of the nozzle throat and (2) chamber volume behind this plate which was also LN_2 cooled. The measured mass flux in these areas was 2×10^{-11} and 8×10^{-10} gm/sec, respectively; both of these measured values of mass flux are significantly lower than the minimum backflow measurements of 5×10^{-7} gm/sec. Therefore, it is suggested that the measured values of mass flux are free of any background scattering effects.

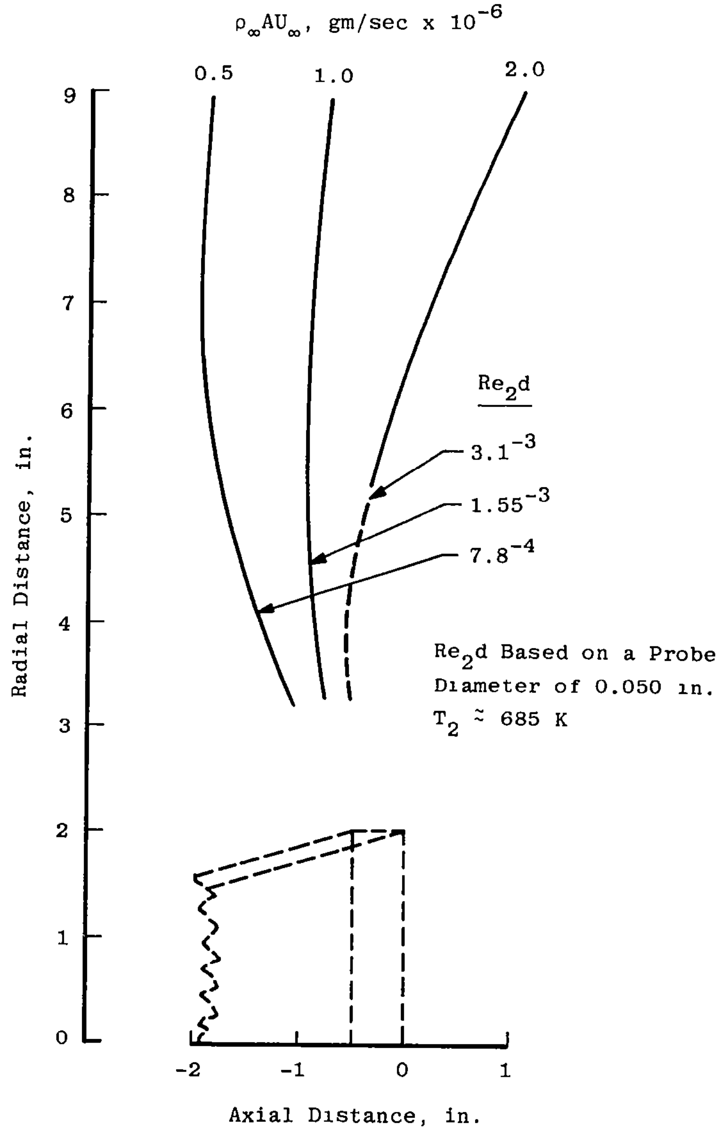

b. p_0 = 36.5 torr, T_0 = 710 K
Figure 35. Concluded.

Table 5. Mass Flux Calibration

Preliminary Evaluation 0.6.-in.-diam. Sonic Orifice				
X/d	p_o, torr	T_o, K	($\varrho_\infty A U_\infty$) Estimated, gm/sec × 10^{-6}	($\varrho_\infty A U_\infty$) Measured, gm/sec × 10^{-6}
29.2	0.66	463	1.84	1.6
29.2	1.00	271	3.64	3.4
29.2	0.5	269	1.82	1.6

The measured pressure in the chamber background behind the nozzle mount structure was on the order of 2 × 10^{-5} torr. If it is assumed that QCM measurements are representative of the random motion of the molecules (as is the pressure measurement), then the effective pressure upstream of the nozzle plate is less than 2 × 10^{-5} torr. This illustrates the difficulty of accurately measuring pressure in a cryopumped chamber of this type.

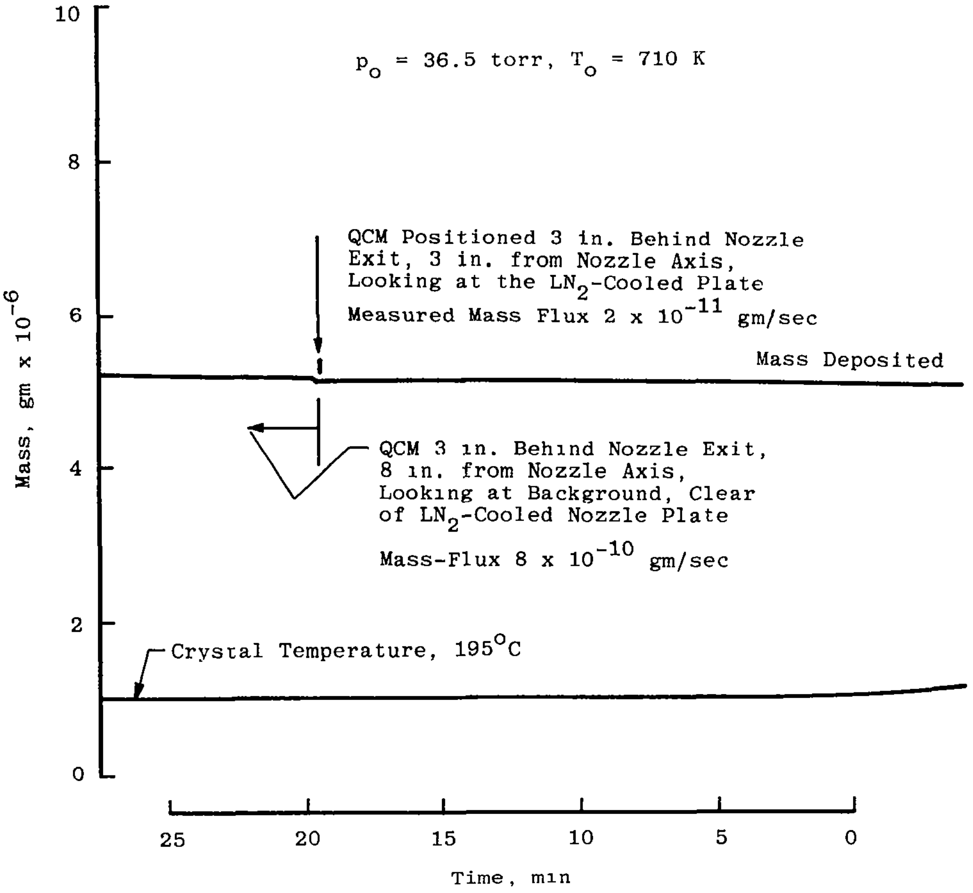

Figure 36. Mass flux in nozzle background.

5.2.2 Comparison with Other Flow Field Measurements

Implicit in the presentation and analysis of QCM mass flux measurements (cf. Refs. 4 and 31) is the assumption that the nozzle flows under investigation are radial. With this assumption, QCM measurements obtained at various angles to the nozzle axis and radial distances from the center of the nozzle exit plane have been combined and presented as the variation of a nondimensional (i.e. essentially $(\varrho_\infty U_\infty)_\theta/(\varrho_\infty U_\infty)_{cl}$) mass flux as a function of angle with respect to the nozzle axis (cf. Ref. 31).

The data obtained in the present investigation (Fig. 35a) are presented in this manner, i.e. $(\varrho_\infty U_\infty)_\theta/(\varrho_\infty U_\infty)_{cl}$, as a function of angle with respect to the nozzle axis and radial distance from the center of the nozzle exit plane (Fig. 37). In this presentation, the centerline values of $\varrho_\infty U_\infty$ have been calculated from the flow calibration data presented in Fig. 18a. These QCM measurements indicate that the flow in this domain of the plume is not radial; although at the larger radii, there is a tendency towards independence of nondimensionalized mass flux at a particular angle with further increases in radial distance.

The variation of mass flux, dynamic pressure, and number density (measurements to be discussed later) with angle to the nozzle axis for both lower area ratio nozzle-heated flows are presented in Fig. 38 for a radius of 3.5 in. (8.9 cm). It will be seen from this comparison that for (1) $\theta \leq 80$ deg, the magnitude of the nondimensional density, dynamic pressure, and mass flux at a fixed angle is the same, and (2) $\theta \geq 80$ deg, the magnitude of these nondimensional ratios is not constant and becomes dependent upon the flow property, i.e. ϱ_∞, $\varrho_\infty U_\infty$, or $\varrho_\infty U_\infty^2$. The manner in which these parameters vary indicates that for (1) $\theta \leq 80$ deg, the changes in flow velocity from the centerline value are small, and (2) $\theta \geq 80$ deg, there are significant decreases in flow velocity. (It should be noted that the dynamic pressure measurements have been corrected for viscous effects using the information presented in Fig. 9.) The measurements presented in Fig. 38 would require further detailed analysis before accurate values of velocity could be derived.

The foregoing comparisons indicate the ϱ_∞ and $\varrho_\infty U_\infty^2$ measurements should provide indications of factors which influence the flow of gas into the nozzle backflow region.

5.2.3 Factors Affecting Mass Flux in the Backflow Region

Mass flux measurements obtained in the present study are compared with those contained in Ref. 31 in Fig. 39. The present results indicate that there is a small decrease in backflow mass flux at a fixed angle and radius when the area ratio is increased from 16 to 44.4 for noncondensed flow. Chirivella's (Ref. 31) experimental measurements show a similar effect with changing area ratio; however, the effects appear to be greater. Some

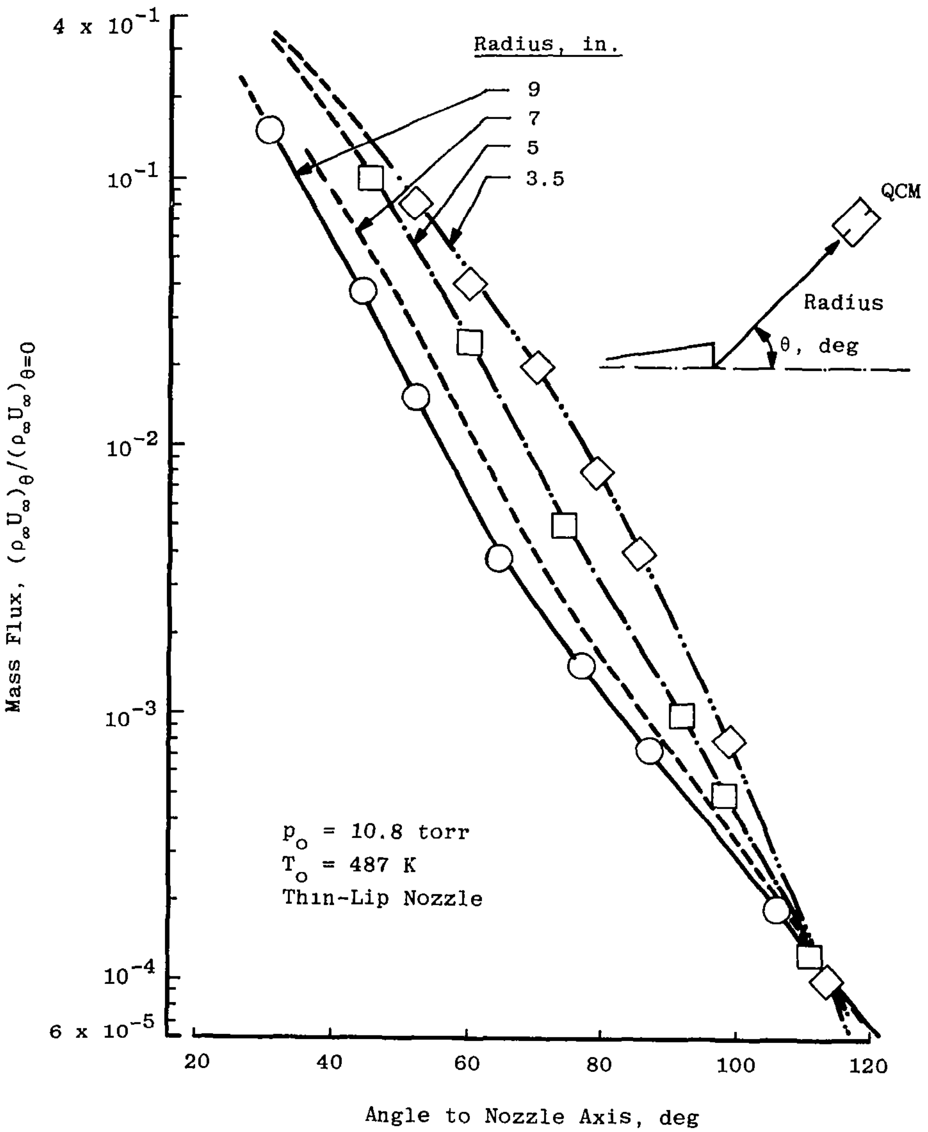

Figure 37. Mass flux measurements as a function of radial and angular position.

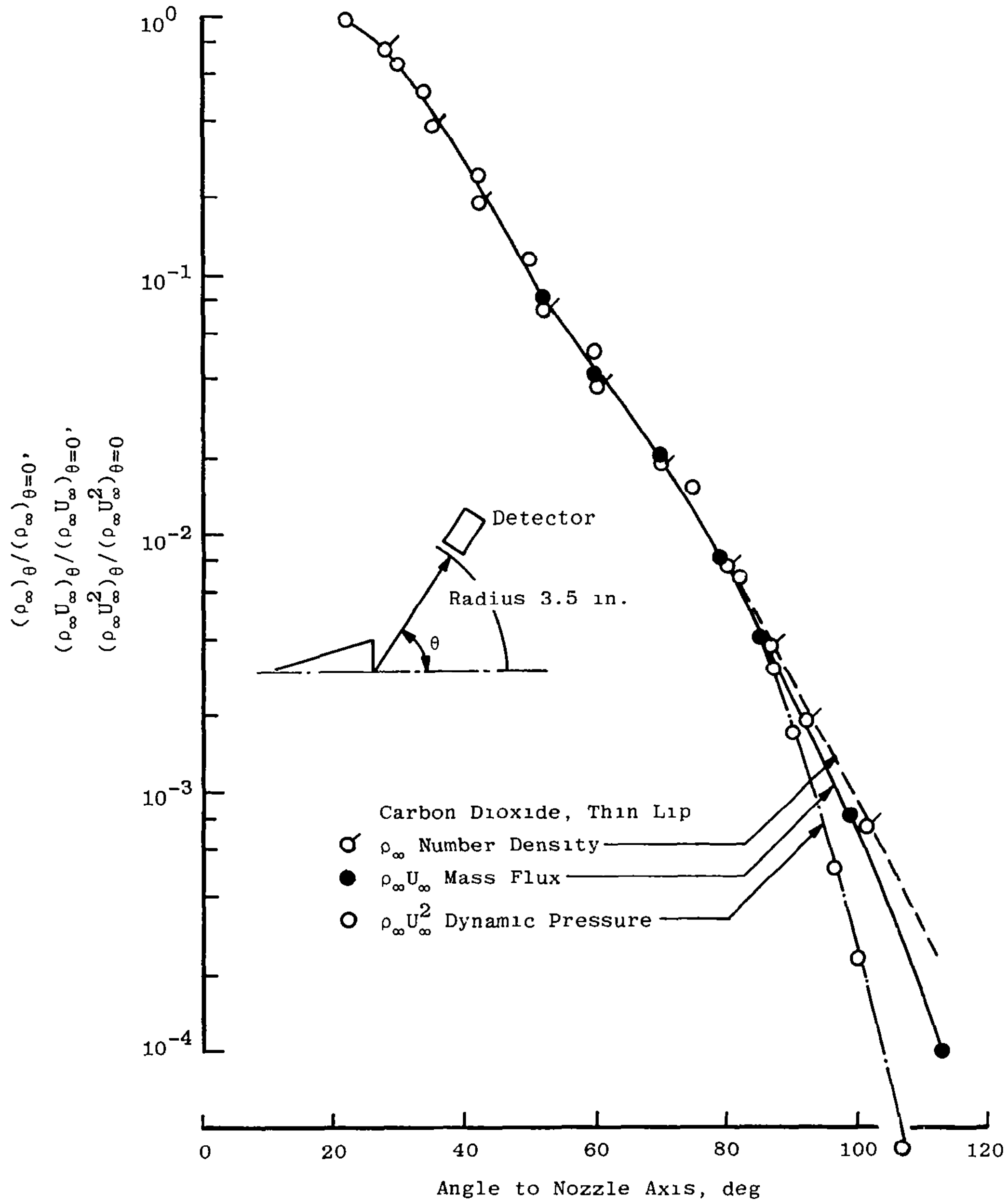

a. p_0 = 10.8 torr, T_0 = 487 K

Figure 38. Angular variation of number density, mass flux, and dynamic pressure at a fixed radius from the center of the nozzle exit plane.

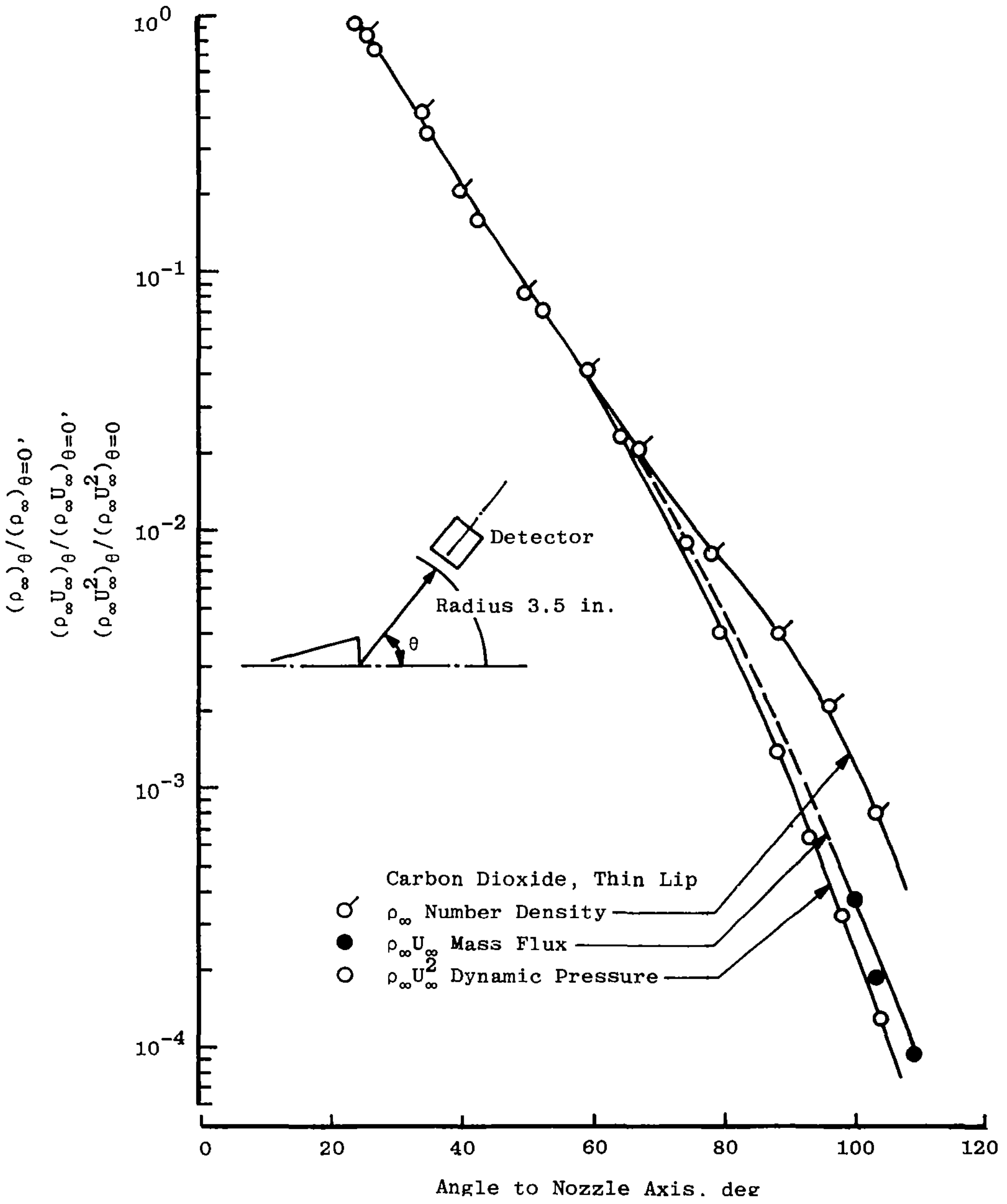

b. p_0 = 36.5 torr, T_0 = 710 K
Figure 38. Concluded.

Carbon Dioxide

	Nozzle Half-Angle, deg	Lip	Area Ratio	T_o, K	p_o, torr	Ref.	Radius, in.
|||	25	Thick	15	294	165 to 905	31	Variable
☰	25	Thick	60	294	165 to 905	31	12 to 24
///	25	Thick	240	294	165 to 905	31	12 to 24
▒	≈16	Thick	320	300	450 to 1,100	Bailey et al.	12
—	15	Thin	16	487	10.8	Present	9
–·–	15	Thin	44.4	710	36.5	Present	9
|||||	≈16	Thin	320	300	450 to 110	Bailey et al.	12

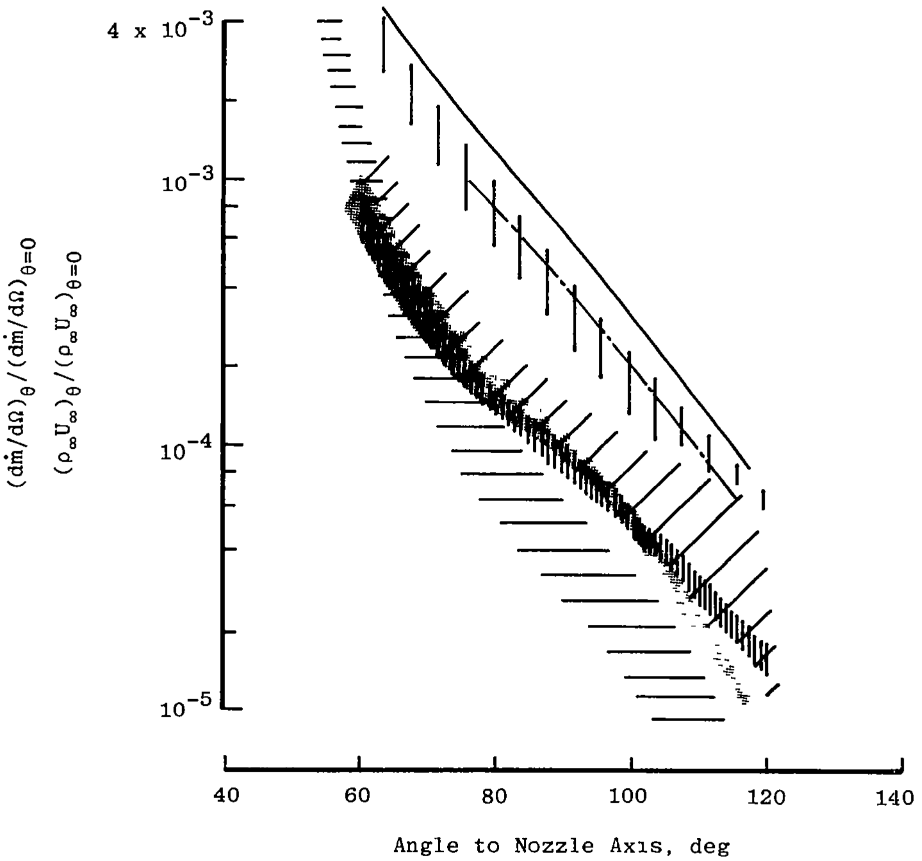

Figure 39. Comparison of mass flux measurements.

additional mass flux measurements by Bailey et al. in the 4- by 10-ft RVC with a large area ratio nozzle ($A/A^* = 320$) are consistent with Chirivella's measurements. For angles to the nozzle axis greater that 90 deg there is evidence that the detailed geometry of the lip, i.e. either thick or thin, has an effect upon the mass flux into the backflow region. The effect of an increase in lip thickness is to reduce the flow into the backflow region. It is of interest to note that the number density measurements currently being documented by Bailey et al. and replotted in Fig. 40 also indicate a similar effect with lip geometry. These effects of lip geometry on mass flux in the backflow region are in agreement with similar observations by Chirivella (Ref. 31).

Mass flux measurements, where condensation in the core flow is possible (Ref. 31) for a nozzle with an area ratio of 15, are in reasonable agreement with the results for a similar area ratio in the present study (Fig. 39). This indicates that mass flow into the backflow region is not affected by condensation in the core flow. A comparison of number density measurements obtained in the present study with those obtained with the $A/A^* = 320$ nozzle where condensation is possible appears to support this conclusion when consideration is given to the nozzle configuration differences (Fig. 40). Additional support for this suggestion is provided by the comparable number density data obtained with nitrogen which is presented in Fig. 41. Again, there is no apparent effect upon mass flow into the backflow region in flows where condensation is and is not possible. The experimental measurements for nitrogen and carbon dioxide presented in Figs. 40 and 41 have been combined in Fig. 42 to illustrate the fact that, as would be expected (since nitrogen has a lower molecular weight), nitrogen is more readily scattered into the backflow region than carbon dioxide. Similar measurements by Chirivella (Ref. 31) indicate the same dependence upon the molecular weight of the gas.

Also shown in Fig. 42 are the summarized results of mass flux measurements made in the plume generated by the pulse firing of a 5-lbf bipropellant thruster in the AEDC Aerospace Chamber 10V (Ref. 4). The thruster nozzle is contoured, has a thick lip, and a wall angle close to the exit plane of approximately 6 deg. A significantly higher proportion of the basic nozzle flow appears to enter the backflow region than for the pure-gas expansions. Intuitively it would be expected that the thick lip and small wall angle near the exit should result in a reduced mass flux in the backflow region. Additional pure-gas studies with different nozzle geometries in the continuous and pulsed modes of operation represent a possible approach to the resolution of the reasons for these differences.

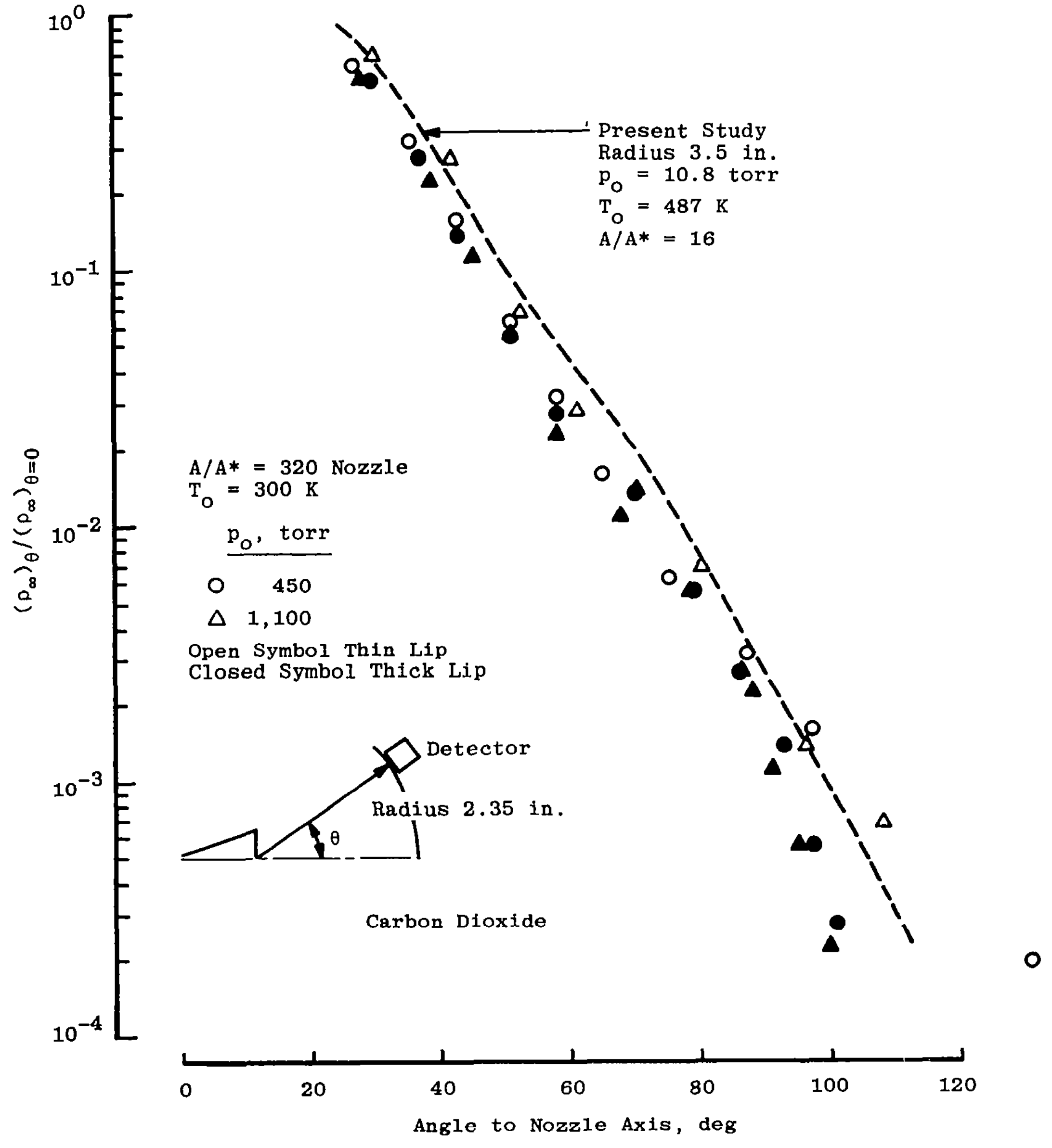

Figure 40. Angular variation of number density at a fixed radius from the center of the nozzle exit plane.

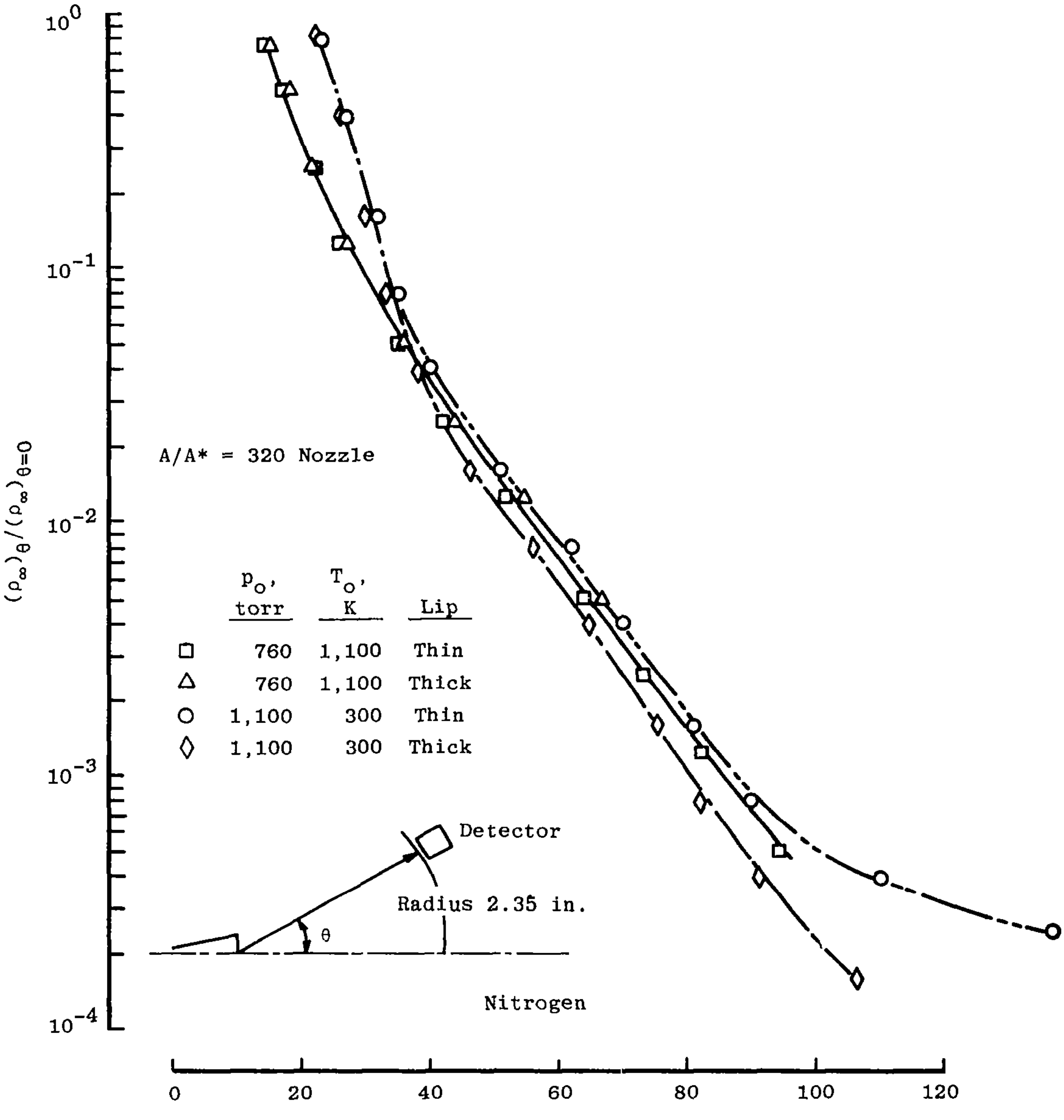

Figure 41. Effect of lip geometry and state-of-the-gas on the angular distribution of number density.

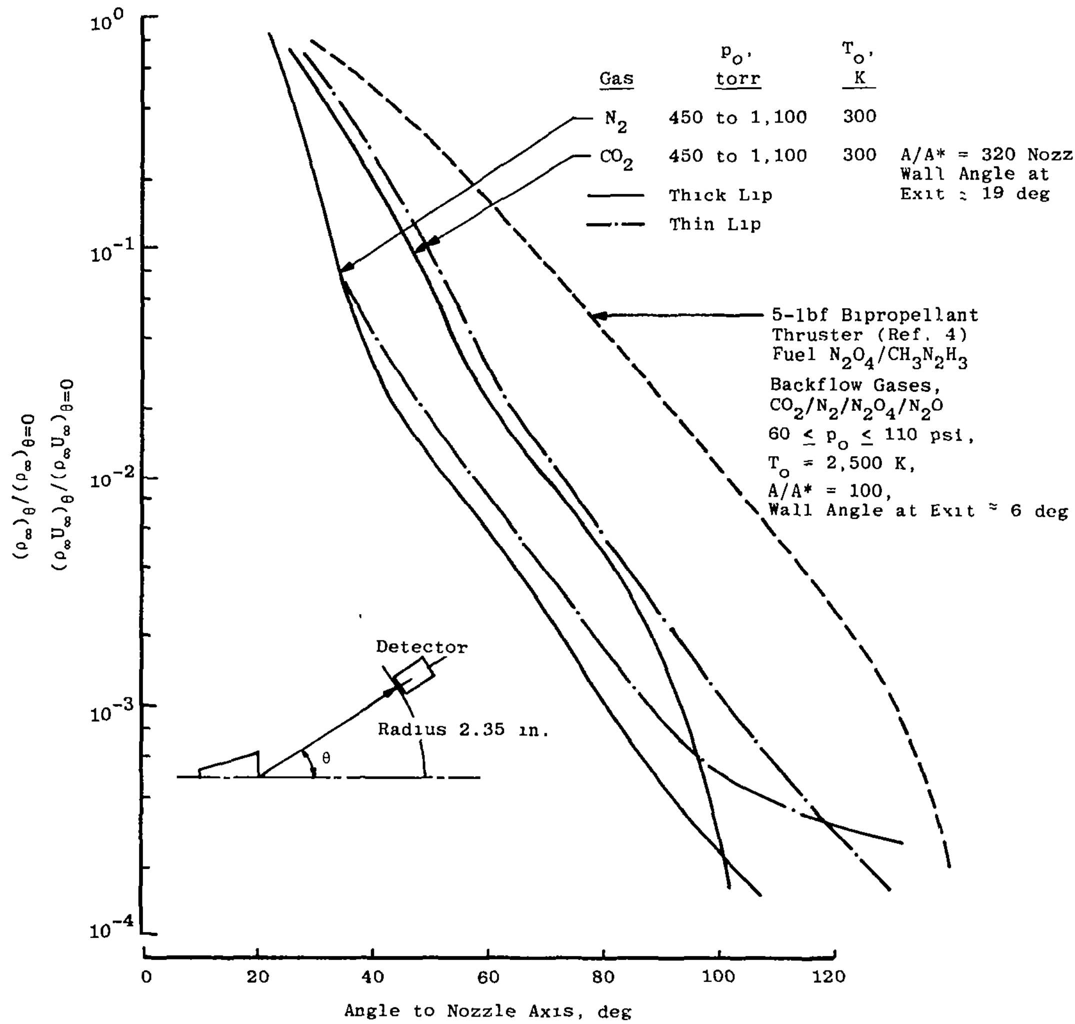

Figure 42. Effect of molecular weight of gas on mass flow into the backflow region.

5.3 EFFECT OF NOZZLE LIP GEOMETRY ON PLUME CHARACTERISTICS

In the foregoing section, it was established on the basis of density and mass flux measurements that mass flux into the nozzle backflow region was affected by the geometry of the lip, i.e. thick or thin, for both condensed and noncondensed nozzle expansions. In the present study, pitot probe measurements of dynamic pressure and local flow angle in the region of the lip have been made in an attempt to improve our understanding of this phenomenon.

Measurements of flow angle and pitot pressure made in the region of the nozzle exit plane with 0.050- and 0.25-in.-diam. (0.127- and 0.635-cm) probes have shown that these measurements are independent of lip geometry (Fig. 43). Flow-angle measurements upstream of the nozzle exit plane (Fig. 43c) in the backflow region are affected by the lip geometry to a small degree. Dynamic pressure measurements upstream of the nozzle exit

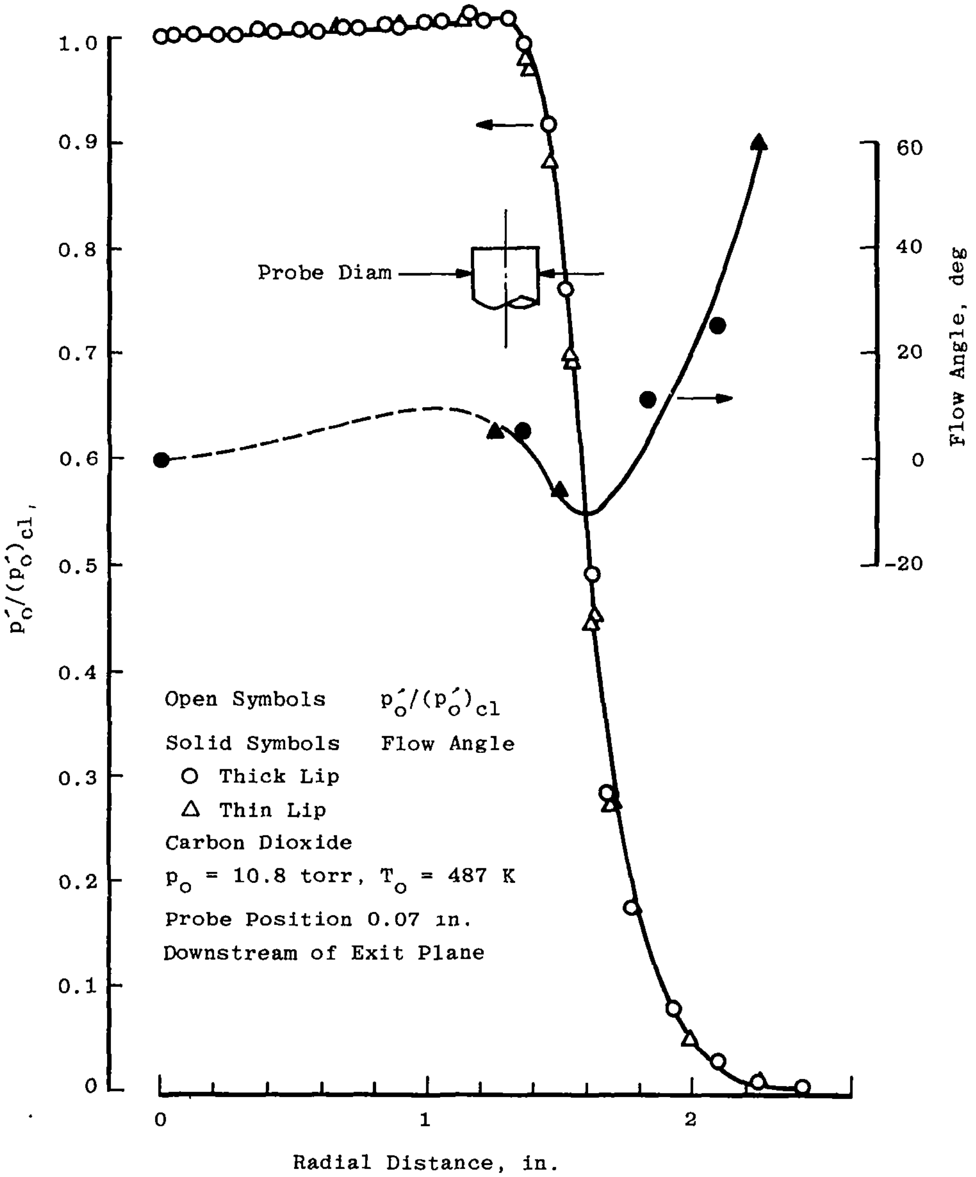

a. 0.25-in.-diam probe

Figure 43. Effect of lip geometry on radial profiles of pitot pressure and flow angle.

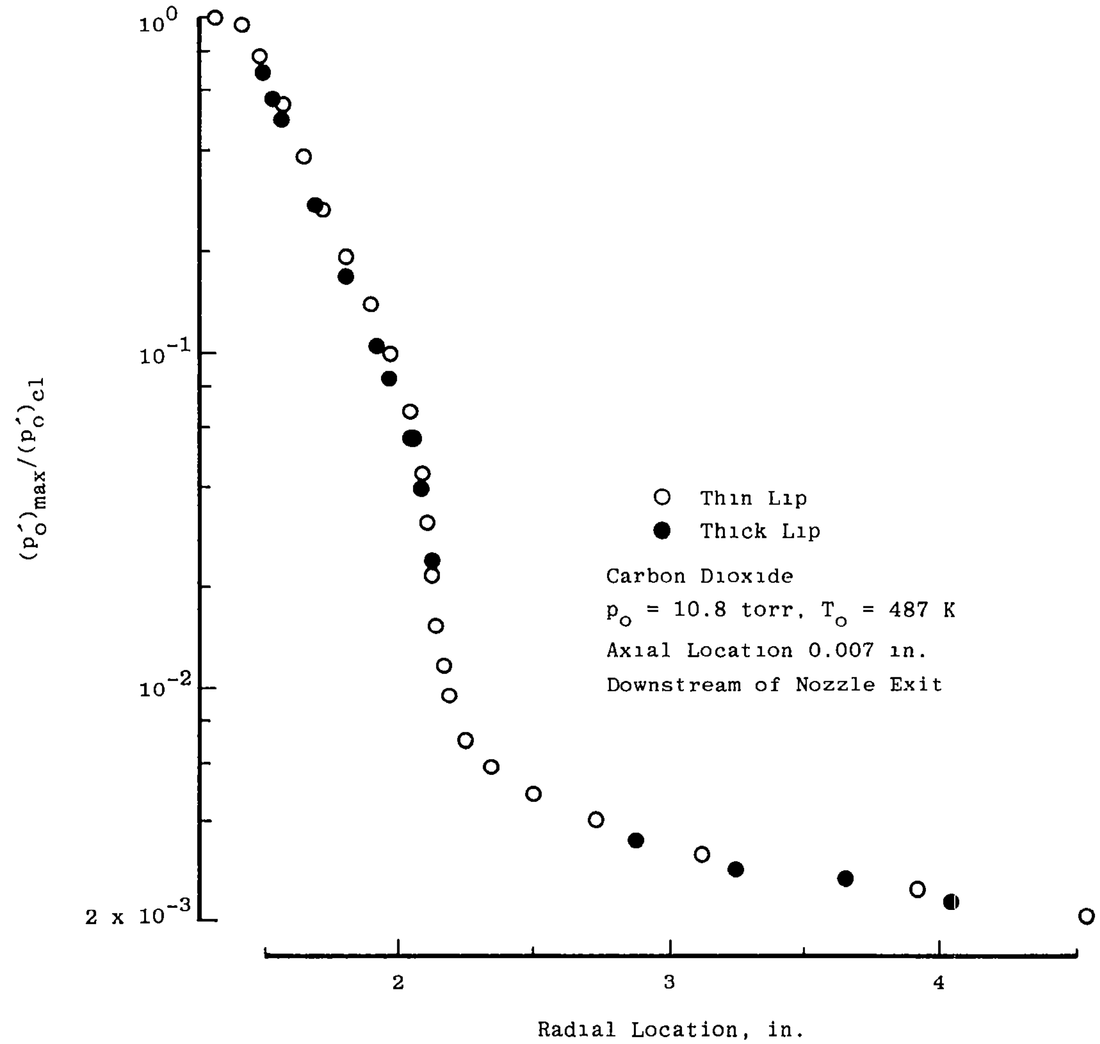

b. 0.050-in.-diam probe, pitot pressure
Figure 43. Continued.

plane with the 0.05-in.-diam (0.127-cm) probe indicate that the thick lip results in a reduction in dynamic pressure in this flow regime. Based on earlier work with a higher area ratio nozzle, Figs. 40 through 42, this was an expected result. The intent of the present study was to define the local flow-angle changes that occur in the lip region as a result of changes in lip thickness. If such changes do occur, they were too small to be reliably detected with the present instrumentation.

The present measurements indicate that there appears to be a small effect of lip geometry upon the centerline Mach number (Fig. 44) variation with axial position. This effect is so

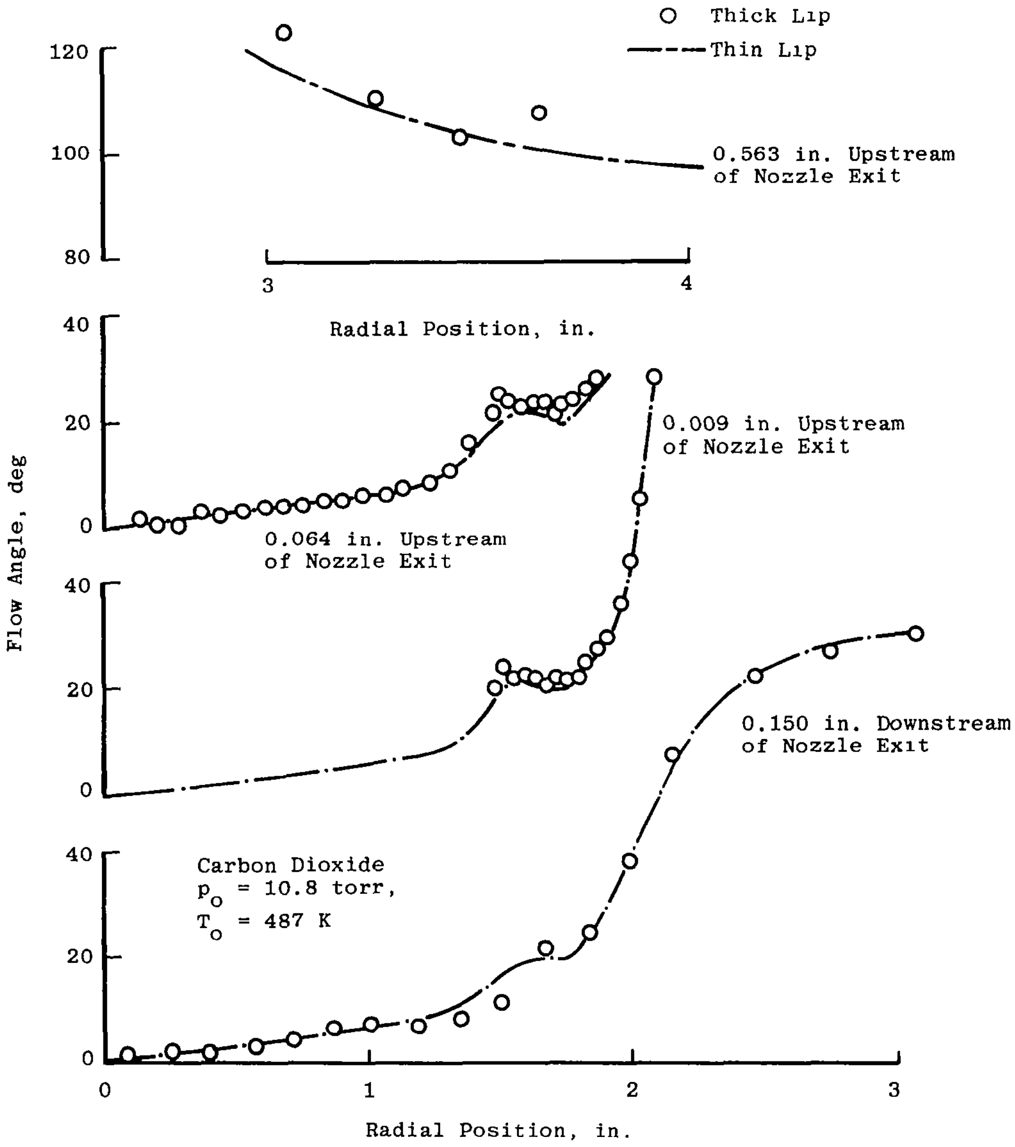

c. 0.050-in.-diam probe, flow angle
Figure 43. Continued.

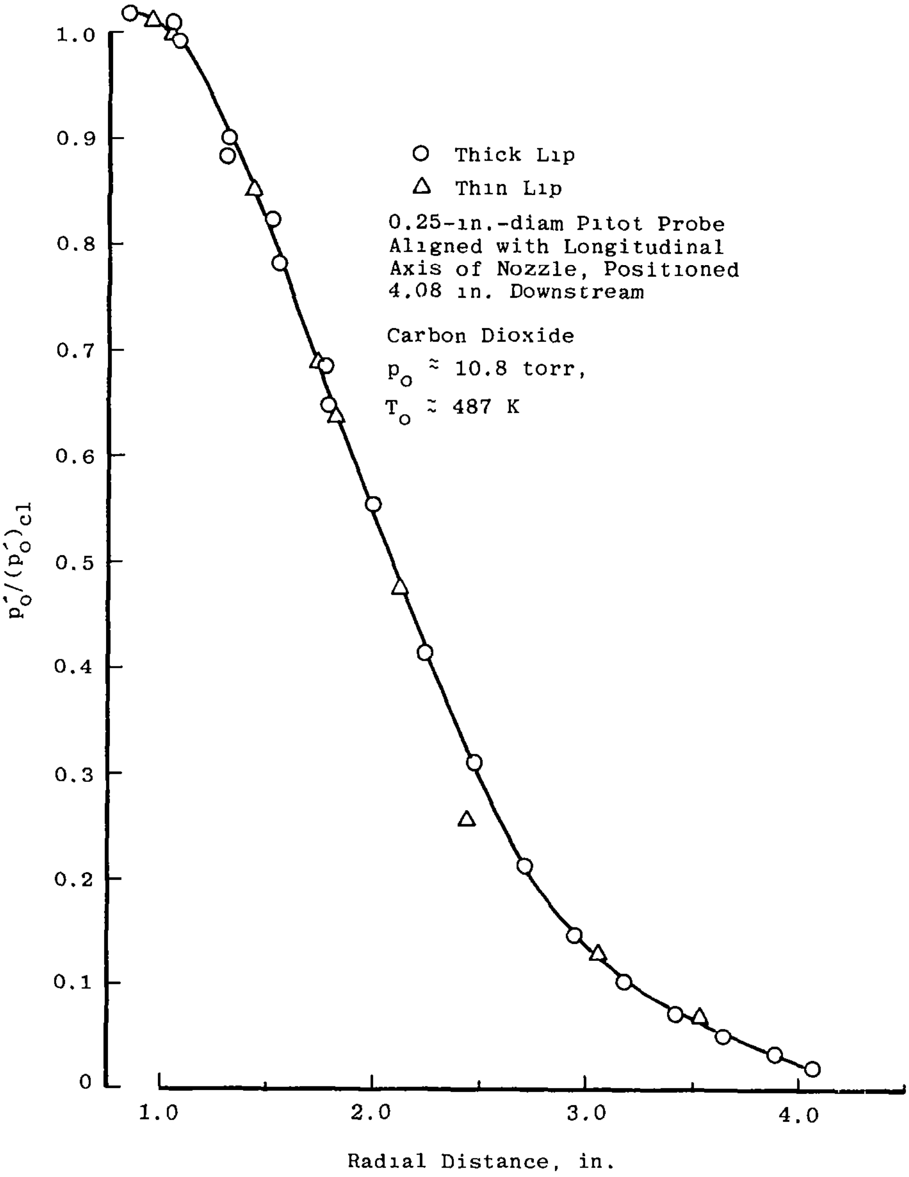

d. 0.25-in.-diam probe, pitot pressure

Figure 43. Concluded.

small that it is tempting to assume that it is representative of experimental uncertainty; however, a similar small effect was found for the higher area ratio nozzle experiments currently being documented by Bailey et al. These measurements were obtained at conditions where condensation in the nozzle exit plane was (1) not possible and (2) probable. When condensation is present, the downstream effects are reversed; there is a small increase in centerline Mach number.

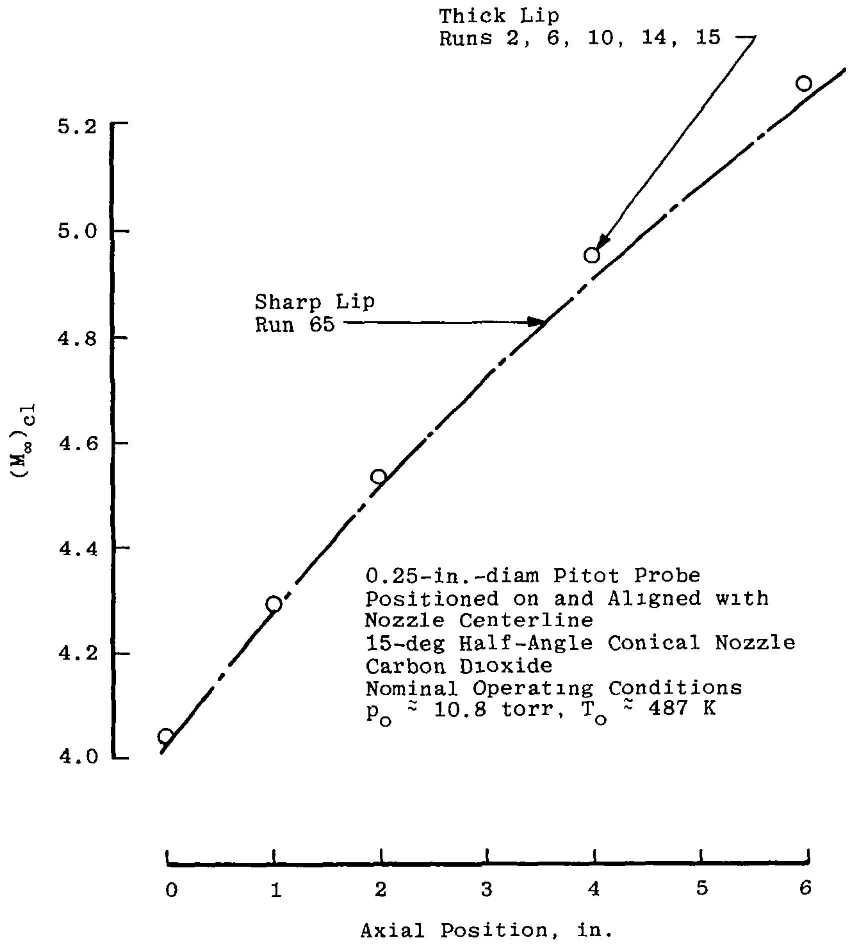

Figure 44. Effect of lip geometry on centerline Mach number as a function of axial distance.

5.4 FREE-MOLECULE PRESSURE PROBE

5.4.1 Probe Performance

As noted earlier, the free-molecule pressure probe can be used to define the properties of low-density gas flows in the free-molecule flow regime, e.g., flow angle and speed ratio. In the initial planning for the use of this probe, it was assumed that as a result of measurements of the variation of pressure with the angle of the sensing orifice to the flow vector, it would be possible to define both of the above parameters. As experience was gained with the operation of the rotary pitot probe/pressure transducer configuration, it became evident that the angle of the flow velocity vector could be obtained by simply peaking the pressure signal and noting the probe angle rather than defining this property from detailed pressure/angle scans. A similar philosophy was therefore considered to be applicable to the free-molecule pressure probe, and the testing with this probe was separated into two separate phases, i.e. flow-angle measurements alone and complete pressure/angle surveys.

Measurements of the variation of local flow angle with radial and axial position obtained with a 0.5-in.-diam (1.27-cm) cylindrical probe, with a 0.0625-in.-diam (0.159-cm) and 0.0153-in.-long (0.039-cm) orifice, and a Schultz-Phelps ion gage are presented in Fig. 45. Best fits to these measurements are replotted in Fig. 46. In the regions where pitot and free-molecule flow-angle measurements overlap, the measurements are in good agreement. The data presented in Figs. 45 and 46 have been used to define a portion of the flow-angle data presented in Fig. 29b.

A 0.25-in.-diam (0.635-cm) cylindrical probe with a 0.039-in.-diam (0.10-cm) orifice was positioned at a radial distance of 6.9 in. (17.5 cm) from the nozzle centerline, and the variation of pressure with probe angle was determined at a number of axial positions both upstream and downstream of the nozzle exit plane. The angle of the flow vector obtained with this probe was in agreement with the values obtained with the larger free-molecule pressure probe and the pitot probe summarized in Fig. 29b. Examples of the pressure measurements obtained in both the backflow and forward-flow regions of the plume are given in Fig. 47. The backflow region measurements are characterized by low pressures, i.e. on the order of 1×10^{-4} torr, whereas the downstream pressures are an order-of-magnitude greater. The lower of these two sets of measurements represents measurements at the limit of the quoted range of the 10-torr absolute pressure gauge, i.e. $1 \times 10^{-4} \leq p \leq 10$ torr. As a result of the scatter in these measurements, it has not been possible to make definitive estimates of speed ratio based on Hughes' analysis (Ref. 29). However, some semiquantitative estimates have been made and are presented in the insert in Fig. 47b. The lower pressure measurements were further complicated by the necessity to correct for changes in the transducer zero which could be related to changes in the transducer temperature.

In an attempt to correct for the above limitations, a series of free-molecule pressure probe measurements were made with the 1-torr absolute pressure transducer using the 0.205-in.-diam (0.511-cm) cylindrical probe with a 0.031-in.-diam (0.079-cm),

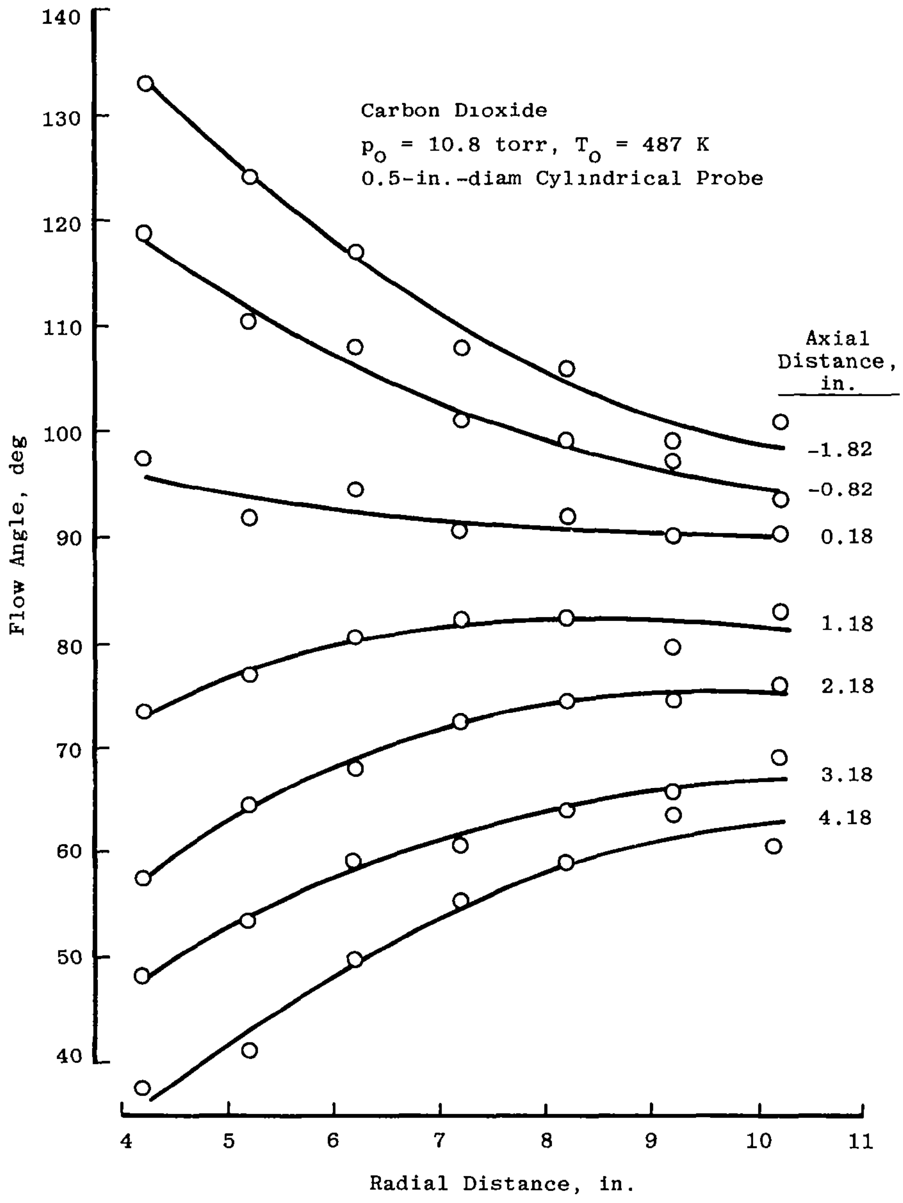

Figure 45. Free-molecule pressure probe—basic flow-angle measurements.

0.011-in.-thick (0.029-cm) orifice. As was the case for the first free-molecule probe evaluation, two types of measurements were attempted, (1) full-pressure scans at fixed axial and radial locations, and (2) axial and radial scans monitoring the angle at which the pressure signal peaked.

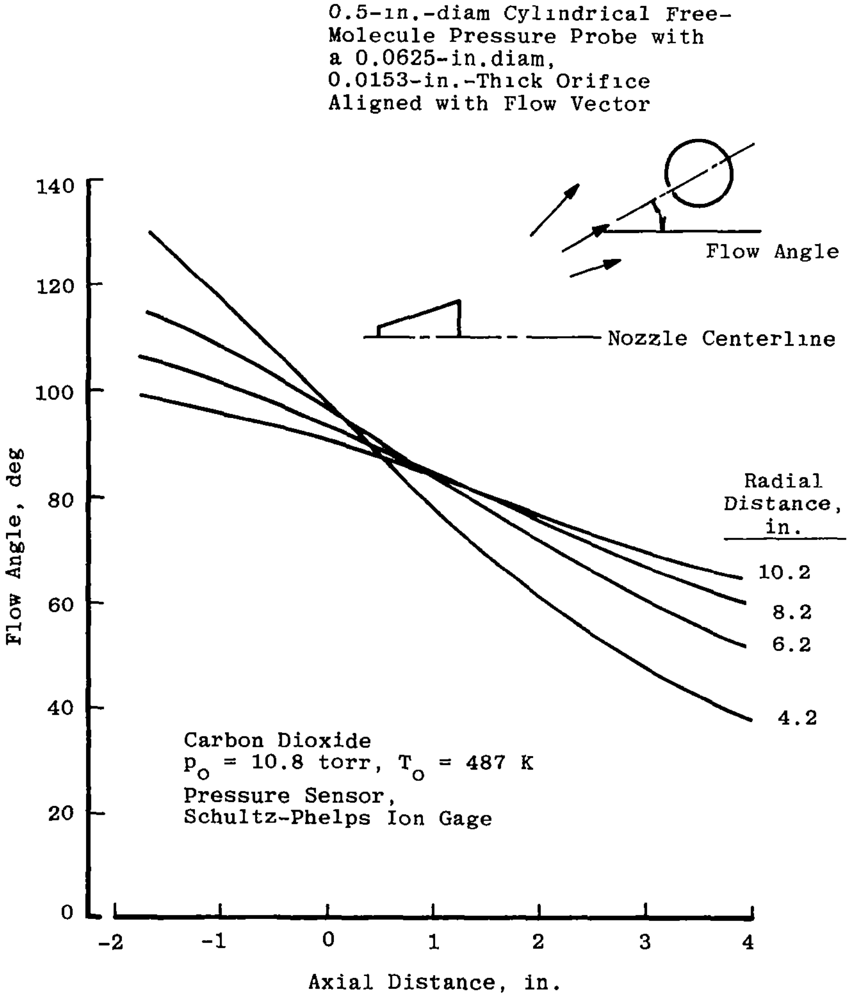

Figure 46. Flow-angle measurements obtained with a cylindrical free-molecule pressure probe.

Examples of the full-pressure scans are given in Fig. 48. It is readily apparent that for the downstream scan (Fig. 48a), the pressure profile is symmetrical and there is a smooth variation of pressure with probe angle. As the probe was moved into the backflow region,

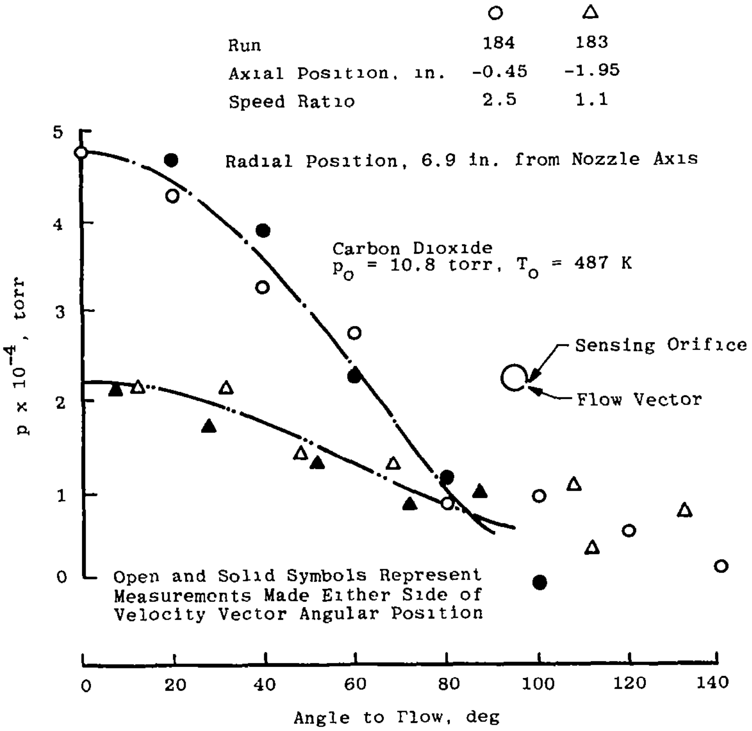

a. Backflow region

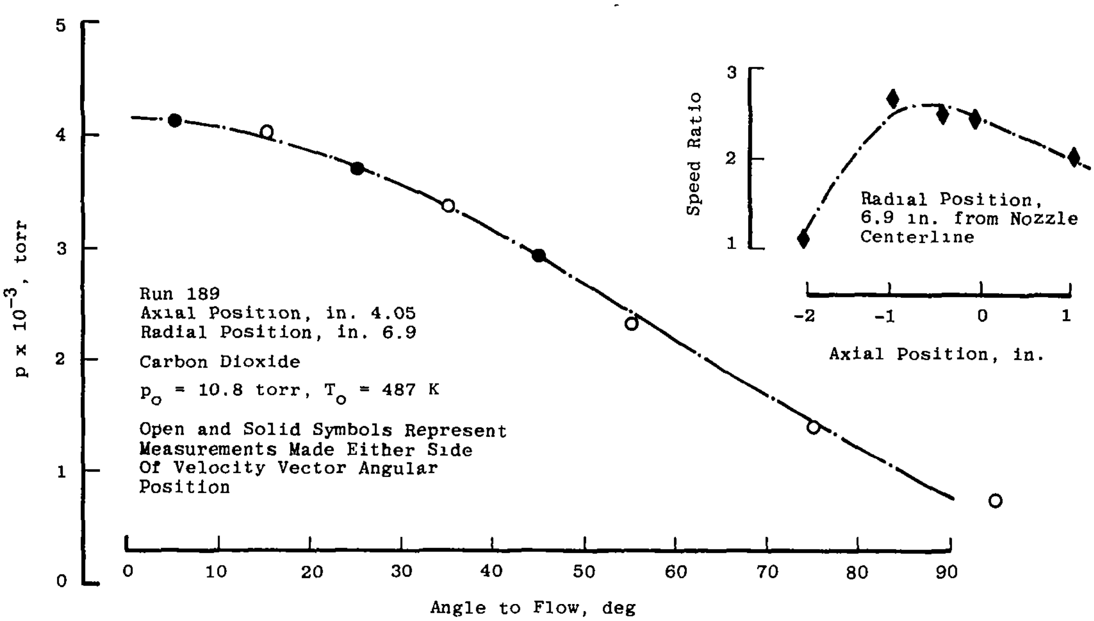

b. Forward-flow region

Figure 47. Free-molecule pressure probe measurements in the nozzle plume.

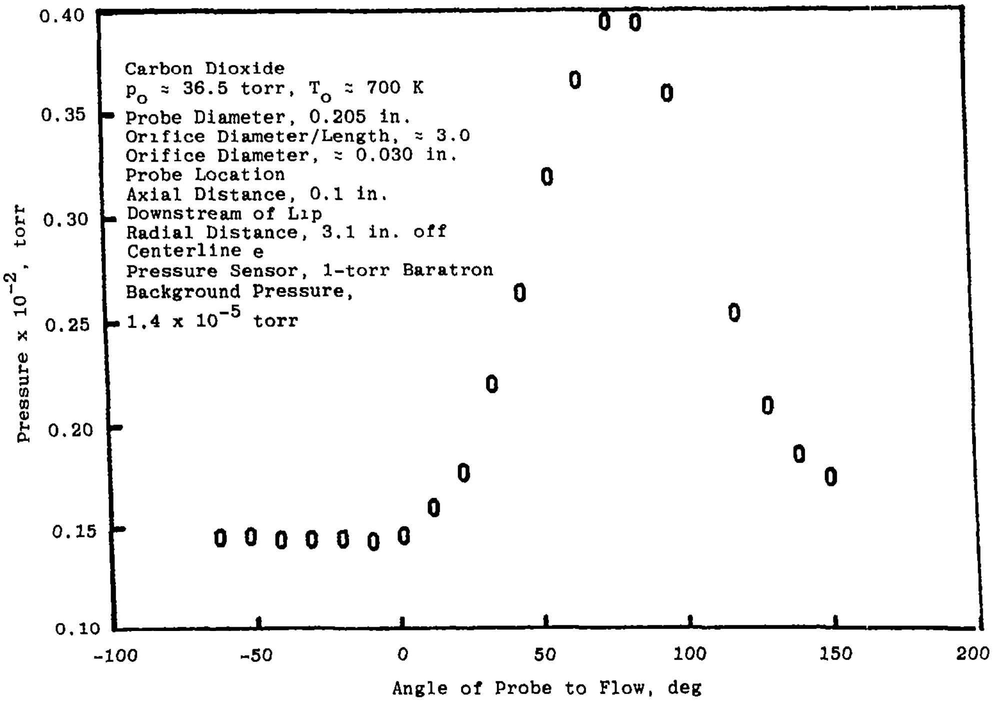

a. 0.1 in. downstream

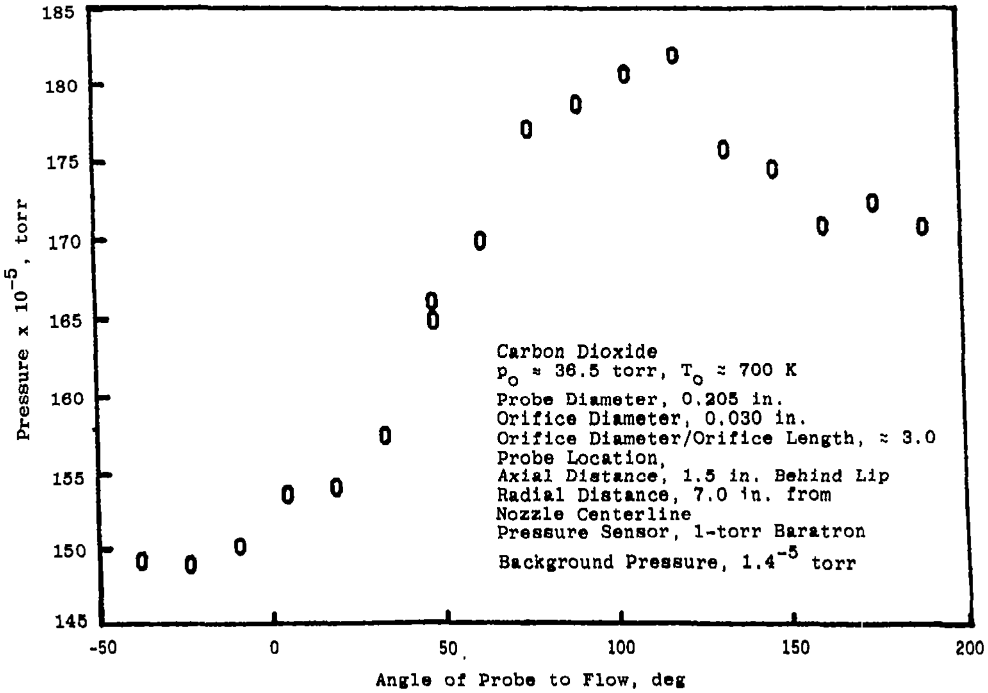

b. 1.5 in. upstream

Figure 48. Pressure variation with angle of orifice to flow.

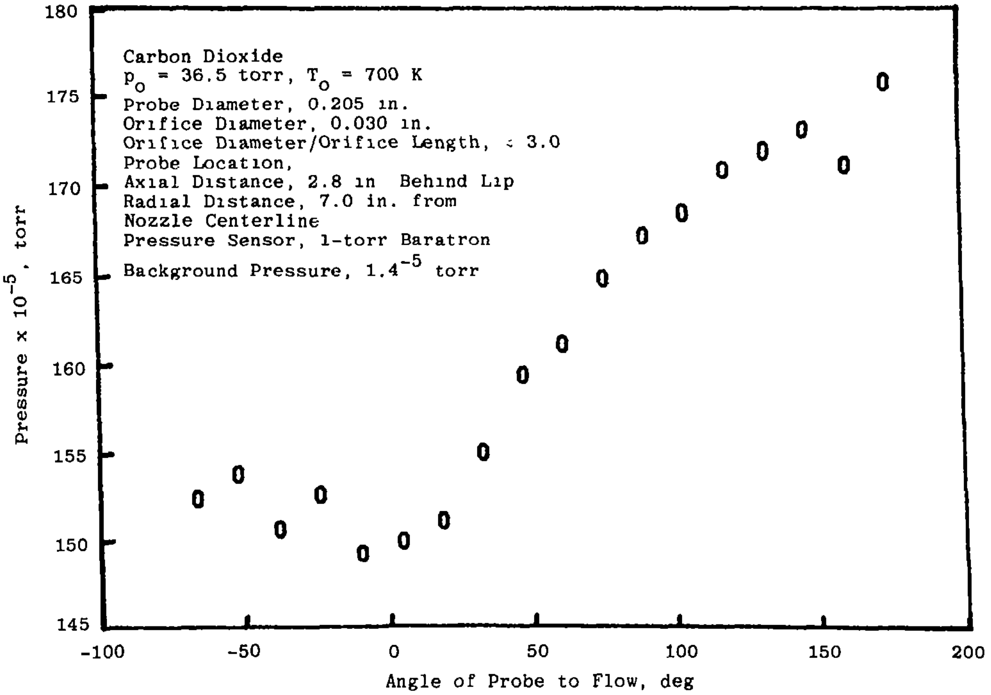

c. 2.8 in. upstream
Figure 48. Concluded.

(1) there is evidence of a small degree of uncertainty in the pressure measurement associated with the lower values of absolute pressure, i.e. on the order of 1×10^{-5} torr, and (2) the pressure profiles are no longer symmetrical. This lack of symmetry (which will be discussed in the next section) precluded any possibility of making realistic estimates of speed ratio from these measurements. The variation of angle at the maximum probe pressure with axial or radial location is similar to other measurements of this type already shown in Figs. 16 and 45. These measurements will also be discussed in the following section.

An attempt was made to check the validity of the theoretical basis (Ref. 25) for the interpretation of free-molecule pressure probes. A cylindrical free-molecule pressure probe was positioned in the flow generated by a 0.6-in.-diam (1.52-cm) sonic orifice expanding into a vacuum. The characteristics of such flows are accurately defined as a result of the studies of Ashkenas and Sherman (Ref. 30). The variation of pressure at the probe orifice as a function of orifice angle to the velocity vector was obtained for two different conditions (Figs. 49a and b). The speed ratio for both tests was nominally 12.4 based on the assumption that the orifice is unaffected by viscous effects. For the cold-flow condition (Fig. 49a), the mean free path is approximately 3 in. (7.5 cm) resulting in a probe Knudsen number of 15.

The mean free path for the heated flow is approximately 8 in. (20 cm) resulting in a probe Knudsen number of 40. It is assumed that these Knudsen numbers should be sufficiently large to ensure that the probe is in free-molecule flow. It can be seen, however, that both sets of experimental data deviate from the theoretical values for orifice angles greater than 70 deg. The deviations at the lower Knudsen number data are slightly greater than for the higher Knudsen number condition. Similar deviations were observed for other calibration runs at Knudsen numbers intermediate between these two examples. The results of this calibration, at a higher speed ratio than was encountered in the present plume studies, suggest that if this technique is to be used for speed ratio measurements in such studies, further, more definitive calibrations will be necessary.

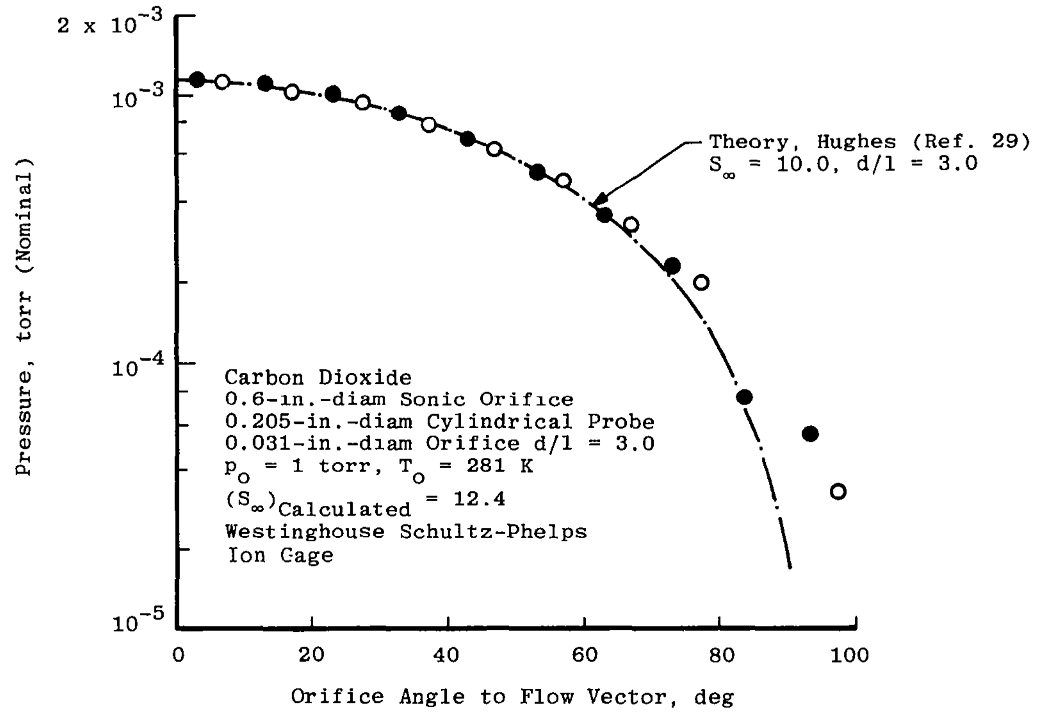

a. $p_0 = 1$ torr, $T_0 = 288$ K

Figure 49. Free-molecule pressure probe calibration.

5.4.2 Effect of Background Cryopumping on Flow Angle

As has been noted earlier the chamber cryopumping system consists of two independent circuits. Basically, one system pumps the gas in the forward flow and the other in the backflow. In the course of establishing chamber operating conditions, it was noted that the

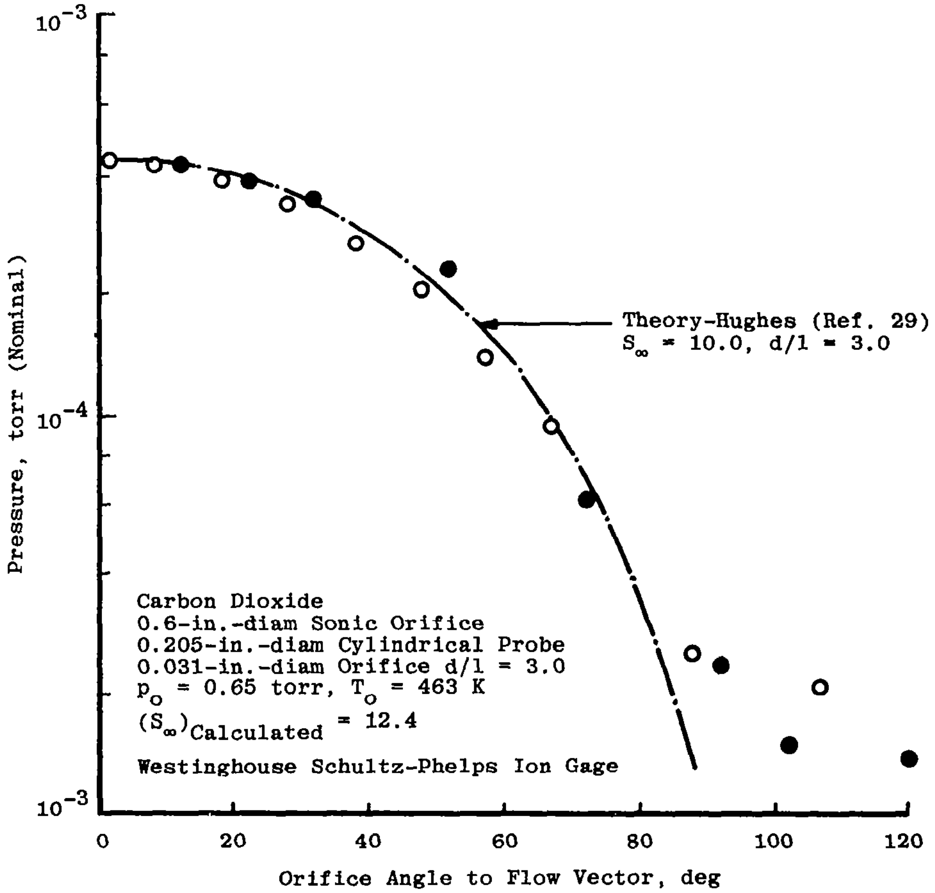

b. p_0 = 0.65 torr, T_0 = 463 K
Figure 49. Concluded.

pressure (as measured with the Westinghouse Schultz-Phelps ion gage) in the region behind the nozzle/support structure was not affected significantly by the presence or absence of cryopumping in this section, provided that there was cryopumping in the forward-flow region. (The effect of changes in chamber pressure on the plume characteristics will be discussed in a subsequent section.) It was found that the pitot pressure profile in the nozzle exit plane was affected by the absence of cryopumping in the backflow region of the nozzle (Fig. 50).

A series of experiments to evaluate the effect of background cryopumping on plume properties were carried out using the free-molecule pressure probe. In these experiments, full-pressure variations with orifice angle to the flow vector were obtained together with the angle at which the measured pressure peaked as a function of radial and axial position.

Examples of the pressure variation with angle are presented in Fig. 51 for various radial and axial positions. It should be noted that the orifice angle as plotted in both Figs. 48 and 51 is referenced to different probe zeros (the probes being rezeroed for each test entry). In order to compare these two sets of data the angle data presented in Fig. 51 have to be subtracted from 180 deg. The main purpose in presenting a profile in the forward-flow region, Fig. 51a, is to illustrate the fact that the pressure profile is essentially symmetrical

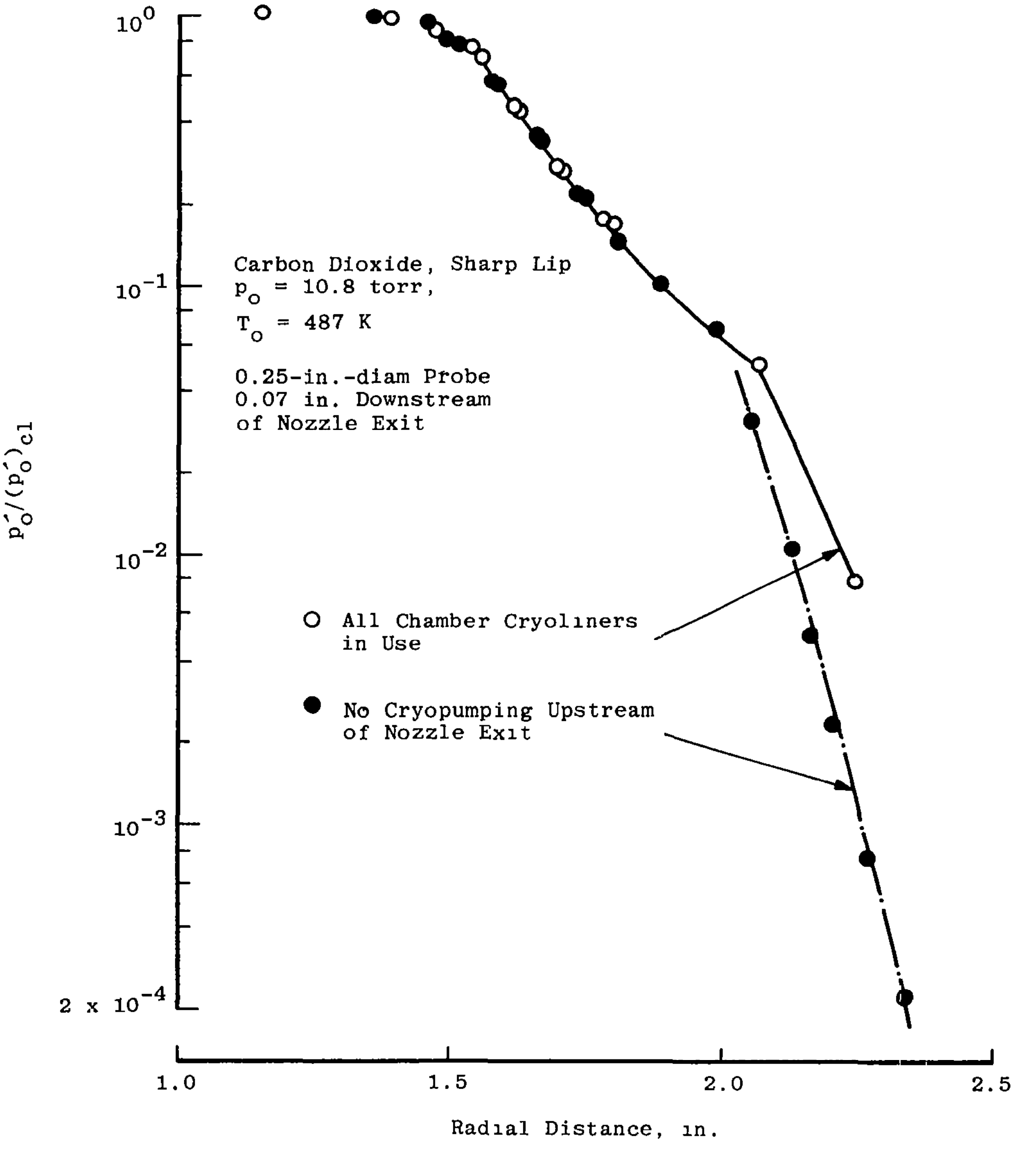

Figure 50. Effect of cryopumping in backflow region on exit-plane pitot profiles.

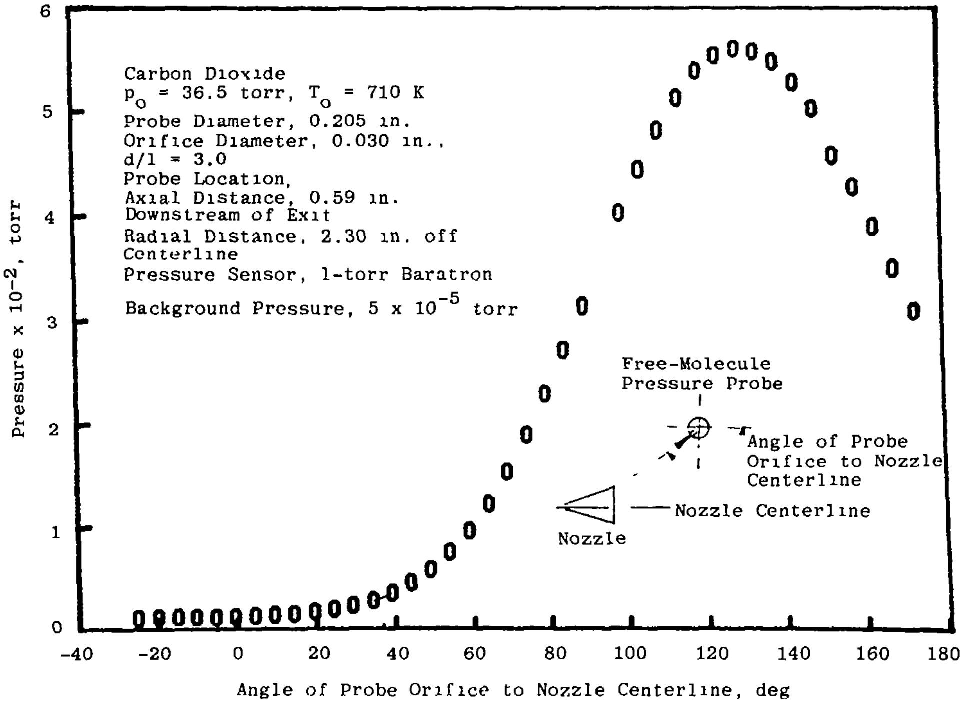

a. Axial distance, 0.59 in.; radial distance, 2.31 in.

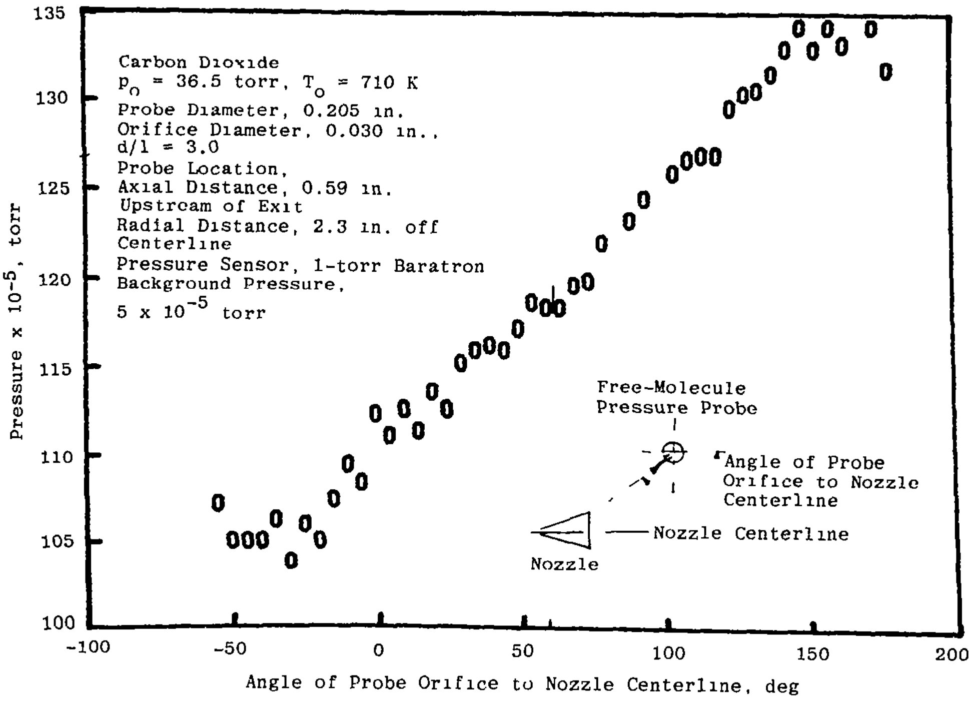

b. Axial distance, 0.59 in.; radial distance, 2.31 in.

Figure 51. Pressure variation with angle of orifice to flow—no background cryopumping.

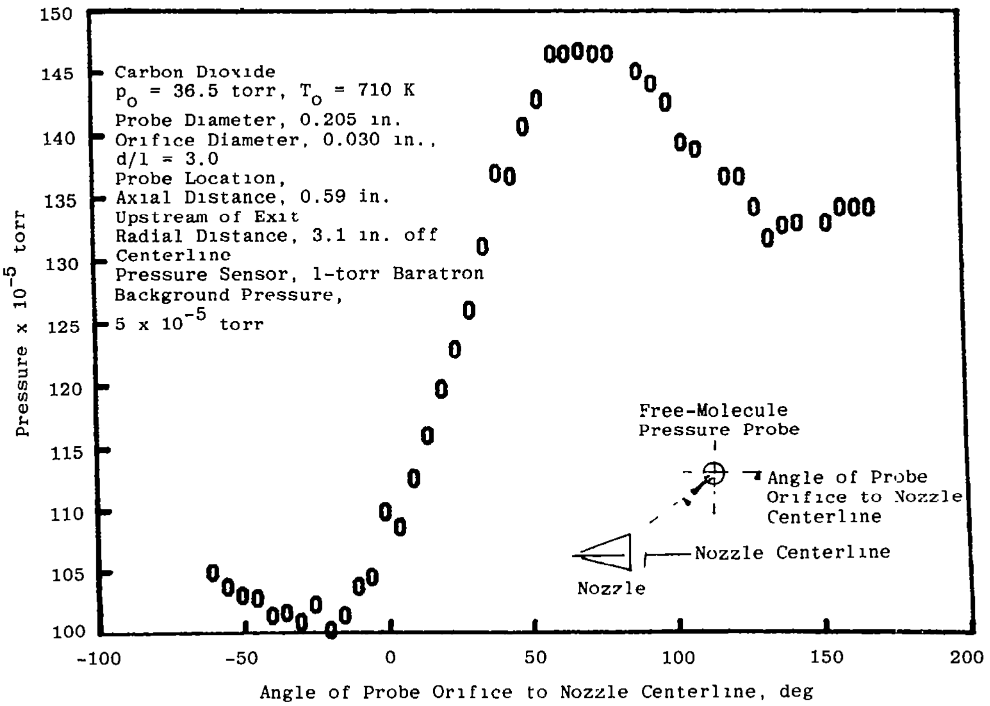

c. Axial distance, 0.59 in.; radial distance, 3.1 in.

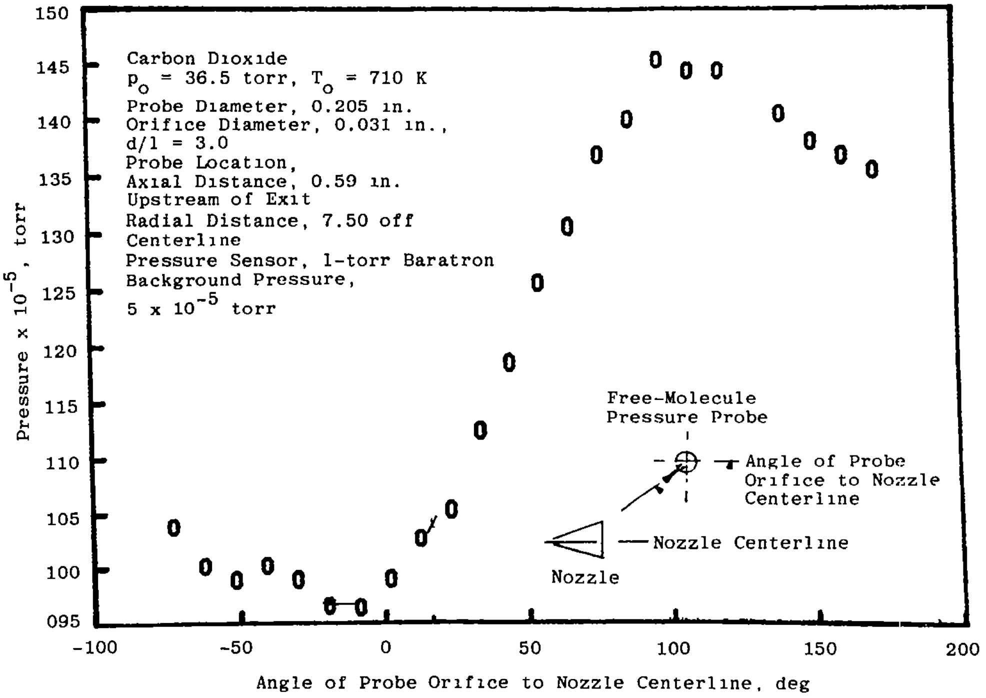

d. Axial distance, 0.59 in.; radial distance, 7.50 in.
Figure 51. Continued.

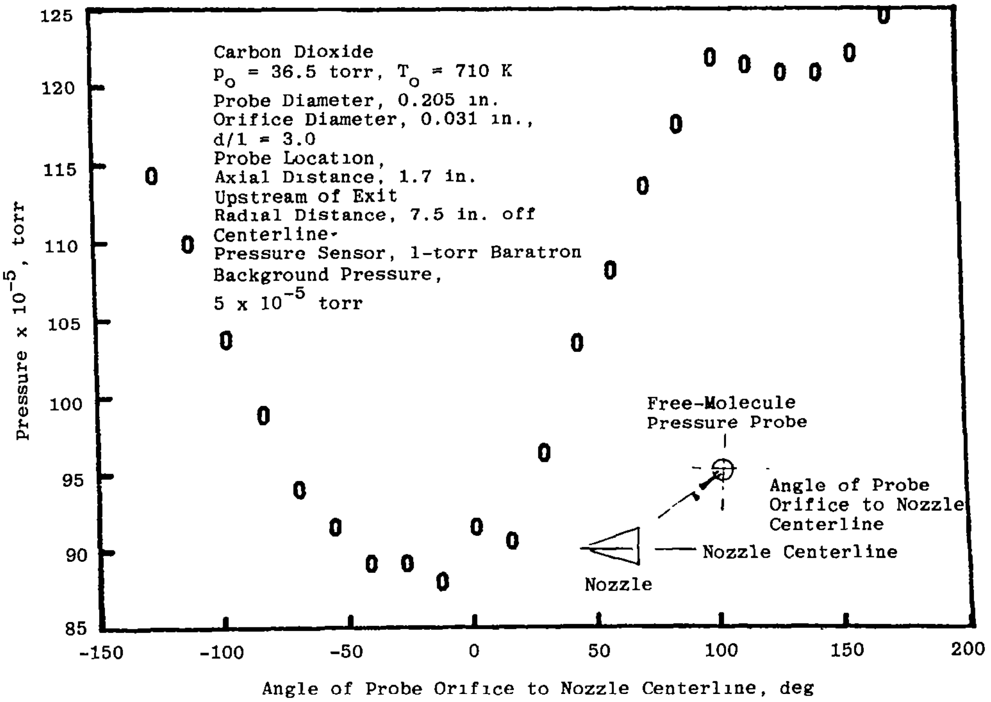

e. Axial distance, 1.7 in.; radial distance, 7.5 in.

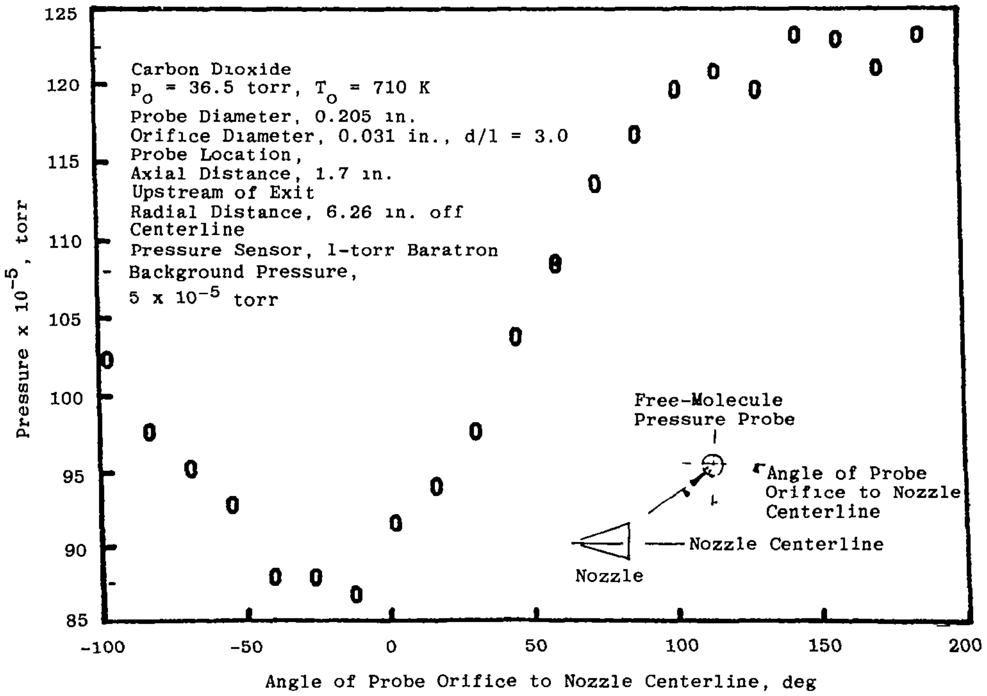

f. Axial distance, 1.7 in.; radial distance, 6.26 in.

Figure 51. Concluded.

about the angle at which the peak pressure occurs. The first profile presented in the backflow region is 0.59 in. (1.5 cm) behind the exit at the same radial position as the forward-flow profile (Fig. 51a). This profile, Fig. 51b, does not have the same form as any of the probe profiles shown to date, e.g., Fig. 48. If there is a peak in the pressure signal, it occurs in the region of 150 deg which corresponds to a flow angle of approximately 30 deg to the nozzle axis, i.e. in the downstream direction. A possible explanation for this could be that the probe is in a region of subsonic recirculating flow. Moving outward approximately 0.8 in. (2 cm) at the same axial position (Fig. 51c) results in a well-resolved pressure peak but an asymmetrical profile of the type already illustrated in Fig. 48b. The flow angle to the nozzle axis is 120 deg which is consistent with pitot probe derived values of angle summarized in Fig. 23a. A further increase in the radial distance at this axial location results in a significant reduction in flow angle to 74 deg, i.e. indicative of flow in the downstream direction. The foregoing pressure/angle measurements indicate that when there is no cryopumping in the backflow region, the flow is more complex than is the case for a cryopumped background illustrated by the data presented in Fig. 29a. This is further illustrated by the last two pressure profiles in this sequence which were obtained at 1.7 in. (4.3 cm) behind the nozzle lip at large radial distances from the centerline. Both of these pressure profiles indicate that the flow direction at these radial and axial locations is downstream away from the backflow region. A number of radial surveys of peak pressure and the angle at which it occurred confirm this variation of flow angle, and an example of these measurements is given in Fig. 52. It will be seen that the pressure decreases rapidly (Fig. 52b) in the first 1.0 in. (2.54 cm) from the edge of the nozzle and then remains essentially constant to the radial limit of these measurements.

A sequence of similar measurements were then made with the backflow cryopumps in operation. Examples of these measurements have already been given in Fig. 48. These two sets of free-molecule probe measurements are compared with those obtained with the pitot probe, Fig. 29a, in Fig. 53. It is readily apparent that for the two axial stations in the backflow region, there is a marked difference between the no cryopumping and cryopumping measurements for the axial station 1.8 in. (4.6 cm) upstream of the exit. However, there is also a significant and unexpected difference between the pitot probe and free-molecule probe data with full cryopumping. Previous evaluations of these two probes show (Fig. 29b) that these angle measurements should be in good agreement. The chamber pressure for the wholly cryopumped chamber was 1.5×10^{-5} torr for both sets of measurements, and on this basis, it was assumed that the chamber cryopumps were operating correctly. However, subsequent to the experiment with the free-molecule probe with "full cryopumping," it was found that the cryopanels in the backflow region were at a temperature at least 10 K higher than normal. Experience with the QCM in the present study has indicated that complete pumping of CO_2 will not occur under these conditions. Thus,

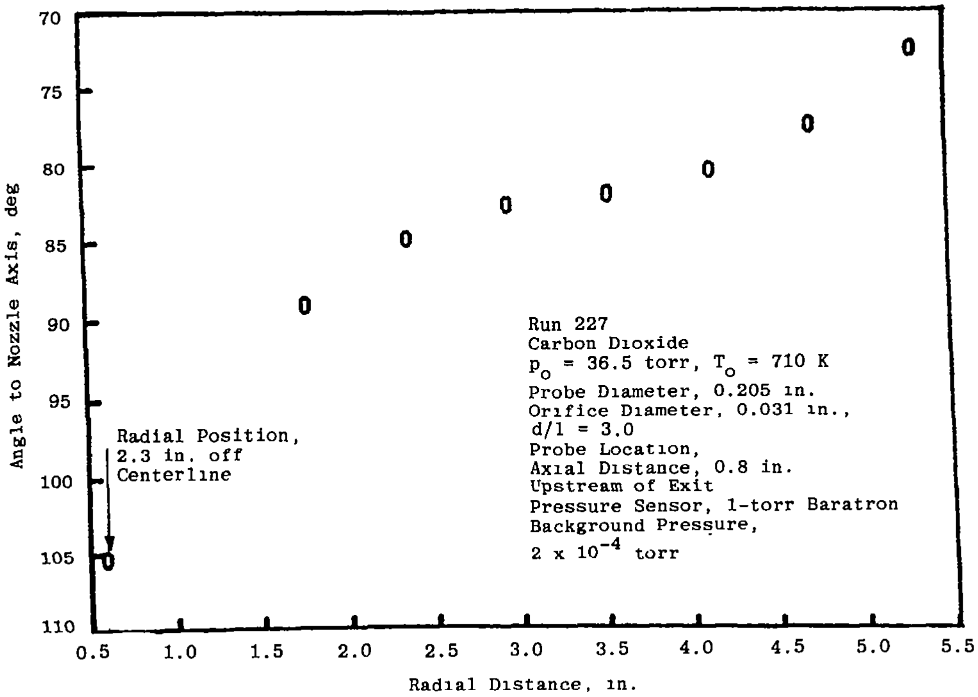

a. Flow angle

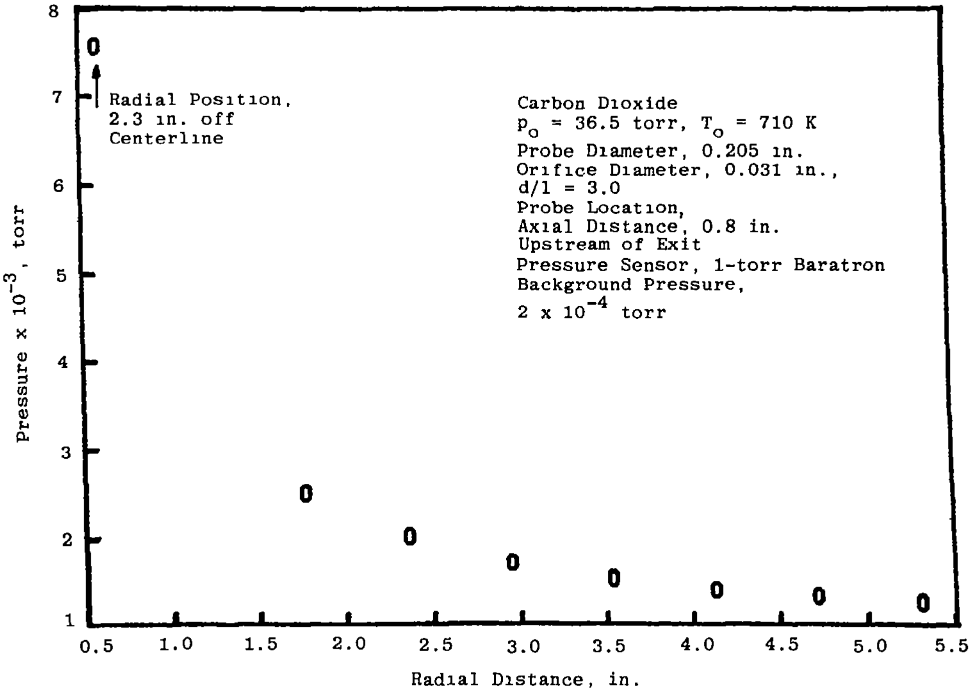

b. Peak pressure

Figure 52. Flow characteristics with no backflow cryopumping.

the free-molecule probe data have been obtained at conditions where the cryopump does not pump the entire gas load, and this has been identified as partial cooling in Fig. 53. The effect of partial pumping in the backflow region on flow angle is illustrated in Fig. 53 where the flow angles for partial pumping are compared with those obtained with complete pumping. This comparison shows that in order to make meaningful measurements in the nozzle backflow region it is necessary to be aware of the pumping condition in this flow field region.

Based on the "no cryopumping" data presented in Fig. 53, there are even greater differences from the full- and partial-cryopumping data presented in Fig. 54.

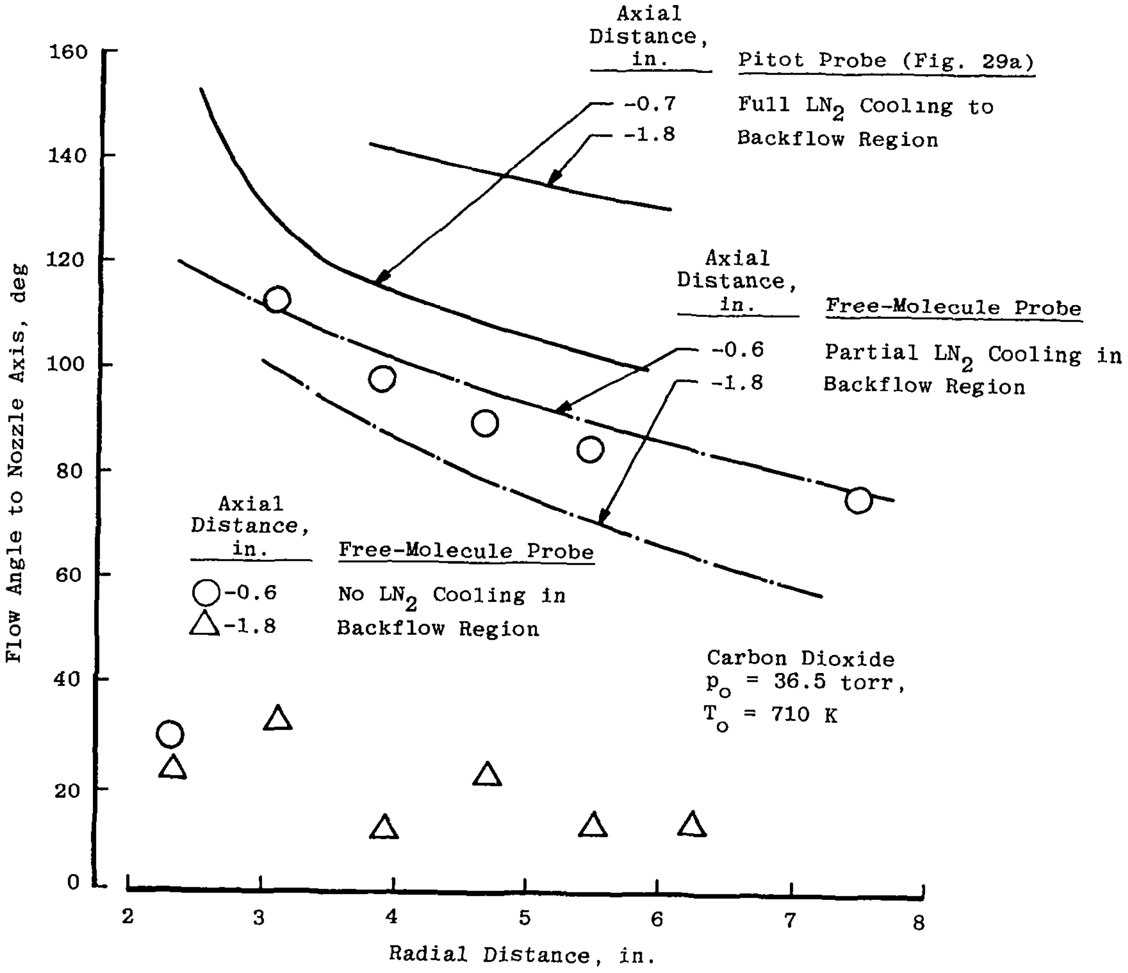

Figure 53. Effect of cryopumping in backflow region on flow angle.

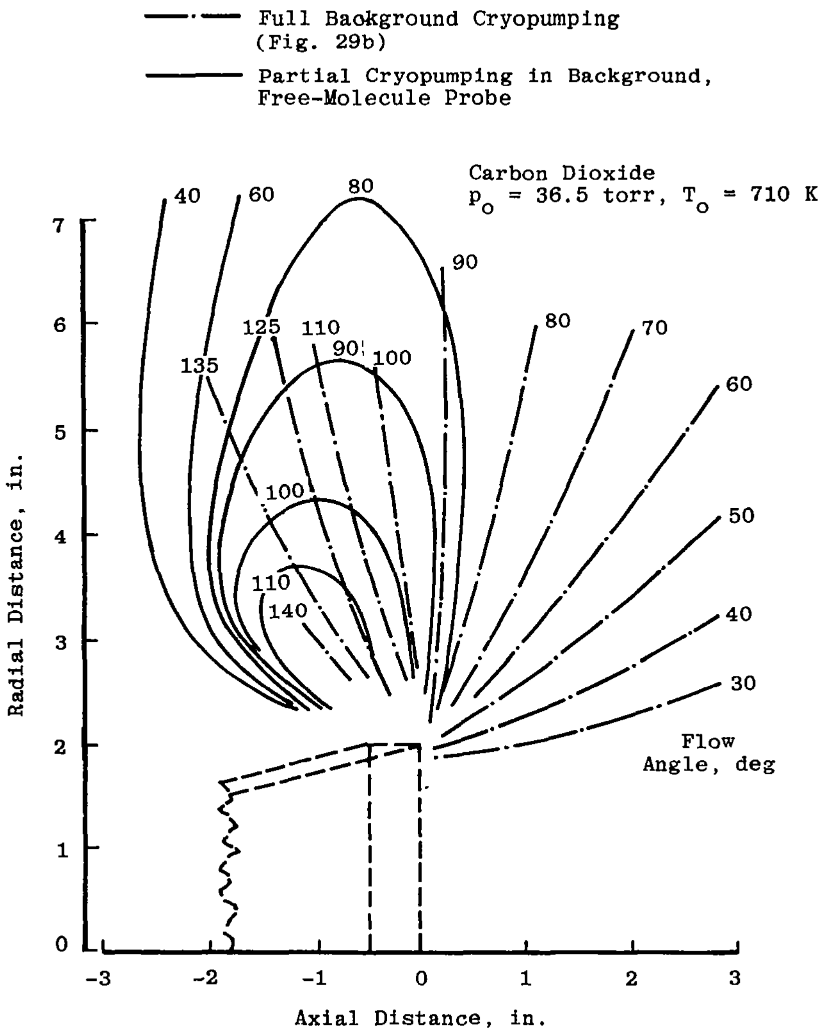

Figure 54. Effect of partial cryopumping in backflow region on flow angle.

5.5 EFFECT OF CHAMBER BACKGROUND PRESSURE ON NOZZLE FLOW

It has been shown in an earlier section that in the absence of significant changes in background pressure, the nozzle plume characteristics are affected by the presence or absence of cryopumping in the backflow region. In the present section, the effect of increased chamber pressure in the presence of full cryopumping in the backflow region will be considered. As has been noted earlier the pumping characteristics of the 4- by 10-ft RVC are such that the RVC can be isolated from the oil diffusion pumps, and a chamber pressure on the order of 2×10^{-5} torr can be maintained with full nozzle flow with the LN_2 cryopumps alone. These pumping characteristics have allowed the chamber pressure to be set at pressures between 2 × 10^{-5} and 4 × 10^{-1} torr by metering argon into the chamber through a micrometer needle valve. Recovery from the high pressure was accomplished by first pumping with the large mechanical pump followed by the two oil diffusion pumps.

Four types of measurements have been made to evaluate the effects of chamber pressure on nozzle characteristics (1) flow-angle and peak pressure measurements using the 0.05-in.-diam (0.127-cm) pitot probe together with a 10-torr Baratron, (2) pitot pressure measurements with the 0.125-in.-diam (0.318-cm) pitot probe aligned with the nozzle axis using the Datametrics 1-torr Barocel absolute pressure transducer, (3) centerline pitot pressure measurements with both probes with varying chamber background pressure, and (4) nozzle wall static pressure measurements using a Granville-Phillips Convectron gage or the 1-torr Barocel.

An example of the data obtained with the rotary probe/transducer configuration close to the nozzle exit plane at a background chamber pressure which exceeds the centerline static pressure in the nozzle exit plane is presented in Fig. 55. The pitot pressure profile Fig. 55a is characterized by an essentially constant pressure for radial distances greater than 2 in. (5.0 cm) from the nozzle centerline. The corresponding flow-angle data, Fig. 55b, show that at a

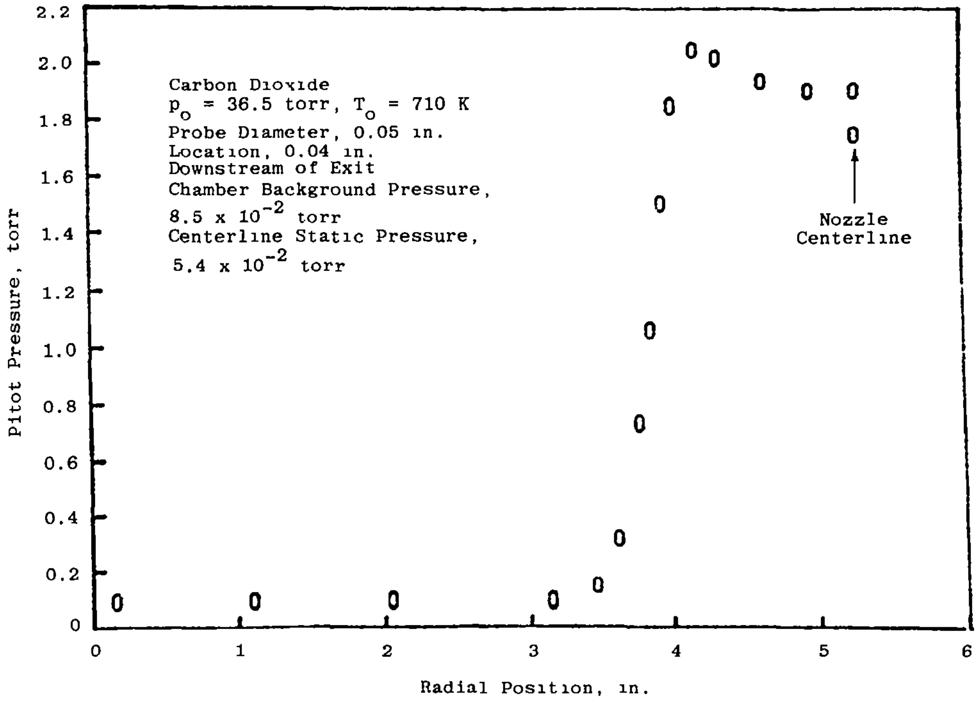

a. Pitot pressure

Figure 55. Flow profiles at elevated chamber pressure—raw data.

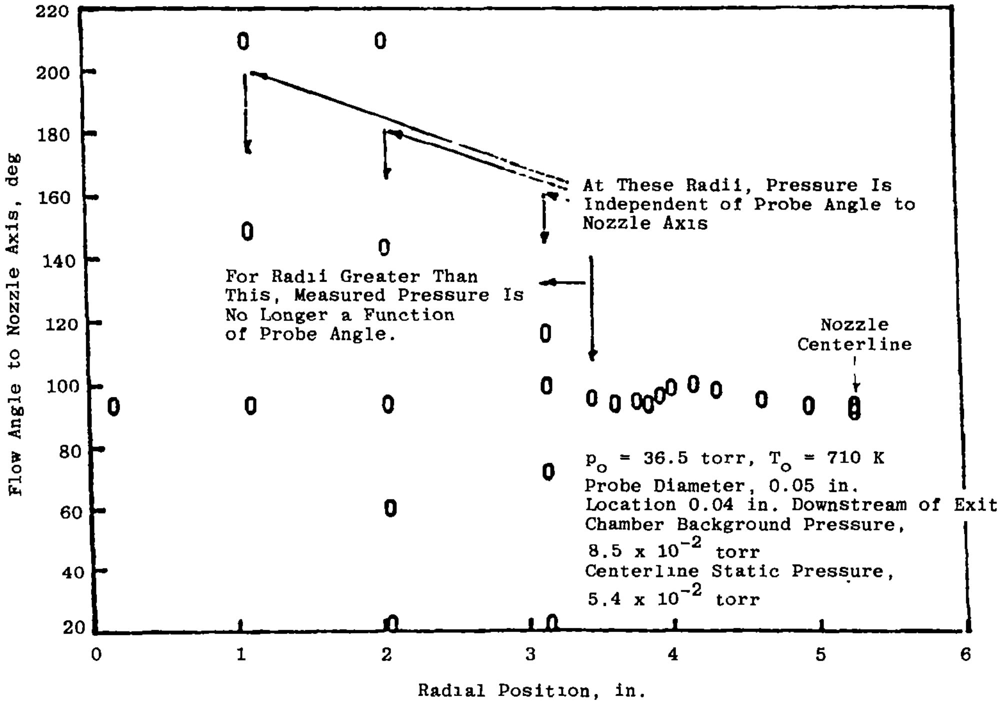

b. Flow angle
Figure 55. Concluded.

radial position of approximately 2 in. (5 cm), the angles at which the corresponding constant values of pressure were measured, Fig. 55a, varied from 20 to 220 deg. It can be inferred from these flow angle and pressure measurements that, for distances greater than approximately 2 in. (5 cm) from the nozzle centerline, probe pressure is essentially independent of probe angle and equal to the chamber background pressure as measured with the Westinghouse Schultz-Phelps ion gage.

The rotary probe/transducer data for a range of nozzle and chamber conditions are summarized in Fig. 56. The regions of almost constant pressure are clearly defined for the different values of chamber pressure, e.g., Fig. 56a. Also associated with the different background pressures are small but consistent changes in the form of the variation of pitot pressure with radial distance in the flow outside of the central core region. These differences are small, and based on these measurements alone, it would be reasonable to assume that the flow in the nozzle exit plane is relatively unaffected when the chamber pressure is equal to or slightly greater than the centerline static pressure. However, the corresponding flow-angle measurements show that deviations from the undisturbed flow-angle profile occur closer to the nozzle centerline than does the first occurrence of constant pressure. Thus, these flow-angle measurements show that for these nozzle conditions (Fig. 56a), when the chamber background pressure is approximately equal to the centerline static pressure, it cannot be assumed that the exit-plane flow is representative of conditions that exist when the chamber pressure is significantly less than the exit-plane static pressure. These measurements indicate that for nozzle flows in a vacuum, backflow and thrust measurements in ground-based test chambers will not be wholly representative of the conditions in space, unless the space environment is accurately simulated.

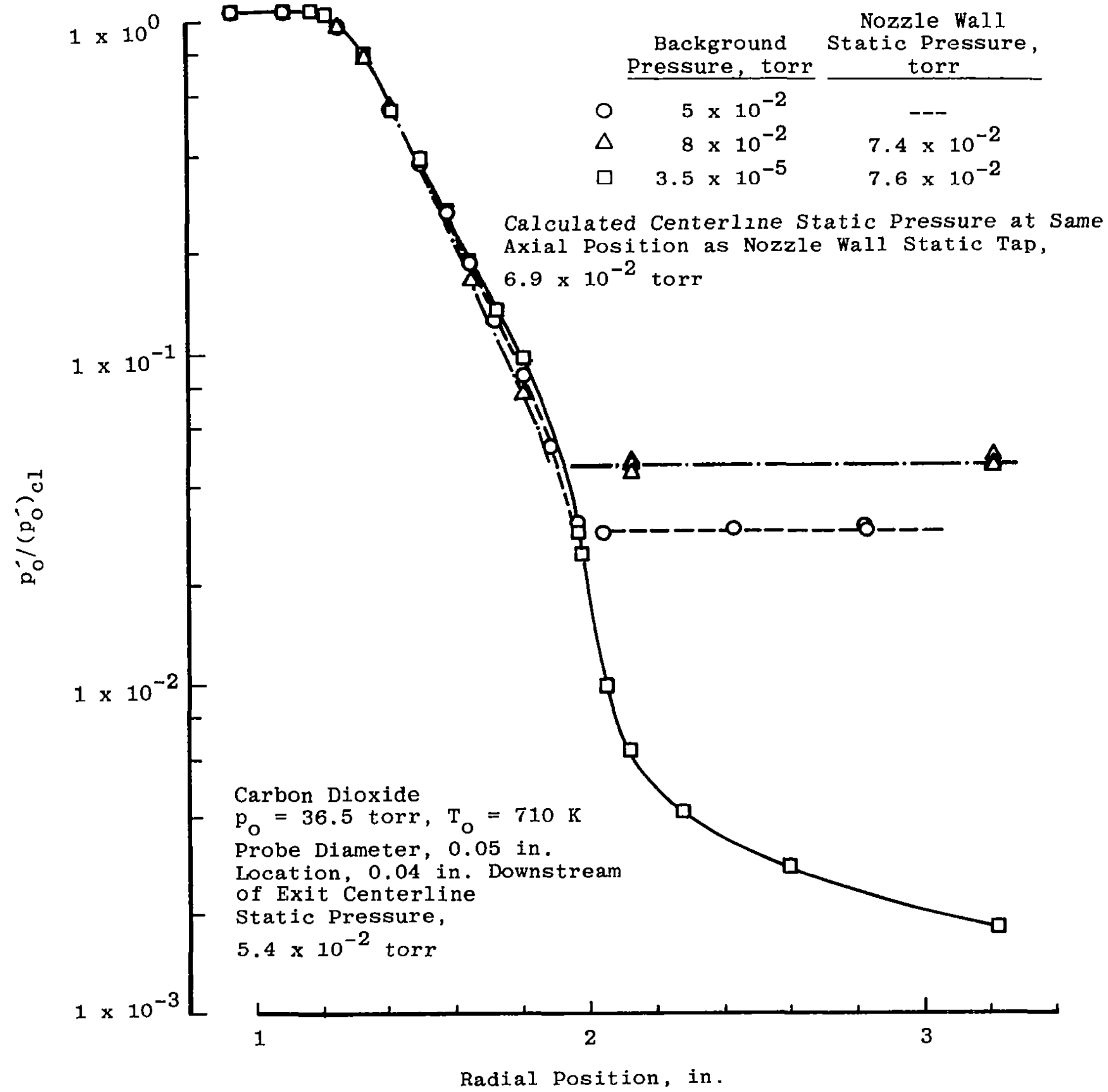

a. Pitot pressure, p_0 = 36.5 torr, T_0 = 710 K
Figure 56. Flow profiles with varying chamber pressure.

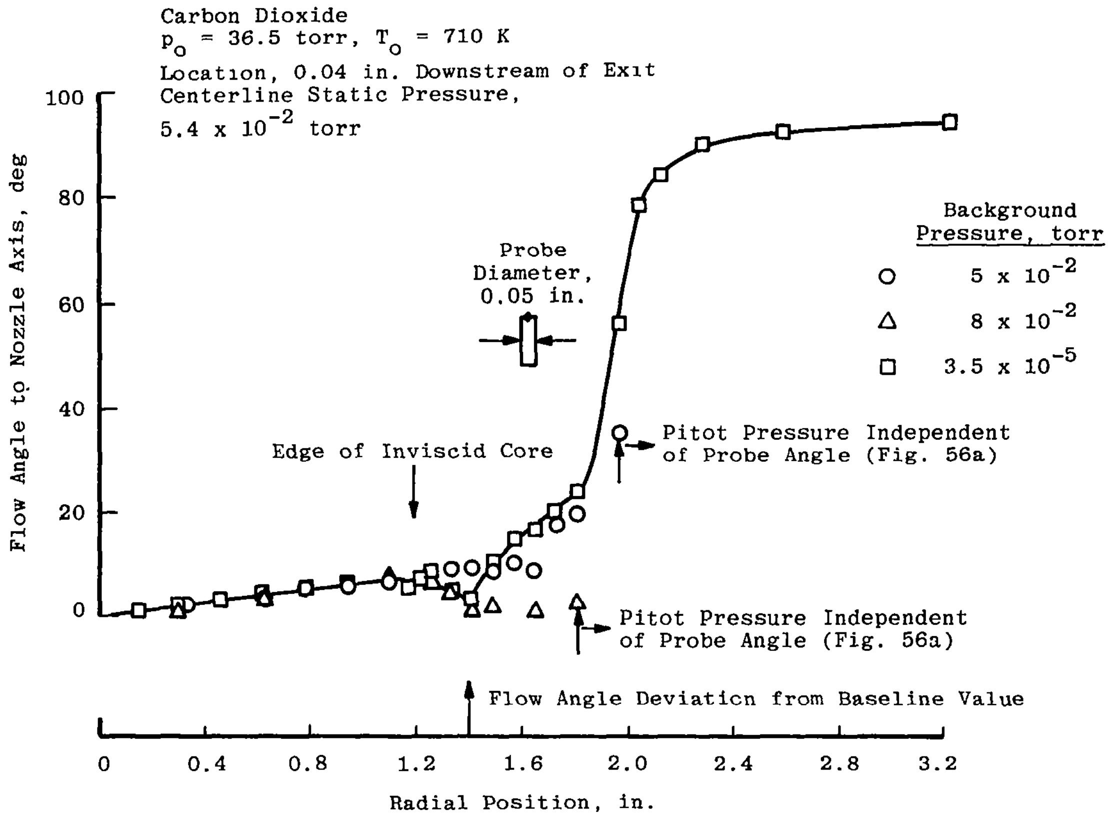

b. Flow angle, p_o = 36.5 torr, T_o = 710 K
Figure 56. Continued.

It was beyond the scope of the present study to make complete pressure/flow-angle studies for the three nozzle configurations. Therefore, the stationary 0.125-in.-diam (0.318-cm) probe, with its longitudinal axis aligned with the nozzle axis, was used to obtain the major portion of the radial pitot profiles in the background pressure variation studies. It has been shown in Fig. 56 that when the background pressure is on the order of the centerline free-stream static pressure, the maximum flow angles in the exit plane are limited to values less than 30 deg. For the flow conditions of these experiments, the data presented in Fig. 23 indicate that misalignments to the flow of this magnitude result in errors in absolute magnitude of the pitot pressure of less than 5 percent. Thus, at the lowest chamber pressure, i.e. on the order of 2×10^{-5} torr, the measured pitot pressure at radial distances greater than 1.8 in. (4.6 cm) will be too low (cf. Fig. 22) in the region of the nozzle exit plane because of probe misalignment to the flow. In this evaluation, it was considered that this probe error would not seriously compromise the determination of chamber pressure effects on exit-plane pitot profiles. It is further assumed (based on the data presented in Fig. 56) that the radial location at which the pitot pressure first becomes constant is an indication that significant changes in the flow angle have already occurred at smaller radial positions.

Radial pitot pressure surveys using this technique have been obtained for the heated and unheated 44.4 and 400 area ratio nozzles. Radial surveys both upstream and downstream of the nozzle exit plane for the $A/A^* = 400$ nozzle are presented in Fig. 57. These measurements have been plotted semilogarithmically (Figs. 57a and b) to illustrate the characteristics of the free shear layer. However, plotting the data in this manner tends to obscure some of the characteristics of the core flow. Therefore, the exit-plane core-flow properties have been replotted in Fig. 57c. It is of interest to note that the core flow for the lower temperature condition, where condensation is considered to be probable, is more uniform than that for the higher temperature condition where condensation may be possible.

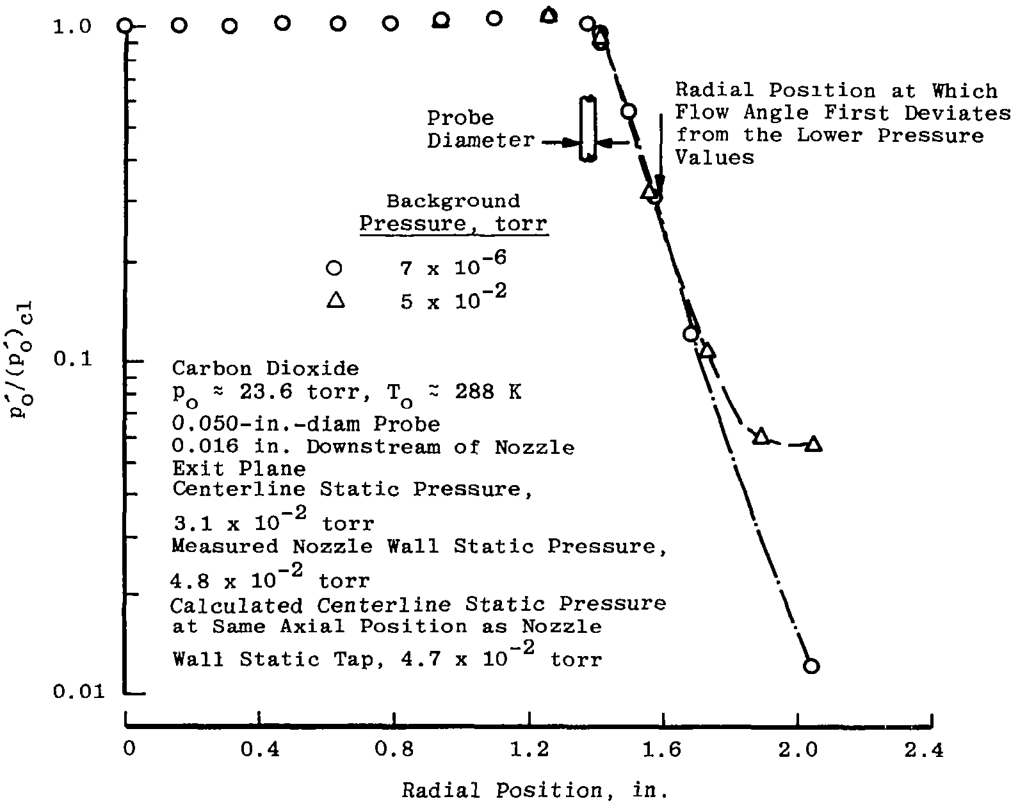

c. Pitot pressure, $p_0 = 23.6$ torr, $T_0 = 288$ K
Figure 56. Continued.

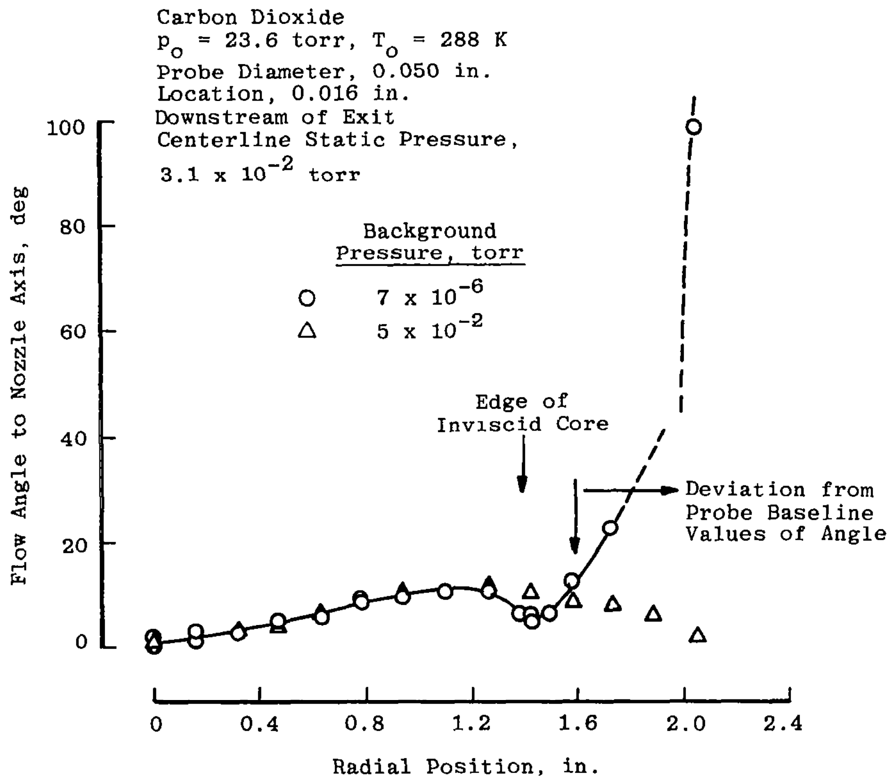

d. Flow angle, p_0 = 23.6 torr, T_0 = 288 K
Figure 56. Continued.

Also shown in Fig. 57c is the exit-plane core-flow profile obtained for the trumpet shaped A/A^* = 320 nozzle. Since the exit-plane radius of this nozzle is approximately 0.7 in. (2 cm), then these measurements can be compared directly if one assumes that the radial position is essentially a true nondimensionalized radial position. Of interest in the A/A^* = 320 nozzle study were the sharp spikes having a maximum radial extent of 0.028 in. (0.07 cm) in the radial pitot pressure profiles. In the present study, pitot pressure measurements were taken at minimum intervals of 0.08 in. (0.2 cm) so that the presence of such a spike could easily have gone undetected. A consideration of the form of the pitot pressure variation at the edge of the central core indicates that there could have been a similar undetected spike in the pitot pressure in the present study. On the basis of other measurements made by Bailey et al., it was concluded that these pressure spikes were indicative of condensation in the nozzle core flow.

The radial pitot pressure surveys for a range of chamber pressures are summarized in Fig. 58. For the A/A^* = 44.4 nozzle, the data indicate (Fig. 58a) that for background pressure greater than 6.5 × 10^{-2} torr, significant portions of the flow in the nozzle shear layer are affected by the chamber background pressure since this constant pressure occurs at

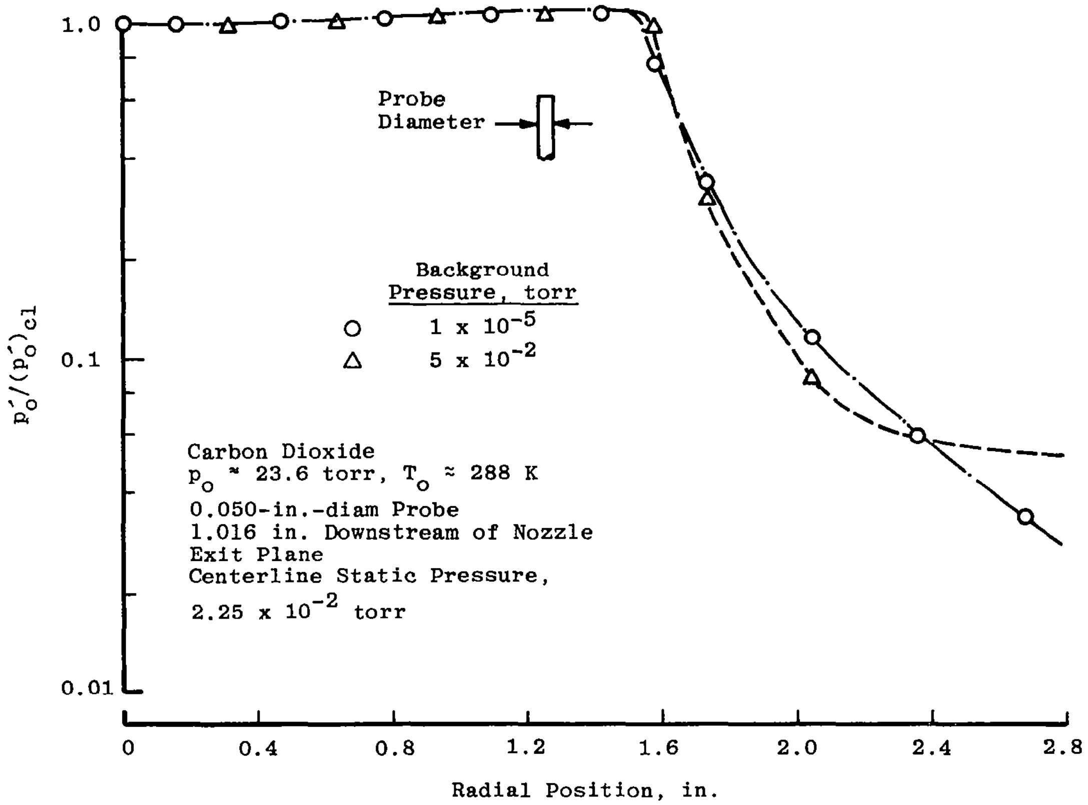

e. Pitot pressure, p_0 = 23.6 torr, T_0 = 288 K

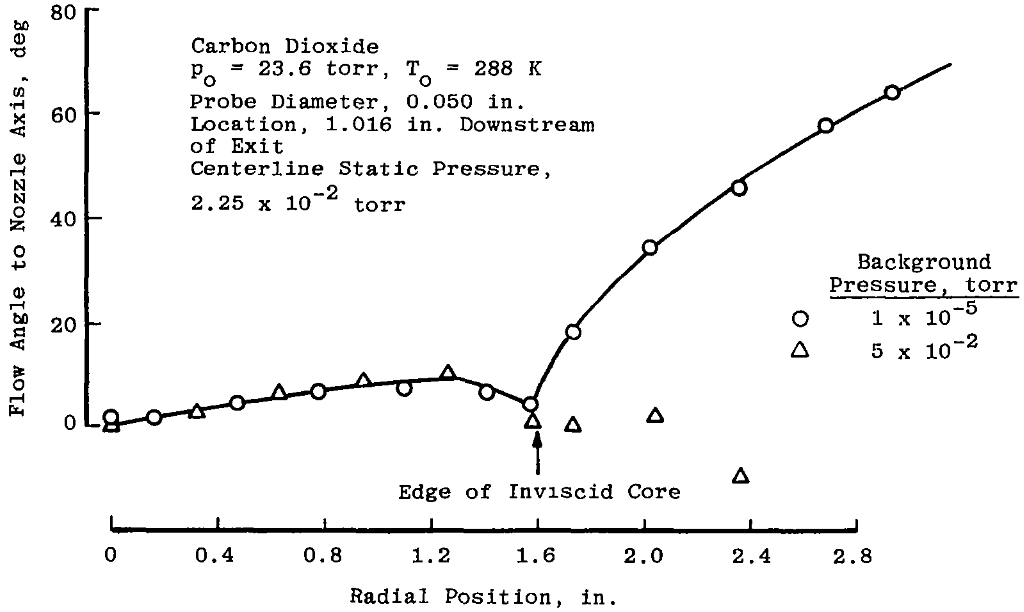

f. Flow angle, p_0 = 23.6 torr, T_0 = 288 K
Figure 56. Concluded.

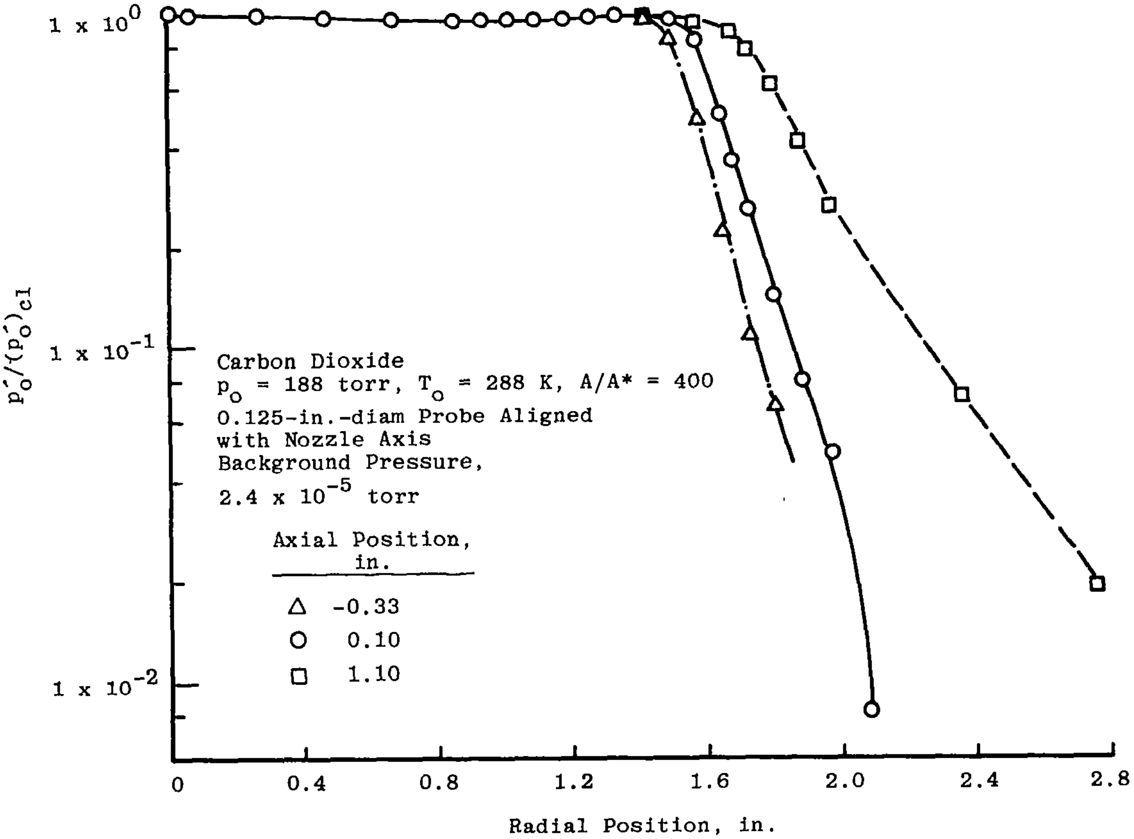

a. p_0 = 188 torr, T_0 = 288 K
Figure 57. Radial pitot profiles for A/A* = 400 nozzle.

a radial distance of less than the nozzle radius, i.e. 2.0 in. (5.0 cm). At high background pressures, e.g., 2.7 × 10^{-1} torr, the radial profiles are characaterized by sharp pressure spikes. For this nozzle, the first clear indication of a pressure spike occurs at a pressure of 1.9 × 10^{-1} torr, and there is evidence to suggest that a small spike may have occured at 1.6 × 10^{-1} torr. It is generally assumed that these pressure spikes result from the presence of a recompression shock in the nozzle flow. Similar observations are applicable to the A/A* = 400 nozzles (Figs. 58b and c) where it may be inferred that the exit-plane shear flow is affected at pressures as low as 6 × 10^{-3} torr.

In the final series of tests, the centerline pitot and wall static pressure were recorded as the ambient pressure varied from 1.5 × 10^{-5} to 4 × 10^{-1} torr (Fig. 59). The wall static pressure for both nozzles has been measured at approximately 0.6 in. upstream of the nozzle exit. This measurement is characterized by no measurable changes in value for a thousand-fold change in background pressure. It is apparent from the radial profile measurements, Fig. 58, that an increase in the wall pressure (Fig. 59) is associated with the first measurable observation of the compression shock in the nozzle exit plane. It is of interest to note that the present measurements indicate that the presence of this compression shock is first identified at a background pressure of approximately three times the value of the exit-plane free-stream static pressure.

There does not appear to be any clearly defined trend in the variation of centerline pitot pressure with chamber background pressure (Figs. 59a, b, and c). A possible reason for the lack of agreement in the form of this variation is that, from a flow condensation point of view, these nozzles represent three different states of condensation, i.e. not possible, possible, and probable. An earlier study of an $A/A^* = 320$ nozzle (Ref. 44) where condensation was possible showed a similar variation (Fig. 59d) to the heated $A/A^* = 400$ data of the present study, Fig. 59c. However, the magnitude of the changes in centerline pitot pressure for the $A/A^* = 400$ nozzle are significantly less than for the $A/A^* = 320$ nozzle. A further difference is that the $A/A^* = 320$ nozzle is trumpet shaped, whereas the present nozzles are conical with a 15-deg half-angle. Further studies with a range of nozzle configurations and operating conditions would be required to provide a definitive resolution of these effects.

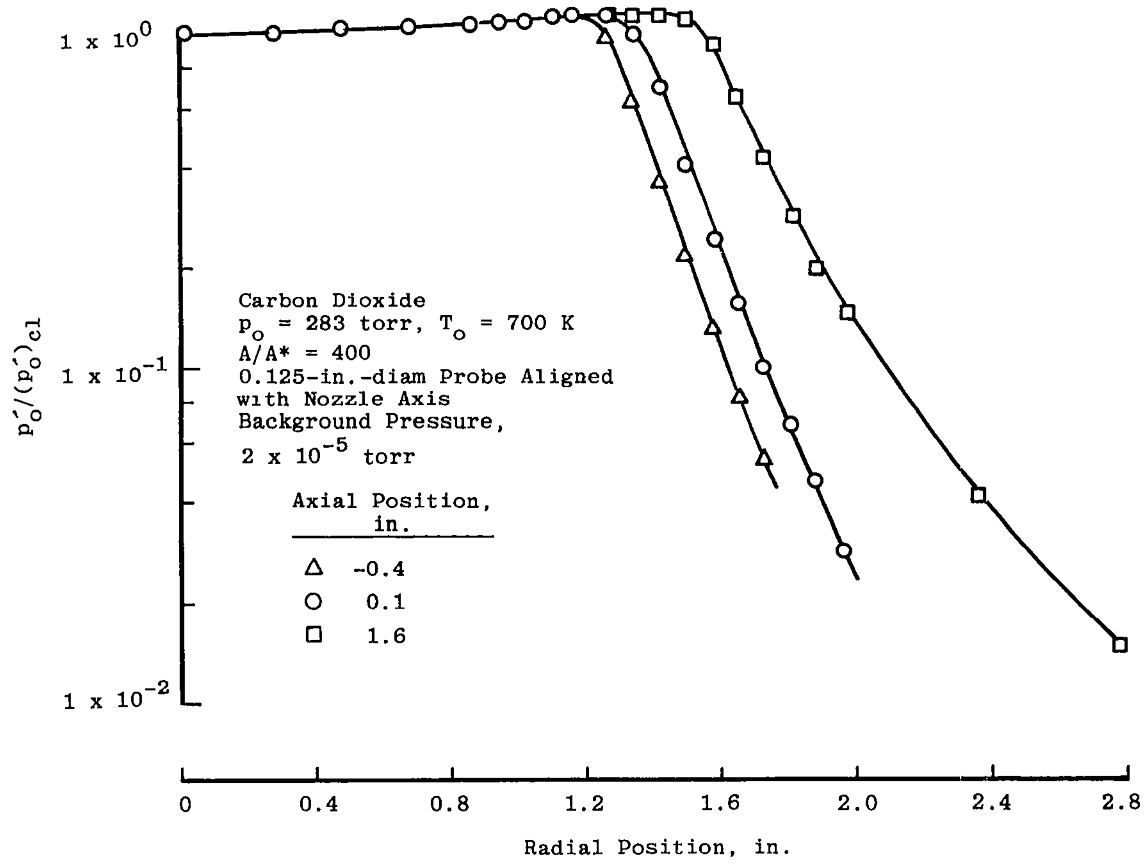

b. $p_0 = 288$ torr, $T_0 = 700$ K
Figure 57. Continued.

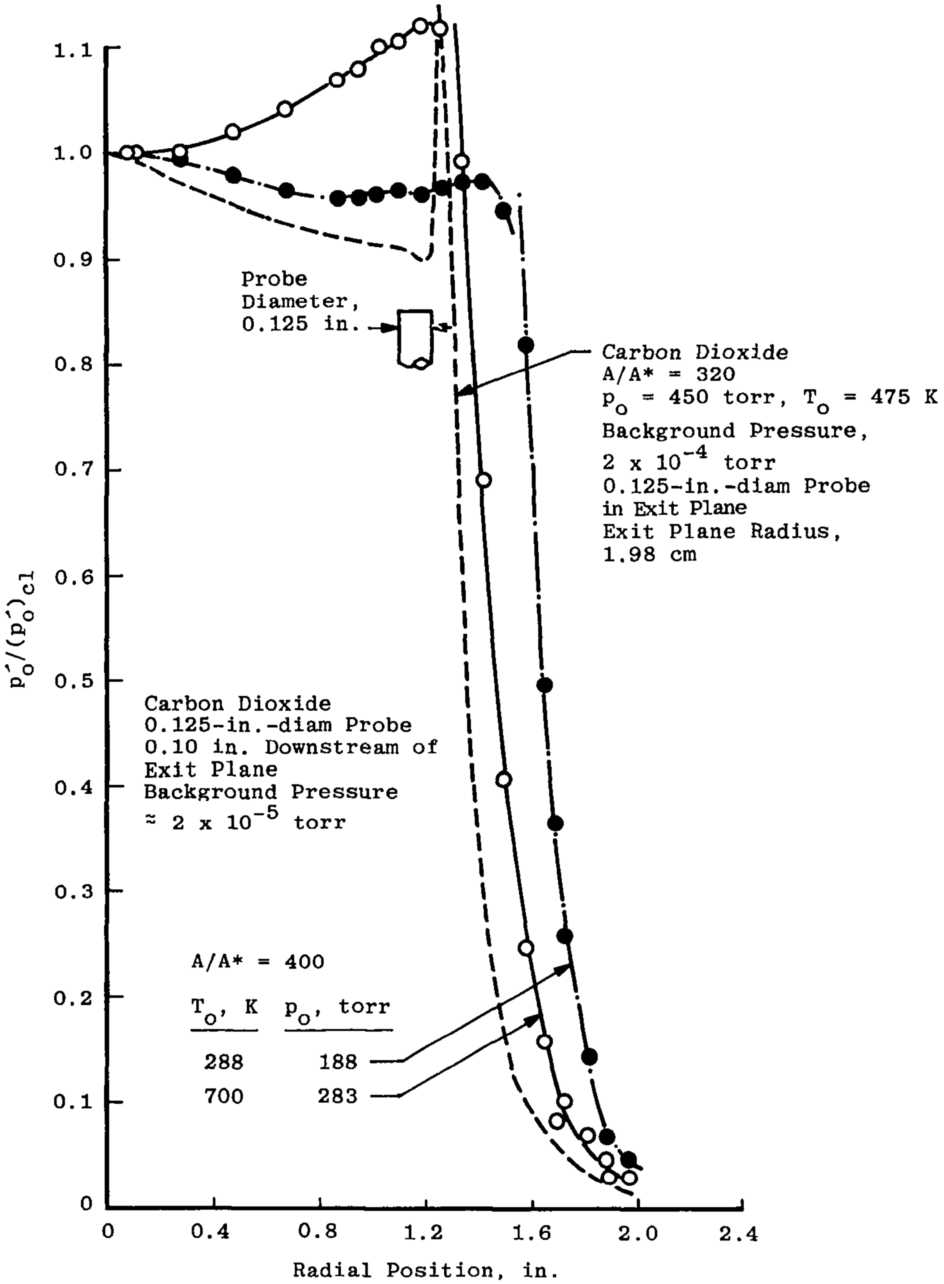

c. Exit plane core flow

Figure 57. Concluded.

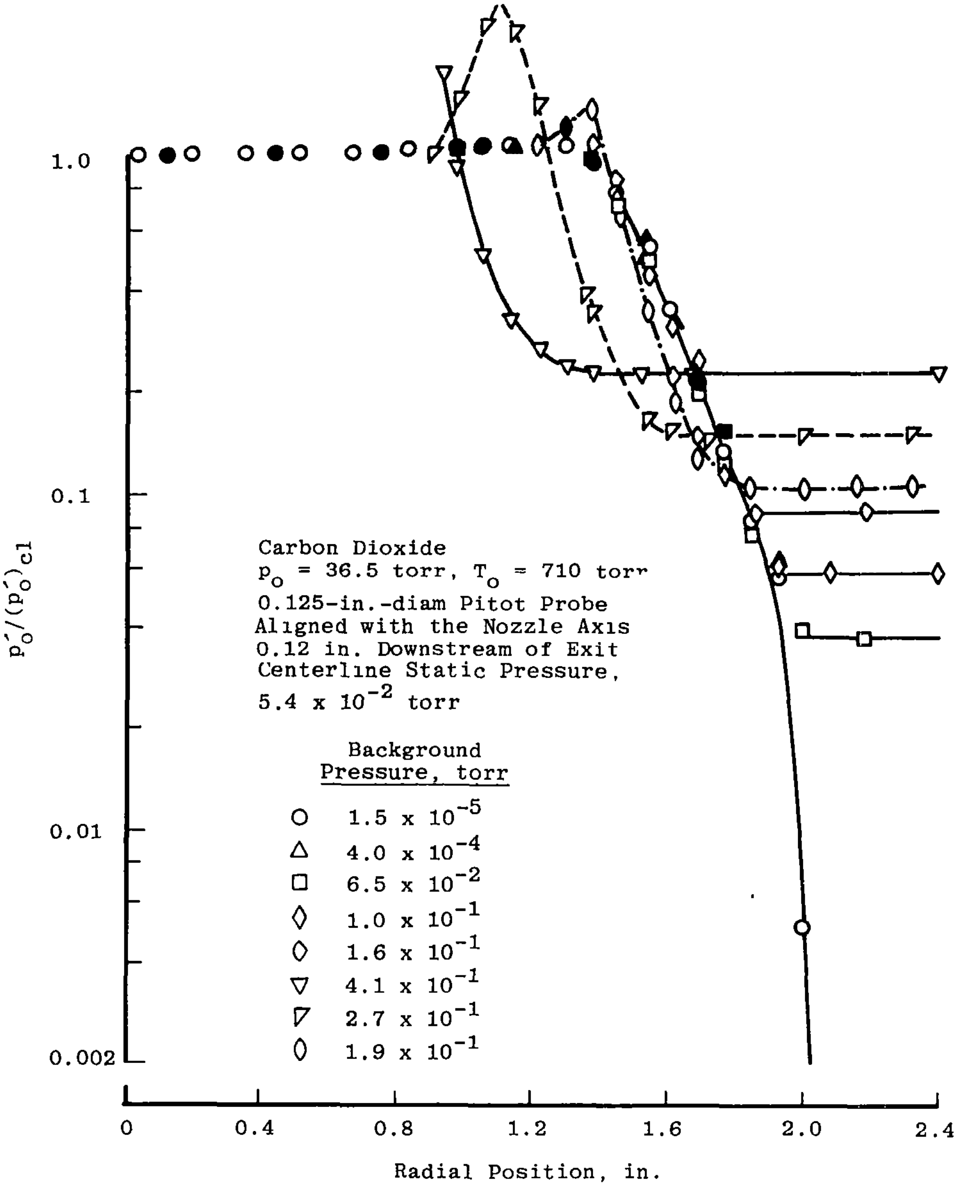

a. p_0 = 36.5 torr, T_0 = 710 K, A/A^* = 44.4
Figure 58. Effect of ambient pressure on exit-plane pitot pressure profiles.

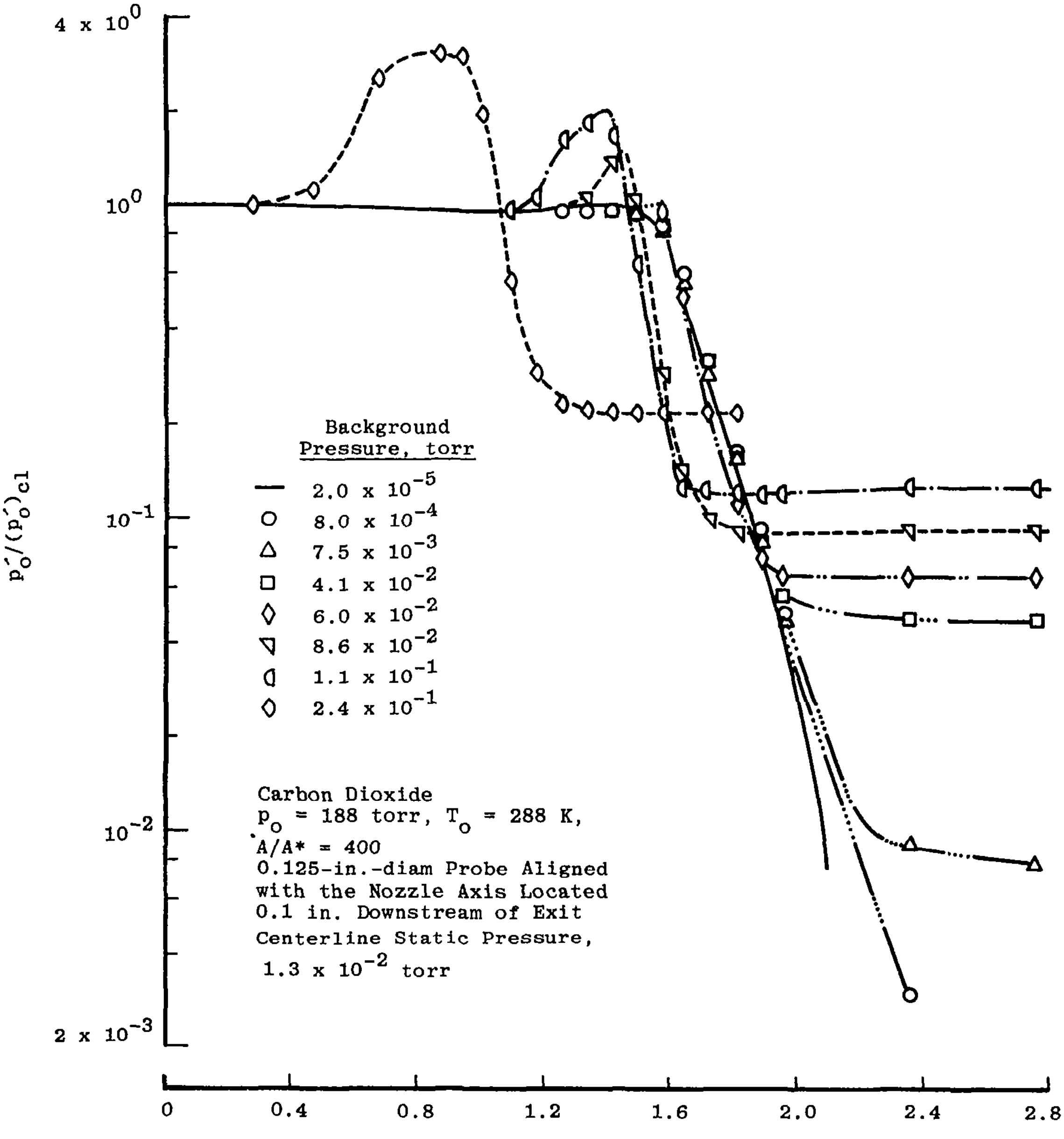

b. p_o = 188 torr, T_o = 288 K, A/A^* = 400

Figure 58. Continued.

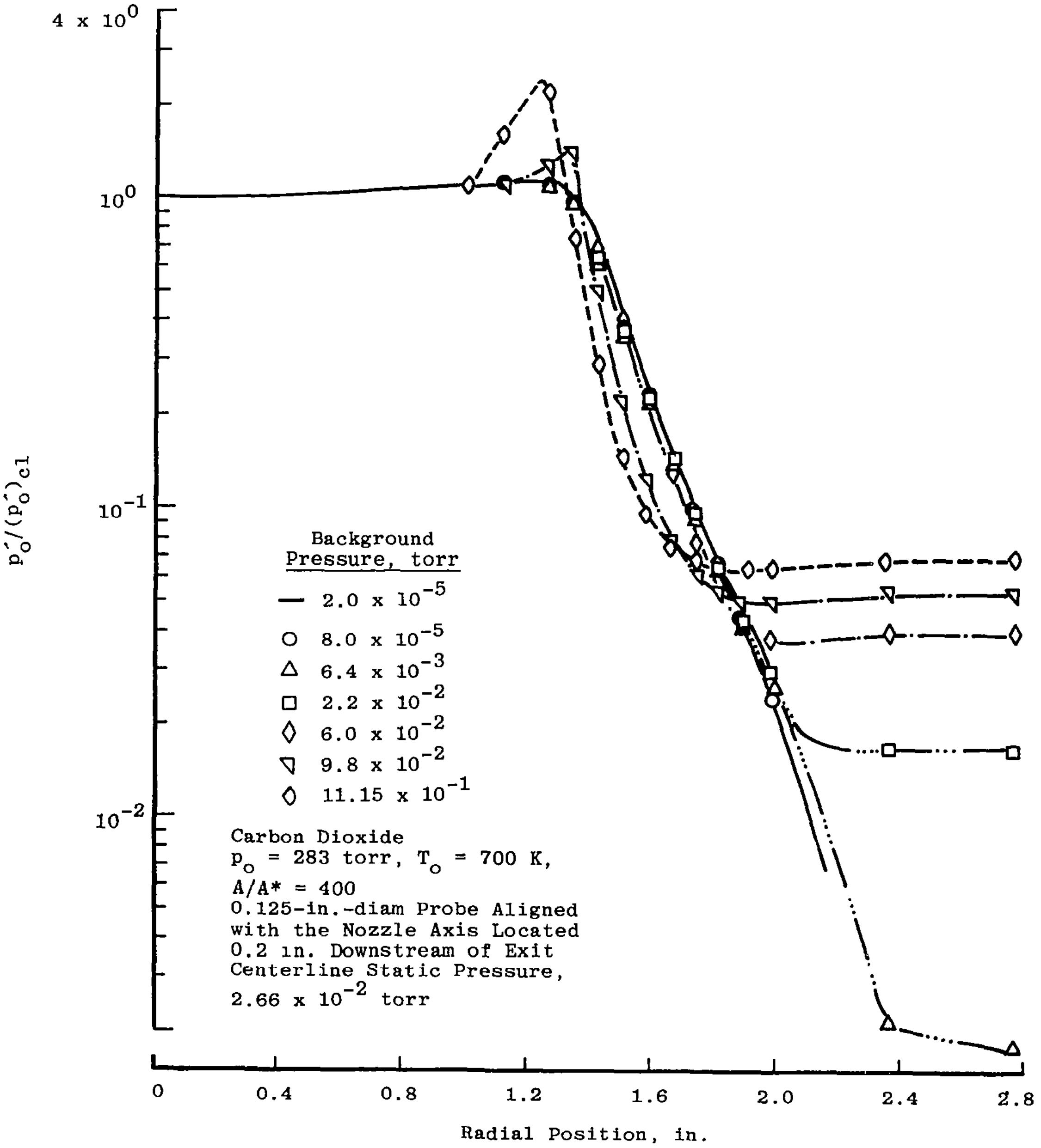

c. p_0 = 283 torr, T_0 = 700 K, A/A* = 400
Figure 58. Concluded.

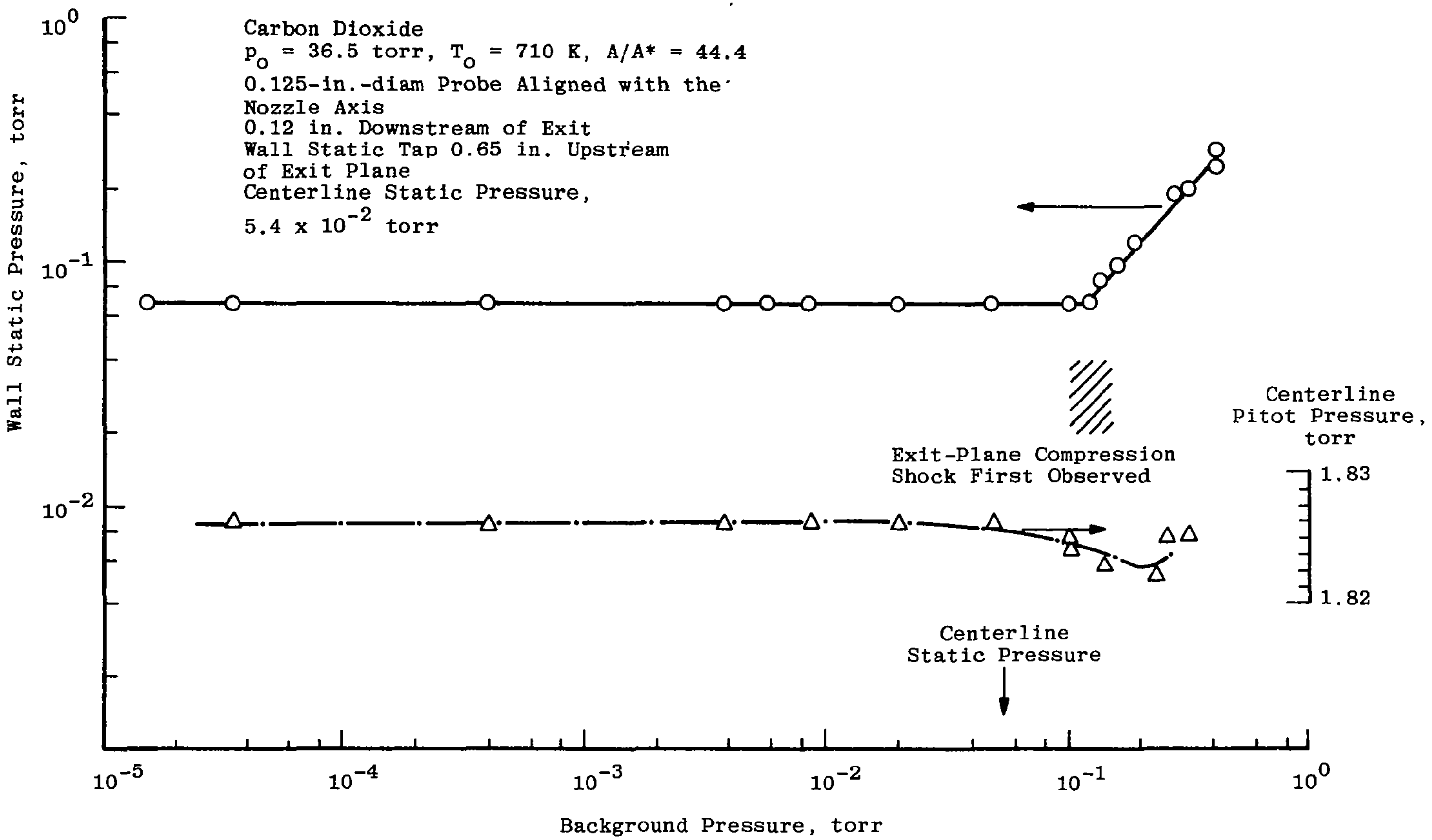

a. p_0 = 36.5 torr, T_0 = 710 K, A/A* = 44.4

Figure 59. Effect of varying background pressure on wall static and centerline pitot pressure.

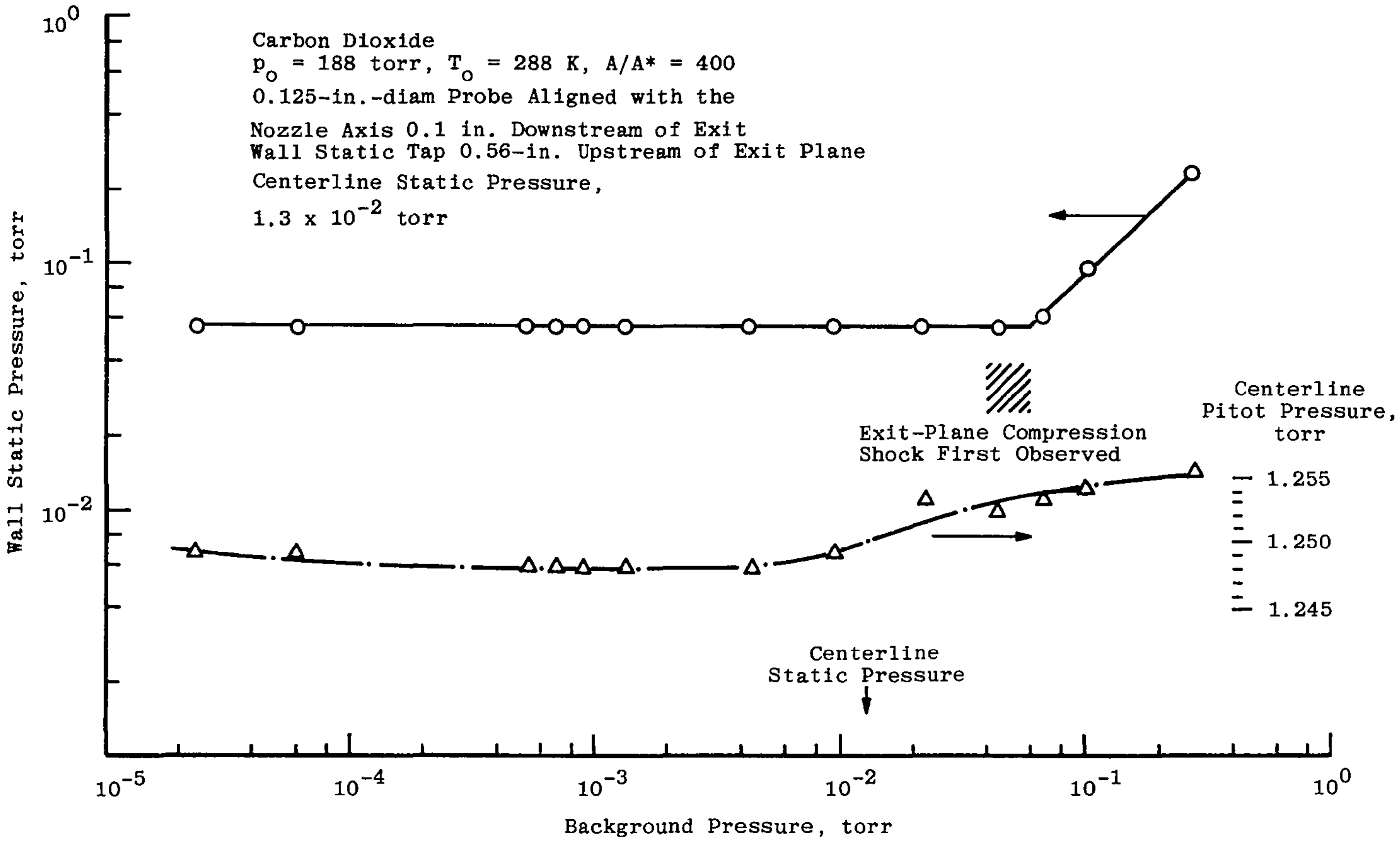

b. p_0 = 188 torr, T_0 = 288 K, A/A^* = 400

Figure 59. Continued.

]

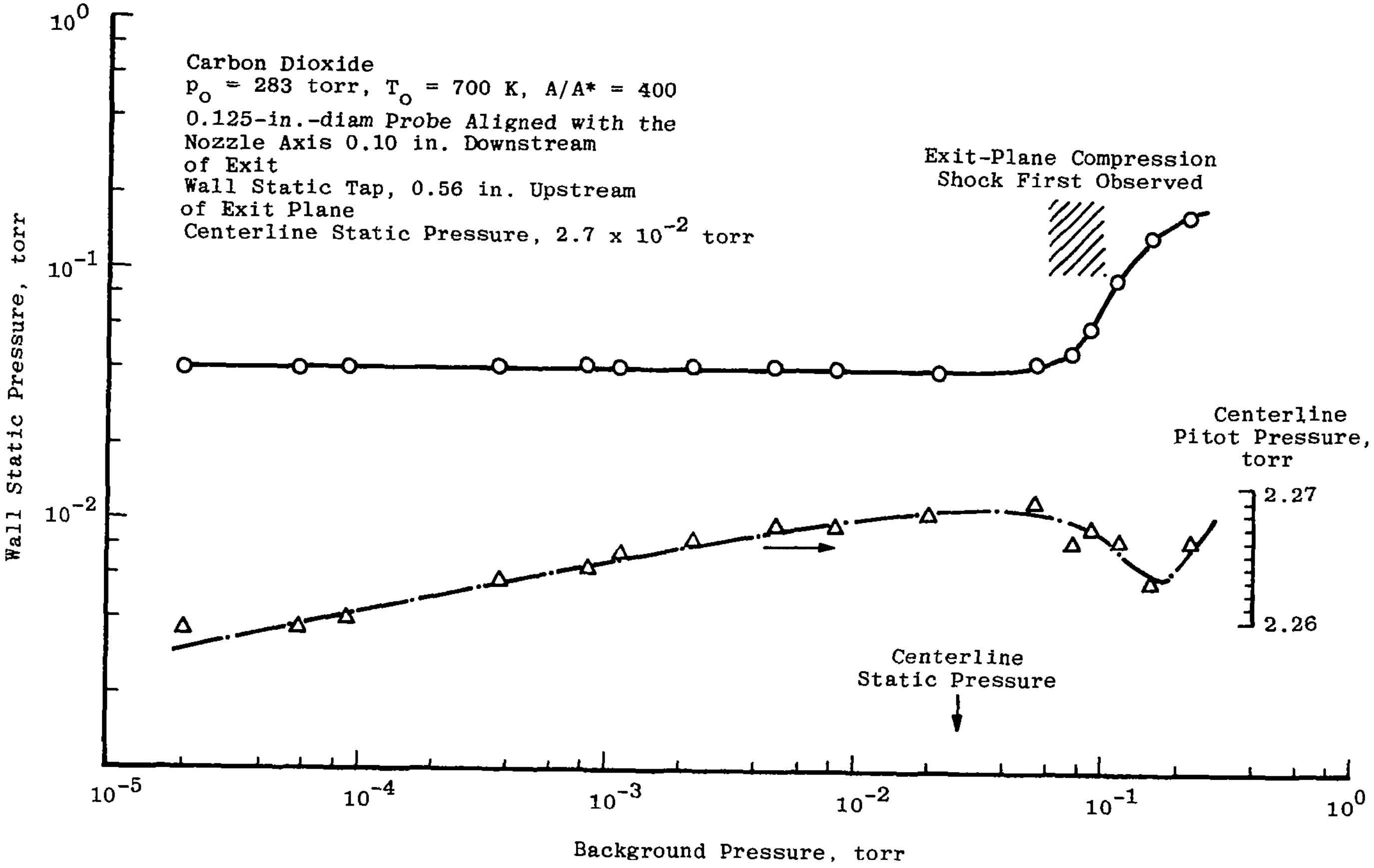

c. p_o = 283 torr, T_o = 700 K, A/A* = 400
Figure 59. Continued.

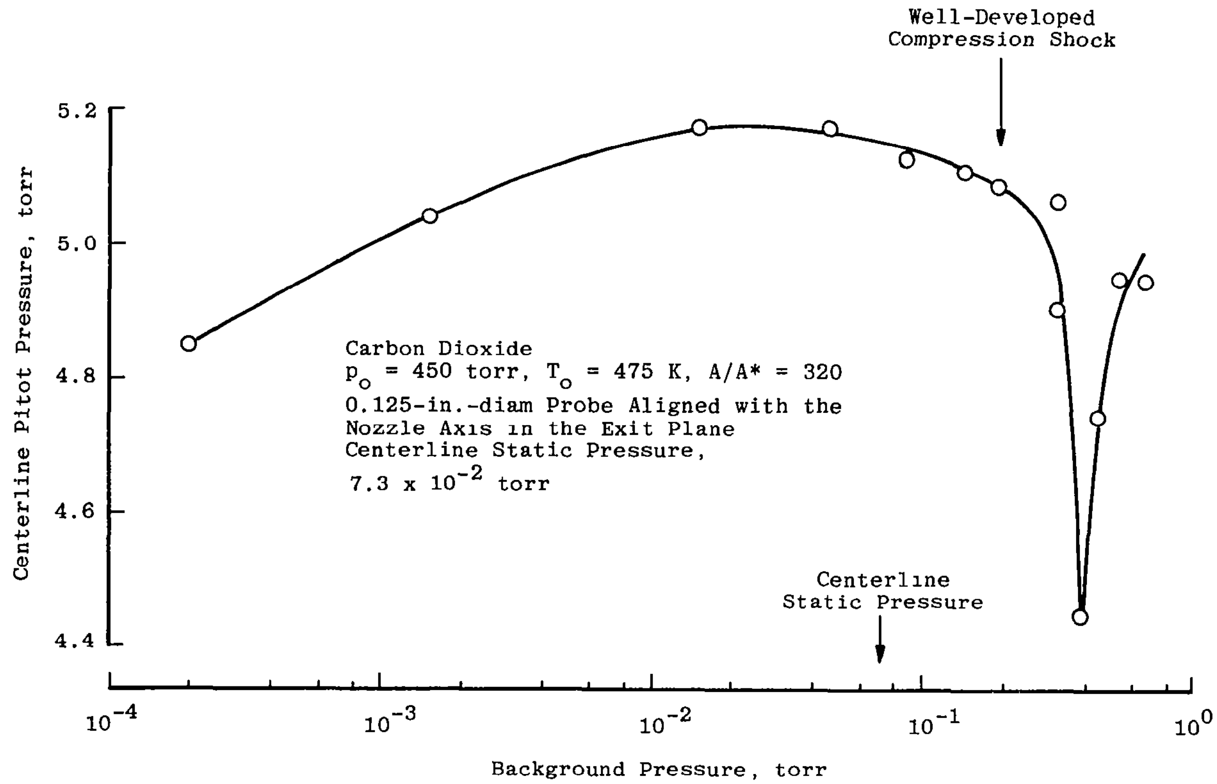

d. p_0 = 450 torr, T_0 = 475 K, A/A^* = 320
Figure 59. Concluded.

5.6 FREE-MOLECULE HEAT-TRANSFER PROBE MEASUREMENTS

Experimentation with the free-molecule heat-transfer probe has been divided into two phases, a static evaluation of the electronic control circuitry followed by an evaluation of the probe and control circuitry in a nozzle plume.

Two probes were constructed to permit a critical evaluation to be made of probe construction techniques and also the operation of the electronic control circuitry. One probe had a 1/4-in.-long (0.635-cm), 1×10^{-4}-in.-diam (2.54×10^{-4}-cm) wire and had a cold resistance of about 240 ohms. The other probe had a 2×10^{-4}-in.-diam (5.08×10^{-4}-cm) wire of similar length with a cold resistance of approximately 44 ohms. Tests with these probes indicated that the electronic control system was able to maintain control over the power delivered to the wire.

A probe with a 0.125-in.-long (0.328-cm), 2×10^{-4}-in.-diam (5.08×10^{-4}-cm) wire was then attached directly to 0.125-in.-diam (0.318-cm) pitot probe such that there was a 0.33-in. (0.84-cm) radial separation between the two probes. With this probe configuration, it was possible to measure heat transfer, adiabatic wall temperature, and pitot pressure simultaneously. In the initial operation of this probe configuration with the A/A* = 16 nozzle, i.e. p_0 = 10.8 torr, T_0 = 487 K, the hot wire was operated without using the end thermistors and without corrections being made for radiation losses. At each position in the nozzle plume, the resistance of the wire was measured at each of five different power levels to the wire. These wire resistances were plotted as a function of power level (Fig. 60), and the heat-transfer coefficient was determined from the slope of the variation, while the adiabatic wall temperature was derived from the intercept and the experimentally determined relationship between wire resistance and temperature. The radial profiles of heat transfer and adiabatic wall temperature derived in this manner are presented in Fig. 61. Radial profiles of the normalized heat-transfer coefficients at three axial stations are compared with similar pitot pressure profiles in Fig. 62.

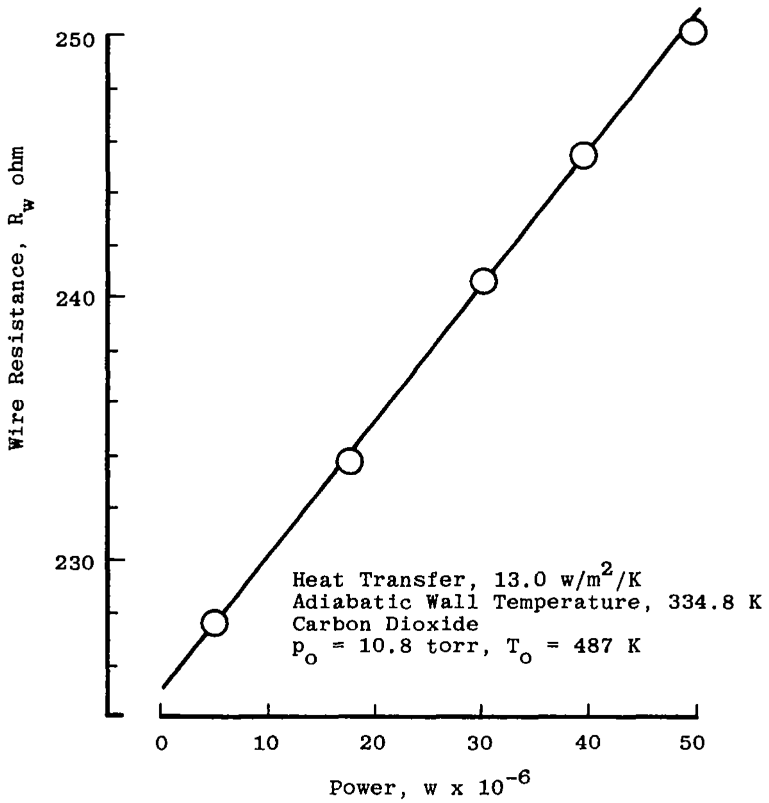

Figure 60. Wire resistance as a function of applied power.

Because of the absence of radiation corrections, these are not absolute measurements. However, it can be seen from Fig. 62 that the hot-wire probe accurately delineates the extent of the core flow and the initial portions of the plume shear layer.

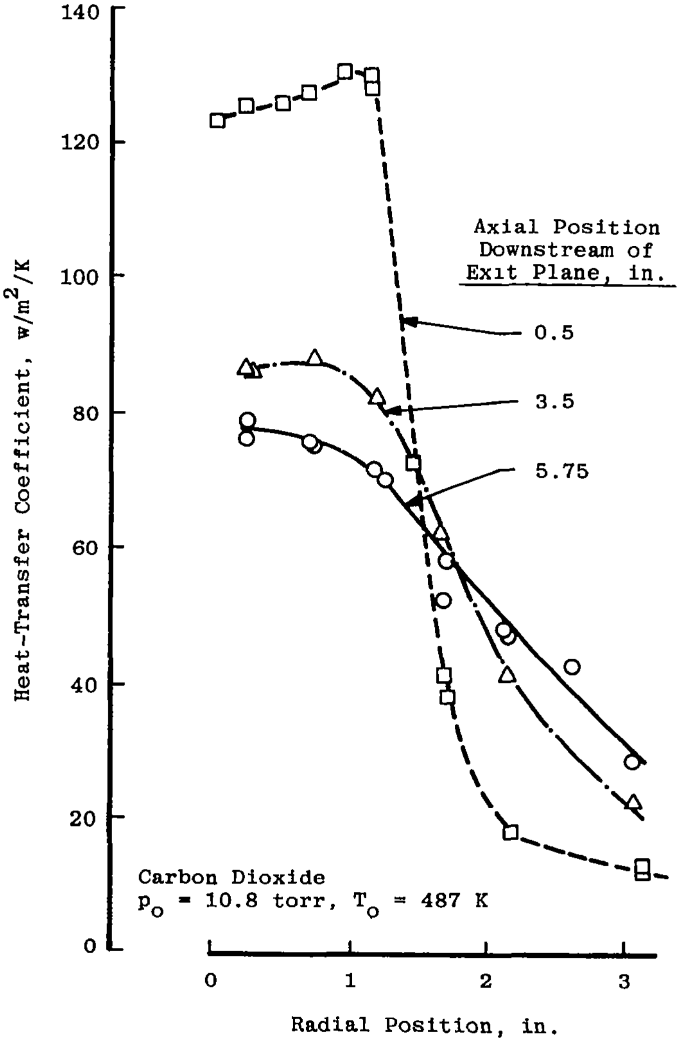

a. Heat-transfer coefficient

Figure 61. Free-molecule heat-transfer probe measurements.

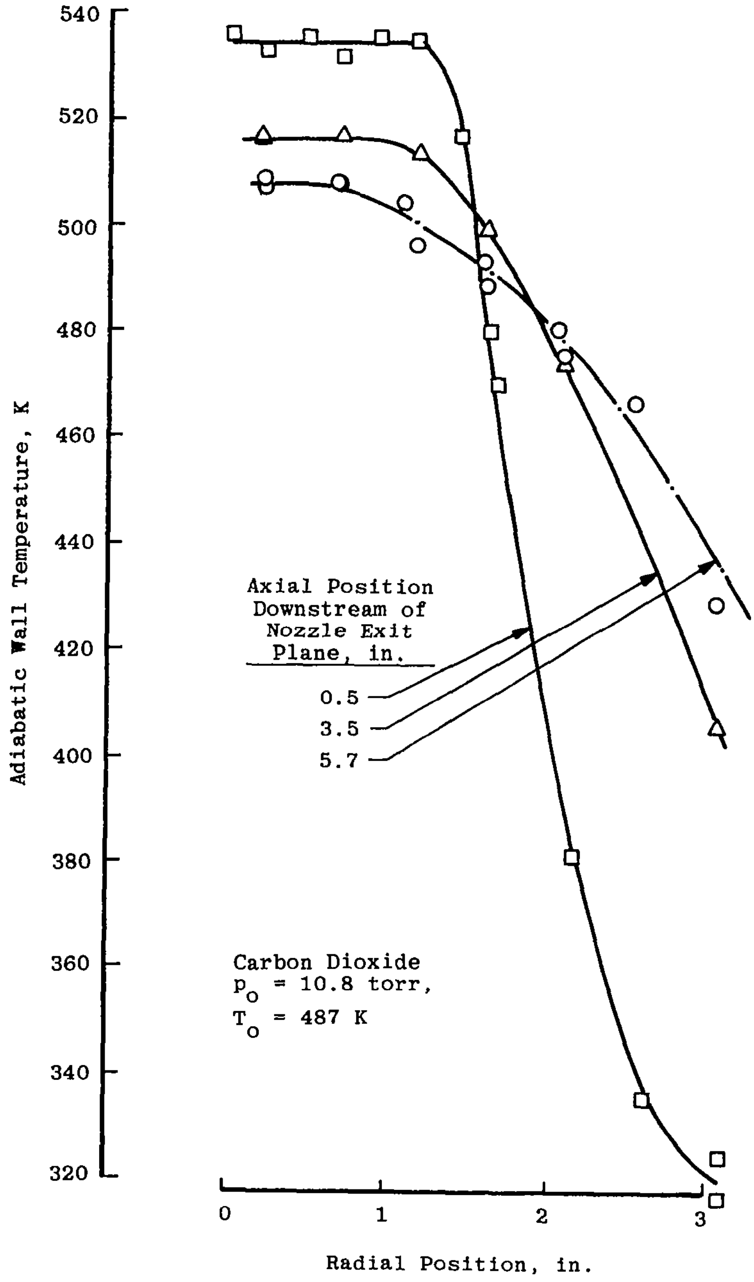

b. Adiabatic wall temperature
Figure 61. Concluded.

This attempt to adapt the probe configuration, successfully developed by Gottesdiener (Ref. 39) for unheated flows, to the present requirement for heated flows, i.e. $T_0 = 500$ K, revealed that the radiation loss from the small thermistors used to control wire temperature was the limiting factor in probe operation. In the initial design of the probe, it had not been anticipated that the radiation loss from these 0.005-in.-diam (0.0127-cm), 600 K thermistors would be a major factor in the operation of the probe. Further experimental studies will be required before this probe can be applied to the accurate measurement of flow field properites in a heated nozzle flow expanding into a vacuum.

Despite the limitations of the present probe configuration, the adiabatic wall temperature and heat-transfer measurements indicate that (1) the radial extent of the central core flow is the same for the pitot pressure, heat transfer, and adiabatic wall temperature measurements; (2) the form of the heat-transfer variation in the central core flow is the same as for the pitot pressure, i.e. a small increase in value with increased radial distance from the nozzle axis; and (3) the adiabatic wall temperature, which can be related directly to flow-stagnation temperature, is constant in the central core-flow region.

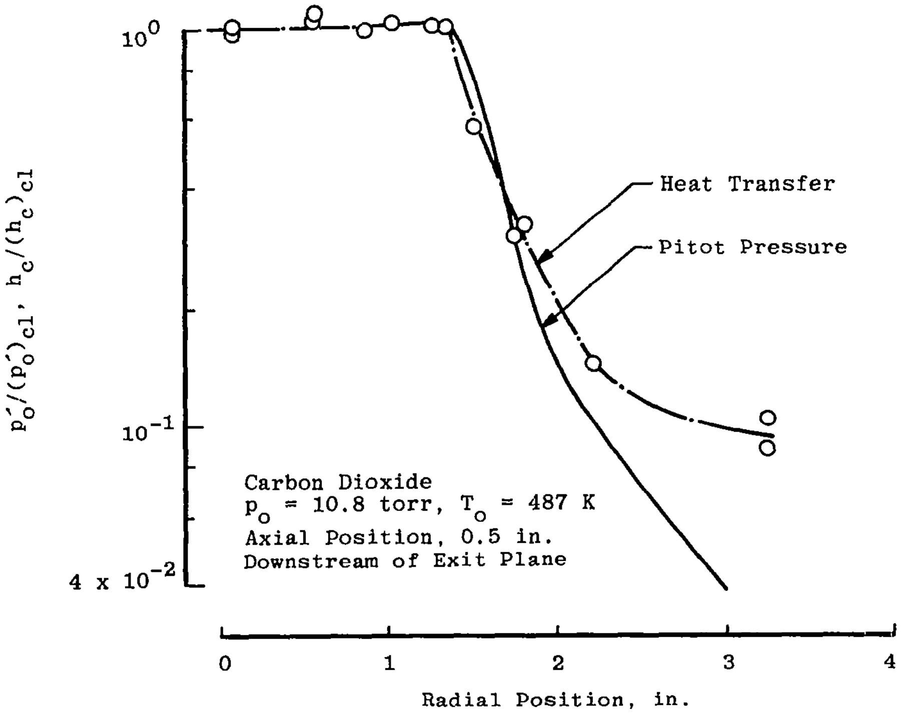

a. Axial position, 0.5 in. downstream of nozzle exit plane
Figure 62. Heat-transfer and pitot pressure profiles.

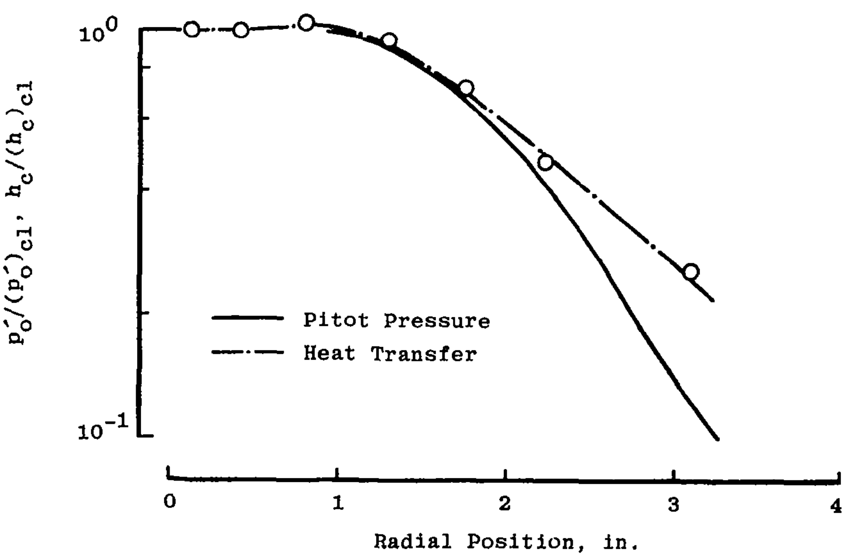

b. Axial position, 3.5 in. downstream of nozzle exit plane

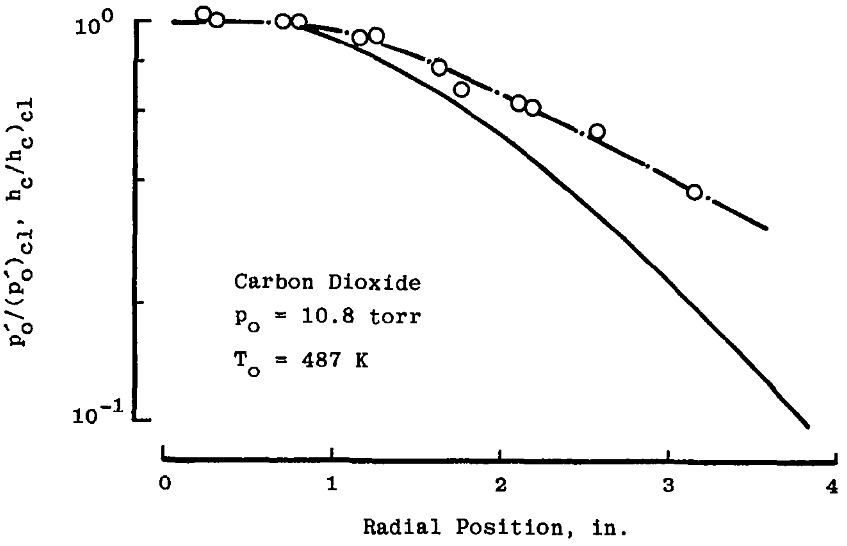

c. Axial position, 5.7 in. downstream of nozzle exit plane
Figure 62. Concluded.

It may be inferred from the constancy of T_0 in the core-flow region that the flow velocity is also constant, a fact which supports one of the assumptions that has been made in the present study, i.e. isentropic flow in the central core. It has been noted earlier that there is a similarity in the form of number density and pitot pressure profile in the core-flow region; i.e., both indicate an off-axis peak. On the basis of this comparison, it was concluded that the off-axis peak was not an artifact of a probe/flow interaction but was a reflection of a change in a flow property, i.e. number density. Additional support for this conclusion is given by the heat-transfer measurements which show a similar off-axis peak.

5.7 ELECTRON BEAM FLUORESCENCE MEASUREMENTS

5.7.1 Number Density

Carbon dioxide number density measurements were accomplished with the use of both 0.5-mm and 1-mm-wide spectrometer entrance and exit slits; the larger width was used in low-density regions to improve the signal-to-noise ratio. Wavelengths used were 3377.77 Å, very near the peak of the CO_2^+ band at the low-temperature range of interest, and 3368.8 Å for the background. Calibration factors for the number density measurements were determined at each nozzle condition from the centerline axial number density variation derived from the measured values of stagnation temperature, stagnation temperature, and pitot pressure. At each nozzle condition, the electron beam calibration factor was selected on the basis of a calculated value of number density close to the nozzle exit plane. The form of the variation of the measured number density variation with axial distance downstream of this matching point is in good agreement with the calculated variation (Fig. 63).

It was determined that the radial variation of number density at each axial position was symmetrical about the centerline. Examples of the form of radial profiles of number density are presented in Fig. 64. These profiles show that at each axial station, the maximum number density occurs at the edge of the central high-density core region rather than on centerline. As has been noted in the discussion of the pitot pressure and heat-transfer measurements, similar off-axis peaks are present in these probe measurements. It had been concluded that such peaks are not an artifact of the method for making the measurement but are indicative of changes in the flow field properties in the core-flow region. Smoothed spatial maps of constant number density have been derived from radial profiles of this type (i.e. Fig. 64) and are presented in Fig. 65 for two of the nozzles.

5.7.2 Rotational Temperature

Both continuous wavelength band scans and stepped wavelength scans for each nozzle were recorded using 0.5-mm spectrometer slits. Data for the $A/A^* = 44.4$ nozzle as

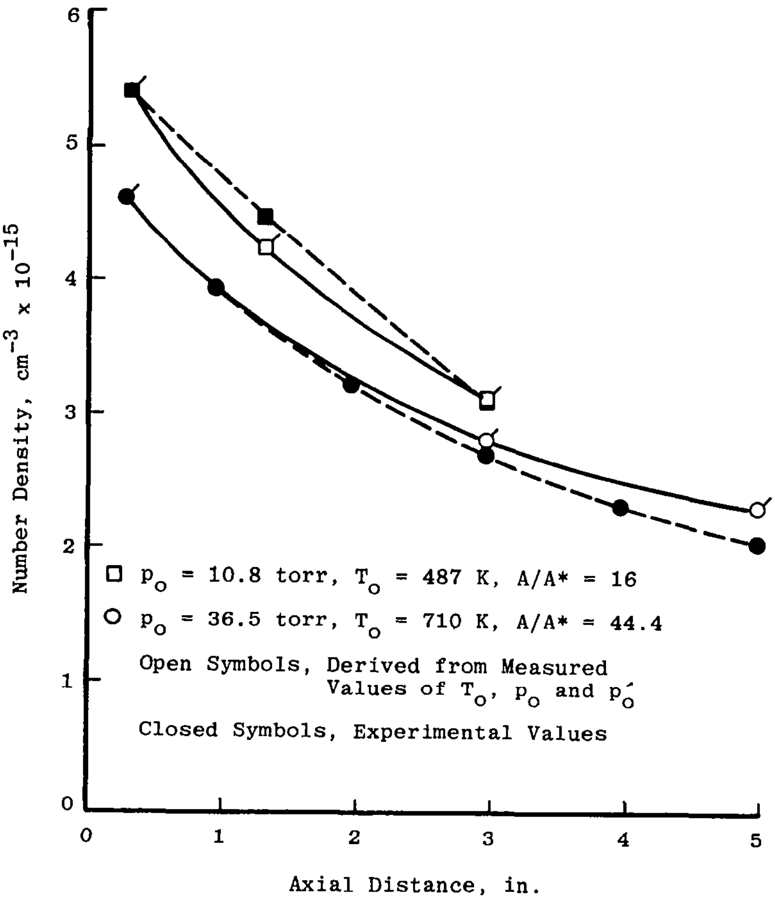

Figure 63. Number density on axial centerline.

obtained by the stepped wavelength method are presented herein. A continuous scan obtained just downstream of the exit plane, where the rotational temperature was calculated to be 108 K, is presented in Fig. 66. After selecting various values of constant background, the value indicated in the figure led to a close band-shape match with the 100 K synthetic curve, as shown in Fig. 67.

In addition to the 3377.77 Å and 3368.8 Å wavelengths, the stepped mode measurements included photon rate determinations at 3380.30 Å. Occasional dark count rates were measured by masking the entrance slit. Band intensity ratios at the 3377.77 Å and 3380.30 Å wavelengths as functions of CO_2 rotational temperature calculated from the synthetic spectra (Ref. 44) are given in Fig. 68. Upon reducing the stepped scan data on axial centerline using an underlying background assumed proportional to the difference between the count rate at 3368.8 Å and the dark count rate, the resultant CO_2 rotational

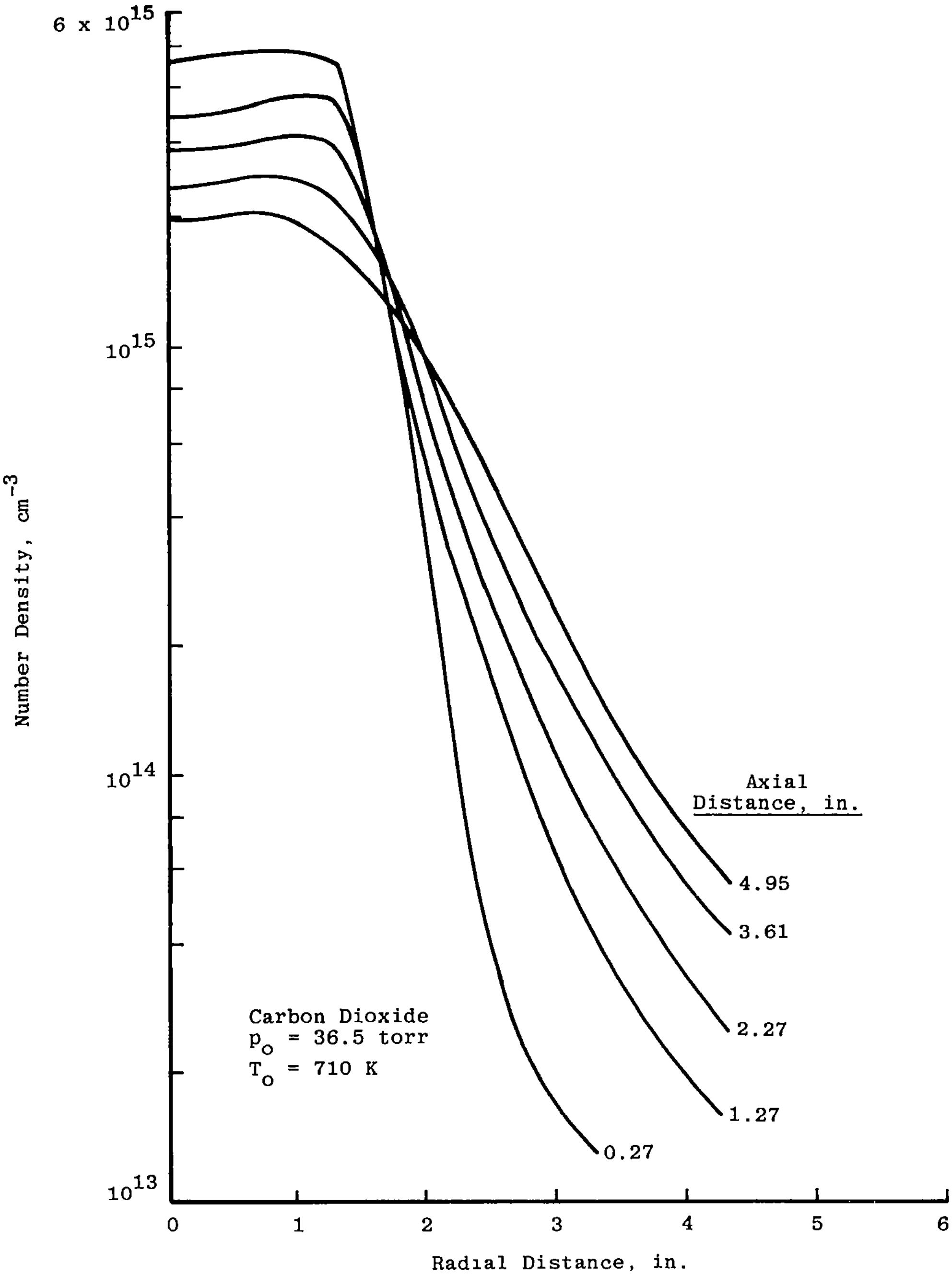

Figure 64. Number density radial profiles.

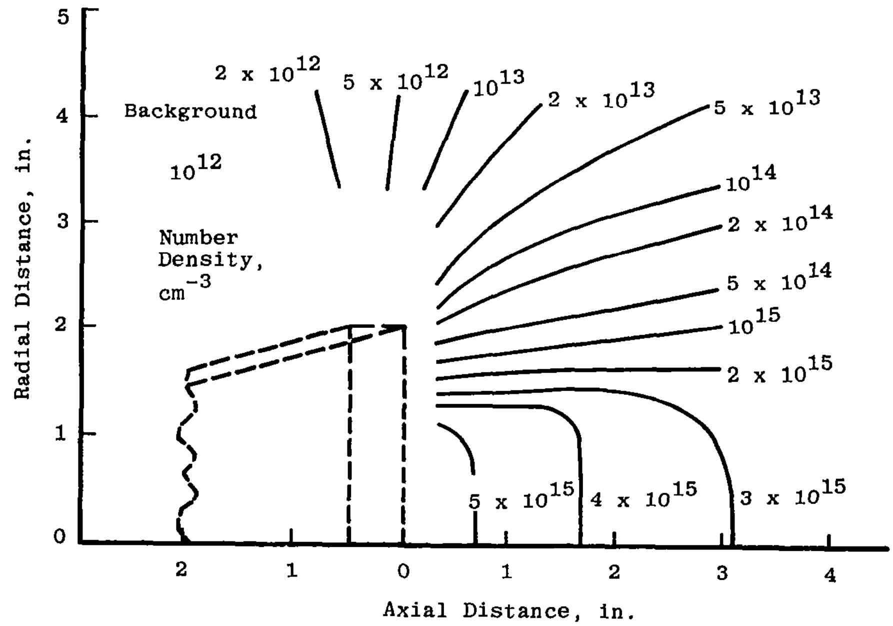

a. p_0 = 10.8 torr, T_0 = 487 K

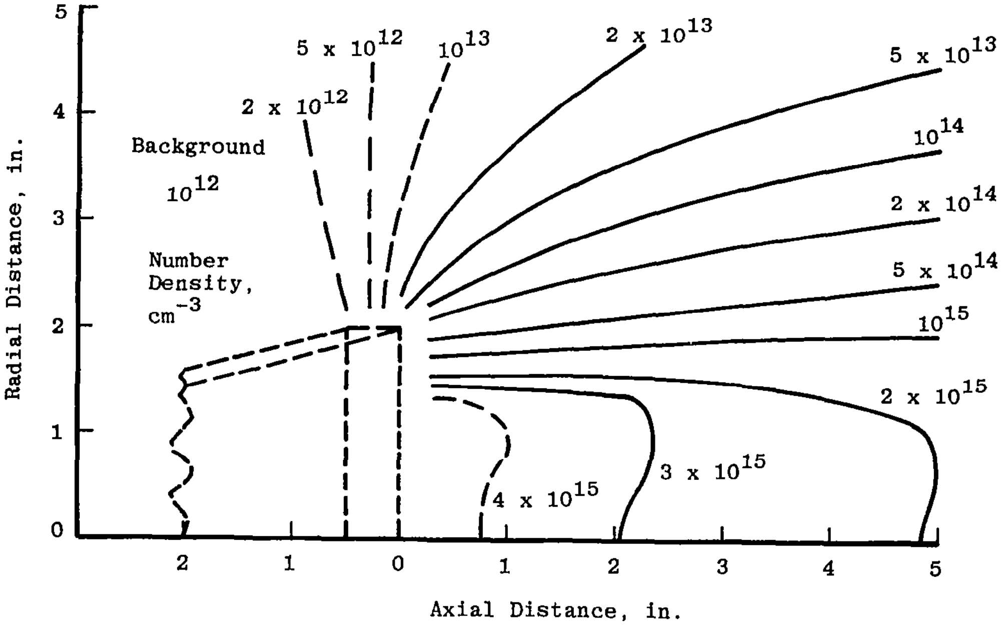

b. p_0 = 36.5 torr, T_0 = 710 K

Figure 65. Spatial map of constant CO_2 number density values.

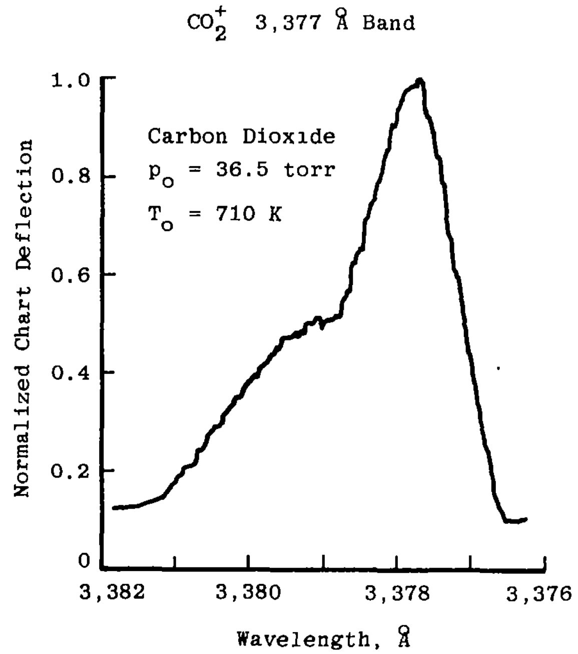

Figure 66. Continuous wavelength CO_2^+ scan near exit plane centerline.

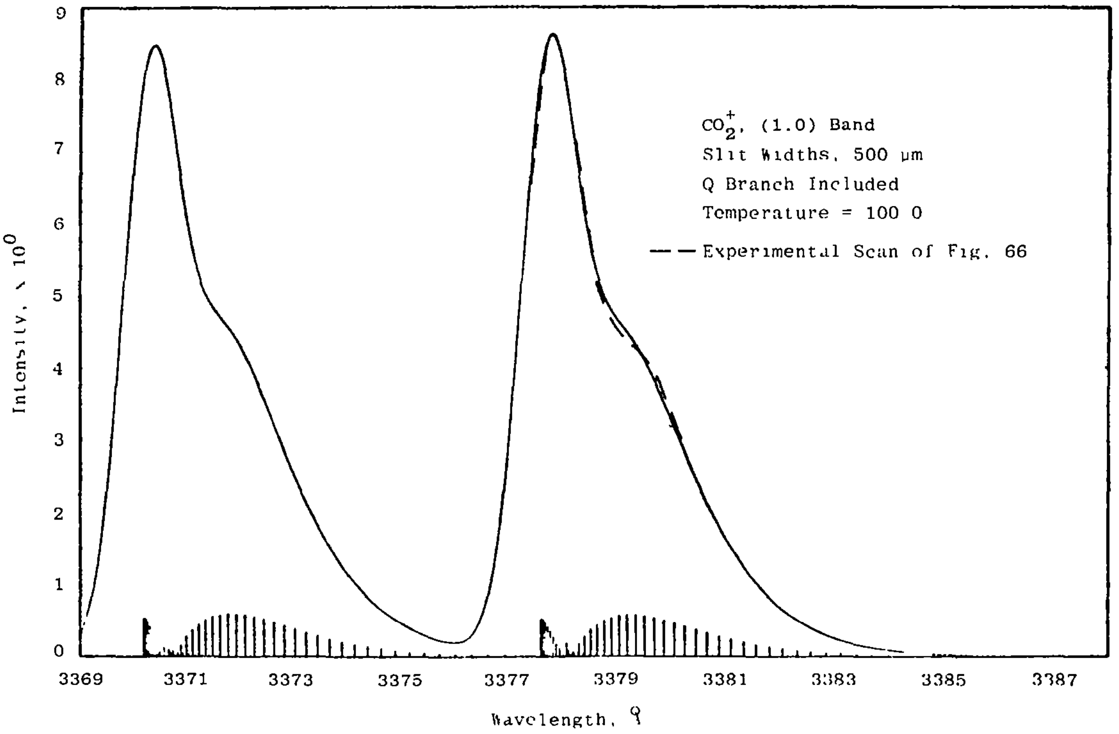

Figure 67. Comparison of 108 K experimental scan with 100 K synthetic spectra.

temperatures decreased with increasing axial distance at a greater rate than that calculated from other experimental measurements. As a result, the data was then reduced using a temperature-dependent underlying background whose form was determined from the measured axial centerline background values at 3368.8 Å and from the analytically predicted centerline temperature values. When completed, the average of the measured centerline values equaled the average of the analytical values. An iterative procedure was necessary to reduce the three-wavelength data using this temperature-dependent-background approach. It should be noted that a temperature-dependent background implies the existence of fluorescence from another transition underlying the band of interest. Such fluorescence was clearly seen in extended wavelength scans; one moderately strong band peak occurs near 3,389 Å. A more thorough understanding of the fluorescence occurring in this wavelength region is needed. Also, the degree of existence of the band's Q branch is as yet unknown. In the meantime, it appears that the adjoining band at 3,370 Å has lower underlying background fluorescence and is preferable for diagnostic measurements of this type.

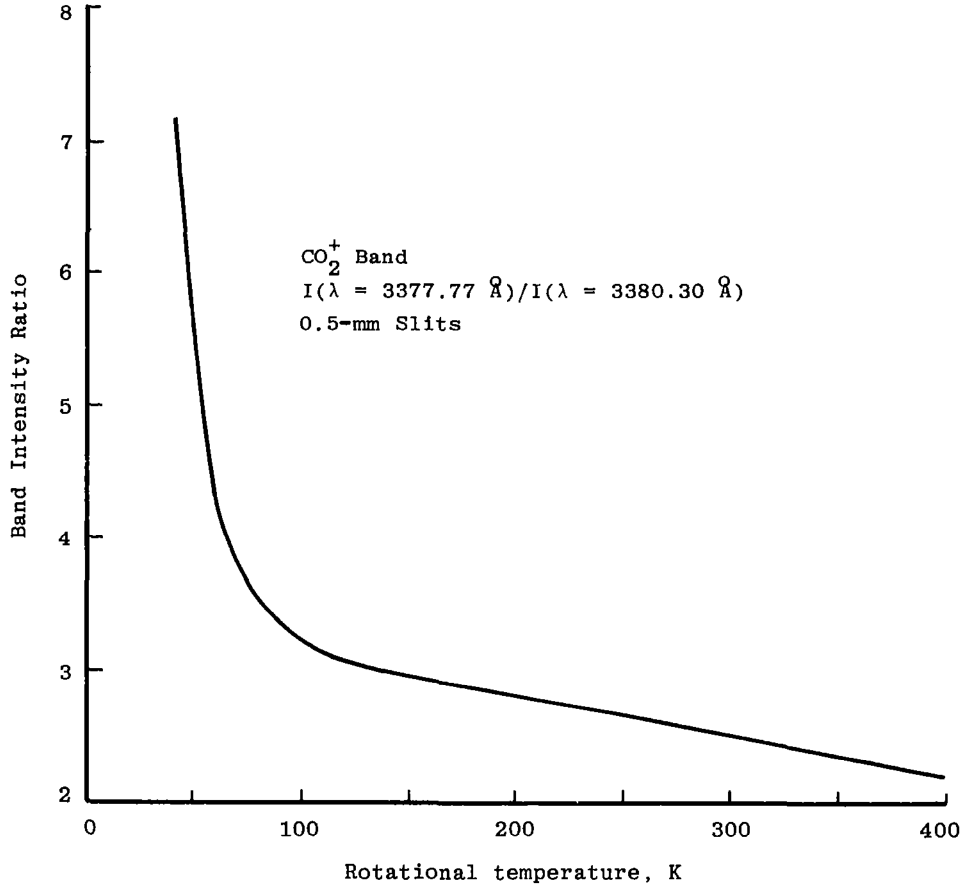

Figure 68. Band intensity ratio versus CO_2 rotational temperature.

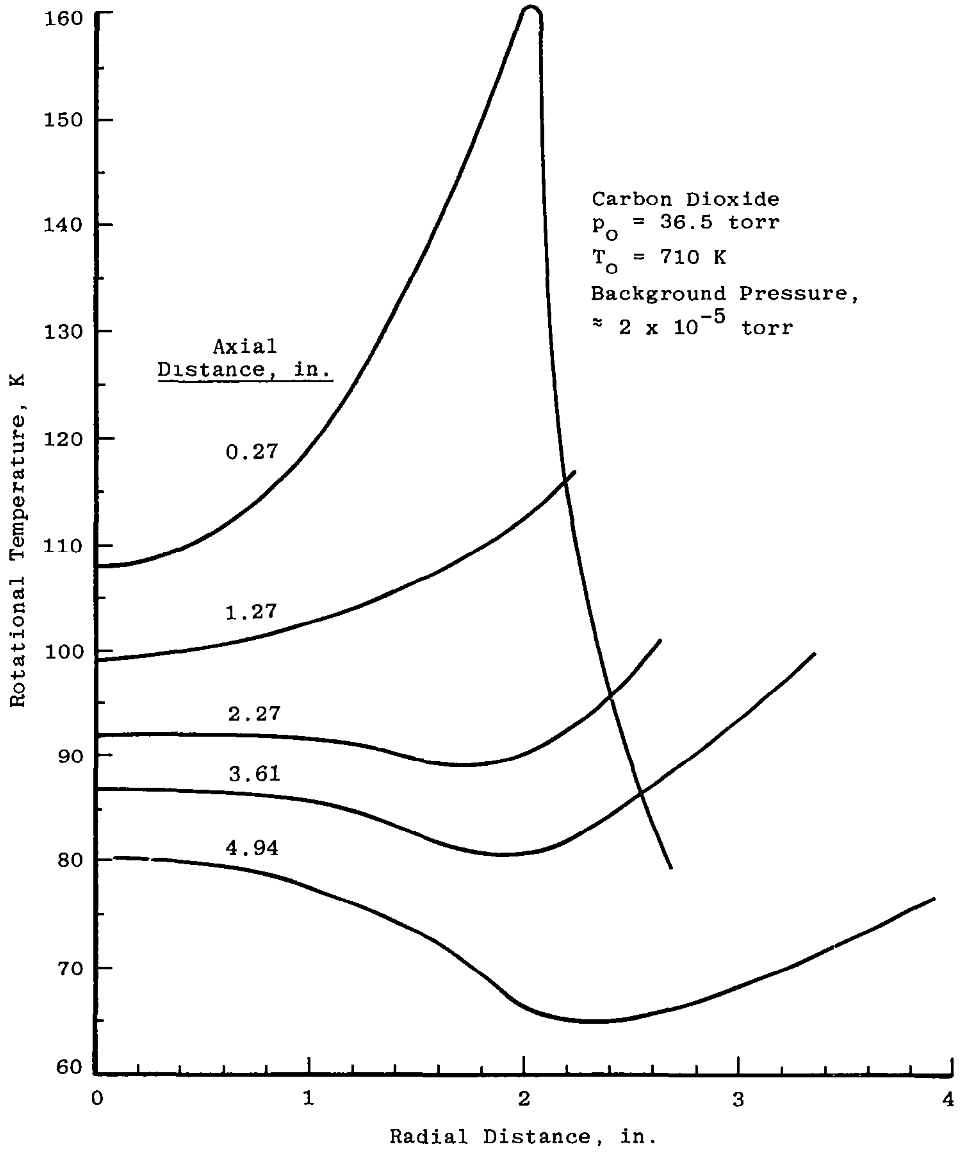

Figure 69. Radial profiles of CO_2 rotational temperature.

Radial profiles of rotational temperatuare at a number of axial stations are presented in Fig. 69. The radial profile close to the nozzle exit plane, 0.27 in. (0.69 cm) (Fig. 69) is characterized by a pronounced off-axis peak. The increase and subsequent rapid decrease in rotational temperature with increasing radial distance is indicative of significant changes in the state of the nozzle boundary layer as it expands into a hard vacuum. Further, more detailed measurements of rotational temperature in this flow region would be required to more fully define the flow in this area of the plume. A smoothed spatial map of rotational temperature is presented in Fig. 70.

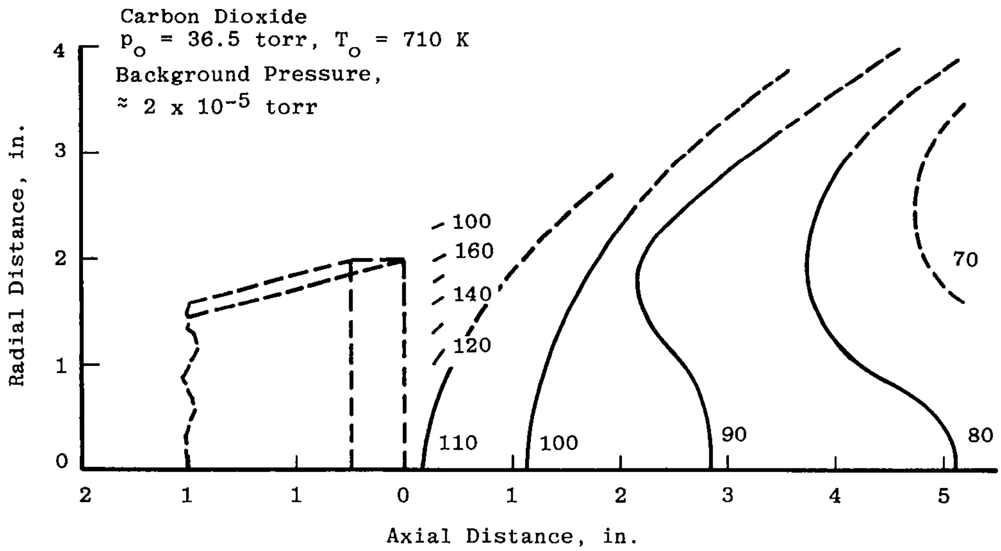

Figure 70. Spatial map of constant CO_2 rotational temperature values.

6.0 CONCLUSIONS AND RECOMMENDATIONS

The validity of the recently developed electron beam (Ref. 44) fluorescence technique to measure number density and rotational temperature in low-density carbon dioxide plumes has been established in this experimental study.

By combining conventional pitot and free-molecule pressure probes with a low-range absolute pressure transducer and a remotely controlled rotary positioning device, it has been possible to make measurements of flow angle inside, downstream, and upstream of the nozzle. It has also been shown that accurate measurements of dynamic pressure can be made from 1×10^{-4} to 1 torr with this system. The successful development and implementation of this system demonstrates that meaningful flow field measurements can be made effectively and efficiently in the nozzle backflow region. Suitably designed probe/transducer configurations of this type could be used to make measurements in the plumes generated by rocket motors in ground-based test facilities.

Attempts to measure the variation of speed ratio in the free-molecule flow regime were not completely successful as the form of the measured pressure variation did not conform to the theoretical form developed by Hughes (Ref. 28). Tests at known speed ratios in free-molecule flow (developed in a sonic orifice expansion) gave indications of these deviations from theory. Thus, to realize the full potential of these simple inexpensive probes, complete calibrations in well-defined free-molecule flows will be required.

It has been shown that by combining a small state-of-the-art quartz crystal microbalance (cooled with liquid nitrogen) with a rotary positioning device measurements of mass flux can be made in the forward and backflow regions of the plume in an effective and efficient manner. This approach has eliminated errors in mass flux measurements that result from misalignment of the sensing crystal with the incident flow since the probe can be aligned with the flow vector (derived from other measurements with the pitot and free-molecule pressure probes).This represents an improvement over previous studies of this type (e.g., Refs. 4 and 31) where many QCM's were positioned at fixed positions and angles with respect to the nozzle axis.

Detailed studies of flow angle in the region of the lip have shown that the local flow angle in the shear layer is not parallel to the local nozzle wall angle but is directed towards the wall. This confirms experimentally for the first time Bird's (Ref. 47) theoretical predictions. Boundary-layer codes which do not account for this flow-angle effect will not be applicable when used to predict flow into the nozzle backflow region.

These same flow-angle studies indicate that the source of flow into the backflow region is confined to a thin layer very close to the nozzle wall. Again, this experimental finding is in agreement with theoretical predictions that have been made by Bird (Ref. 47).

Changes in lip geometry from thick to thin do result in small changes in flow angle in the backflow, supporting the experimentally observed mass flux and number density observations of Bailey et al.'s study.

Flow-angle measurements in regions of high shear have been found to be susceptible to probe/flow interaction effects and care must be exercised in the selection of a probe for studies of this type to ensure that such effects are minimized.

It can be concluded on the basis of the number density, heat transfer, and pitot pressure measurements that, in the regions of high density in the core flow, there are no detectable flow perturbations that can be attributed to the presence of the probe.

Significant effects upon the flow of gas into the backflow region have been found when changes have been made in the degree of cryopumping in this region, in the absence of significant changes in the background pressure. This indicates that while it is necessary to simulate the true background pressure, it is also necessary to simulate the gas pumping environment. Changes in the exit-plane flow characteristics as a result of changes in the chamber background pressure in the presence of full-chamber cryopumping indicate that measurable changes occur in the flow angle at pressures significantly less than the centerline static pressure.

Increases in the value of wall static pressure close to the nozzle lip occur only after the nozzle recompression shock is present in the nozzle exit plane. When this occurs, significant changes have already occurred in the exit-plane flow characteristics making the use of a constant value of wall static pressure as a measure of exit-plane flow quality inappropriate.

The use of a free-molecule heat-transfer probe to measure flow field properties both inside and outside the nozzle was not wholly successful. The primary reason for the lack of success was a large unforeseen radiation loss associated with the small thermistors, 0.005-in.-diam (0.0127-cm), used to control wire temperature. Although it was not possible (because of the radiation loss) to make absolute measurements of heat transfer and wire temperature, it has been shown that the radial profiles of the uncorrected values are consistent with the electron beam and pitot probe profiles. The results of this limited experimental investigation with the free-molecule heat-transfer probe were such that further developmental work on wire temperature control through the use of smaller thermistors would be warranted. The successful development of a free-molecule heat-transfer probe would result in the ability (when used in conjunction with a pitot probe) to define nozzle boundary flow properties upstream of the nozzle exit plane.

The present investigation was limited to obtaining experimental measurements of the flow field characteristics of the nozzle and the nozzle plume. A brief review of these measurements suggest areas for further study.

The rotary QCM, free-molecule pressure probe and pitot pressure probe have been shown to be well suited to the measurement of mass flux, flow angle, and dynamic pressure. Based on the probe configurations developed in this study, standard probes of this type should be designed and fabricated such that they can be used in future plume studies in any of the AEDC space chambers.

The free-molecule pressure probe has the potential for measuring not only flow angle but also speed ratio. To provide for the ability to define speed ratio, each of these probes will need to be calibrated in a flow of known properties. This can be accomplished in the expanding flow from a sonic orifice into a vacuum.

Further development of a means for controlling the wire temperature of the free-molecule heat-transfer probe should be pursued, because of the value such a probe would have in defining the flow field properties in the nozzle boundary layer.

A low-load thrust balance should be developed to determine the effect of changing ambient pressure on nozzle thrust under simulated space conditions.

A review and analysis of all ground-based experimental studies of rocket and pure-gas plumes should be completed with a view to establishing the factors which have a dominant effect upon the flow of gas into the backflow region.

Whether any of the existing nozzle boundary-layer codes can successfully predict the nozzle flow properties obtained in the present study should be determined.

Whether any of the Monte Carlo-based computer codes can predict the measured mass flux in the backflow region as a function of background pressure and background cryopumping should be investigated.

REFERENCES

1. Hoffman, R. J. et al. "Plume Contamination Effects Prediction—The Contam Computer Program, Version II." McDonnell Douglas Astronautics Co. AFRPL-TR-73-46, August 1973.

2. Williams, W. D. et al. "Experimental Study of Monopropellant Hydraxine Thruster Exhaust." *Proceedings of the JANNAF 10th Plume Technology Meeting*, Vol. II, San Diego, California, September 1977, pp. 209-225.

3. Williams, W. D. et al. "Experimental Study of the Plume Characteristics of an Aged Monopropellant Hydrazine Thruster." AEDC-TR-79-2, (AD-A068326), April 1979.

4. Alt, R. E. et al. "Bipropellant Engine Plume Contamination Program, Vol. I." AEDC-TR-79-28 (AD-A077435), December 1979.

5. Pipes, J. G. et al. "SRM Plume Simulation-Flow Field of a Mach 7.0 Nitrogen Expansion into Vacuum." CPIA Pub 357, *Proceedings of the JANNAF 13th Plume Technology Meeting*, Johnson Space Center, Houston, Texas, April 27-29, 1982.

6. Bailey, A. B. et al. "Measurements of Flow-Field Properties in the Forward-and-Back-Flow Region of a Nozzle Plume." CPIA Pub 384, *Proceedings of the JANNAF 14th Plume Technology Meeting*, China Lake, California, November 15-17, 1983.

7. Whitfield, D. L., "Viscous Effects in Low-Density Nozzle Flows." AEDC-TR-73-52 (AD-761489), June 1973.

8. Edwards, R. M. "Low-Density Flows Through Tubes and Nozzles." *Proceedings of the Tenth Symposium of Rarefied Gas Dynamics*, Vol. 51, Part I: Progress in Astronautics and Aeronatuics, AIAA, New York, 1977.

9. Busby, M. R. and Gilley, B. W. "Simulation of the Ionosphere Utilizing Microwave Ion Generation Techniques." AEDC-TR-71-254 (AD-734256), December 1971.

10. Lewis, J. W. L., Price, L. L., and Powell, H. M. "Electron Excitation Cross Sections of N_2^+ B^2 Σ_u^+, NI, and NII States and Their Temperature Dependence." Physical Review A, Vol. II, No. 4, April 1975, pp. 1214-1222.

11. Price, L. L. and Lewis, J. W. L. "Collisional Quenching of Atomic and Molecular Nitrogen: I, Experimental Results." AEDC-TR-75-151 (AD-A018780), December 1975.

12. Lewis, J. W. L. et al. "Nitrogen Condensation in a Sonic Orifice Expansion Flow." AEDC-TR-74-36 (AD-783254), July 1974.

13. Lewis, J. W. L., Price, L. L., and Kinslow, M. "Rotational Relaxation of N_2 in Heated Expansion Flow Fields." *Proceedings of the Ninth International Rarefied Gas Dynamics Symposium*, Vol. I, DFVLR-Press, Porz-Wahn, West German, 1974, pp. B.17-1—B.17-9.

14. Williams, W. D. et al. "Experimental Study of the Plume Characteristics of a New Monopropellant Hydrazine Thruster." AEDC-TR-79-54 (AD-A080556), January 1980.

15. Rothe, D. E. "Electron-Beam Studies of Low Reynolds-Number Flows Inside a DeLaval Nozzle." AIAA Paper No. 70-810, Presented at the Third Fluid and Plasma Dynamics Conference, Los Angeles, California, June 29-July 1, 1980.

16. Potter, J. L. and Carden, W. H. "Design of Axisymmetric Contoured Nozzles for Laminar Hypersonic Flow." *Journal of Spacecraft and Rockets*, Vol. 5, September 1968, pp. 1095-1100.

17. Whitfield, D. L. et al. "Specie Number Density, Pitot Pressure, and Flow Visualization in the Near Field of Two Supersonic Nozzle Banks Used for Chemical Laser Systems." AEDC-TR-73-11 (AD-760132), May 1973.

18. MacDermott, W. N., Shirley, B. H., and Dix, R. E. "Low Density Boundary Layer Control by Liquid Hydrogen Cryopumping." *Proceedings of the Fourth International Symposium on Rarefied Gas Dynamics*, Vol. II., Academic Press, New York, 1966, pp. 209-224.

19. Hickman, R. S. "An Experimental Study of Hypersonic Rarefied Flow over a 10-deg Cone." *Proceedings of the Fifth International Symposium on Rarefied Gas Dynamics*, Vol. II., Academic Press, New York, 1967, pp. 1067-1085.

20. Wada, I. "Experimental Study of Hypersonic Low Density Flow by Using the Electron Beam Fluorescence Method." *Proceedings of the Fifth International Symposium on Rarefied Gas Dynamics*, Vol. II., Academic Press, New York, 1967, pp. 1193-1204.

21. Broadwell, J. E. and Rungaldier, H. "Structure of the Shock Layer on Cylinders in Rarefied Gas Flow." *Proceedings of the Fifth International Symposium on Rarefied Gas Dynamics*, Vol. II., Academic Press, New York, 1967, pp. 1147-1160.

22. Smithson, H. K., Price, L. L., and Whitfield, D. L. "Wind Tunnel Testing of Interaction of High Altitude Rocket Plumes with the Free Stream." AEDC-TR-71-118 (AD-731141), September 1971.

23. Abraham, O. et al. "Gasdynamics of Very Small Laval Nozzles." *Physics of Fluids*, Vol. 24, No. 6, June 1981, pp. 1017-1031.

24. Stephenson, W. B. "Use of the Pitot Tube in Very Low Density Flows." AEDC-TR-81-11 (AD-A106374), October 1981.

25. Graybeal, G. A. "Impact-Probe Rarefaction Effects Measured in CO_2 Free Jet Expansions." University of Virginia UVA-ER-741-820, March 23, 1982.

26. Potter, J. L., Kinslow, M. K., and Boylan, D. E. "An Influence of the Orifice on Measured Pressures in Rarefied Flows." *Proceedings of the Fourth Rarefied Gas Dynamics Symposium*, Vol. II., Academic Press, New York, 1966, pp. 175-194.

27. Pollard, M. G. "Interpretation of Impact Pressure Rarefied Gas Flow." *Proceedings of the Sixth Rarefied Gas Dynamics Symposium*, Vol. I., Academic Press, New York, 1968, pp. 811 - 834.

28. Patterson, G. N. "Theory of Free-Molecule Orifice-Type Pressure Probes in Isentropic and Non-Isentropic Flows." Institute of Aerophysics, University of Toronto, UTIA-R-41 (Revised), April 1959.

29. Hughes, P. C. "Theory for the Free-Molecule Impact Probe at an Arbitrary Angle of Attack." UTIAS-R-103, May 1965.

30. Ashkenas, H. and Sherman, F. S. "The Structure and Utilization of Supersonic Free Jets in Low Density Wind Tunnels." *Proceedings of the Fourth International Symposium on Rarefied Gas Dynamics*, Vol. II., Academic Press, New York, 1966, pp. 84-105.

31. Chirivella, J. E. "Mass Flux Measurements and Correlations in the Backflow Region of a Nozzle Plume." AIAA Paper No. 73-731, Presented at Eighth Thermophysics Conference, Palm Springs, California, July 16-18, 1973.

32. Sherman, F. S. "A Low-Density Wind-Tunnel Study of Shock-Wave Structure and Relaxation Phenomena in Gases." NACA TN 3298, July 1955.

33. Wong, H. "Design and Development of a Free-Molecule Heat-Transfer Probe." University of California, Berkeley, Report No. HE-150-143, October 15, 1956.

34. Laurmann, J. A. and Ipsen, I. C. "Use of a Free-Molecule Probe in High-Speed Rarefied Gas Flow Studies." WADC TR 57-440, October 1957.

35. Rajasooria, G. P. D. and Brundin, C. L. "Use of Hot Wire in Low-Density Flows." *AIAA Journal*, Vol. 9, May 1971, pp. 979-981.

36. Lord, R. G. "Hot-Wire Probe End-Loss Corrections in Low Density Flows." *Journal of Physics E*, Vol. 7, January 1974, pp. 56-60.

37. Lord, R. G. "The Dynamic Behavior of Hot-Wire Anemometers with Conduction End Losses." *Journal of Physics E*, Vol. 14, May 1981, pp. 573-578.

38. Muthoo, S. K. and Brundin, C. L. "Near Wake Flow Field Measurments Behind Spheres in Low Reynolds Number Hypersonic Flow." *Proceedings of Ninth International Symposium on Rarefied Gas Dynamics*, Vol. I, DFVLR-Press, Proz-Wahn, West Germany, 1974, pp. B.10-1 — B.10-10.

39. Gottesdiener, L. "Hot Wire Anemometry in Rarefied Gas Flow." *Journal of Physics E*, Vol. 13, September 1980, pp. 908-913.

40. Schaaf, S. A. and Talbot, L. "Mechanics of Rarefied Gases." *Handbook of Supersonic Aerodynamics*, Sec. 16, NAVORD Report 1488 (Vol. 5), February 1959.

41. Muntz, E. P., Abel, S. J., and Maguire, B. L. "Electron Beam Fluorescence Probe in Experimental Gas Dynamics." Supplement to IEEE Transaction on Aerospace, Vol. AS-3, 1965, pp. 210-222.

42. Williams, W. D. et al."Raman Scattering Diagnostics Development Using an Excimer/Dual Dye Laser System, I." AEDC-TR-83-15 (AD-B075604), July 1983.

43. Beylich, A. E. "Experimental Investigation of Carbon Dioxide Jet Plumes." *The Physics of Fluids*, 14, No. 5, May 1971, pp. 898-905.

44. Price, L. L., Lewis, J. W. L., and Lauer, M. R. "Development of Electron Beam and Laser-Induced Fluorescence Diagnostics for Plume Simulation Testing at AEDC." AEDC-TR-84-11 (AD-B082836), May 1984.

45. Lewis, J. W. L. and Williams, W. D. "Profile of an Anisentropic Nitrogen Nozzle Expansion." *The Physics of Fluids*, No. 19, No. 7, July 1976, pp. 951-959.

46. Williams, W. D. and Lewis, J. W. L. "Rayleigh Scattering Studies of CO_2 Expansion Flow Fields." AEDC-TR-75-146 (AD-A019386), December 1975.

47. Bird, G. A. "Breakdown of Continuum Flow in Freejets and Rocket Plumes." *Proceedings of the Twelfth International Symposium on Rarefied Gas Dynamics*, Vol. 74, Part II, Progress in Astronautics and Aeronautics, AIAA, New York, 1981, pp. 681-694.

48. Drzewiecki, R. F., Moselle, J. R., and Tsu, C. N. "Characterization of the Peacekeeper Post Boost Vehicle Rocket Exhaust Plumes." CPIA Pub 384,Vol. II, *Proceedings of the JANNAF 14th Plume Technology Meeting*, China Lake, California, November 15-17, 1983.

APPENDIX A

ESTIMATE OF UNCERTAINTIES

The estimated uncertainties in the measurements contained in the body of this report are presented in this appendix. The uncertainty estimates are summarized in Table A-1. Discussion of the reasoning leading to the estimates of uncertainty for the special instrumentation and diagnostic techniques are included. The quoted uncertainties are on the basis of one standard deviation.

QUARTZ CRYSTAL MICROBALANCE (QCM) DATA

Evaluation of the QCM data uncertainty will follow closely a similar analysis contained in Scott, H. E., Frazine, D. F., and Lund, E. G. "Bipropellant Engine Plume Contamination Study," presented at the Joint NASA/USAF International Spacecraft Contamination Conference, USAF Academy, Colorado Springs, Colorado, March 7-9, 1978. No attempt has been made to quantify the random error as there were insufficient repeat measurements. However, on the basis of measurements made in the backflow region of a bipropellant rocket motor (Ref. 4), it is unlikely that this error is in excess of ± 5 percent.

Systematic fractional error in the measured values of m can be estimated by differentiating the functional relationship between m and its parameters.

$$\dot{m} = \dot{m}\,(C_m, \Delta f, \phi, R, T_{QCM})$$

C_m—QCM calibration constant

$$(1/\dot{m})\,(\partial\dot{m}/\partial C_m)\,C_m = 0.15$$

This estimate in the uncertainty in C_m is based on a calibration of a similar QCM in a molecular beam facility.

> Δf—error in frequency measurement estimated to be 1 Hz or less. The noise equivalent mass flux resulting from this frequency change is estimated to be at least two orders-of-magnitude less than the measured value of m. The error associated with this frequency shift has been estimated to be 0.1.
>
> r—distance from the nozzle exit plane to QCM location. Error is estimated to be

$$(1/\dot{m})\,(\partial\dot{m}/\partial r)\Delta r = -2\Delta r/r = -0.07$$

ϕ—angle from plume axis to QCM location. Error is estimated to be

$$(1/\dot{m})\ (\partial\dot{m}/\partial\phi)\Delta\phi = -0.0752\ \Delta\phi \cong -0.15$$

T_{QCM}—QCM temperature; the error attributable to variation in T_{QCM} values is difficult to evaluate. Condensed mass does depend upon crystal temperature when the gas species being evaluated has a sufficiently high-vapor pressure to evaporate. In the present series of experiments, the crystal temperature is on the order of 80 K. At this temperature, the vapor pressure of CO_2 is so low that it has been assumed that the errors associated with changes in crystal temperature are so small that they can be ignored.

The systematic error associated with the mass flux measurement is

$$\begin{aligned}(\Delta\dot{m}/\dot{m})_S &= \pm\ [(0.15)^2 + (0.1)^2 + (0.07)^2 + (0.15)^2]^{1/2} \\ &= \pm\ 0.25\end{aligned}$$

The total error estimate (i.e. random plus systematic) is

$$(\Delta\dot{m}/\dot{m}) = \pm\ 0.30$$

ELECTRON BEAM DATA

The uncertainties associated with the electron beam number density and rotational temperature measurements are complex functions of the spectrometer slit width, the electron beam current and voltage fluctuations, the nozzle reservoir pressure and temperature fluctuations, the detector system sensitivity variations, nozzle spatial position errors, excited state collisional quenching, instrument dead-time corrections, the degree of rotational nonequilibrium, and the accuracies of the calculated molecular number densities for absolute calibrations. Consideration was given to the magnitudes of each of these error sources and the errors were then combined by standard procedures to give typical overall uncertainties.

Electron beam and nozzle reservoir operational fluctuations were estimated from the repeatability of the several centerline number density measurements taken for each radial profile; ± 1- to 2-percent random errors were found. Errors in radial flow field positions were negligible as a result of the highly symmetric flow field; axial positioning errors are estimated to result in individual number density measurement errors of ± 4 percent, but the averaging process followed in constructing the spatial number density and rotational temperature maps reduced these to insignificant levels on the maps. Quenching corrections, a strong function of number density, were as high as 30 percent for near exit-plane number density measurements. These corrections resulted in good agreement with calculated centerline values. However, the temperature dependency of the correction resulted in estimated errors of up to ± 5 percent. For the temperature measurement, the maximum estimated error because of quenching was ± 1 percent. The largest dead-time correction was 4 percent; negligible errors resulted from a 10-percent variation in the dead-time constant. In the rarefied portion of the flow field, data gate times were increased to reduce the random variations in the number of detected photons. Signal repeatability in these low-density regions indicated a ± 1-percent random error in addition to the electron beam and nozzle reservoir operational fluctuations. Based on the independent CO_2 ultraviolet Raman centerline number density measurements, absolute calibration accuracies are estimated to be ± 3 percent. Finally, estimates of rotational temperature in regions where rotational temperature measurements were not made resulted in number density uncertainties of ± 1 percent for 1-mm-slit cases and ± 5 percent for 0.5-mm-slit cases.

Upon combining the various errors, the overall uncertainty for number densities ranged from ± 6 to 9 percent. Temperature measurement uncertainties ranged from ± 4 to ± 6 percent.

PRESSURE DATA

The evaluation of the uncertainty in the basic pressure measurements is well defined since the absolute pressure transducers used in the present investigation are calibrated and compared with the base standard (cf. Table A-1). The absolute pressure transducers used in the present study, i.e. MKS Type 220 and Type 370, Datametrics Barocel, and Taber, cover the pressure range from 1×10^{-5} to 1×10^{3} torr. A continuous record of the output of these gages was maintained such that gage-to-gage comparisons in regions of pressure overlap could be made. In this way, any change in gage performance could be determined and accounted for. Bayard-Alpert and Schultz-Phelps ion gages together with the Granville-Phillips Convectron gage were also used for pressure measurements from 1×10^{-7} to 5×10^{-1} torr. These gages and controllers are normally calibrated for use with nitrogen, and therefore, have to be recalibrated if a gas other than nitrogen is used. In the present instance where carbon dioxide was the test gas, these gages were calibrated using the MKS Type 370 absolute pressure gage as the standard. In general, the measurements made with these nonabsolute pressure gages were not as critical as those that have been made with absolute gages. In the interpretation of any of the probe pressure measurements, account must be taken of the probe characteristics, e.g., temperature and Reynolds number, that can have an effect upon the measured pressure before any definitive interpretation of the measurement can be made.

Table A-1. Instrumentation Summary and Measurement Uncertainty

Parameter Desingation	Range	Instrument Type	Recording Device	Calibration Method	Uncertainty
Plenum Chamber Total Pressure	1 to 300	Strain-Gage Transducer	Digital Recording Voltmeter (DRVM)	Calibrated Curve from Comparison with Standard Transducer	± 0.25 percent
Plenum Chamber Total Temperature	300 to 1,000 K	Chromel®-Alumel® Thermocouple	DRVM	mv, Substitution Based on NBS Tables	± 3 percent
Nozzle Wall Temperature	300 to 1,000 K	Chromel®-Alumel® Thermocouple	DRVM	mv, Substitution Based on NBS Tables	± 3 percent
Nozzle Position	± 7.5 cm	Optical Encoder	DRVM	Received Calibrated	± 0.008 cm
Gas Density	10^{11} – 10^{16} cm^{-3}	Electron Beam	Photon Counter	Theoretical Nozzle Flow	± 6 to 9 percent
Rotational Temperature	N/A	Electron Beam	Photon Counter	N/A	± 4 to 6 percent
Mass Flux	N/A	Quartz Crystal Microbalance	Frequency to Voltage Converter, DRVM	Sonic Orifice Flow	$\Delta\dot{m}/\dot{m}$ – 0.30
Probe Pressure	0 to 10 torr	Capacitance Absolute Transducer	DRVM	Calibration Curve from Comparison with Standard Transducer	± 0.25 percent

NOMENCLATURE

A	Nozzle exit-plane area, sensing area of QCM
A_s	Surface area of hot wire
A^*	Nozzle throat area
C_m	QCM calibration constant
d	Pitot probe diameter
f	QCM resonant frequency
h_c	Convective heat-transfer coefficient from wire, equal to $Q_c/[A_s(T_w - T_{aw})]$
I	Emitted photon flux
K	Constant, Eq. (2)
l	Orifice thickness
$\dot{m}$	QCM mass change per unit time
M_L	Nozzle Mach number, based on geometric area ratio A/A^* ignoring nozzle boundary layer
M	Mach number
n	Number density
p	Pressure
p_o'	Pitot pressure
Q_c	Rate of heat transfer
R	Distance of QCM from nozzle exit plane
$\tilde{R}$	Gas Constant

r^*	Nozzle throat radius
Re_0r^*	Throat Reynolds number
Re_2d	Probe Reynolds number, $\varrho_\infty U_\infty d/\mu_2$
R_w	Hot-wire resistance
S	Speed ratio, $U_\infty(2\,\tilde{R}\,T_0)^{1/2}$
T	Temperature
U	Velocity
γ	Ratio of specific heats
θ	Nozzle wall angle, local flow angle
μ	Viscosity
ϕ	Angle of QCM to nozzle axis
ϱ	Density

Subscripts

0	Stagnation chamber
2	Downstream of normal shock
aw	Adiabatic wall
cl	Centerline
w	Wire, wall
∞	Free-stream static
$\theta = 0$	At angle 0